Electrochemical Synthesis of Transition Metal Nitride Films & Powders

or

'New Routes to Old Materials'

Lucy E. Griffiths

a thesis presented for the degree of

Doctor of Philosophy

The University of Edinburgh

2000

EX BIBL. UNIV. EDINBURGH

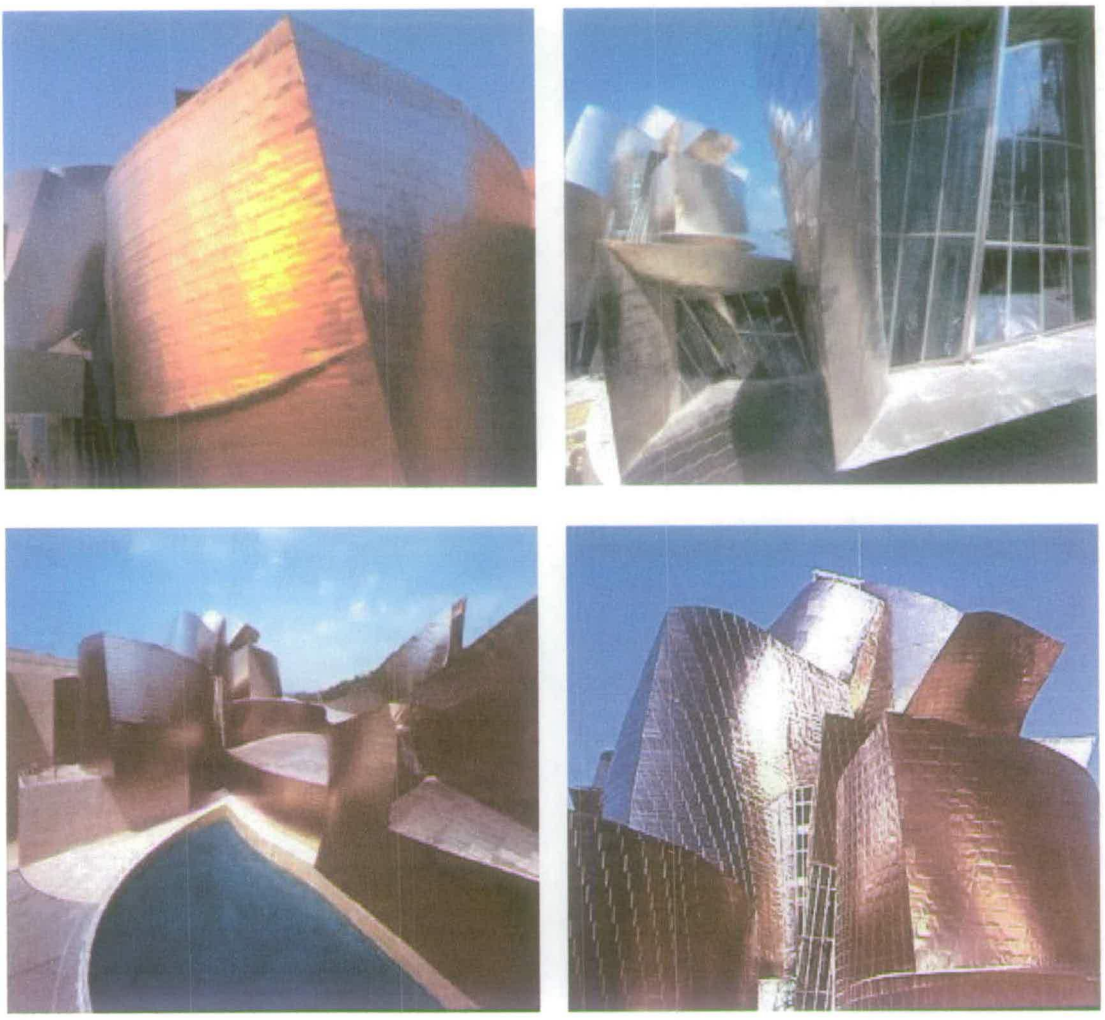

Images of Bilbao's **Guggenheim Museum**, (designed by architect Frank O. Gehry) built from limestone covered in 'fish-scale' panels of titanium guaranteed to last 100 years

Declaration

This thesis has not been submitted, in whole or in part, for any degree at this or any other university. The work is original and my own, carried out under the direction of Drs C. R. Pulham & A. R. Mount; where this is not so credit has been duly given.

Abstract

A novel method for the electrochemical synthesis of titanium nitride thin films and powders has been developed. This involves the anodisation of an oxide-free titanium electrode in a solution of potassium amide in liquid ammonia. The system is inherently free from carbon-, halide- and oxygen-containing contaminants. At -78°C and atmospheric pressure gold-coloured films of titanium nitride are produced, which adhere very well to the substrate. The amount of charge passed may be used to control the thickness of the resulting film. The films have been characterised by electrochemical studies, scanning electron microscopy with energy dispersive X-ray spectroscopy, Raman spectroscopy, magnetic and reflectance measurements, microhardness testing and X-ray photoelectron spectroscopy.

A thick-walled pressure cell has been constructed in order to contain liquid ammonia at 25°C at a pressure of 10 bar. Operation under these conditions favours the synthesis of nano-particulate powders. The powders have been characterised by scanning electron microscopy with energy dispersive X-ray spectroscopy, Raman spectroscopy, transmission electron microscopy and electron diffraction. The method has also been extended to the synthesis of molybdenum, tungsten, tantalum, aluminium and iron nitrides.

A new route for the electrodeposition of titanium metal has also been designed. The precursor $K_3[Ti(SCN)_6]$ in acetonitrile solution or dissolved in a novel 1-butyl-3-methylimidazolium thiocyanate 'ionic liquid', has been used to deposit titanium on copper or iron under ambient conditions. The films have been characterised by electrochemical studies and SEM-EDXS.

Acknowledgements

I am very grateful for the training and patient guidance offered by my two supervisors *Dr Colin Pulham* and *Dr Andy Mount* over the past three years. Their infectious enthusiasm has made this project extremely enjoyable to work on.

I would also like to thank *Dr Martin Lee* and *Dr John Craven* in the Department of Geology, and *Mr John Findlay* at the Science & Engineering Electron Microscope Facility for their invaluable help with the TEM, electron diffraction and SEM-EDXS work. I also appreciate the assistance of *Dr Paul Wilthew* at the Analytical Research Section of the National Museums of Scotland with the earlier SEM-EDXS work.

Thanks also to *Prof. Andrew Harrison* and research group for powder XRD and SQUID support and for the use of furnaces. *Mr Derek Jardine* also kindly granted me access to the Department of Mechanical Engineering's hardness testing apparatus. Special thanks to *Mr Stuart Johnstone* for performing the tricky glassblowing required for various pressure cell designs, and numerous repairs.

I am indebted to the *British Council* for their generous sponsorship of a Monbusho Research Fellowship in the Summer of 1999 which allowed me to work in the research group of *Prof. Toshiaki Ohta* at the Department of Chemistry, The University of Tokyo, Japan. Thanks to Prof. Ohta and group (especially *Dr Kondoh* and *Ms Kaoru Okamoto*) for making it possible for me to take vital XPS measurements and for such a warm reception in Japan.

Finally I would like to acknowledge the *EPSRC* for the funding of my studentship, and *The Royal Society of Chemistry* for subsidising my attendance at several conferences.

Contents

Declaration i

Abstract ii

Acknowledgements iii

Contents iv

1. Introduction to Binary Nitrides 1

1.1 Occurrence 1

1.2 Properties, Structure and Applications 5

1.2 Synthesis 7

1.3 Characterisation 9

1.4 Bibliography 9

2. Characterisation Methods 10

2.1 Carbon, Hydrogen, Nitrogen (CHN) Analysis 10

2.2 Magnetic Measurements 10

2.3 Raman Spectroscopy 12

2.4 Reflectance Measurements 13

2.5 Scanning Electron Microscopy - Energy Dispersive X-Ray Spectroscopy (SEM-EDXS) 13

2.6 Transmission Electron Microscopy (TEM) - Electron Diffraction 15

2.7 UV-Visible Spectroscopy 17

2.8 Vickers Hardness Testing 18

2.9 X-Ray Photoelectron Spectroscopy (XPS) 18

2.9.1 Spin-Orbit Coupling 21

2.9.2 Chemical Shifts 21

2.9.3 Depth Profiling 23

2.10 X-Ray Powder Diffraction 24

2.11 Bibliography 26

3. Synthesis of Titanium Nitride at Low Temperature **27**
3.1 Introduction 27
3.1.1 Gas-Phase Methods of Synthesis 28
3.1.2 Laser Ablation and Sputtering 31
3.1.3 Solution-Phase Methods of Synthesis 33
3.1.4 Solid-Phase Routes 34
3.1.5 Electrochemical Routes 35
3.2 Strategy 39
3.3 Experimental 40
3.3.1 Preparation of Potassium Amide in Liquid Ammonia 40
3.3.2 Set-up of Electrochemical Cell 42
3.4 Electrochemistry 43
3.4.1 Electrochemical Protocol 43
3.4.2 Stripping of Oxide Layer 43
3.4.3 Nitride Synthesis 45
3.5 Characterisation 51
3.5.1 Powder X-Ray Diffraction (XRD) 51
3.5.2 Magnetic Measurements 52
3.5.3 Reflectance Measurements 53
3.5.4 Raman Spectroscopy 54
3.5.5 Energy Dispersive X-Ray Spectroscopy (EDXS) 57
3.5.6 X-Ray Photoelectron Spectroscopy (XPS) 58
3.5.6.1 Surface Measurements 58
3.5.6.2 Sputtering Experiments 65
3.5.7 Vickers Hardness Testing 72
3.6 Summary and Conclusions 75
3.7 Bibliography 78

4. Synthesis of Titanium Nitride at Ambient Temperatures **82**
4.1 Strategy 82
4.2 Experimental 83
4.2.1 Set-up of Electrochemical Cells 83
4.2.1.1 Single Compartment Pressure Cell 84

4.2.1.2 Two-Compartment Pressure Cell 85
4.3 Electrochemistry 86
4.3.1 Stripping of Oxide Layer 86
4.3.1.1 Single Compartment Cell 86
4.3.1.2 Two Compartment Cell 86
4.3.2 Nitride Synthesis 87
4.3.2.1 Single Compartment Cell 87
4.3.2.2 Two Compartment Cell 93
4.4 Characterisation of Pressure Cell Products 96
4.4.1 Raman Spectroscopy 97
4.4.2 Scanning Electron Microscopy (SEM) 98
4.4.3 Diffraction Methods 99
4.4.3.1 Single Crystal X-Ray Diffraction 99
4.4.3.2 X-Ray Powder Diffraction (XRD) 99
4.4.3.3 Transmission Electron Microscopy (TEM) - Electron Diffraction 102
4.4.4 Carbon, Hydrogen, Nitrogen (CHN) Analysis 107
4.5 Summary and Conclusions 108
4.6 Bibliography 111

5. Electrochemical Synthesis of Group 6 Nitrides 112
5.1 Introduction 112
5.1.1 Properties and Applications 112
5.1.2 The Mo-N System 113
5.1.3 The W-N System 114
5.1.4 Synthesis 114
5.1.3.1 Molybdenum Nitrides 115
5.1.3.2 Tungsten Nitrides 117
5.2 Strategy 119
5.3 Experimental 119
5.4 Electrochemistry 120
5.4.1 Stripping of Oxide Layer 120
5.4.1.1 Molybdenum 120
5.4.1.2 Tungsten 121

5.4.2 Nitride Synthesis 122
5.4.2.1 Molybdenum 123
5.4.2.2 Tungsten 126
5.5 Characterisation of Molybdenum Nitride 131
5.5.1 X-Ray Photoelectron Spectroscopy (XPS) 131
5.5.1.1 Surface Measurements 131
5.5.1.2 Sputtering Experiments 135
5.5.2 Transmission Electron Microscopy (TEM) - Electron Diffraction 142
5.5.3 Raman Spectroscopy 144
5.6 Characterisation of Tungsten Nitride 149
5.6.1 X-Ray Photoelectron Spectroscopy (XPS) 149
5.6.1.1 Surface Measurements 149
5.6.2 Transmission Electron Microscopy (TEM) - Electron Diffraction 153
5.6.3 Raman Spectroscopy 158
5.7 Summary, Conclusions and Further Work 159
5.8 Bibliography 162

6. Electrochemical Synthesis of Tantalum, Aluminium & Iron Nitrides 165
6.1 Introduction 165
6.1.1 Tantalum Nitride 165
6.1.1.1 Properties and Applications 165
6.1.1.2 Methods of Synthesis 166
6.1.2 Aluminium Nitride 168
6.1.2.1 Properties and Applications 168
6.1.2.2 Methods of Synthesis 169
6.1.3 Iron Nitride 172
6.1.3.1 Properties and Applications 172
6.1.3.2 Methods of Synthesis 173
6.2 Strategy 176
6.3 Experimental 176
6.4 Electrochemistry 177
6.4.1 Tantalum 177
6.4.1.1Stripping of Oxide Layer 177

6.4.1.2 Nitride Synthesis 178
6.4.2 Aluminium 179
6.4.2.1 Stripping of Oxide Layer 179
6.4.2.2 Nitride Synthesis 180
6.4.3 Iron 181
6.4.3.1 Stripping of Oxide Layer 181
6.4.3.2 Nitride Synthesis 181
6.5 Characterisation of Tantalum, Aluminium and Iron Nitrides 184
6.5.1 Tantalum 184
6.5.1.1 Transmission Electron Microscopy (TEM) - Electron Diffraction 184
6.5.1.2 Raman Spectroscopy 186
6.5.1.3 Scanning Electron Microscopy (SEM) 190
6.5.2 Aluminium 191
6.5.2.1 Transmission Electron Microscopy (TEM) - Electron Diffraction 191
6.5.3 Iron 192
6.5.3.1 X-Ray Photoelectron Spectroscopy (XPS) 192
6.5.3.2 Transmission Electron Microscopy (TEM) - Electron Diffraction 196
6.5.3.3 Raman Spectroscopy 197
6.7 Summary, Conclusions and Further Work 200
6.8 Bibliography 203

7. Electrodeposition of Titanium Metal **209**
7.1 Introduction 209
7.1.1 Existing Methods for the Isolation of Pure Titanium 210
7.1.1.1 From Ore to Metal: Reduction of Titanium Dioxide 210
7.1.1.2 Reduction of Titanium Tetrachloride 211
7.1.1.3 The Van Arkel and De Boer Process 212
7.1.1.4 Electrochemical Methods 212
7.2 Strategy 218
7.3 Synthesis and Characterisation of Titanium-Containing Precursors 220
7.3.1 Preparation and Purification 220
7.3.1.1 Synthesis of $M_3[Ti(SCN)_6]$, (M = K, NH_4) 220
7.3.1.2 Synthesis of $K_2[Ti(SCN)_6]$ 221

7.3.2 Analysis and Spectroscopy 222
7.3.2.1 Carbon, Hydrogen, Nitrogen (CHN) Analysis 222
7.3.2.2 UV-Visible Spectroscopy 222
7.3.2.3 Crystal Growth 226
7.4 Electrochemical Studies of the Thiocyanato Complexes and Characterisation of Electrodeposited Films 227
7.4.1 Set-up of Electrochemical Cell 227
7.4.2 Electrochemical Protocol 228
7.4.2.1 Cyclic Voltammetry 228
7.4.2.2 Electrodeposition 228
7.4.3 $K_3[Ti(SCN)_6]$ Solution with a Copper Working-Electrode 229
7.4.3.1 Cyclic Voltammetry 229
7.4.3.2 Electrodeposition and Characterisation of Films 230
7.4.4 $K_2[Ti(SCN)_6]$ with Copper Working-Electrode 241
7.4.4.1 Cyclic Voltammetry 241
7.4.4.2 Electrodeposition 242
7.4.5 $(NH_4)_3[Ti(SCN)_6]$ with a Copper Working-Electrode 243
7.4.5.1 Cyclic Voltammetry 243
7.4.6 $K_3[Ti(SCN)_6]$ with an Iron Working-Electrode 243
7.4.6.1 Cyclic Voltammetry 243
7.4.6.2 Electrodeposition and Characterisation of Films 244
7.4.7 $(NH_4)_3[Ti(SCN)_6]$ with an Iron Working-Electrode 245
7.4.7.1 Cyclic Voltammetry 245
7.4.7.2 Electrodeposition and Characterisation of Films 246
7.5 Electrochemistry of Thiocyanato Derivatives in and Electrodeposition from an 'Ionic Liquid' 249
7.5.1 Strategy 249
7.5.2 Synthesis and Characterisation of 1-Butyl-3-Methylimidazolium Thiocyanate 250
7.5.3 Set-up of the Electrochemical Cell 251
7.5.4 Electrochemistry of $K_3[Ti(SCN)_6]$ in BmimSCN with a Copper Working-Electrode 252
7.5.4.1 Cyclic Voltammetry 252

7.5.4.2 Electrodeposition and Characterisation of Films 253
7.6 Summary, Conclusions and Further Work 255
7.7 Bibliography 259

A.1 Conferences & Courses **A.1**

Chapter 1:

Introduction to Binary Nitrides

1.1 Occurrence

Although the Earth's atmosphere is 78% nitrogen, the elements present in the crust are almost all present as oxides. Nitrides are far less numerous than oxides (or sulfides and phosphides), for two thermodynamic reasons. Firstly, although nitrides are comparable in stability to oxides with respect to dissociation to the free gaseous atoms, nitrides are less stable with respect to dissociation to the elements in their standard states. This is because of the huge bond enthalpy of dinitrogen (941 $kJmol^{-1}$) compared with that of dioxygen (500 $kJmol^{-1}$). This situation is demonstrated for silicon oxide and nitride respectively in *equations 1.1-1.4*. The Gibbs free energy changes for the processes are also shown (in $kJmol^{-1}$ of diatomic gas). *Equations 1.1* and *1.2* show formation of the two materials from the free gaseous atoms where ΔG_f is similar for both the oxide and the nitride, and *equations 1.3* and *1.4* show formation from the elements in their standard states clearly indicating that the oxide would be formed preferentially [1].

$$3/2\ Si\ (g) + 2\ N\ (g) \rightarrow 1/2\ Si_3N_4\ (s) \qquad -1228\ kJmol^{-1} \quad \textbf{(1.1)}$$

$$Si(g) + 2\ O\ (g) \rightarrow SiO_2\ (s) \qquad -1183\ kJmol^{-1} \quad \textbf{(1.2)}$$

$$3/2\ Si\ (s) + N_2\ (g) \rightarrow 1/2\ Si_3N_4\ (s) \qquad -125\ kJmol^{-1} \quad \textbf{(1.3)}$$

$$Si\ (s) + O_2\ (g) \rightarrow SiO_2\ (s) \qquad -644\ kJmol^{-1} \quad \textbf{(1.4)}$$

The implication of this is that synthesis of nitrides generally occurs at high temperature with the use of nitrogen-containing reagents such as ammonia, which are more reactive than molecular nitrogen [2]. *Table 1.1* shows some free energies of formation of some relevant nitrides and oxides [3].

Oxides		Nitrides	
Compound	**ΔG°_f / kJmol^{-1}**	**Compound**	**ΔG°_f / kJmol^{-1}**
Li_2O	-560.7	Li_3N	-154.8
CaO	-602.5	Ca_3N_2	-410.0
Al_2O_3	-1573	AlN	-287.0
TiO_2	-891.2	TiN	-309.2
Ta_2O_5	-1920	Ta_3N_5	~-1154
MoO_3	-669.4	Mo_2N	-50.2
WO_3	-756.7	W_2N	-46.0
Fe_2O_3	-744.8	Fe_2N	+12.6
CuO	-128.4	Cu_3N	+74.5

Table 1.1: Standard Gibb's free energies of formation of some binary metal oxides and nitrides [3]

The second thermodynamic factor is that although nitrogen is a very electronegative element (3.1 on the Allred-Rochow scale), the ionic contribution to bonding is only small. This is due to the high enthalpy of formation of N^{3-} from atomic N (2300kJmol^{-1}) compared to the enthalpy of formation of O^{2-} from atomic O (700kJmol^{-1}) [3]. Although nitrogen is often considered to be formally in the -3 oxidation state, in reality there is a large degree of covalent bonding in many metal nitrides. In many compounds, nitrogen behaves in a way which is intermediate (conventionally) between carbon and oxygen in the first row. Sometimes nitrides show similarities with carbides in terms of metallic structure and properties. The fact that oxynitrides can be formed also demonstrates the similarity to oxides [2]. The N^{3-} ion has been assigned a radius of 146pm, slightly larger than the isoelectronic O^{2-} ion (140pm). The nitride

1.1 Occurrence

Although the Earth's atmosphere is 78% nitrogen, the elements present in the crust are almost all present as oxides. Nitrides are far less numerous than oxides (or sulfides and phosphides), for two thermodynamic reasons. Firstly, although nitrides are comparable in stability to oxides with respect to dissociation to the free gaseous atoms, nitrides are less stable with respect to dissociation to the elements in their standard states. This is because of the huge bond enthalpy of dinitrogen (941 $kJmol^{-1}$) compared with that of dioxygen (500 $kJmol^{-1}$). This situation is demonstrated for silicon oxide and nitride respectively in *equations 1.1-1.4*. The Gibbs free energy changes for the processes are also shown (in $kJmol^{-1}$ of diatomic gas). *Equations 1.1* and *1.2* show formation of the two materials from the free gaseous atoms where ΔG_f is similar for both the oxide and the nitride, and *equations 1.3* and *1.4* show formation from the elements in their standard states clearly indicating that the oxide would be formed preferentially [1].

$$3/2\ Si\ (g) + 2\ N\ (g) \rightarrow 1/2\ Si_3N_4\ (s) \qquad -1228\ kJmol^{-1} \quad \textbf{(1.1)}$$

$$Si(g) + 2\ O\ (g) \rightarrow SiO_2\ (s) \qquad -1183\ kJmol^{-1} \quad \textbf{(1.2)}$$

$$3/2\ Si\ (s) + N_2\ (g) \rightarrow 1/2\ Si_3N_4\ (s) \qquad -125\ kJmol^{-1} \quad \textbf{(1.3)}$$

$$Si\ (s) + O_2\ (g) \rightarrow SiO_2\ (s) \qquad -644\ kJmol^{-1} \quad \textbf{(1.4)}$$

The implication of this is that synthesis of nitrides generally occurs at high temperature with the use of nitrogen-containing reagents such as ammonia, which are more reactive than molecular nitrogen [2]. *Table 1.1* shows some free energies of formation of some relevant nitrides and oxides [3].

Oxides		Nitrides	
Compound	ΔG°_f / kJmol^{-1}	Compound	ΔG°_f / kJmol^{-1}
Li_2O	-560.7	Li_3N	-154.8
CaO	-602.5	Ca_3N_2	-410.0
Al_2O_3	-1573	AlN	-287.0
TiO_2	-891.2	TiN	-309.2
Ta_2O_5	-1920	Ta_3N_5	~-1154
MoO_3	-669.4	Mo_2N	-50.2
WO_3	-756.7	W_2N	-46.0
Fe_2O_3	-744.8	Fe_2N	+12.6
CuO	-128.4	Cu_3N	+74.5

Table 1.1: Standard Gibb's free energies of formation of some binary metal oxides and nitrides [3]

The second thermodynamic factor is that although nitrogen is a very electronegative element (3.1 on the Allred-Rochow scale), the ionic contribution to bonding is only small. This is due to the high enthalpy of formation of N^{3-} from atomic N (2300kJmol^{-1}) compared to the enthalpy of formation of O^{2-} from atomic O (700kJmol^{-1}) [3]. Although nitrogen is often considered to be formally in the -3 oxidation state, in reality there is a large degree of covalent bonding in many metal nitrides. In many compounds, nitrogen behaves in a way which is intermediate (conventionally) between carbon and oxygen in the first row. Sometimes nitrides show similarities with carbides in terms of metallic structure and properties. The fact that oxynitrides can be formed also demonstrates the similarity to oxides [2]. The N^{3-} ion has been assigned a radius of 146pm, slightly larger than the isoelectronic O^{2-} ion (140pm). The nitride

ion is an excellent ligand, particularly towards second- and third-row transition metals. It is considered to be the strongest π donor known [3].

A result of these energetic considerations is that nitrides are generally refractory i.e. they are difficult to sinter and crystallise, yet have high dissociation pressures. On heating, decomposition with loss of dinitrogen is common. From a practical point of view, synthesis of metal nitrides is challenging as many are moisture-sensitive and react with water to produce hydroxides and ammonia [1].

The extent of binary nitride formation in the periodic table is shown in *Figure 1.1* [4]. The absence of binary alkali metal (Group 1) nitrides other than Li_3N is striking. This is a consequence of the importance of stoichiometry in influencing the structure and stability of solids. For example, Na_3N with four coordinate sodium would require nitride ions to be surrounded by twelve sodium ions, a situation that would result in significant repulsion between the sodium ions. By the time groups 13 and 14 are reached, the metal to non-metal ratio is closer to one and stable ceramics such as AlN and Si_3N_4 are formed. The low decomposition temperatures of the heavier alkaline earth (Group 2) nitrides can be explained by the decreasing lattice energy of the material and the increasing ionisation potential of the metal as the group is descended. The instability of the later transition element nitrides such as Co_3N_2 and Ni_3N_2 compared to, say, the readily formed Mg_3N_2, is due to the larger energy of atomisation of the metallic elements. Thus the enthalpy of sublimation of magnesium at 0K is 145kJmol^{-1}, while for nickel it is 428kJmol^{-1} [1].

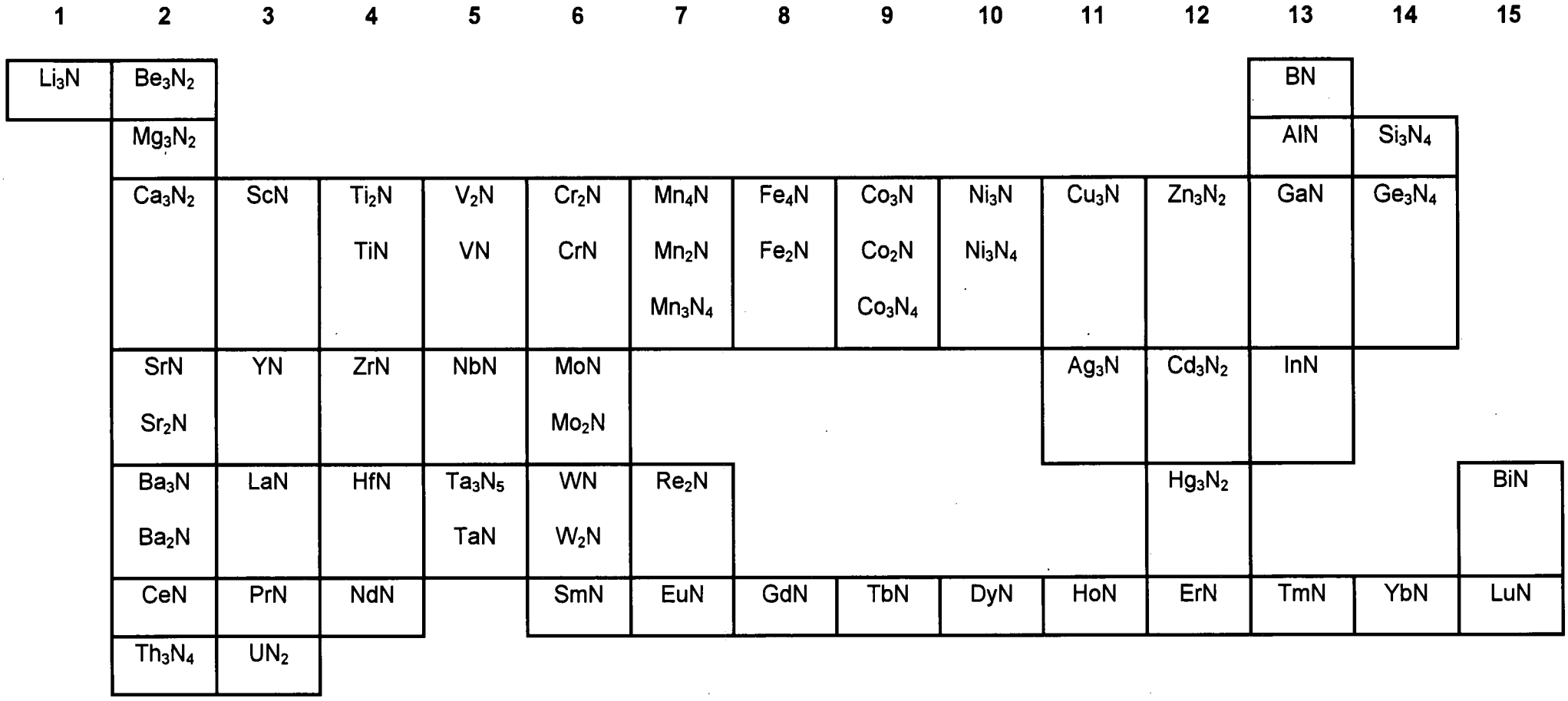

Figure 1.1: The extent of binary nitride formation in the periodic table. The heavier alkali metals, the heavier late transition metals and the late main-group metals do not form stable nitrides [4].

1.2 Properties, Structure and Applications

The transition metal nitrides are generally materials with extremely high melting points (2000-4000°C) and hardness, which leads to their main commercial use as thin films on cutting surfaces and as wear-resistant coatings (in gears, bearings and in sliding parts). *Table 1.2* shows the melting points of some transition metals and their nitrides [5]. These materials normally adhere strongly to the substrate (usually steel, sometimes with the aid of a carbide interlayer), and are stable, so show little tendency to stick to the component being worked. Unless the operating temperature is very high, nitride coatings are stable to aerial oxidation. In general they are only slowly attacked by very concentrated acid solutions. Nitrides have smaller band gaps than oxides and so they are frequently highly coloured. For example, Ta_3N_5 and Li_3N are a brilliant red, Mg_3N_2 is green, and AlN and Ca_3N_2 are brown [1].

4	5	6	4	5	6
Ti	V	Cr	TiN	VN	Cr_2N
1677	1917	1900	2949	2177	~1500
Zr	Nb	Mo	ZrN	NbN	MoN
1852	2487	2610	2982	2204	D
Hf	Ta	W	HfN	TaN	WN
2222	2997	3380	3387	3093	D

Table 1.2: Melting points (°C) of some transition metals and their binary nitrides. 'D' indicates decomposition [5].

Nitrides show high strength at elevated temperature and good corrosion resistance. They are also exploited for their electrical properties in integrated circuits. Many are superconductors, with relatively high superconducting critical temperatures (T_c). NbN-based alloys have a T_c of about 18K, and show excellent upper critical fields and critical currents. T_c in nitrides is sensitive to the degree of defect structure. Nitrides have been suggested as materials for thin film miniature superconducting solenoids, high-Q inductors, Josephson junctions and bolometers [5].

Nitrides are not primarily stoichiometric phases, but have a range of compositions and vacancy concentrations (up to 50% on non-metal lattice sites) which strongly influence the physical properties. Even at the stoichiometric ratio, appreciable vacancy concentrations (a few atomic percent) can exist on both sublattices. When a large fraction of non-metal sites are vacant, the vacancies tend to exhibit long-range order, which significantly affects the properties. Different processing techniques tend to produce different defect structures and hence materials with variable properties [5].

Because of the possibility of vacancies ordering in the defect structure, the crystal chemistry of nitrides is complex. Nitrogen is a smaller atom than the transition metal atoms which means it is always located interstitially in the lattice to form close-packed structures. The structure can either be viewed as an arrangement of interstitial atoms and vacancies in a relatively simple metal atom structure, or as a geometric arrangement of co-ordination polyhedra, the principle ones being either an octahedral or trigonal prismatic grouping of metal atoms around a nitrogen atom. Most binary nitride crystals can be reconstructed from arranging only a few different polyhedra; in other words there are recurring structural motifs as in oxide chemistry. Bonding in these phases consists of a complex combination of localised

metal-to-metal and non-metal-to-metal interactions resembling both covalent and metallic bonding. There is only a slight degree of ionic bonding. The octahedral arrangement of metal atoms around a central nitrogen maximises the metal to non-metal bonding, but the presence of the nitrogen also increases the strength of metal-to-metal bonds [5]. Ionic contribution to bonding does become important when large mole fractions of very electropositive elements are present, e.g. in Li_3N. This effect also explains the stability of ternary nitrides containing both an electropositive element and a transition metal. A good example of this is the difference between Ni_3N, which decomposes to the elements at 700°C (even under 1 atmosphere pressure of nitrogen), and CaNiN which remains stable until 1100°C under N_2. In both materials the nickel is formally in the +1 oxidation state [4]. This has been referred to as an inductive effect by Etourneau *et al.* [6].

Transition metal nitrides are typically metallic in their electrical, magnetic and optical properties. Most of these properties vary only slightly from those of the parent transition metal element. The electrical and magnetic properties are extremely sensitive to defect structure, in particular vacancies. This is why the temperature dependence of the thermal and electrical conductivities can differ considerably from the metal itself. The electrical resistivities show very little temperature dependence [5].

1.2 Synthesis

Polycrystalline samples of nitrides are usually prepared by powder metallurgy. Direct reaction of metal, metal hydride, metal oxide (in the presence of carbon), or metal chloride powders with nitrogen or ammonia is often the best route to pure compounds. The exclusion of moisture and oxygen is of paramount importance. Group 6 elements cannot be nitrided

with nitrogen but ammonia can be used for an often extended reaction time. The preparation of high purity, homogeneous samples requires very high temperatures and highly purified gases. *Table 1.3* shows some typical reaction temperatures for some refractory nitride syntheses [5].

Reaction	Temperature / °C
Ti or TiH_2 + N_2 → TiN	1200
Zr or ZrH_2 + N_2 → ZrN	1200
Hf or HfH_2 + N_2 → HfN	1200
V + N_2 → VN	1200
Nb + N_2 → NbN	1200
Ta + N_2 → TaN	1100-1200
Cr + NH_3 → CrN + H_2	800-1000
Mo + NH_3 → MoN + H_2	400-700
W + NH_3 → WN + H_2	700-800

Table 1.3: Typical reaction temperatures for some transition metal binary nitride syntheses [5]

Single crystals of metal nitrides have been grown by vapour transport processes. Thin films can be formed either by laying down a film of the metal using vacuum sublimation followed by heating in nitrogen or ammonia (chemical vapour deposition), or by reactive sputtering when both elements are laid down together from a flux of metal and nitrogen or ammonia vapours [5]. This latter process is sometimes assisted by a plasma to reduce the operating temperature (to avoid distortion of the substrate), with the added benefit of producing a very

uniform coat. In general the highest operating temperature compatible with the substrate is employed as this gives the best adhesion of the coating [7].

1.3 Characterisation

The complete characterisation of nitrides is very difficult. As discussed above, the properties of the material will depend upon the crystal structure and lattice parameters, the chemical composition (including impurities such as oxygen), defect structure and vacancy concentration, grain size and porosity, and sample homogeneity [5]. The techniques used for the characterisation of the nitrides synthesised in this work are discussed in chapter 2. Methods that required minimal post-processing of the materials were chosen.

1.4 Bibliography

[1] N. E. Brese and M. O'Keeffe, '*Crystal Structure of Inorganic Nitrides*' in '*Structure and Bonding*', **79**, 309-378, 1992

[2] R. Marchand, Y. Laurent, J. Guyader, P. L'Haridon and P. Verdier, *Journal of the European Ceramic Society* **8**, 197-213, 1991

[3] N. N. Greenwood and A. Earnshaw, '*Chemistry of the Elements*' Pergamon Press 1984

[4] F. J. DiSalvo and S. J. Clarke, *Current Opinion in Solid State and Materials Science*, **1**, 241-249, 1996

[5] L. E. Toth, '*Refractory Materials: Transition Metal Carbides and Nitrides*', **7**, 1-28, 1971

[6] J. Etourneau, J. Portier and F. Menil, *J. Alloys and Compounds*, **188**, 1-7, 1992

[7] N.J. Archer, *Brit. Ceram. Proc.*, **34**, 187-194, 1984

Chapter 2:

Characterisation Techniques

2.1 Carbon, Hydrogen, Nitrogen (CHN) Analysis

CHN analysis was performed using a Perkin-Elmer 2400 CHN Elemental Analyser. A potential problem was the air sensitive nature of the powders and their tendency to form oxides. This was overcome by sealing samples in pre-weighed aluminium capsules in a nitrogen-filled dry box. As nitrides are also refractory materials, it was found that incomplete combustion made reliable results difficult to obtain.

2.2 Magnetic Measurements

Magnetic properties depend on the presence of unpaired electrons, especially in *d* or *f* orbitals. If a substance is placed in a magnetic field, 'H' (in Gauss), then the density of lines of force in the sample, known as the magnetic induction, 'B' (in Gauss), is given in *equation 2.1* where 'I' is the magnetic moment of the sample per unit volume (in Gauss).

$$B = H + 4\pi I \qquad (2.1)$$

The permeability, 'P', and the susceptibility, 'κ' (both dimensionless), are defined as in *equations 2.2* and *2.3*.

$$P = \frac{B}{H} = 1 + 4\pi\kappa \qquad (2.2)$$

$$\kappa = \frac{I}{H} \qquad (2.3)$$

The molar susceptibility, 'χ' (in cm^3mol^{-1}) , is given in *equation 2.4* where 'F' is the formula weight and 'd' is the density of the sample.

$$\chi = \frac{\kappa F}{d} \qquad (2.4)$$

The different kinds of magnetic behaviour may be distinguished by the values of P, κ, and χ, and their temperature and field dependence, as in *Table 2.1*.

Material	P	Typical χ / cm^3mol^{-1}	Effect on χ of increasing T	Field dependence?
Diamagnetic	< 1	-1×10^{-6}	none	no
Paramagnetic	> 1	0 to 10^{-2}	decreases	no
Ferromagnetic	>> 1	10^{-2} to 10^{6}	decreases	yes
Antiferromagnetic	>1	0 to 10^{-2}	increases	(yes)

Table 2.1: Magnetic permeabilities and susceptibilities [1]

The Curie Law states that the magnetic susceptibility is inversely proportional to temperature; a plot of the inverse of χ against temperature is a straight line which intercepts the origin. The Curie-Weiss Law often provides a better fit with experimental data through the introduction of the Weiss constant 'θ'. This allows the plot of the inverse of χ against temperature to intercept at negative values of T. For ferro- and antiferromagnetic substances, the temperature dependence of χ does not fit the simple Curie/Curie-Weiss Laws. Ferromagnetic materials show a very large susceptibility at low temperatures that decreases exponentially with rising temperature. Above a certain temperature (the ferromagnetic Curie temperature,

T_c), the material becomes paramagnetic. For antiferromagnetic materials, the value of χ increases with rising temperature up to a critical temperature known as the Neel point, T_N. Again, above T_N the material reverts to paramagnetic behaviour [1]. These critical temperatures are often characteristic of particular compounds or phases, and can give a good indication of purity and the degree of defect structure within the material.

Magnetic measurements were made using a Quantum Design $MPMS_2$ Superconducting QUantum Interference Device (SQUID). Samples were cooled to 1.8 K in a 100 Gauss applied field and then in zero applied field (to assess the field dependence), and measurements made on warming. The magnetic data were converted into molar susceptibilities,χ, by use of *equation 2.5*, where 'M' is the magnetisation and the empirical constant $2x10^{-5}$ in this case corrects for the effect of the gelatine sample capsule containing the sample.

$$\chi = \left[\left(M + 2x10^{-5}\right)/H\right] / \text{ no. moles of sample} \qquad \textbf{(2.5)}$$

2.3 Raman Spectroscopy

Atoms in solids vibrate at frequencies of approximately 10^{12} to 10^{13} Hz. In the standard Raman experiment, the sample is illuminated with monochromatic light, usually generated by a laser, and two types of scattered light are produced. Rayleigh scattering emerges with unchanged energy and wavelength, and Raman scattering emerges with either shorter or longer wavelength than the incident light, also with a much lower intensity than the Rayleigh scattering. Photons of light from the laser, of frequency 'ν_0', induce transitions in the sample and the photons gain or lose energy as a consequence. For a vibrational transition of frequency 'ν_1', associated Raman lines of frequency $\nu_0 \pm \nu_1$ appear in the scattered beam.

The principal selection rule for a vibrational mode to be Raman active is that the nuclear motions involved must produce a change in polarizability [1].

Raman spectra were recorded using a LabRam (Instruments S.A.) confocal microscope with 25 mW laser excitation at 632.8 nm focused to a diameter of 126 μm with a x 50 objective lens which also served to collect the scattered light. The same objective allowed the sample to be viewed in white light and Raman spectra could be collected from areas as small as 2μm in diameter. Spectra on the anti-Stokes side ($\nu_0 + \nu_1$) are shown.

2.4 Reflectance Measurements

A Spex Fluoromax fluorescence spectrometer was used to take surface reflectance measurements under synchronous scan conditions. The sample orientation was adjusted to ensure that the scattered light entered the detector, and the wavelength of excitation and emission monochromators were set to be equal. Spectra are plotted as wavelength (in nm), against the ratio of the intensity of the reflected light to the incident light (in arbitrary units); assuming the intensity of the incident light is constant at any wavelength, the intensity of the reflected light is plotted unaltered in practice.

2.5 Scanning Electron Microscopy - Energy Dispersive X-Ray Spectroscopy (SEM-EDXS)

Scanning Electron Microscopy is useful for studying the texture, topography and surface features of solids. Features up to tens of micrometres in size can be observed (the resolution range is $\sim 10^{-2}$ to $\sim 10^{2}$ μm), and because of the depth of focus possible, the images have a

definite three-dimensional quality. Electrons from the electron gun are focused by a series of electromagnetic lenses to a small spot, 50 to 100Å in diameter, on the surface of the sample. The electron beam is scanned systematically over the sample and both X-rays and secondary electrons are emitted. The secondary electrons are used to build up an image of the sample, and the X-rays can be used for chemical analysis. The main limitation of SEM is that the lower resolution limit is ~100Å [1].

Elemental analysis is a possible additional feature with SEM. During Energy Dispersive X-ray Spectroscopy (EDXS), an electron beam is targeted on the sample and ejection of a core electron occurs. Decay of an electron from a higher energy level to fill the vacancy leads to emission of X-ray energy which can be detected. The exact energy of this emission is governed by the energy of the transition and is therefore characteristic of the element under analysis. The incident electron beam analyses a volume of the sample of approximately 3μm dimensions, so sometimes peaks due to the underlying substrate are observed for thin films.

Initial analyses were performed on a CamScan Scanning Electron Microscope equipped with an Oxford Instruments AN10000 Energy Dispersive X-ray Spectrometer, which can detect elements heavier than sodium. Later analyses were performed using a Phillips XL30CP SEM equipped with an Oxford Instruments Isis EDXS system which can detect elements heavier than carbon. Small sections of the electrode were mounted on metal stubs for entry into the microscope. Powder samples were gold coated to prevent electrostatic charging.

2.6 Transmission Electron Microscopy (TEM) - Electron Diffraction

TEM allows study of very fine particles which are too small to be viewed by SEM. The particles are mounted conventionally on conducting grids from solvent suspension. Samples should be thinner than ~2000Å to allow electron transmission (electrons have low penetrating power) and image formation. Collection of electron diffraction patterns on photographic film is also possible. Electrons are scattered mainly by interaction with the electric fields of atomic nuclei. As with X-ray diffraction the diffracted intensity depends on the square of the atomic number, and this aids the location of heavy atoms but makes light atoms difficult to define [3]. The advantage of electron diffraction over X-ray diffraction is that the scattering efficiency of electrons is higher. In principle this allows the less ambiguous determination of the type of ordering of light atoms, such as nitrogen and oxygen, in the presence of heavy atoms. It also allows small amounts of sample to be used.

The electron wavelengths used are much smaller than typical X-ray wavelengths. Consequently the Bragg angles for diffraction are small and the strong diffracted beams are concentrated into a narrow cone centred on the undiffracted beam. There is a large, but finite, number of lattice planes in a crystal and in theory all of these can diffract the incident beam. However in practice in some cases the resultant intensity is zero. This situation is usually encountered when the material possesses a particular symmetry or type of lattice. These missing reflections are known as 'systematic absences'. Systematic absences arise if either the lattice type is non-primitive or if elements of space symmetry are present [1]. The rules governing the values that the Miller indices (h, k, and l) can take in certain unit cells are shown in *Table 2.2* [2].

Cell (Bravais Lattice)	Values of h, k and l
Primitive, P	all values of h,k,l (i.e. none are forbidden)
Body centred, I	(h+k+l) must be even
Face centred, F	h, k and l must be all odd or all even
Base centred, C	h and k must be both odd or both even

Table 2.2: Systematic absences of Miller indices in diffraction [2]

One disadvantage of electron diffraction is the possible occurrence of secondary diffraction. As the diffracted electron beams are of high intensity, these can go on to interact with further planes of atoms in the sample. Secondary diffraction can lead to the appearance of additional spots in the diffraction pattern which complicates indexing. Also the intensities recorded can be very unreliable, and so are not used quantitatively for structure determination [1].

TEM imaging was performed on a Philips CM 120 Biotwin microscope. The powder samples were prepared for analysis by mounting in epoxy resin, which was ion thinned on one side. This side was then attached to a plastic mount, and the top side was then also ion thinned so the total sample thickness was of the order of micrometres. It is possible that such ion bombardment may lead to structural modification of the sample, so caution must be exercised when interpreting sample morphologies. A suitable area of the sample was then framed by a copper ring and the section cut out and coated with amorphous carbon to prevent electrostatic charging in the microscope Electron diffraction patterns were indexed with a magnifier, and the d-spacings were calculated by dividing the 'camera factor' (= 23.786) by the ring radii (in mm). An accurate camera factor was calculated by sputtering the sample with gold, and multiplying the inner ring radius (10.1mm) by the known d-spacing for this plane of

diffraction (2.355Å). The gold, in effect, acted as an *in situ* standard. The d-spacings obtained were compared with those of known phases.

2.7 UV-Visible Spectroscopy

UV-visible spectroscopy involves the absorption or emission in UV or visible regions due to electronic transitions within molecules. Energies of these electronic transitions, and sometimes resolved vibrational or rotational detail can be obtained.

Solutions of transition metal complexes are often highly coloured, and UV-visible spectroscopy can provide information on the electronic structure of the species responsible for such transitions. Electronic transitions in transition complexes take place between occupied and vacant orbitals. These orbitals can be considered to lie predominantly on the metal, the ligands or to be shared between the metal and ligands, leading to five types of transition:

(a) ligand-based transitions

(b) metal-based (*d-d*) transitions

(c) metal-to-ligand transitions

(d) ligand-to-metal transitions

(e) intervalence transitions

Transitions in UV-visible spectra can be assigned to one of the above categories by studying the number, positions and intensities of bands, and comparing these with data for well established species [3].

Experiments were performed on a Unicam UV-visible spectrometer over the wavelength range 190-900nm. The resolution was set at 1nm. Sample solutions were run in quartz cuvettes with solvent spectra subtracted as blanks.

2.8 Vickers Hardness Testing

Many of the materials synthesised in this work are employed industrially for their extreme strength and wear-resistant properties. Hardness testing can be performed in order to assess how well the materials perform compared with their counterparts produced by conventional methods.

Hardness tests were performed using a Leitz Miniload 2 optical microscope equipped with a variable mass diamond indentation probe. Loads between 15 and 100g were used to make indents in the films. The lengths of the two diagonals of the indent were measured and averaged, and then used to calculate a Vickers Hardness value ('H_v' in kg/mm^2), by using *equation 2.6*, where 'F' is the measuring force (in Newton), and 'd' is the mean indent diagonal (in μm) [4].

$$H_V = \frac{\left(1.89x10^5 F\right)}{d^2} \qquad \textbf{(2.6)}$$

2.9 X-Ray Photoelectron Spectroscopy (XPS)

Surface analysis by XPS is accomplished by irradiating a sample with monochromatic soft X-rays and analysing the energy of the electrons emitted. Magnesium K_α radiation (1253.6 eV)

was used here. Such photons have limited penetrating power in a solid, of the order of 1-10 micrometers. They interact with atoms in this surface region by the photoelectric effect, causing electrons to be emitted (*Figure 2.1a*). The emitted electrons have kinetic energies, 'KE', according to *equation 2.7*, where 'hν' is the energy of the photon, 'BE' is the binding energy of the atomic orbital from which the electron originates, and 'ϕ_s' is the work function (the value of which depends on the spectrometer and the sample).

$$KE = h\nu - BE - \phi_s \qquad (2.7)$$

The binding energy may be regarded as an ionisation energy of the atom for the particular shell involved. Since there is a variety of possible ions from each type of atom, there is a corresponding variety of kinetic energies of the emitted electrons. In addition there is a different probability, or cross-section, for each process.

In addition to the photoelectrons emitted in the photoelectric process, Auger electrons are emitted due to relaxation of the energetic ions left after photoemission. This Auger electron emission occurs roughly 10^{-14} seconds after the photoelectric event. In the Auger process an outer electron falls into the inner orbital vacancy and a second electron is emitted, carrying off the excess energy (*Figure 2.1b*). The Auger electron possesses kinetic energy equal to the difference between the energy of the initial ion and the doubly-charged final ion, and is independent of the mode of the initial ionisation. Thus, photoionisation normally leads to two emitted electrons, a photoelectron and an Auger electron.

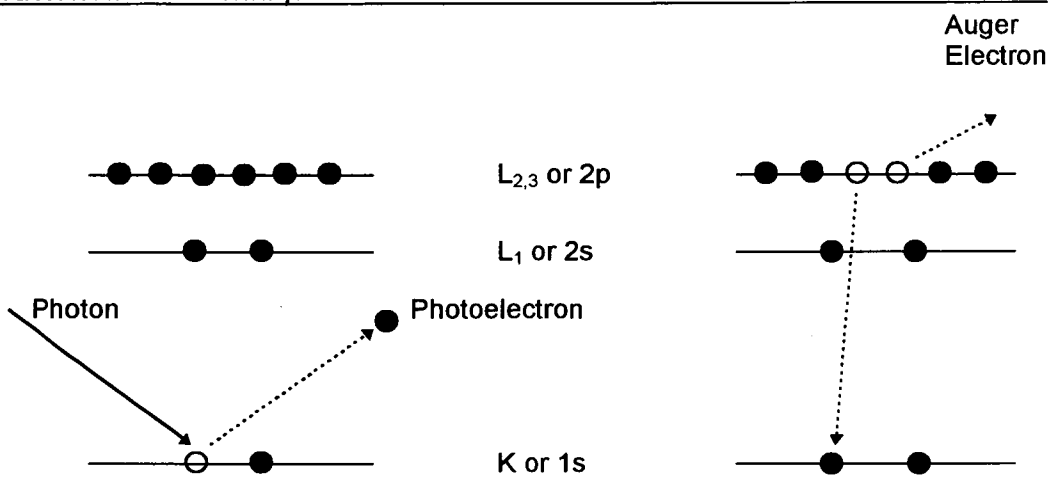

Figure 2.1: (a) (left) the photoelectric process, and **(b)** (right) the Auger process

The path length of the emitted electrons is only of the order of tens of Ångstroms. So while ionisation occurs to a depth of a few micrometres, only those electrons that originate within tens of Ångstroms below the solid surface can leave the surface without energy loss. These electrons are detected according to their kinetic energy and produce peaks in the spectra [5].

XPS measurements were taken using a Rigaku 7000 Spectrometer under vacuum (approximately 10^{-7} Pa) in the group of Professor Toshiaki Ohta at the Department of Chemistry, The University of Tokyo, Japan. The X-ray spot size was approximately 5mm in diameter. The gold 4f lines (83.8 and 87.45 eV), were used as a standard for spectrum calibration. Wide scans were recorded between 0 and 1000eV with a step size of 1eV, a path energy of 50eV and a dwell time of 0.2s. Narrow scans were recorded over the appropriate photon energy range for the element under study with a step size of 0.1eV, a path energy of 15eV and a dwell time of 0.5s. At least three scans were recorded and averaged for each element, with ten scans used for nitrogen because of its low cross-section of photoionisation.

2.9.1 Spin-Orbit Coupling

The orbit of an electron around a nucleus induces a magnetic field, the intensity and direction of which depend on the electron velocity and on the radius of the orbit respectively. The latter two variables can be characterised by the orbital angular momentum, $\underline{l}$ (for which $\underline{l}$ = 0, 1, 2, 3, 4....), which is quantized as the electron can only travel in certain discrete orbitals. Another property of an orbiting electron is its spin which also induces a magnetic field. This magnetic field has an associated spin momentum, $\underline{s}$ (for which $\underline{s} = \pm 1/2$). The total electronic angular momentum is the vector sum of $\underline{l}$ and $\underline{s}$. To arrive at what is known as the j-j coupling, the total angular momentum, $\underline{j}$ (for which $\underline{j}$ = 1/2, 3/2, 5/2,...), of a single isolated electron is obtained by summing vectorially the individual electronic spin and angular momenta. To arrive at the total angular momentum for the atom, summation is performed for all electrons, the result being the total atomic angular momentum, $\underline{J}$, where $\underline{J} = \Sigma\underline{j}$. The j-j coupling scheme nomenclature is summarised in *Table 2.3*.

Peaks in the photoelectron spectra are assigned in terms of the spectroscopic name of the atomic level from which the photoelectron was ejected. It can be seen that all but the *s* levels are split into doublets. The relative intensities of the doublet peaks are given by the ratio of their respective degeneracies ($2\underline{j} + 1$), and are shown in *Table 2.4* [6].

2.9.2 Chemical Shifts

Non-equivalent atoms of the same element in a solid can give rise to core-level peaks with measurably different binding energies. This effect, which is a measure of the effective charge

of the atom, can be due to difference in formal oxidation state, molecular environment, or lattice site is known as the 'chemical shift' [6].

Quantum Numbers n	l	j	X-Ray Suffix	X-Ray Level	Spectroscopic Level
1	0	1/2	1	K	$1s_{1/2}$
2	0	1/2	1	L_1	$2s_{1/2}$
2	1	1/2	2	L_2	$2p_{1/2}$
2	1	3/2	3	L_3	$2p_{3/2}$
3	0	1/2	1	M_1	$3s_{1/2}$
3	1	1/2	2	M_2	$3p_{1/2}$
3	1	3/2	3	M_3	$3p_{3/2}$
3	2	3/2	4	M_4	$3d_{3/2}$
3	2	5/2	5	M_5	$3d_{5/2}$

Table 2.3: X-ray and spectroscopic notation [6]

Subshell	j Values	Area Ratio
s	1/2	-
p	1/2, 3/2	1 : 2
d	3/2, 5/2	2 : 3
f	5/2, 7/2	3 : 4

Table 2.4: Spin-orbit splitting parameters [6]

2.9.3 Depth Profiling

Sputtering is a destructive technique for the *in situ* 'sectioning' of samples. The sample is bombarded with noble gas ions accelerated in an ion gun to energies above 100eV. A small fraction of this energy is transferred to surface atoms and causes their ejection, thereby allowing the underlying layer to be analysed. In principle the rate of sputtering, 'Z' (in ms^{-1}), can be calculated from *equation 2.8*, where 'M' is the atomic mass, 'ρ' is the density of the sample (in kgm^3), 'N_A' is the Avogadro number, 'e' is the electronic charge, 'S' is the sputtering yield from literature data (in number of atoms/ion) and 'j_p' is the primary ion current density (in Am^{-2}).

$$Z = \frac{M}{\rho N_A e} S j_p \qquad \textbf{(2.8)}$$

Only a rough estimate of Z can be achieved in practice as S depends on several parameters including the element under study, energy, mass, angle of the incident ions, and surface composition. The sputtering yield for an atom depends on the rate of energy loss of the incident ion, the energy transfer from atom to atom and the binding energy in the outermost layers. Using a 500eV argon ion beam, the sputtering yield of titanium is calculated to be 1.24 atoms/ion, oxygen 1.3 atoms/ion, nitrogen 0.6 atoms/ion and carbon 0.36 atoms/ion [6]. A better way to measure the sputtering rate is to measure the time taken to sputter through a standard layer of known thickness.

Depth profiling studies using sputtering were achieved by eroding the surface with an argon ion gun. The argon gas pressure was 1.5-1.7 x 10^{-3} Pa, with an accelerating voltage of 200 or 500V, and a beam current of 0.1mA (the magnitude of the beam current is proportional to the

sputtering yield). Measurements were taken normal to the surface (0 degrees). To calibrate the sputtering rate under the conditions of the experiment, a layer of silicon of 100Å thickness was eroded, which took 60s at a voltage of 200V. The calculated rate was increased proportionally for use with data collected at a high voltage of 500V. For the electrodeposited TiN and MoN films, peak areas were calculated by integration of the narrow scan peaks (over the ranges 394.6-399.6 eV for nitrogen, 528.6-535.6 eV for oxygen, 452.6-456.6 eV for titanium and 226.5-229.5eV for molybdenum), and these were plotted against the approximate depth, based on silicon. For titanium metal, peak areas had to be calculated by integration of peaks in the wide scan spectra, as narrow scans were not recorded at all time intervals. Fewer data points were available for this, so the error is greater. Clearly the sputtering rate of the nitride films may differ significantly from that of silicon, but unfortunately the lack of a suitable nitride standard made it impossible to obtain a closer estimate.

2.10 X-Ray Powder Diffraction

Although the determination of structure is most readily achieved using single crystal X-ray diffraction, there are many compounds for which sufficiently large single crystals are not available. In this situation X-ray powder diffraction methods can be employed to gain structural information. A powder is made up of many microcrystallites orientated in a random manner, and this assembly will produce cones of reflection when irradiated. These cones are observed as a pattern of rings on a photographic plate and can be described by their Bragg angle and intensity. Although much information is lost compared to single crystal diffraction, the pattern of lines produced can sometimes be indexed and used to provide information on cell dimensions, symmetry and atomic positions. This process is substantially easier if the structure is partially known or is very simple. More commonly, powder diffraction patterns

are used to provide a 'fingerprint' of a material, and in this way unknown materials can be identified by qualitative comparison with a database of patterns of well characterised materials [3]. Powder patterns can also be used to give an indication of particle size, provided that the average particle size is less than ~2000Å. As the particle size decreases, the line width increases, with lines eventually disappearing into the background radiation when the particles are as small as 20-100Å [1].

Experiments were performed on a Phillips diffractometer over a 2θ range of 5-70° using copper K_α radiation. Aluminium slides were used to mount powder samples which had been thoroughly ground to ensure a random orientation of crystallites. Glancing angle experiments were performed with an incident beam at 2° to the sample. This allows analysis of the surface layer, and is particularly suitable for the characterisation of thin films. PC-APD and PC-Identify Philips software was used for recording, analysis and phase matching of patterns.

2.11 Bibliography

[1] A. R. West, '*Solid State Chemistry and its Applications*', Wiley 1984

[2] M. H. Loretto, '*Electron Beam Analysis of Materials*', Chapman & Hall, (2nd Edition), 1994, 234

[3] E. A. V. Ebsworth and D. W. H. Rankin, S. Cradock, '*Structural Methods in Inorganic Chemistry*', Blackwell Scientific Publications (2nd Edition) 1987

[4] Leitz Miniload 2 Instruction Manual

[5] C. D. Wagner, W. M. Riggs, L. E. Davis and J. F. Moulder, '*Handbook of X-Ray Photoelectron Spectroscopy*', Perkin-Elmer Corporation

[6] Ed. D. Briggs and M. P. Seah, '*Practical Surface Analysis*', J. Wiley and Sons 1983

Chapter 3:

Preparation of Titanium Nitride Films at Low Temperature

3.1 Introduction

Titanium nitride occurs naturally as the mineral osbornite in which it adopts a cubic NaCl-type structure with a lattice constant for the stoichiometric material (TiN) of 4.24Å. It also exhibits vacancy defect structures which are stable over the composition range ($0.6<N/Ti<1.16$) [1]. ε-Ti_2N is also known, which has the anti-rutile structure [2]. Neutron diffraction studies have shown δ-Ti_2N to have an ordered structure with a unit cell twice the volume of the original rocksalt cell [3]. The ε-form seems to have a wider range of stoichiometry and is generally more deficient in nitrogen than the δ-form. [4]. The nitride Ti_3N_4 is known as the product of the reaction between $Ti(NH_2)_4.TiBr_4.8NH_3$ and KNH_2, but no structural characterisation has been reported [5].

In recent years there has been much interest in titanium nitride for a variety of functional applications owing to the fact that that it displays a number of properties that make it useful under relatively extreme conditions. As a result of predominantly covalent bonding, TiN is harder than all elemental metals and sapphire, and is nearly as hard as diamond [6]. It has a very high melting point (2950°C), so that it is classified as a refractory material. Its lack of reactivity makes it resistant to corrosion, and it demonstrates strong adhesion to most metals, semiconductors and insulators. It is superior to titanium metal in terms of both thermal and electrical conductivity. It exhibits *d*-band metallic conductivity, and calculations of the electronic structure reveal that there is charge transfer from titanium to nitrogen [7]. Titanium nitride has seen service as a functional coating on steel cutting tools and high-wear engineering components [8]. It is effective as a diffusion barrier between silicon and aluminium or a low resistance contact in integrated circuits [9]. It has also been suggested for use in low barrier Schottky diodes. In warmer climates it is used as a wavelength-selective transparent optical

film in solar control coatings on windows [6]. Its attractive gold colour also allows use as a decorative coating for jewellery [10].

The suitability and performance of TiN in these roles depend, in brief, on the exact film stoichiometry, thickness, hardness, level of contaminant inclusion, and microstructure. In turn, these factors are governed by the method of film growth employed. The physical properties of the films produced may vary over several orders of magnitude depending on both the technique and conditions used. For example for perfectly stoichiometric films, resistivities have been reported ranging from 25 to 4500 $\mu\Omega$cm [11-13], and Vickers hardness values between 340 and 4000 $kgmm^{-2}$ [14-16].

3.1.1 Gas-Phase Methods of Synthesis

TiN can be prepared by direct reaction of titanium with nitrogen or ammonia at temperatures near 1200°C for extended periods of time [1]. The standard Gibb's free energy of formation of TiN (-309.2 kJ mol^{-1}) from the elements is not as exothermic as that of TiO_2 (-891.2 $kJmol^{-1}$) because atomic nitrogen has to be formed from dinitrogen due to the triple bond dissociation energy 941 $kJmol^{-1}$, compared with the dioxygen double bond dissociation energy of 500 $kJmol^{-1}$.

Chemical Vapour Deposition (CVD) involves the chemical reaction of precursors in the gas phase or at a heated substrate surface. The technique can produce dense, powder-free films at high growth rates and with good step coverage. A high degree of control of the film morphology, stoichiometry, and microstructure can be attained. Pure TiN can be formed by the reaction of titanium tetrachloride with nitrogen and hydrogen at around 1000°C (*Equation*

3.1) [17]. The deposition temperature can be lowered to around 550°C by using ammonia instead of a nitrogen-hydrogen mixture (*Equation 3.2*) [18].

$$TiCl_4 + 1/2\ N_2 + 2\ H_2 \rightarrow TiN + 4\ HCl \qquad (3.1)$$

$$6TiCl_4 + 8\ NH_3 \rightarrow 6\ TiN + 24\ HCl + N_2 \qquad (3.2)$$

This work was repeated more recently by another group using rapid thermal CVD equipment, allowing the operating temperature to be brought down to as low as 450°C [19]. At 400°C a new crystalline phase was observed, and identified as TiNCl. Chloride contamination is always a problem with this system (always greater than 2 atomic %), as it may cause high film resistivity and corrosion of the substrate. A proportion of weakly bound chloride can be removed by annealing, but the remainder stays bonded as TiNCl.

Such high temperatures give excellent bonding of coat to substrate, but can lead to problems when the substrate has a low melting point (e.g. polymers), or where diffusion of boundary layers can occur (e.g. silicon wafers, alloys). For example, the core hardness of steel substrates is reduced at such temperatures, and so objects have to be re-hardened after the 'nitriding' process. Unfortunately this sometimes leads to dimensional changes, which are unacceptable in precision tools [1]. The need for lower operating temperatures has initiated the search for single-source CVD precursors which could undergo more facile intramolecular decomposition. These molecules contain the required elements strongly bound sometimes in the correct stoichiometry together with other ligands to aid volatility and which detach easily during the reaction, hence avoiding contamination. Winters *et al* [20] produced the first single-source TiN precursor by the reaction between titanium tetrachloride and *tert*-

butlyamine in dichloromethane (*Equation 3.3*). TiN was prepared from the chloro-alkylamido- precursor at 500°C and a pressure of 0.05mm Hg (*Equation 3.4*).

$$TiCl_4 + 6\ {}^tBuNH_2 \rightarrow [TiCl_2(NH{}^tBu)_2(NH_2{}^tBu)_2]_n + 2\ {}^tBuNH_3{}^+Cl^- \quad \textbf{(3.3)}$$

$$[TiCl_2(NH{}^tBu)_2(NH_2{}^tBu)_2]_n \rightarrow TiN \quad \textbf{(3.4)}$$

There has also been some success using alkylamido derivatives of titanium in the presence of ammonia. A well-studied precursor is tetrakis(dimethylamido) titanium, 'tdmat', a volatile yellow liquid (b.pt. 50°C at 0.05 mmHg). This precursor can be prepared relatively easily (*Equation 3.5*), and contains no potentially corrosive chloride ligands.

$$TiCl_4 + 4\ LiNMe_2 \rightarrow Ti(NMe_2)_4 + 4\ LiCl \quad \textbf{(3.5)}$$

Reaction of tdmat with excess ammonia (5% in a helium gas carrier) takes place at atmospheric pressure between 150-450°C as proposed in *Equation 3.6*. The N/Ti ratios in the resulting films, as elucidated by Rutherford backscattering spectrometry, were independent of deposition temperature, although there was no deposition below 350°C without ammonia. The films were reported to be free from oxygen and carbon impurities, although they did contain a significant amount of hydrogen, probably due to incomplete decomposition of the precursor at these temperatures. Carbon impurities also reached significant levels when hydrogen was used instead of ammonia [6].

$$6\ Ti(NMe_2)_4 + 8\ NH_3 \rightarrow 6\ TiN + 24\ NHMe_2 + N_2 \quad \textbf{(3.6)}$$

Isotopic labelling studies were performed on this system by Dubois [10]. Although the precursor contains N directly bound to Ti, the nitrogen in the TiN films was found to be derived from ammonia, which also had the secondary role of reducing carbon contamination.

The crystal structure of the first organometallic nitride cubane was published in 1995 [21]. The complex, prepared by an ammonolysis reaction in toluene at 90°C (*Equation 3.7*) has a Ti_4N_4 core similar to the structural motif in cubic TiN. It was suggested that the molecule might be a suitable starting material for titanium nitride polymer formation.

$$4\,[Ti(\eta^5\text{-}C_5Me_5)(NMe_2)_3] + 4\,NH_3 \rightarrow [\{Ti(\eta^5\text{-}C_5Me_5)\}_4(\mu_3\text{-}N)_4] + 12\,NHMe_2 \quad \textbf{(3.7)}$$

A method that was developed specifically for TiN synthesis is Physical Vapour Deposition (PVD). Here a titanium target is sputtered by an argon ion beam in an atmosphere of nitrogen or ammonia at 400-550°C [22]. The nitrogen reacts with titanium atoms deposited on the hot substrate surface. An alternative to heat as the source of energy is the use of a plasma to induce molecular excitement. TiN can be formed in this way from a low pressure nitrogen gas plasma at temperatures below 500°C (Plasma-Assisted CVD) [1].

3.1.2 Laser Ablation and Sputtering

Ablation, or sputtering, is the process by which atoms or clusters are ejected from a solid surface as a result of high energy beam bombardment [23]. Much work has been done on the interaction of pulsed lasers with solids. In particular, the rare-gas halide (RGH) excimer laser, discovered in 1975, has demonstrated many materials-processing capabilities with applications in the semiconductor industry. Excimer lasers are a class of electronically

excited molecular gas lasers that emit high intensity, short pulses (tens of nanoseconds in duration) of ultraviolet light. The exact wavelength of emission depends on the gas mixture employed. There are two types of laser ablation mechanisms: thermal and electronic. Thermal processes depend on very rapid heating of the target, leading to vaporisation of solid and melted regions, as well as ablation caused by thermal shock between different layers of solid. Electronic processes cause either direct bond cleavage in the solid, or generation of electron-hole pairs with subsequent energy transfer to the surface atoms, with both mechanisms initiating ejection of material [24]. The energy of particles ejected *via* electronic processes is comparable to that reached during other non-thermal sputtering processes (approximately 10-20eV), but much higher than during standard thermal evaporation (0.1eV) [25].

Biunno *et al* [26] (and Auciello *et al* [27]), have produced polycrystalline films of TiN on silicon by a laser-induced physical vapour deposition method (LPVD, also known as radio frequency (r.f.) sputtering or pulsed laser deposition, PLD). The films were deposited between 25 and 550°C by the laser ablation of a hot-pressed TiN pellet in the presence of neutral or ionised nitrogen gas using a XeCl excimer laser. Atomic titanium and nitrogen as well as clusters of TiN were exfoliated from the target in this way and re-aggregated on the heated silicon substrate orientated perpendicular to the target pellet. Impurities present in the pellet were also carried over. The average grain size of 100Å stayed approximately constant as the substrate temperature was increased, although higher operating temperatures did reduce the oxygen impurity content of the film. The film thickness could be controlled by the energy density of the laser pulses, the number of pulses used, and the set-up geometry. Smooth films of uniform thickness (approximately 400-600Å) were produced in this way. Later Biunno *et*

al reported an equivalent method for epitaxial TiN growth on (100) magnesium oxide [28], and Vispute *et al* have deposited TiN on polymethylmethacrylate (softening point 80°C) [25].

High quality TiN films on steel were also prepared by Altshulin *et al via* a variation of the above LPVD method [29]. A titanium target was laser-ablated in an atmosphere of ammonia, and the ejected titanium atoms reacted with nitrogen atoms in the laser-induced plasma to yield a polycrystalline film. The optimum substrate temperature in terms of both adherence of the film and maintenance of the core strength of the steel was found to be 270°C.

Amorphous thin films of titanium oxynitride were produced by ion assisted deposition by Bittar *et al* [30] Titanium metal was sputtered in a nitrogen/oxygen atmosphere by an electron gun and films were deposited on copper, silicon or glass initially held at room temperature, but rising to 100°C during deposition owing to ion bombardment.

3.1.3 Solution-Phase Methods of Synthesis

The gas-phase methods discussed above operate at relatively high temperatures and require expensive equipment and/or precursors. During the late 1950s, investigations took place looking into low temperature preparative routes to the metal nitrides using chemistry in liquid ammonia. Under a pressure of one atmosphere ammonia exists as a liquid between -78 and -33°C, and it has physical and chemical properties quite similar to those of water. Both liquids are extensively hydrogen bonded and have anomalously high enthalpies of vaporisation. The two solvents are analogous in their auto-ionisation equilibria (*reactions 3.8* and *3.9*).

$$2NH_3 \rightarrow NH_4^+ + NH_2^- \qquad (3.8)$$

$$2H_2O \rightarrow H_3O^+ + OH^- \qquad (3.9)$$

Ammonia has a lower relative permittivity than water (ε_r = 22 and 82, respectively), and is not therefore as good a solvent for ionic substances. However, it is superior to water in its ability to dissolve covalent compounds.

Stepwise ammonolysis occurs (equivalent to hydrolysis in aqueous systems), when chlorides of titanium are added to liquid ammonia, leading to the formation of bright yellow insoluble amido/imido-bridged polymers [31]. More recently, analogous reactions have been performed with titanium alkylamides. On ammonolysis of $Ti(NMe_2)_4$ ('tdmat') a brick-red precipitate was obtained which was polymeric, non-volatile, and imido/nitrido-bridged with a high titanium content. Vacuum pyrolysis at 800°C brought about quantitative conversion to TiN; this process also occurred at much lower temperatures under a hydrogen atmosphere [32].

3.1.4 Solid-Phase Routes

Self-propagating high-temperature synthesis has been used to prepare nitrides by heating or igniting fine metal powders in the presence of nitrogen at high pressures, or by using sodium azide as a solid source of nitrogen. These types of reaction rarely go to completion, leaving unreacted metal or lower nitrides in the product. Cubic TiN has been produced as a powder by the exothermic, rapid metathesis reaction between solid titanium(III) chloride or titanium(IV) iodide and solid lithium nitride. The reaction was initiated by a resistively-heated wire and then became self-propagating. Temperatures up to 1400°C can be reached very

rapidly in these reactions, followed by prompt return to room temperature. Significant amounts of titanium metal were also produced, but these can be minimised by adding sodium azide to the lithium nitride [33].

Hector and Parkin have reported a similar metathesis reaction, this time between liquid $TiCl_4$ and lithium amide in a sealed tube (*Equation 3.10*). The reaction could be initiated thermally (at 400°C) or by friction (rapid stirring at room temperature). The micron sized TiN particles were washed free of LiCl with thf or water [34].

$$3\ TiCl_4\ (l) + 4\ Li_3N\ (s) \rightarrow 3\ TiN + 12\ LiCl + \tfrac{1}{2}\ N_2 \qquad \textbf{(3.10)}$$

3.1.5 Electrochemical Routes

Some electrochemical routes to titanium nitride have also been proposed. This is a promising synthetic strategy since the energy required for the process can be supplied electrically, and, in principle, without the use of high temperatures. Potentially this allows the coating of both thermally fragile and irregularly shaped substrates. The challenge is to find non-aqueous solvent systems that will support suitable titanium- and nitrogen-containing precursors.

Goto *et al.* announced a new nitriding process based on a LiCl-KCl eutectic melt at 450°C [35]. Nitrate or nitrite ions could be introduced into the melt (as KNO_3 or KNO_2), and then cathodically reduced at +0.4V (vs. Li^+/Li) to nitrogen atoms at the surface of a titanium electrode (*Equations 3.11-3.13*).

$$NO_3^- + 2e^- \rightarrow NO_2^- + O^{2-} \qquad (3.11)$$

$$NO_2^- + 2e^- \rightarrow NO^- + O^{2-} \qquad (3.12)$$

$$NO^- + e^- \rightarrow N_{ads} + O^{2-} \qquad (3.13)$$

Likewise, nitride ions could be directly introduced (as Li_3N) and the nitriding performed by anodic oxidation at +0.8V (vs. Li^+/Li) as in *Equation 3.14*.

$$N^{3-} \rightarrow N_{ads} + 3e^- \qquad (3.14)$$

It was suggested that the adsorbed N, in both cases, diffused into the titanium metal under the influence of the applied field to form various phases of TiN. The films were characterised by X-ray photoelectron spectroscopy, although no data for oxygen were reported. When using nitrate anions in the melt there is always a possibility of contamination of the films by oxide.

Schrechenbach *et al* obtained TiN films *via* a electrochemical route using high voltages [36, 37]. It is known that acetonitrile is chemisorbed on titanium at 0V, and thin polymeric films can be produced at +5V. In this method, titanium was anodically polarised in acetonitrile at 1500-3000V. Not surprisingly, in view of the amount of energy supplied, the acetonitrile molecules dissociated to form adsorbed nitrogen and carbon atoms at the titanium surface. These diffused into the metal to form cubic TiN and TiC phases, the crystallinity of which increased with the potential applied. No attempt was made to remove the native oxide layer from the titanium, so the film also contained significant amounts of oxygen.

Russel and Seibold have reported an electrochemical route for the preparation of precursors for ceramic metal nitrides which involved the oxidation of a metal anode in an acetonitrile solution consisting of a primary amine and tetrabutylammonium bromide (TBABr) [38]. The titanium-containing precursor formed after electrolysis produced TiN/TiC mixtures after calcination. Oxygen and carbon impurities ranged from 2-6% and 5-31% respectively, depending on the conditions. Nakajima and Shimada carried out a similar experiment by synthesising a TiN precursor at room temperature by galvanostatic electrolysis of titanium in an acetonitrile solution of n-butylamine/TBABr [39]. A black solid, believed to be butylamidotitanium, was obtained after removal of solvent and heating to 200°C. Pyrolysis under vacuum or in ammonia between 200 and 1000°C led to TiN powder production, with significant carbon inclusion if ammonia was omitted. Most titanium-containing species would produce TiN if subjected to these conditions, so the advantage of these methods is not apparent.

Systematic electrochemical studies performed in liquid ammonia were published in 1987 by Gill *et al* [40]. Anodic dissolution of twenty transition metals in acidic solutions was documented. The electrolytes studied were NH_4BF_4, NH_4SCN, $Cd(CN)_2$, KCN, and NH_4CN. For titanium metal, anodic dissolution produced primarily gaseous dinitrogen, but also a pale yellow compound independent of the electrolyte used. This compound decomposed to hydrated titanium dioxide on contact with air, and was proposed to be an amido complex of titanium, the same as that produced chemically from titanium tetrachloride and liquid ammonia. The authors also claimed that there was a small degree of plating of titanium at the cathode in these experiments, although they gave no evidence for the identity of the deposit obtained.

Ross, Wade and Crooks claimed to have improved on the earlier synthesis of precursors by reducing the level of oxygen and carbon contamination [41, 42]. They used NH_4Br/liquid ammonia electrolyte solutions. Electrolysis took place at -70°C, between +8 and 25V, for 6-10 hours. The dry residue (which was proposed to be a titanium amide/imide polymer), could be converted to TiN in 50% yield by calcination at 1100°C under flowing ammonia. This last step rather devalues the method as almost any titanium-containing compound would form TiN if heated in ammonia gas at such a temperature.

3.2 Strategy

The aim of this work was to produce thin films of pure titanium nitride in one step at moderate temperatures. In order for such a process to be of potential use in the semiconductor industry, an operating temperature of below 400°C is required. Above this temperature, silicon and aluminium begin to alloy. Ideally the operating temperature should be even less to allow deposition on lower melting substrates, such as polymers.

The chosen strategy involved modification of titanium metal through anodization in liquid ammonia solutions containing the *basic* electrolyte potassium amide, KNH_2. This approach draws on analogies with aqueous solvent systems where the use of high pH frequently encourages formation of metal oxides; it was thought that the strongly basic solutions employed here could promote direct nitride synthesis. Furthermore, it ensures that solution species attracted to the anode contain nitrogen rather than halide as is the case when NH_4Cl or NH_4Br are used as electrolytes. These acidic electrolytes (discussed in *section 3.1.3, 3.1.5*), also appear to promote the formation of amides and/or imides. The choice of electrically conducting titanium as the electrode should ensure close 'keying in' and hence good adhesion of the film with the substrate

Ammonia is a liquid in the range -78°C to -33°C. At such low processing temperatures, nucleation is enhanced over growth (although both are reduced with decreasing temperature) and deposits are expected to be microcrystalline or perhaps amorphous. Diffusion distances are short and diffusion times are long. These are precisely the process characteristics necessary for materials processing at nanoscalar dimensions [43].

3.3 Experimental

3.3.1 Preparation of Potassium Amide in Liquid Ammonia

All manipulations were performed under dry, oxygen-free nitrogen using a Schlenk line unless otherwise stated. In a typical experiment, ammonia gas (BOC) was condensed in a Schlenk tube at liquid nitrogen temperature (-196°C). The solid collected was allowed to melt in a dry ice/acetone bath (-78°C) to give approximately 200cm^3 of liquid ammonia. Potassium metal (approximately 0.5g, Aldrich) which had been cut free from oxide under paraffin, washed with cyclohexane (BDH), and then dried in a nitrogen gas stream was added to the liquid ammonia to produce a deep inky-blue solution. In such a dilute solution potassium ionizes to give K^+ and a quasi-free electron distributed over a cavity in the solvent of radius 300-340pm formed by the displacement of 2-3 ammonia molecules. These electrons are responsible for the blue colour [44]. Under these conditions, any water which is present reacts to give dihydrogen and potassium hydroxide. The solution was then allowed to evaporate under vacuum *via* the Schlenk line and the pure, dry ammonia was re-condensed in a Schlenk tube held at -196°C. The original solution turned from deep blue through black to bronze in colour during this process as the concentration of potassium increased. This is due to the concurrent removal of mobile electrons from their cavities as the complex K^- and the formation of K_2 dimers. Eventually the solution behaves as a molten metal in which the potassium cations are ammoniated [44]. The dry liquid ammonia thus produced could be stored indefinitely at -78°C under an atmosphere of dry nitrogen, but was stored for a maximum of 24 hours in the experiments described here.

Saturated solutions of potassium amide were formed by addition of oxide-free potassium metal (Aldrich) to the dry liquid ammonia. The resulting blue colour was discharged by the addition of catalytic Fe_3O_4 powder (Aldrich), with stirring according to *Equation 3.15*. Potassium amide was formed and hydrogen gas was evolved.

$$2\,K + 2\,NH_3 \rightarrow 2\,KNH_2 + H_2 \qquad (3.15)$$

The solubility of potassium amide in liquid ammonia at various temperatures is shown in *Table 3.1* [31]. It can be seen that, unusually, the solubility is greater at low temperature than at room temperature.

Temperature / °C	Solubility / g/100g NH_3
+25	3.6
-32.4	65.8
-50.5	39.1

Table 3.1: Solubility data for potassium amide in liquid ammonia [31]

The conductance of KNH_2 in liquid ammonia at -33.2°C is 351 $cm^2\ \Omega^{-1}\ mol^{-1}$. The conductivities of most electrolytes are similar in both aqueous and liquid ammonia solutions, despite their differing relative permittivities. Strong electrolytes which are completely ionised in water may exist as ion-pairs in ammonia up to concentrations of 10^{-3}M. Above this concentration, higher ion aggregates are formed. However, owing to the lower viscosity of ammonia compared with water, any ions produced have increased mobility [31].

3.3.2 Set-up of Electrochemical Cell

The saturated solution of potassium amide in liquid ammonia (approximately 125cm^3) was transferred to the nitrogen-flushed electrochemical cell *via* a filter cannula. This process removed the iron oxide catalyst and any excess potassium amide which had precipitated. The cell was maintained at -78°C by means of a dry ice/acetone bath.

The working electrode was a piece of titanium foil, of approximate area of 1cm^2 for each side (Aldrich, 0.025-0.5mm thickness, 99.98% purity), with a titanium wire (Aldrich, 0.81mm diameter, 99.7% purity) connection. The counter electrode was a platinum gauze (Johnson Matthey) of approximate area 2 cm^2, which was of sufficient area to ensure that the current was never limited by reaction at the counter electrode, and the pseudo-reference electrode was a polished platinum wire (Johnson Matthey). All potentials are quoted with respect to this pseudo-reference electrode. Ideally, a well defined reference electrode should be used, e.g. the standard hydrogen electrode, or a calomel electrode. Unfortunately these electrodes, whilst being very stable at moderate temperatures, are difficult to use in a sealed or high pressure environment and also can introduce small amounts of contaminant, which may in turn be incorporated into the deposited film. It was found that the platinum wire pseudo-reference electrode was stable for this system, although caution must be exercised when comparing with potentials measured in different systems.

3.4 Electrochemistry

3.4.1 Electrochemical Protocol

Electrochemical control was by means of a PP2 3-electrode potentiostat (Oxford Electrodes) and data were recorded using a Bryans 60000 x-y-t chart recorder (Advance Bryans), and later on a PC using in-house custom-written software using Visual Designer 3.0 [45].

3.4.2 Stripping of Oxide Layer

Prior to anodisation of the titanium working electrode, it was cycled for approximately 40 minutes at sweep rates of 50-100 mVs^{-1} between 0 V and a negative potential limit, always in excess of -1.5 V, such that a large negative current in the order of several mA was observed.

Figure 3.1a shows the initial cyclic voltammogram (CV) recorded for the titanium working electrode in a potassium amide solution of liquid ammonia. A large negative current (A) was observed on the reductive sweep, and is most likely to be due to reduction of the oxide layer and the production of free electrons which gave rise to a blue colour near the working electrode. During the reverse sweep to 0V, an associated oxidation peak was observed at *ca.* -1.50V (B). On continued cycling, this oxidation peak was observed to diminish as the reduction wave shifted to more negative potentials (*Figure 3.1b* and *c*). The cyclic voltammogram recorded after 30 minutes showed little decrease in the negative sweep and no oxidation peak in the positive sweep at these potentials (*Figure 3.1d*). It seems likely that this reaction is associated with the initial reduction of the thin layer of titanium(IV) oxide at negative potentials, followed by re-oxidation on the reverse sweep. On repeated cycling, a

fraction of the reduced oxide would be lost to the bulk by diffusion. Thus the cycling eventually results in the production of an oxide-free titanium surface. It is not clear in what form the oxide moves away from the electrode. It is possible that it is (a) lost as superoxide, peroxide, or oxide ions into solution; or (b) removed mechanically i.e. it drops off the electrode as an insoluble, lower oxidation state titanium oxide. The first explanation is more likely given that re-oxidation is seen to occur in the cyclic voltammogram.

The only other reactions which might be responsible for the peak observed during the reduction sweep are the plating of potassium or the evolution of gaseous dihydrogen. However, no change in the appearance of the titanium surface was observed, and no evolution of gas was seen.

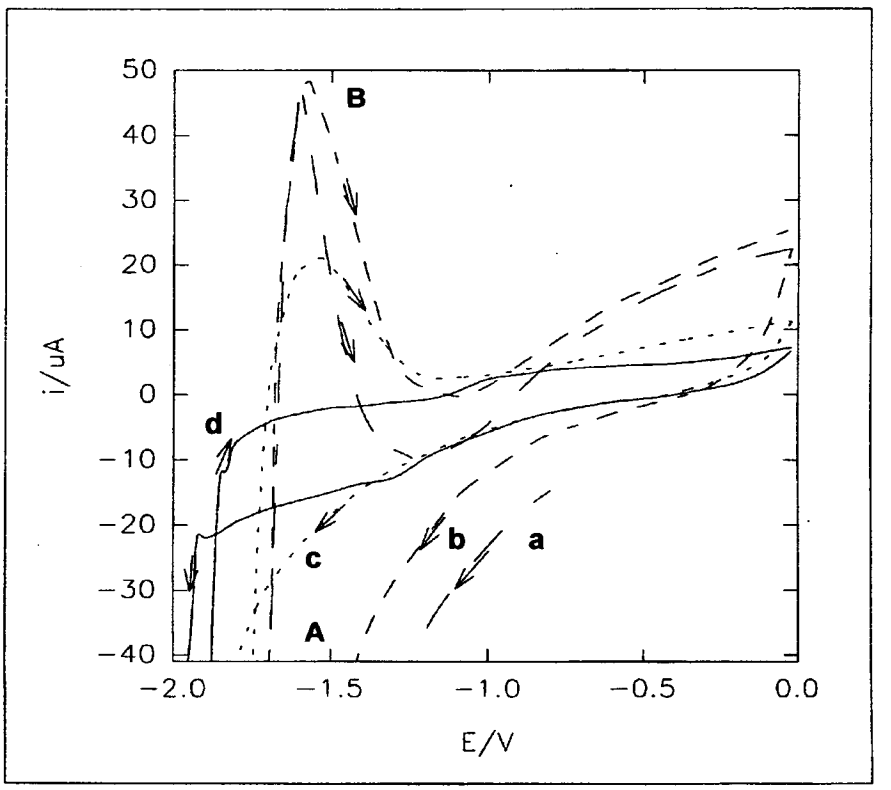

Figure 3.1: Cyclic voltammogram of titanium working electrode in liquid ammonia solution of potassium amide (**a**) initial scan, (**b**) and (**c**) after continued cycling, and (**d**) after 30 minutes.

3.4.3 Nitride Synthesis

Nitride syntheses took place between 0.00 and +5.00V using a 1kΩ resistor at -78°C. The voltage was always stepped up in increments small enough to ensure that the current decayed after each change. In one later experiment, the dry ice/acetone bath was lowered and the cell allowed to warm up slightly to observe the effect of increased temperature on the magnitude of the current passed.

On stepping the potential of the cleaned electrode from 0.00 V to +3.00 V, a large positive current in the order of several milliamperes was initially observed, indicative of oxidation at the electrode surface, which fell slowly with time (*Figure 3.2*). Increasing the electrode potential (first to 4.00 V, then to 5.00 V) resulted in an increase in the oxidation current, as did increasing the temperature of the solution from -78°C to -33°C by lowering the dry ice/acetone bath. At +5.00 V the current decayed to a steady value of approximately 0.1mA. Blue ammonia-solvated electrons were observed at the counter electrode surface. There was no sign of gas evolution at the electrodes. Stirring of the stagnant solution did not result in an increased current, indicating that the current was not limited by mass transport of solution species to the electrode. These results are consistent with the growth of a surface film on the electrode surface by an oxidation which involves liquid ammonia and/or amide.

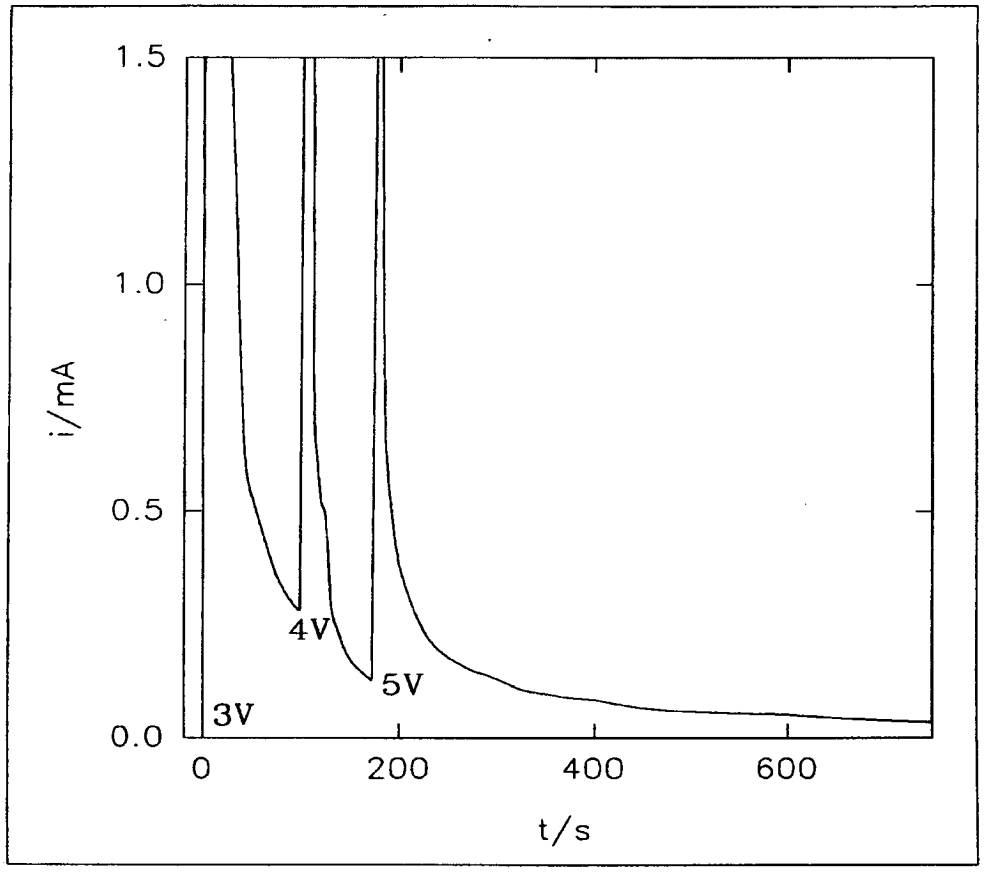

Figure 3.2: Current-time transient with potential step-up

CV studies of the clean titanium surface also indicated the growth of a surface film. The first sweep to oxidising potential showed an oxidation current due to nitride film growth. Subsequent cycles resulted in the progressive shift of this oxidation current to more positive potentials (*Figure 3.3*). The increase by more than 1.00 V in the potential window accessible by this electrode, coupled with the retention of a similar pseudocapacitance (indicated by the relatively constant area of the cyclic voltammogram in the region 0.00 V to 1.00 V), suggested that the deposited film was relatively inert and was conducting; this is a promising indication that the film was titanium nitride.

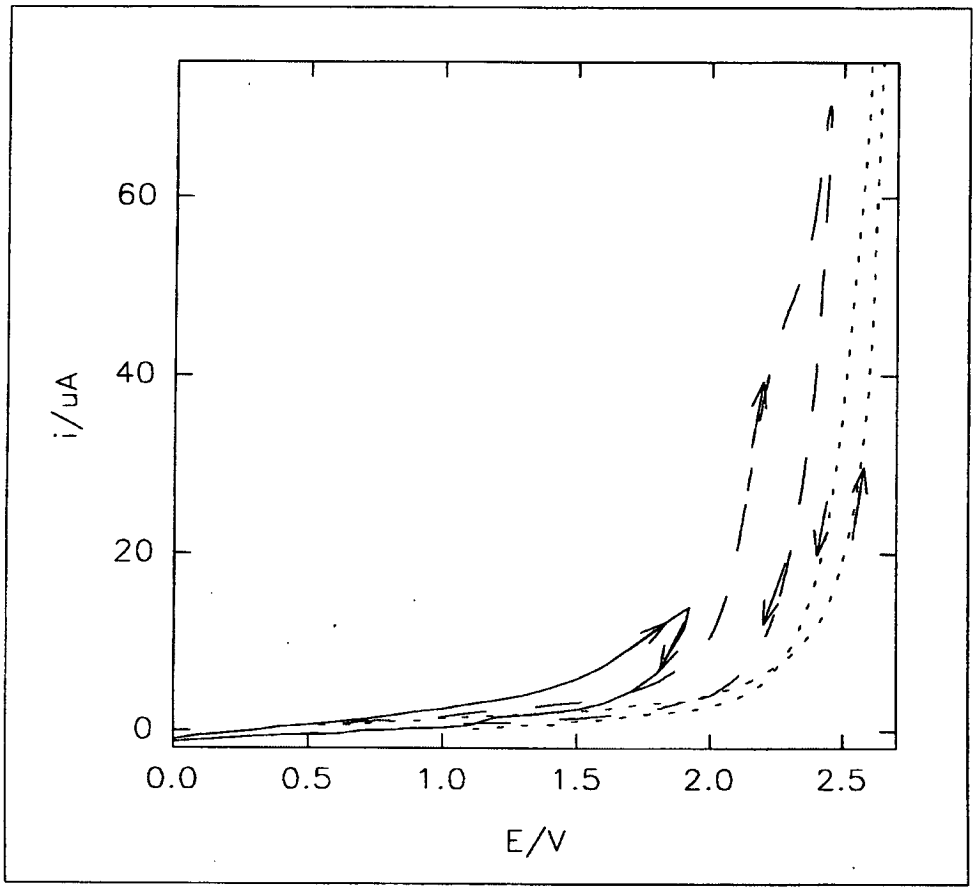

Figure 3.3: CV study showing sweeps to progressively more oxidising potentials

These studies also indicate that complete oxide removal is not an essential prerequisite to film deposition. CV experiments with titanium electrodes which had not had the oxide layer fully removed show similar oxidation characteristics, suggesting the growth of a surface nitride film. It was noticeable though that smaller currents were passed in the 'nitriding' of oxide-coated films and that coverage of the surface was uneven.

Assuming 100% current efficiency, an approximately 600nm thick film was grown by passing 3 Coulombs of charge on a titanium working electrode with an effective surface area of approximately $2cm^2$ (density of TiN = 5.22 gcm^{-3} [46]), according to *Equation 3.16.*

$$Ti + 3\,NH_2^- \rightarrow TiN + 2\,NH_3 + 3\,e^- \qquad \textbf{(3.16)}$$

Figure 3.4 shows the Cottrell plot of charge against the square root of time for data recorded during the initial stages of an electrochemical modification of titanium at +5.00 V and at -78°C. These data follow a linear trend. Integration of the Cottrell Equation (*Equation 3.17*) with respect to time, 't', reveals that a plot of charge, 'Q'(= i t, where 'i' is current), against the square root of time will have the gradient, 'm', as shown in *Equation 3.18*, where 'n' is the number of electrons involved in the reaction, 'F' is the Faraday constant, 'A' is the surface area of the electrode, 'D' is the diffusion coefficient of the electroactive species, and '[A]' is the concentration of the electroactive species in solution [47].

$$|i| = \frac{nFAD^{1/2}[A]_{bulk}}{\pi^{1/2}t^{1/2}} \qquad \textbf{(3.17)}$$

$$m = \frac{2nFAD^{1/2}[A]_{bulk}}{\pi^{1/2}} \qquad \textbf{(3.18)}$$

A linear fit of the data plotted in *Figure 3.4* gave a value for the gradient of $4.86(12)\times10^{-3}$ $Cs^{-1/2}$. This allows the calculation of a diffusion coefficient of 2.01×10^{-11} cm^2s^{-1} [1] for the process assuming that the overall reaction occurring is as given in *Equation 3.16*. Using the Nernst-Einstein equation (*Equation 3.19)* the expected diffusion coefficient of NH_2^- in liquid ammonia can be calculated, where 'k' is the Boltzmann constant, 'T' is the absolute

[1] n = 1 (1 electron per NH_2^-), A ≈ $2cm^2$, F = 96487 $Cmol^{-1}$, $[NH_2^-]_{NH3}$ calculated as 4.98×10^{-3} $molcm^{-3}$ using solubility of KNH_2 at -50°C (= 39.1g/100g NH_3) and density of liquid ammonia at -50°C (= $0.7020gcm^{-3}$) [31]. Unfortunately data were not available at -78°C.

temperature, 'λ_{NH2-}' is the conductivity of amide in liquid ammonia, 'z' is the charge on the amide ion, and 'e' is the electronic charge. The diffusion coefficient was thus found to be $2.32 \times 10^{-5} cm^2 s^{-1}$ [2].

$$D = \lambda_{NH2-} \frac{kT}{z^2 e^2} \qquad (3.19)$$

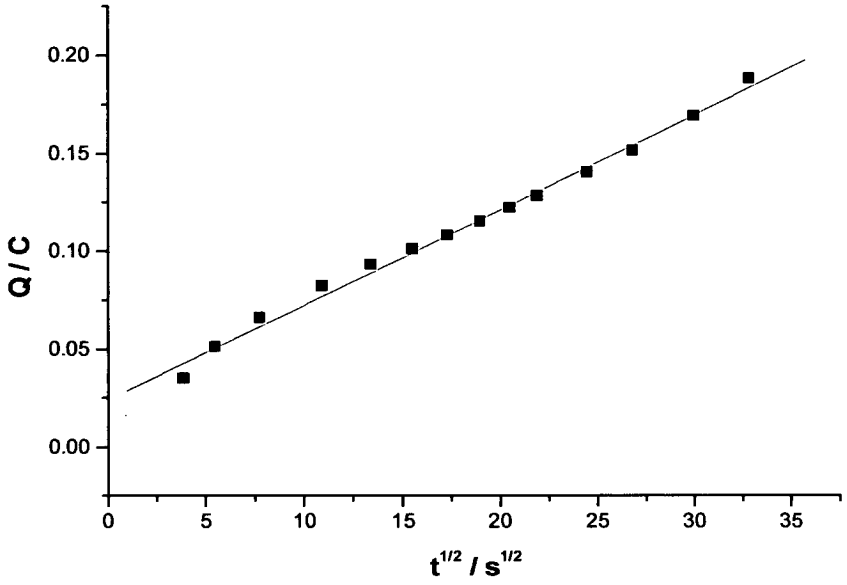

Figure 3.4: Cottrell plot of Q against $t^{1/2}$ for the electrochemical modification of titanium at -78°C

This predicted value is six orders of magnitude larger than the value obtained from the experimental data. Interpretation of this result is complicated by the fact that the experimental diffusion coefficient calculation uses the concentration of NH_2^- as measured at -50°C, and the predicted diffusion coefficient calculation uses the conductivity of NH_2^- as derived at -33.5°C (higher than it would be at -78°C). Nevertheless, the diffusion coefficient obtained from the Cottrell plot is still remarkably low compared to that predicted for amide diffusing through the solution. It is possible that the data recorded actually chart the diffusion of 'N' atoms, formed

[2] $k = 1.380 \times 10^{-23} JK^{-1}$, $T = 195$ K, $\lambda_{NH2-} = 133\ cm^{-2}\Omega^{-1}mol^{-1}$ at -33.5°C [48], $z = 1$, $e = 1.602 \times 10^{-19}$C

from NH_2^- at the electrode, through the bulk titanium metal. The diffusion coefficient for this process would certainly be expected to be lower than that of an ion moving through solution as it involves rearrangement of the metal lattice.

3.5 Characterisation

After anodisation, the titanium electrode was removed from the cell and washed with water (to ensure that the film was free from precipitated electrolyte), and acetone (to ensure that it was dry), to reveal a golden coloured film, characteristic of titanium nitride.

3.5.1 Powder X-Ray Diffraction (XRD)

Glancing angle X-ray powder diffraction of the thin film showed no peaks other than those of the titanium substrate. There was, however, significant background scattering indicative of either amorphous material or a nano-crystalline phase. The low degree of crystallinity is perhaps unsurprising considering the low temperature at which the film was produced. Attempts to anneal the sample at 800°C under argon resulted in some degree of sharpening but were inconclusive. It is questionable whether such a treatment would ever provide conclusive evidence for single-phase polycrystalline TiN thin surface films generated on titanium in this way given that thermally induced diffusion of N atoms down a concentration gradient might be expected to result in a range of stoichiometries, TiN_x, with x ranging from 0 to 1.

Given the amorphous or nano-crystalline nature of the TiN film and the desire to modify it as little as possible, characterisation of the film relied on a range of techniques that required as little post-processing of the film as possible. Heat treatment was to be avoided in particular as titanium is known to scavenge even traces of oxygen at elevated temperature leading to the formation of TiO_2.

EX BIBL. UNIV. EDINBURGH

3.5.2 Magnetic Measurements

TiN exhibits a transition from metallic to superconducting behaviour in the range 1.17-5.8 K depending on stoichiometry [46]. The data obtained for bulk TiN (Aldrich), shown to be stoichiometric by CHN analysis, are shown in *Figure 3.4*. The electrodeposited film showed just such a transition at *ca.* 4.5 K in a field of 100 Gauss (*Figure 3.5*). The measured susceptibilities for the film are multiplied by a factor of 100 for scaling purposes in the diagram. The magnitude of the transition, when correlated with the charge passed during synthesis, further indicated that titanium nitride is the major product of reaction. The temperature of the transition also suggests that the stoichiometry of the TiN_x film is such that x is very close to unity [46].

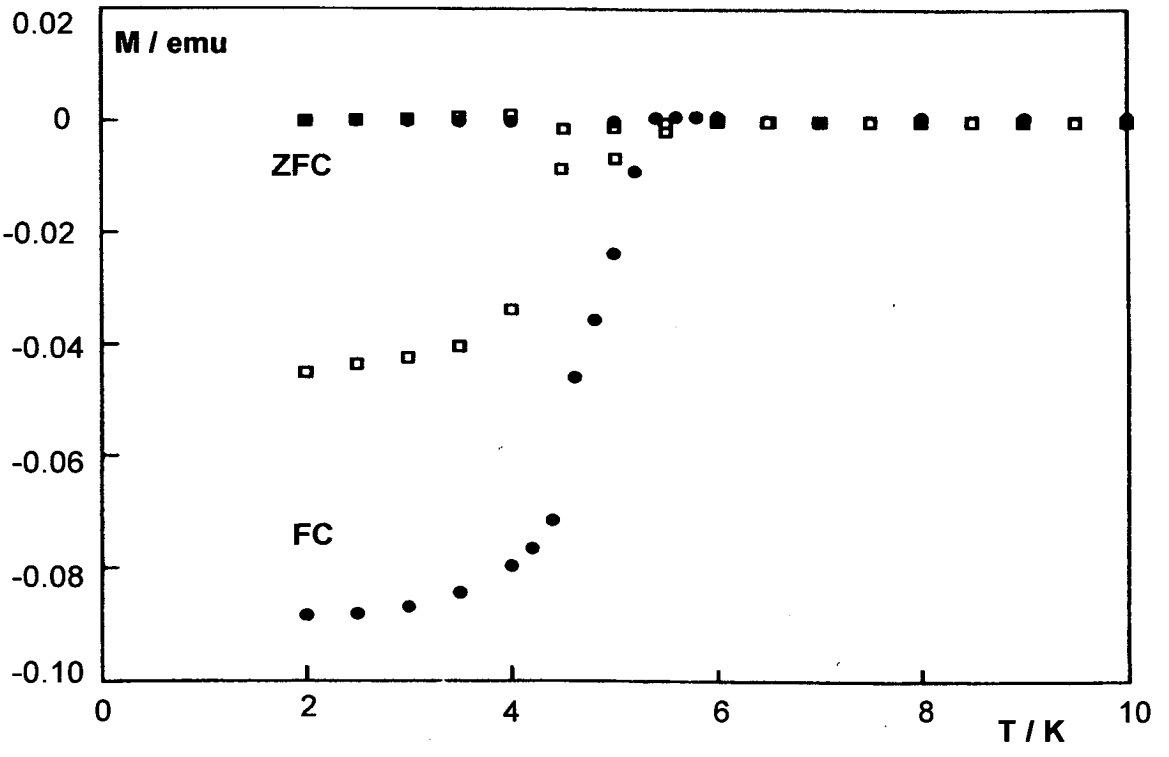

Figure 3.5: SQUID data for the electrochemically produced film (filled circles), and bulk TiN (open squares), cooled in zero field (ZFC), and a 100 Gauss field (FC)

3.5.3 Reflectance Measurements

The reflectance spectra of the electrochemically produced film, TiN produced by chemical means, and a piece of unmodified titanium metal (with native oxide layer), are shown in *Figure 3.6.* Reference samples of TiN were prepared chemically by heating titanium foil (0.025mm thickness), in a tube furnace under flowing ammonia (dried by condensing into a pressure vessel containing sodium), at 700°C for 3 hours. The foils were a deep blue-purple colour. Although by no means conclusive, the reflectance spectrum of the thin film showed not only increased reflectivity below 300nm when compared with an unmodified piece of titanium, but was very similar to the reflectance spectrum obtained for the chemically produced TiN.

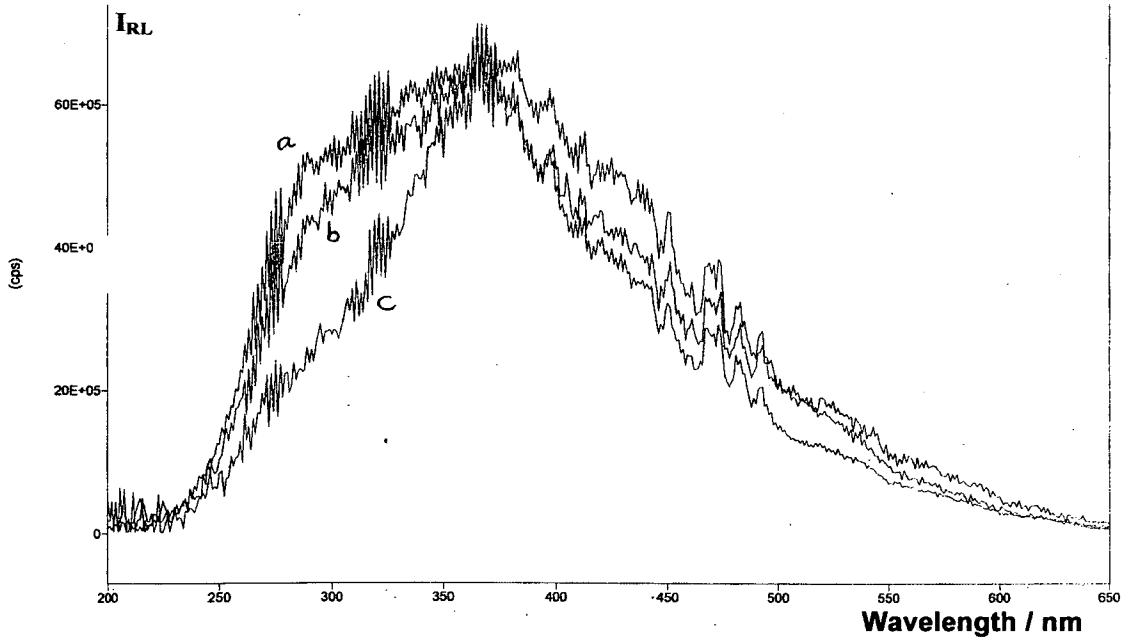

Figure 3.6: Reflectance spectra for **(a)** chemically produced TiN, **(b)** the electrochemically produced thin film, **(c)** titanium metal with its surface oxide layer

3.5.4 Raman Spectroscopy

Interpretation of crystal Raman spectra is generally complex, and most work has been centred on simple alkali metal halides which have cubic structures [49, 50]. Since TiN adopts a face-centred cubic structure, comparisons can be readily made with the halides. Owing to the octahedral symmetry of the material, first-order fundamental Raman scattering is forbidden. However, because of the high degree of intrinsic defects and vacancies in the lattice, even for stoichiometric TiN, defect-induced first-order scattering can occur [51]. This is because the translational and inversion symmetry are broken by the defects [52]. This scattering becomes more predominant as the percentage of defects increases. The interaction of the incident laser light with the crystal sets up phonons, or elastic lattice vibrations, within the solid. These phonons are labelled as 'optical' when a dipole moment is generated, or 'acoustic' when there is no net charge displacement [53]. For simplicity, it is best to consider the vibrations of the titanium and nitrogen sub-lattices independently. This is a valid simplification because of the large mass difference between the two types of atom. From the defect-induced scattering the perturbed projected phonon density of states can be obtained for the three Raman active modes A_{1g}, E_g and T_{2g} [54]. These are often compared with theoretical predictions and results from neutron scattering experiments to aid interpretation.

The frequency range of high phonon density for TiN has been reported as from 180 to 370cm^{-1} in the acoustic branch, and from 520 to 610 cm^{-1} in the optical branch [54]. Spengler *et al* also report that the scattering shifts continuously to higher frequencies the lower the nitrogen concentration of the sample [52]. These previous studies therefore show that the relative intensities of the Raman bands centred on 550 and 235 cm^{-1} depend upon the stoichiometry of the titanium nitride. The band at higher energy is ascribed to nitrogen vacancies in the lattice

and its intensity relative to the band at 235 cm^{-1} increases rapidly with increasing nitrogen deficiency [51].

Figure 3.7 shows the Raman spectra obtained from (*a*) the electrochemically produced film, (*b*) commercial TiN powder (Aldrich), and (*c*) a film of TiN produced by chemical means (as described in *section 3.5.3*). The spectrum obtained from commercial TiN powder displays three broad bands, the positions of which are in good agreement with spectra described in the literature. There is a small shoulder visible on the left hand peak at approximately $190cm^{-1}$. This may indicate a degree of aerial oxidation, as the most intense peak in the Raman spectrum of anatase (*Figure 3.8b*), occurs at this position.

Figure 3.7a and *3.7b* demonstrate the difficulty in obtaining good spectra for thin, highly reflective samples. The peaks are very broad but are quite different in intensity and position from the Raman spectra of titanium(IV) oxide (both anatase and rutile phases, see *Figure 3.7*). This indicates that both films were free from significant amounts of TiO_2. The Raman spectrum of the TiN film produced by chemical means shows very broad peaks with some similarity to the electrochemically produced sample. This shows that the sample is of very variable stoichiometry, as the peak position and intensity is sensitive to composition. Presumably this is because the method of synthesis relies on the diffusion of 'N' species generated from ammonia gas to diffuse through the metal. A material with a variety of different compositions could be prepared in this way.

The Raman spectrum of the electrochemically produced film is significantly sharper than that produced by chemical means suggesting a better defined stoichiometry with this method. The pattern of bands more closely resembles the spectrum of commercial TiN powder which was

found to have a ratio of Ti:N of 1:0.994 by CHN analysis, so is almost perfectly stoichiometric. For the electrochemically produced film this suggests a value of x for the TiN_x that is also close to unity.

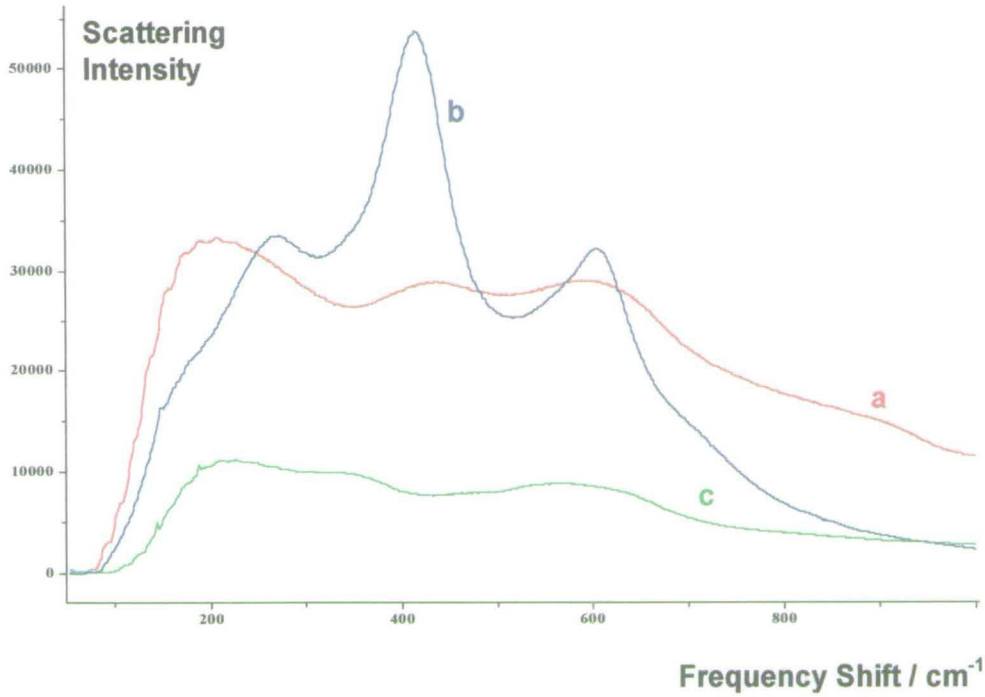

Figure 3.7: Raman spectra of (**a**) the electrochemically produced film, (**b**) commercial TiN, and (**c**) chemically produced TiN film

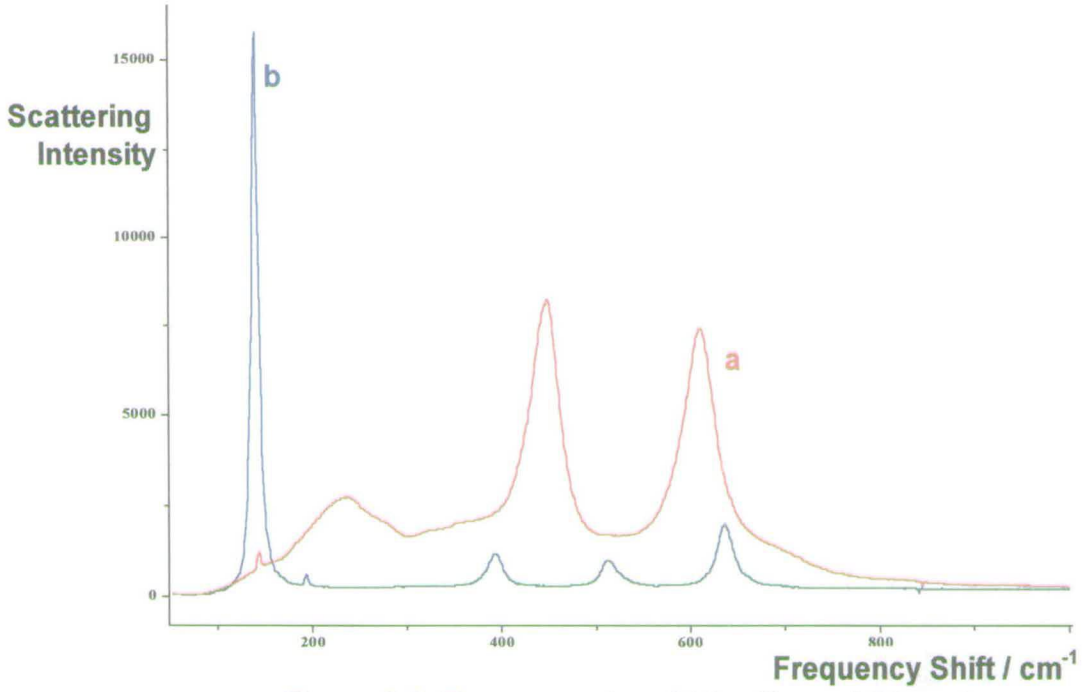

Figure 3.8: Raman spectra of (**a**) rutile, and (**b**) anatase

3.5.5 Energy Dispersive X-Ray Spectroscopy (EDXS)

The SEM-EDX spectrum of the film (*Figure 3.9*) also points to a nitride-containing film. Not surprisingly given the nature of the sample (TiN on bulk Ti) the spectrum was dominated by the strong Ti K_α-line but clearly discernible was the N 2p line (adjacent to the Ti L_α line). Quantitative assessment of the stoichiometry was not possible owing to the considerable contribution to the intensity from the titanium substrate, and the overlap of the N 2p and Ti L_α lines. It is significant, however, that no peaks corresponding to either oxygen or potassium were observed demonstrating that a clean film had been produced.

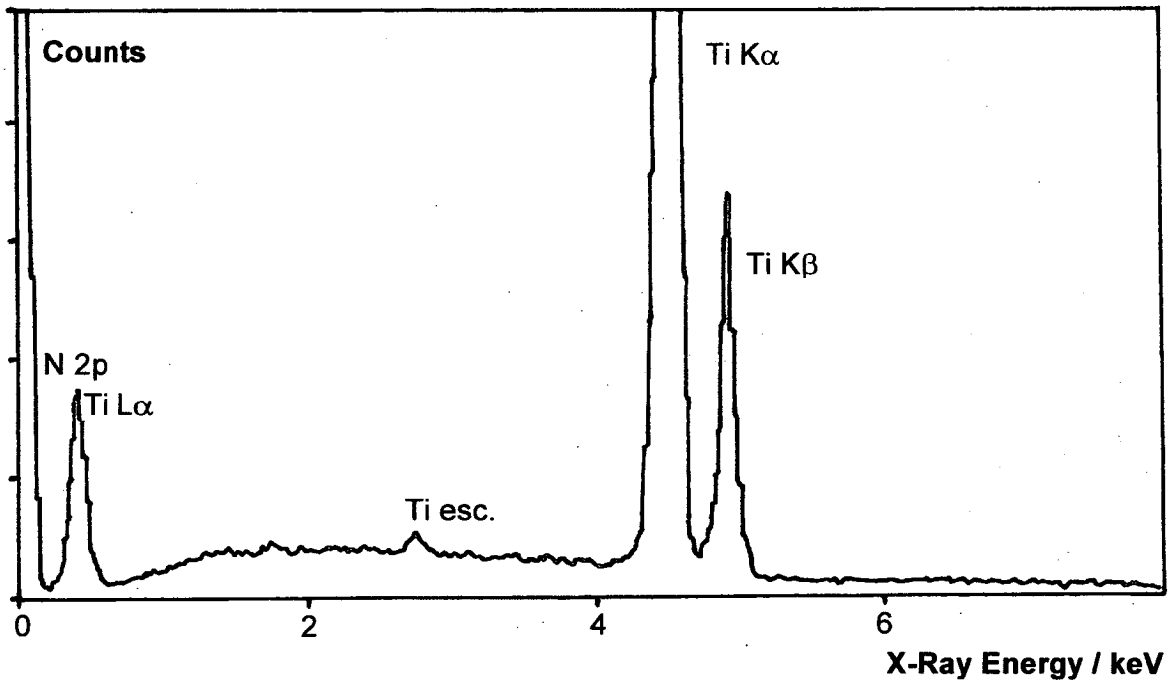

Figure 3.9: EDX spectrum of the electrochemically produced film. The y-scale has been expanded in order to view the peaks of lower intensity

3.5.6 X-Ray Photoelectron Spectroscopy (XPS)

3.5.6.1 Surface Measurements

The wide scan spectrum obtained from the electrochemically produced thin film (on 0.5mm Ti foil), is shown in *Figure 3.10*. This is compared with the spectra obtained from the titanium metal staring material (0.5mm) *(Figure 3.11)*, and the chemically produced TiN thin film (0.025mm), (*Figure 3.12*). The first feature to note is that the background generally increases to the high photon (or binding), energy end of the spectrum, with step-like increases on the right hand side of each peak. This effect is due to secondary electrons created by inelastic photo-emission (energy loss within the solid). There is also a broad background due to photoemission by Bremsstrahlung, or background, radiation which is caused by the non-monochromatic X-ray source. This effect dominates in the low binding energy region of the spectrum [55].

The sharp peaks superimposed on the background are due to photoemission from core levels. Very little valence structure (in the region 0-20eV) due to photoemission of low binding energy electrons from de-localised or bonding orbitals is observed on this scale. In all three spectra, singlets due to oxygen and carbon 1s peaks are visible at 531 eV and 285 eV respectively. The carbon is a consequence of hydrocarbon vapour deposited on the sample from the high vacuum pump equipment, and the oxygen peak arises because of adsorbed water or oxygen or aerial oxidation of the surface after preparation. All three samples are heavily oxidised as they had been stored in air for some time. The titanium 2p doublet is also observed at approximately 459 eV. A nitrogen 1s peak is observed at 397 eV in the spectrum of the chemically produced TiN. A nitrogen peak for the electrochemically produced film is

not visible on this scale. No other elemental peaks are observed, indicating that the samples are relatively free from other contaminants.

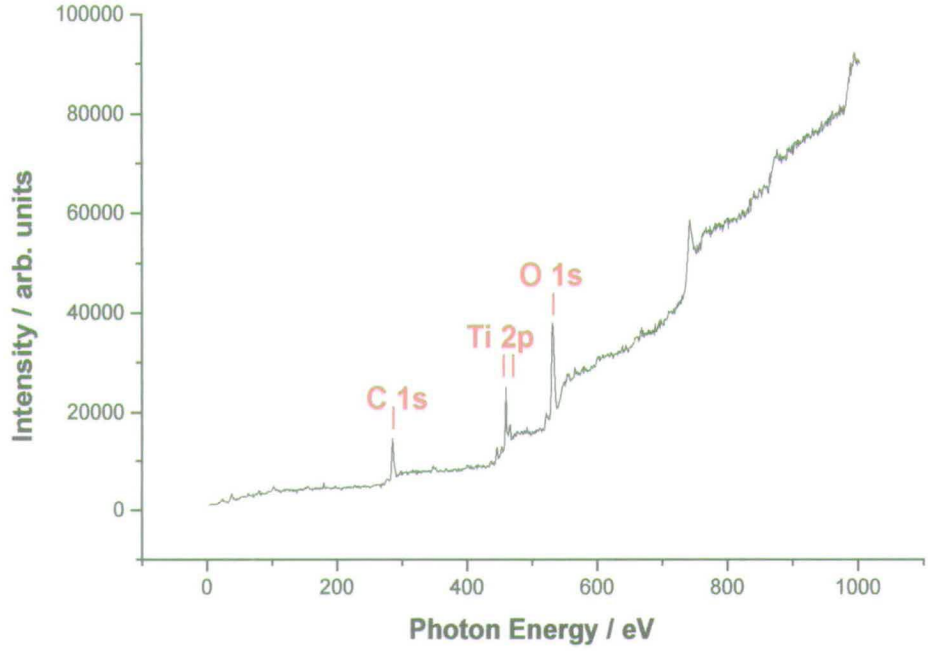

Figure 3.10: Wide scan XPS spectrum of the electrochemically produced film

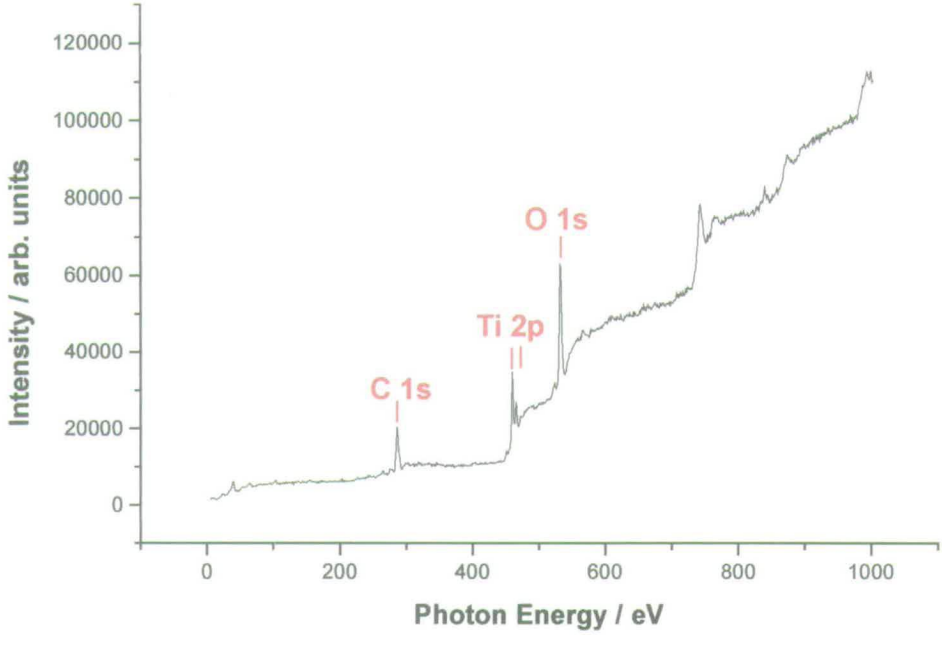

Figure 3.11: Wide scan XPS spectrum of titanium metal

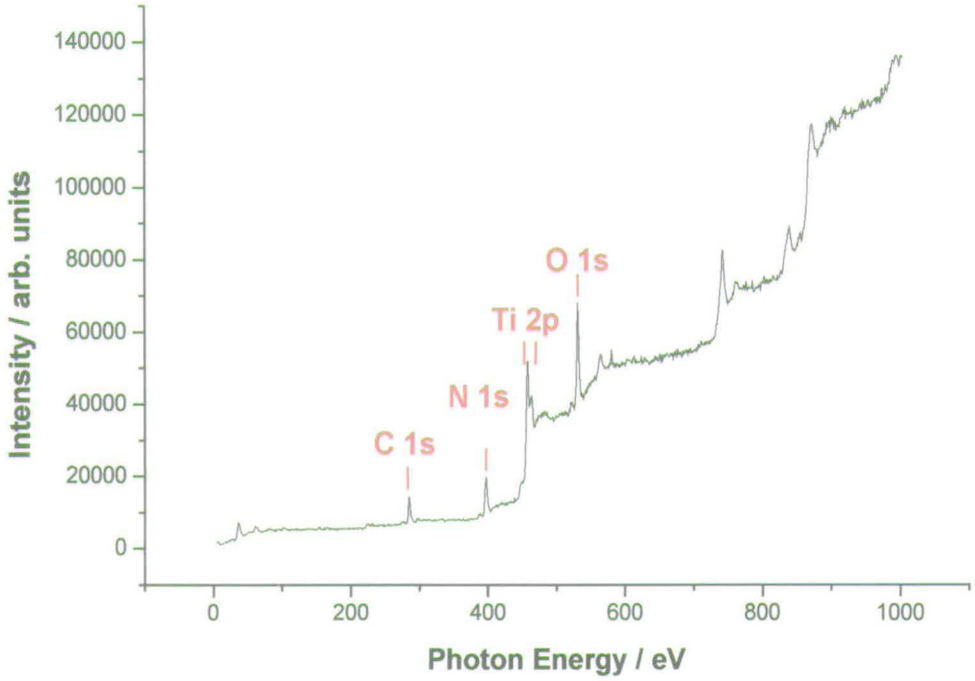

Figure 3.12: Wide scan XPS spectrum of chemically produced TiN

The narrow scan spectra obtained for titanium (*Figure 3.13*), oxygen (*Figure 3.14*), and nitrogen (*Figure 3.15*), were also recorded for the three samples. The peak positions are recorded in *Table 3.2*. The literature Ti $2p_{3/2}$ peak positions are shown in *Table 3.3*.

Previous XPS studies have shown that it is possible to distinguish TiN from both TiO and TiO_2 on the basis of the Ti $2p_{3/2}$ chemical shift [55]. The titanium 2p peak (*Figure 3.13*) is split into a doublet as a result of spin-orbit coupling (discussed in *section 2.9.1*). The $2p_{3/2}$ and $2p_{1/2}$ peaks are in the expected area ratio of 2:1. The spectra obtained from the electrochemically prepared film and the titanium metal are very similar, with the peak positions characteristic of Ti^{4+} in titanium dioxide, again indicating that the surface of the metals was substantially oxidised. The titanium $2p_{3/2}$ peaks are shifted up by approximately 5.1eV compared to the expected value for titanium metal, which is in line with published data

obtained for TiO_2 [56]. In addition the splitting of the 2p doublet is 5.7eV for the electrochemically prepared film (compared to 6.15eV for pure titanium metal [56]), which again agrees with published data for TiO_2. There is one additional low intensity peak at 453.1eV in the spectrum of the electrochemically synthesised film. This may be due to titanium metal, underlying titanium nitride or TiO at the surface [57].

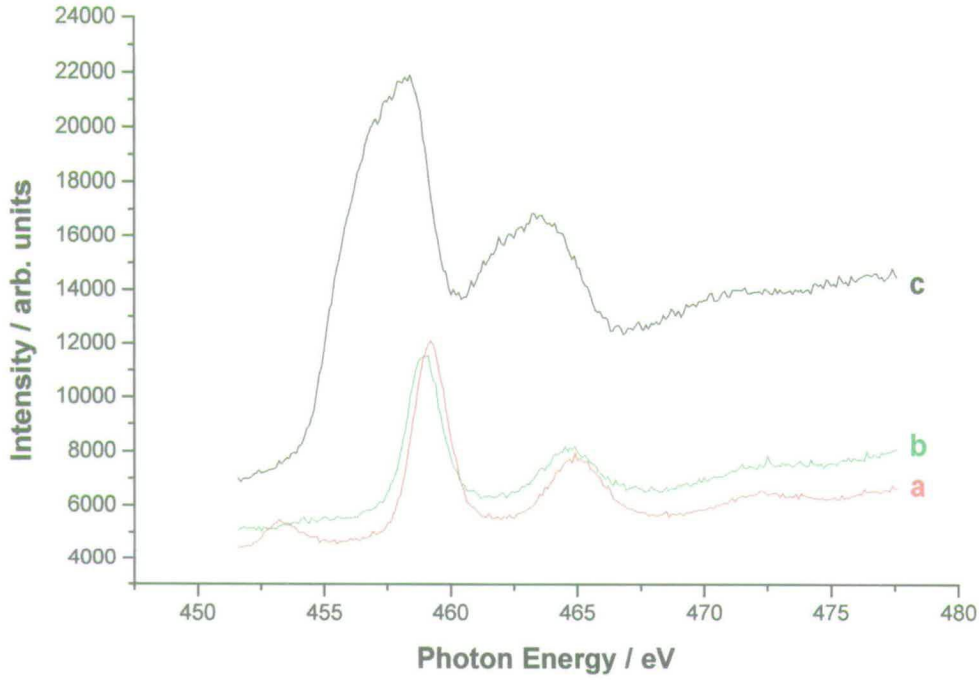

Figure 3.13: Titanium 2p XPS spectra for **(a)** the electrochemically produced film, **(b)** titanium metal, and **(c)** chemically produced TiN

The spectrum obtained for the chemically produced TiN is more intense than the previous two with broad peaks shifted to higher binding energy, this time by +4.4eV compared with pure titanium. This suggests that there is also a degree of oxidation of the titanium at the surface in this sample, although the peak positions are a little low to be attributable to TiO_2. It is possible that the surface layer consists of a titanium oxynitride phase which would produce an electron density on titanium slightly higher than in TiO_2, and hence a lower binding energy.

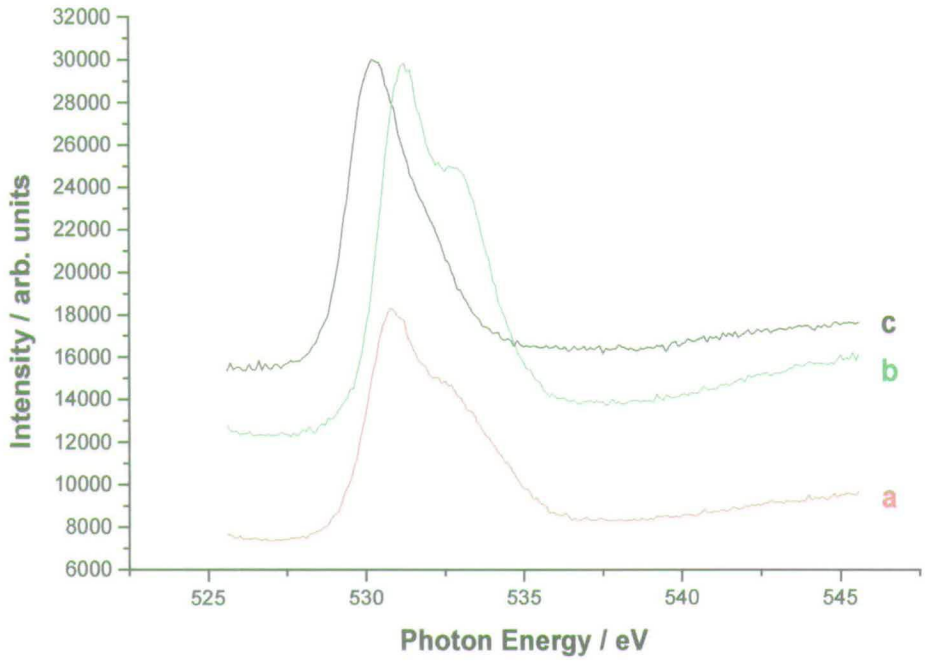

Figure 3.14: Oxygen 1s XPS spectra for **(a)** the electrochemically produced film, **(b)** titanium metal, and **(c)** chemically produced TiN

Although no simple correlation can be drawn between metal oxide bond character and O 1s binding energy, differences between experimental values for some oxides are sufficiently large to allow differentiation between phases. The O 1s spectra for both the electrochemically prepared film and titanium metal show broad asymmetric peaks at approximately 531eV (*Figure 3.14*). This is in line with peak positions reported in the literature, and can be assigned to oxygen in the -2 oxidation state present as TiO_2 [56-59]. The shoulder at approximately 533eV is from oxygen in TiO [57]. The O 1s spectrum obtained from the chemically synthesised TiN also shows a broad peak, but shifted to slightly lower binding energy at 530eV. This could be again due to the formation of titanium oxynitride species. The titanium metal used for the chemical preparation of TiN would have possessed a native oxide layer. The ions in this TiO_2 lattice are held together by strong Coulombic forces. The introduction of nitrogen (from ammonia), would alter the local environment of the atoms [55]

and instigate a degree of covalent bonding. More precisely this change would result in an increase in the electron density on oxygen, decreasing the O 1s binding energy.

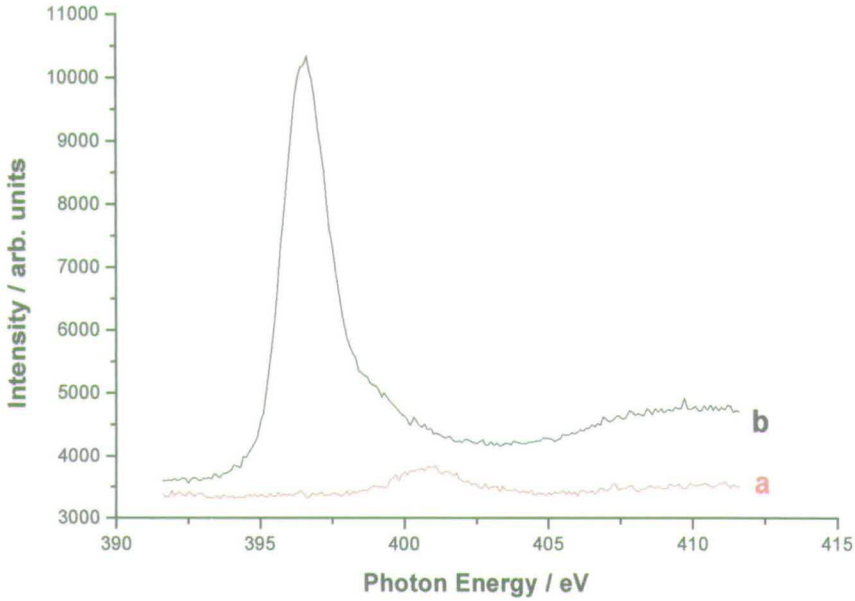

Figure 3.15: Nitrogen 1s XPS spectra for **(a)** the electrochemically produced film, and **(b)** chemically produced TiN

For both inorganic and organic compounds it has been found that the N 1s binding energy increases with formal oxidation number of the nitrogen atom [55]. The chemically produced TiN demonstrates a sharp N 1s peak at 396.6eV (*Figure 3.15*). This is in good agreement with literature spectra of TiN [56-58], and identifies nitrogen in the -3 oxidation state (formally). The electrochemically prepared film shows a very weak, broad N 1s line at 401.1eV. This is a little high to be attributed to nitrogen present in the -3 oxidation state. Esaka *et al* assigned a similar feature in the N 1s spectrum of a TiN film to interstitial molecular nitrogen in the surface oxide layers. The nitride films were heated in air (effectively accelerating the ageing process), and the feature grew into the XPS spectrum at around 300°C while oxynitride species were formed. Eventually molecular nitrogen was released from the surface [60]. Brundle [61] reported that gaseous dinitrogen and adsorbed dinitrogen on nickel

exhibited their N 1s XPS features at 409.9 and 400.6eV respectively. The lower binding energy for the adsorbed molecules is due to the extra atomic relaxation which is absent for the gaseous molecule. As the electrochemically produced film had been prepared some time before XPS analysis, it is possible that slow aerial oxidation of the surface at ambient temperature had caused the release of the uppermost nitride species as molecular nitrogen, which became trapped in the surface layer of the film (*Equation 3.20*).

$$2\,TiN + 2\,O_2 \rightarrow 2\,TiO_2 + N_2 \qquad \textbf{(3.20)}$$

Sample	N 1s	O 1s	Ti $2p_{3/2}$	Ti $2p_{1/2}$
Electrochem. film	401.1	530.8	459.2	464.9
Titanium	-	531.2	459.1	464.5
Chemical TiN	396.6	530.2	458.4	463.3

Table 3.2: Peak positions (eV) recorded at the surface for the three samples

Material	Ti $2p_{3/2}$ Peak Position	Chemical Shift Ti relative to Ti(0)
Ti	454.0	-
TiO	455.0	+1.0 ± 0.2
TiN	454.2-456.0	+1.5 ± 0.2
TiC	454.6	+1.3 ± 0.1
TiO_2	458.7	+4.9 ± 0.2

Table 3.3: Published Ti $2p_{3/2}$ peak position data [55, 56]

3.5.6.2 Sputtering Experiments

As all of the samples were found by surface scans to be heavily oxidised, sputtering was carried out to erode this oxide layer and to reveal the original composition of the films, and to discover how it varied with depth. Sputtering experiments were performed on the electrochemically produced thin film and on the titanium metal starting material (0.5mm thickness). *Figure 3.16-3.18* show the stack plots of the narrow scan spectra obtained for the electrochemically synthesised film for titanium, oxygen, and nitrogen respectively after different sputtering times.

As sputtering progresses, the structure seen in the initial scan due to TiO_2 is lost and a broad, unresolved spectrum is obtained (*Figure 3.16*). After 12 minutes sputtering the Ti 2p doublet begins to reappear at a significantly lower binding energy as two broad peaks and these shift progressively to lower binding energy as sputtering continues. The peaks pass through a range of intermediate positions indicating that the titanium is present with an oxidation state between +4 and zero as the depth increases. This is what would be expected if a sub-surface nitride layer was present as in stoichiometric TiN the formal oxidation state of titanium is +3. The peaks become sharp and well resolved after 88 minutes. The final position of the $2p_{3/2}$ peak is 454.0eV and the position of the $2p_{1/2}$ peak is 460.1eV. The peak separation is 6.1eV. This data agrees well with that reported in the literature for pure titanium metal or titanium nitride [56], and indicates that the oxide layer has been removed.

The O 1s spectrum obtained after four minutes sputtering is more intense than the initial spectrum recorded at the surface, and the peak shape is more symmetrical (*Figure 3.17*). This indicates that the TiO detected in the surface scan (indicated by the shoulder on the main peak) has been removed, leaving only TiO_2. The exact peak position when it reaches its

maximum intensity is 531.0eV. Over time, the O 1s peak decreases in intensity indicating progressive erosion of the oxide layer. By the end of the experiment the oxygen levels are very low.

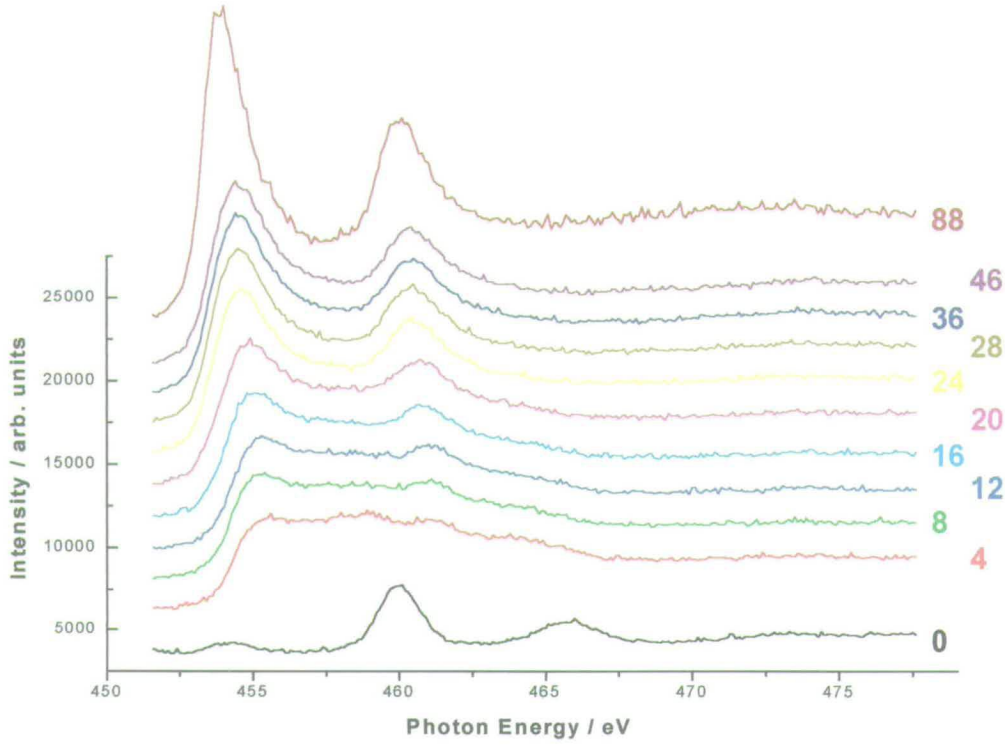

Figure 3.16: Titanium XPS spectra obtained through sputtering. Sputtering time (in minutes), is given at the right hand side of each trace

The N 1s spectrum obtained initially shows a broad peak at 401eV which was assigned to molecular dinitrogen trapped in the interstices of the surface oxide layer (*Figure 3.18*). The spectrum obtained after four minutes sputtering shows an immediate peak shift to higher binding energy. This demonstrates that the nitrogen under analysis is now in a lower oxidation state. As sputtering continues, this peak becomes sharp and grows in intensity to a maximum after 72 minutes at which point it is located at 397.2eV. This is in excellent

agreement with literature values reported for stoichiometric TiN [58]. It is important to note that the position of this peak does not vary as sputtering continues, indicating that only one phase is present. This depth profiling also makes clear that it was the oxide layer detected at the surface which was preventing the detection of this nitrogen in surface scans.

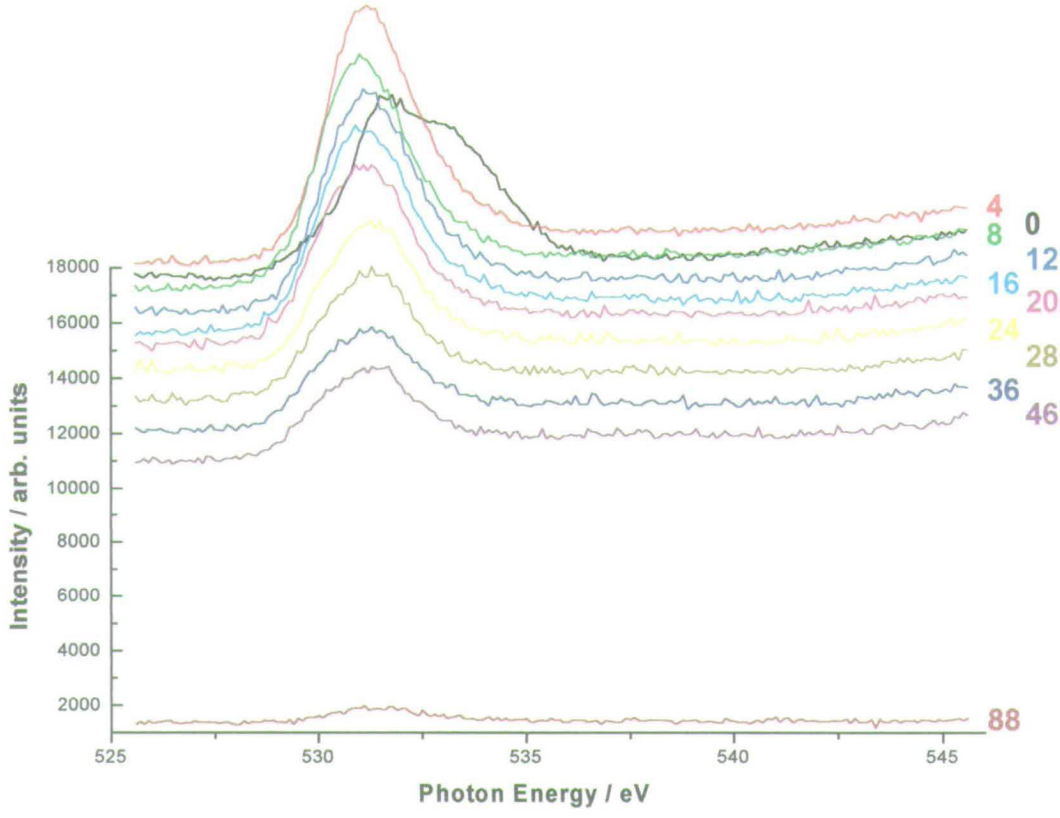

Figure 3.17: Oxygen XPS spectra obtained through sputtering. The black trace is the initial spectrum. Sputtering time (in minutes), is given at the right hand side of each trace

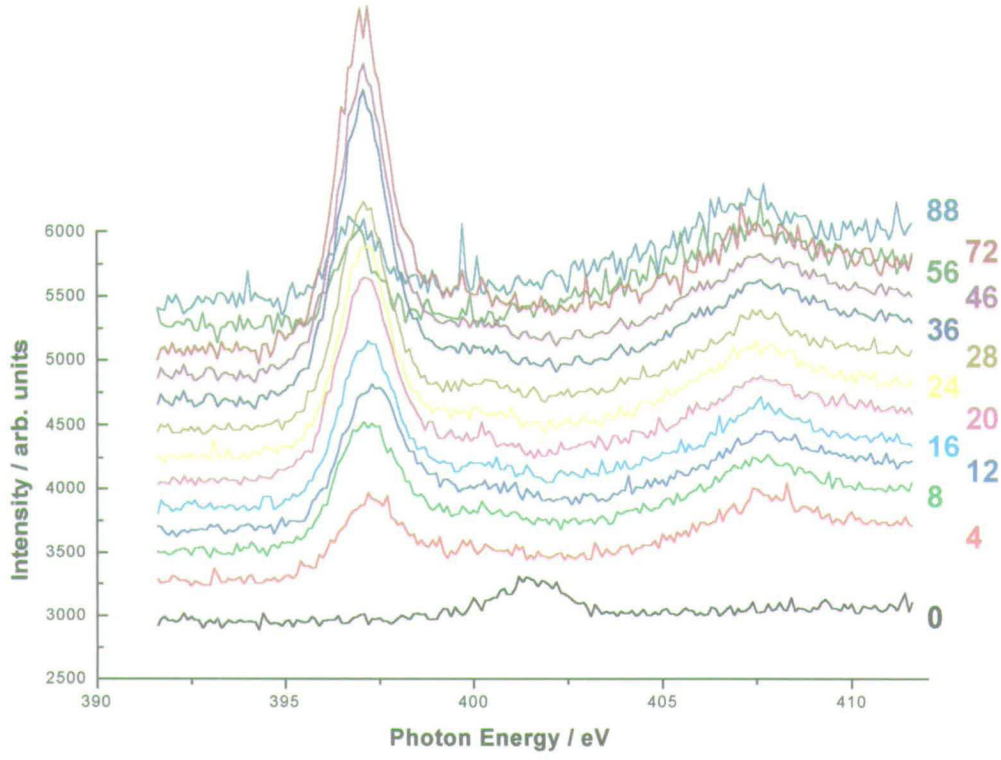

Figure 3.18: Nitrogen XPS spectra obtained through sputtering. Sputtering time (in minutes), is given at the right hand side of each trace

Figures 3.19-3.21 show the 'depth profiling' plots of the elements for the electrochemically synthesised film. These plots were obtained by integrating peaks (between 452.6 and 456.6eV for titanium, 528.6 and 535.6eV for oxygen, and 394.6 and 399.6eV for nitrogen), in the spectra obtained through sputtering and plotting the values obtained against a depth based on sputtering times for silicon at 200V, as unfortunately a nitride standard was not available (see *section 2.9.3*). The error in the peak areas (shown as error bars on the graphs) was approximately 5%.

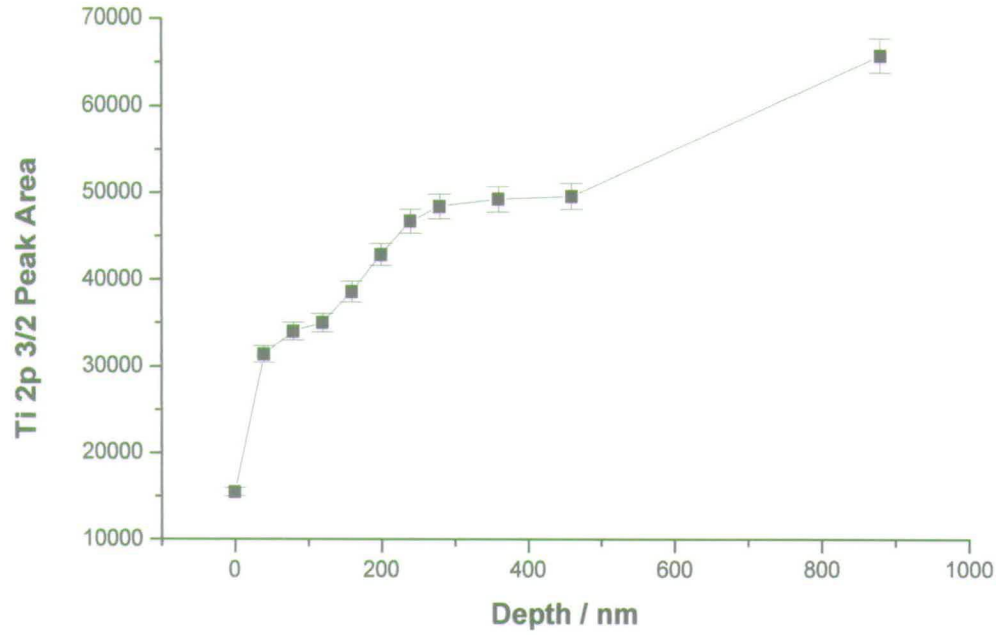

Figure 3.19: Depth profile plot of titanium in the electrochemically produced film

The integration range of 452.6-456.6eV was chosen to analyse the amount of titanium present as the metal and as TiN, but not as TiO_2. *Figure 3.19* clearly shows that the chosen Ti $2p_{3/2}$ peak area increases as sputtering progresses. This can be explained by the removal of the surface oxide film which reveals TiN and eventually bulk metallic titanium.

The chosen integration range of 528.6-535.6eV allows analysis of all forms of oxygen in the film. *Figure 3.20* shows that there is a fairly uniform concentration of oxygen in the sample until a depth of approximately 500nm. Beyond this, the oxygen is sputtered away until it reaches low levels by the end of the experiment. It should be noted that it is very difficult to remove all traces of oxygen, as there may be residual amounts in the vacuum chamber which can react with the newly sputtered, clean surface. Titanium metal is particularly reactive towards oxygen, and will scavenge traces of oxygen. In addition, small amounts of oxygen

may be introduced through the argon gas supply. Therefore, the oxygen detected in the sample at depth does not necessarily originate from the sample itself.

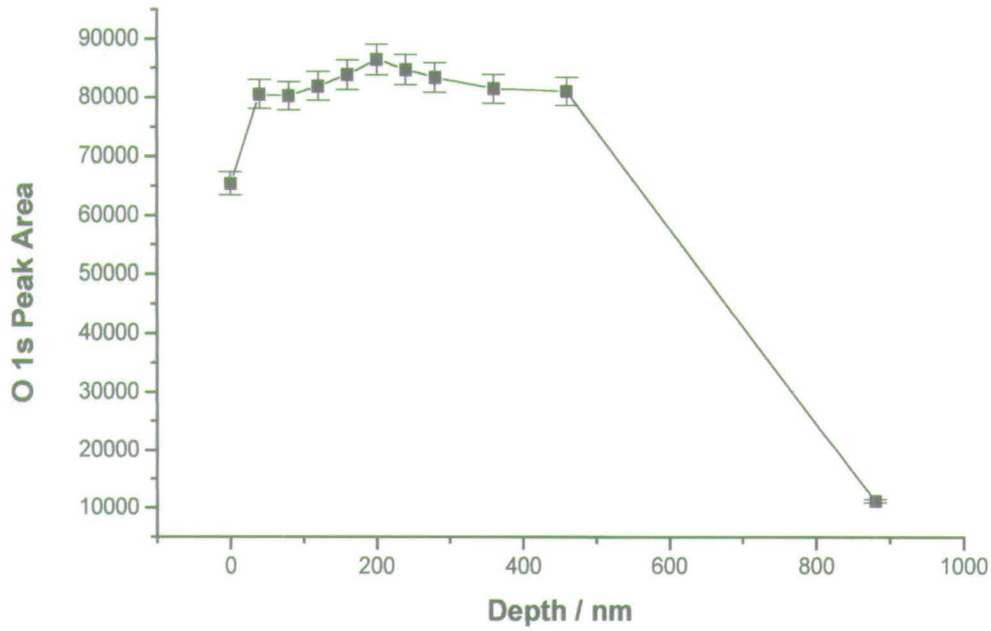

Figure 3.20: Depth profile plot of oxygen in the electrochemically produced film

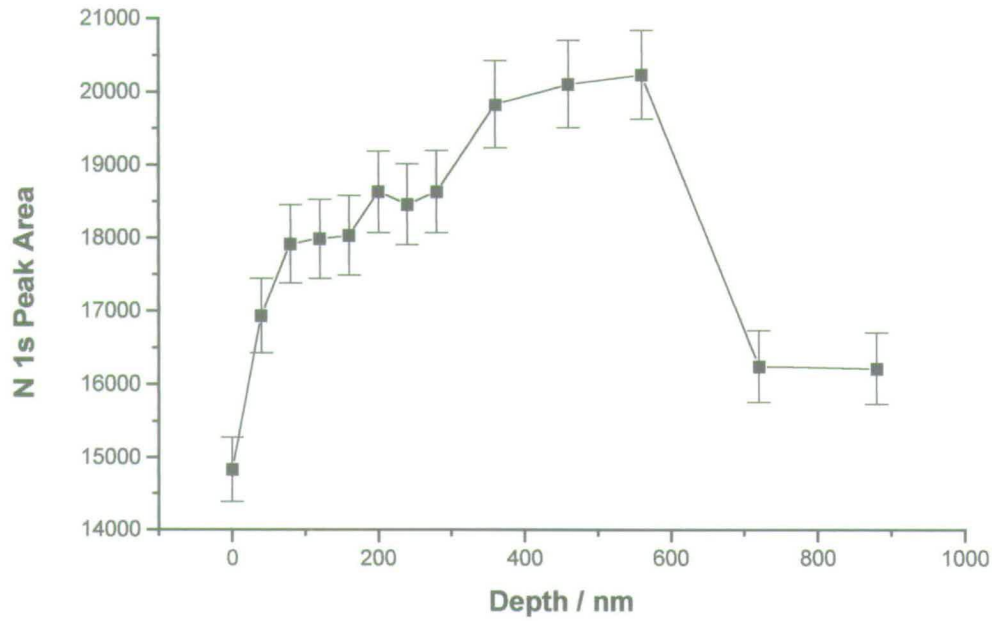

Figure 3.21: Depth profile of nitrogen in the electrochemically produced film

Figure 3.21 shows the concentration gradient of nitrogen (as nitride) in the sample. From very low levels at the surface, the concentration increases as the oxide layer is sputtered away revealing the nitride film. The nitrogen concentration is greatest at a depth of 560nm, before abruptly decreasing again, as the concentration of titanium increases and eventually metal is reached. This is in good agreement with the depth profile of titanium: the amount of titanium increased more rapidly beyond 560nm. The interpretation of the nitrogen depth profile is complicated by the masking effect of the oxide layer. The invariable position of the N 1s peak (*Figure 3.18*) suggests that a range of phases of TiN_x, (where x takes values from 0 to 1 at the maximum), is not produced. This would suggest that the nitrogen is located in a reasonably well defined region of the metal as stoichiometric TiN with abrupt boundaries, not distributed as a diffusion gradient. The steep drop off in N levels after 560nm is in line with this argument. However the initial increase in N levels is rather gradual; this can be attributed to the masking effect of the oxide layer.

A total of 1C of charge was passed during the production of this sample (of approximately $2cm^2$ surface area). Assuming 100% current efficiency, a layer of approximately 200nm thickness would be expected to form. On initial inspection XPS measurements suggest that the film is rather thicker than this estimate. However the matter is again complicated by the formation of a surface oxide layer.

Comparison of the relative amounts of the elements for the establishment of exact stoichiometry is complicated by the fact that the elements have differing sputtering yields, as mentioned in *section 2.9.3.* It can be seen that the sputtering yield of nitrogen is approximately half that of titanium, and this can affect the composition as sputtering progresses. For example, oxygen is sputtered selectively over titanium and this leads to the

sample becoming disproportionately richer in the metal. This phenomenon is known as 'reductive sputtering'. For the assessment of stoichiometry, it is better to rely on the peak position as compared with those obtained for well characterised materials.

3.5.7 Vickers Hardness Testing

Vickers hardness testing was carried out to compare the durability of the electrochemically synthesised films with that of titanium metal and titanium nitride prepared by chemical means and by reported methods. The size of the applied loads was varied in order to get consistent results for different samples of electrochemically produced TiN. The applied load effectively determines the penetration depth of the diamond point. If the load was too heavy, the diamond point penetrated into the underlying titanium metal, giving an artificially low hardness value. If the load was too light, the indent made by the diamond was too small to be measured accurately. Clearly the choice of load is crucial when analysing thin films. The ideal load is the minimum load to make a measurable indent. It was found that a load of 15g met this criterion and gave a consistent % increase in hardness over two samples when comparing the titanium metal starting material with the films produced. Three indents were made in each sample, to ensure that the values obtained were representative of the entire film. Results were compared with those obtained for the appropriate titanium metal starting materials (of two thickness values: 0.5mm and 0.025mm), and chemically produced TiN (see *section 3.3.4*).

Table 3.4 summarises the results obtained. It can be seen that the mean indent diagonal values vary considerably for each sample, and the uncertainty is significant. In addition the values obtained for the two types of titanium metal are quite different. This highlights the difficulty in obtaining reliable data for thin films using this apparatus, and leaves room for

doubt that the samples were measured at the optimum depth. The matter is further complicated by the unknown extent of oxide layers on the samples.

Sample	Titanium Metal Starting Material		Electrochemically Produced TiN	
	Mean Indent Diagonal ± 0.5 / μm	Vickers Hardness / kgmm^2	Mean Indent Diagonal ± 0.5 / μm	Vickers Hardness / kgmm^2
1a	12.5	178 (19)	9.5	308 (36)
1b	9.0	344 (48)	9.3	322 (44)
1c	9.5	308 (36)	8.8	359 (53)
2a	8.5	385 (58)	8.0	435 (69)
2b	9.0	344 (48)	7.7	469 (78)
2c	8.3	404 (62)	7.7	469 (78)

Table 3.4: Hardness data using 15g load for two samples of TiN on titanium metal. Sample 1 was deposited on 0.5mm thickness titanium, and sample 2 on 0.025mm titanium. The uncertainty in the figures is shown in parentheses.

Table 3.5 shows a summary of the mean hardness values for the two samples. It can be seen that there is a consistent increase in Vickers hardness of approximately 20% from titanium metal to the electrochemically deposited film, although again the uncertainty in these figures is considerable.

Sample	Mean Vickers Hardness / kgmm^2		% Increase in Hardness
	Ti	TiN	
1 (0.5mm)	277 (22)	330 (24)	19 ± 33
2 (0.025mm)	378 (25)	458 (29)	21 ± 38

Table 3.5: Summarised hardness data using 15g load for the two samples. The % error in the figures is shown in parentheses.

Measurements were also made on the chemically produced TiN (on 0.025mm thickness Ti foil). With a 50g load, the Vickers hardness was found to be 253(37) $kgmm^{-2}$. When a 25g load was used the Vickers hardness value was calculated as 593(153) $kgmm^{-2}$. Clearly the diamond probe had pressed through the film into underlying metal in the first measurement. When a load of 15g was applied, no indent could be observed. Titanium metal (0.025mm thickness), measured with a 25g applied load gave a hardness value of 348(78) $kgmm^{-2}$. The chemically produced TiN therefore shows an approximately 70% increase in hardness over the titanium metal starting material under these conditions. It appears that the TiN produced chemically was much harder than the electrochemically deposited TiN (approximately 30% harder). This may be a reflection on the relative degree of crystallinity of the samples. The chemically produced TiN was prepared at 700°C and is likely to be polycrystalline. The same cannot be said for the electrochemically synthesised film which was seen to be amorphous or nanocrystalline to X-rays by powder XRD.

Literature values for the Vickers hardness of stoichiometric TiN have been reported over a huge range between 340 and 4000 $kgmm^{-2}$ [14-16].

3.6 Summary and Conclusions

This chapter describes a novel electrochemical process which operates at low temperature to give in one step thin films of titanium nitride. The electrochemical solvent used was liquid ammonia and the electrolyte of choice was potassium amide, KNH_2. The high pH of this solution was thought to promote direct nitride synthesis. Furthermore the nature of the process is such that carbon and oxygen incorporation is inherently low.

A procedure was developed for the reduction of the native oxide layer on the titanium electrode prior to nitridation. This involved the continued cycling of the electrode between 0.00 V and a negative potential limit, always in excess of -1.50 V, such that a large negative current in the order of several mA was generated and blue ammonia-solvated electrons were observed at the electrode surface. This process was judged to result in an oxide-free surface as the magnitude of the associated oxidation peak was observed to diminish and the accessible potential window of the electrode expanded.

Anodisation of the titanium between 0.00 and +5.00 V (vs. Pt) and at atmospheric pressure and -78°C produced a coherent film which was a characteristic gold colour. Failure to thoroughly remove the native oxide layer from the titanium prior to nitridation resulted in a more patchy film. Blue ammonia-solvated electrons were observed at the counter electrode during the electrochemical modification. The magnitude of the current at +5.00 V was approximately 0.1mA after film formation had settled. The thickness of the film could be controlled by the amount of charge passed. Cottrell analysis suggested a diffusion coefficient for the diffusion of 'N' atoms (formally N^{3-}) through the titanium lattice of 2.01×10^{-11} cm^2s^{-1} (too low to be attributed to the diffusion of amide ions through solution). This process is very

slow as insertion of 'N' atoms requires structural changes in the metal lattice; it is likely to be the rate-limiting step for the reaction.

Energy dispersive X-ray spectroscopy demonstrated that the film was composed of only titanium and nitrogen. Raman spectroscopy showed the film to be free from significant amounts of TiO_2 and showed a pattern of lattice phonons similar to that recorded for commercial TiN powder. Differences in the two spectra were probably attributable to the highly reflective nature of the film and the presence of the underlying titanium substrate. The electrochemically produced film appeared to have a more defined stoichiometry than that of a film of TiN produced by reaction of titanium and ammonia at 700°C (implied by peak width).

XPS studies revealed that the surface of the electrochemically synthesised film was significantly oxidised. TiO_2, TiO and possibly titanium oxynitride species were detected at the surface. The N 1s spectrum also revealed the presence of molecular nitrogen trapped in the uppermost layers of the film. These materials were postulated to be generated by the aerial oxidation of TiN after synthesis as this particular sample had been stored in air for some time and the synthetic method excluded sources of oxygen. Sputtering measurements were performed in order to erode the surface oxide layer and to probe the underlying composition of the film, and to discover how this varied with depth. The titanium and oxygen data show the progressive removal of firstly TiO then TiO_2 to leave only background levels of oxygen after 88 minutes sputtering (an approximate depth of 900nm, based on silicon). The nitrogen spectra show a maximum nitride concentration at an approximate depth of 560nm. The depth profile of nitrogen in the film was complicated by the masking effect of oxygen but the invariable N 1s peak position suggests a well defined region of stoichiometric TiN with abrupt boundaries.

Magnetic and reflectance measurements were also in agreement with the production of TiN. Hardness testing indicated an approximate 20% increase in hardness over the titanium metal starting material.

3.7 Bibliography

[1] L. E. Toth, *'Transition Metal Carbides and Nitrides'*, Academic Press, New York, 118, 1971

[2] B. Holmberg, *Acta. Chem. Scand.*, **16**, 1255, 1962

[3] A.N. Christensen, A. Alamo and J.P. Landesman, *Acta. Cryst.*, **C41**, 1009, 1985

[4] I. Khidirov, I. Karimov, V.T. Em and V.E. Loryan, *Inorg. Mater.*, **22**, 1467, 1986

[5] O. Ruff and O. Treidel, *Ber.*, **45**, 1364, 1912

[6] D. M. Hoffman, *Polyhedron,* **13**, (8), 1169-1179, 1994

[7] A. Neckel, P. Rastl, R. Eibler, P. Weinberger and K. Schwartz, *J. Phys.*, C, **9**, 579, 1976

[8] R. L. Hatschek, *Am. Mach. Special Report* **752**, March, 129, 1983

[9] M. Witmer, B. Studer and H. Melchiar, *J. Appl. Phys.*, **52**, 5722, 1981

[10] L. H. Dubois, *Polyhedron*, **13**, (8), 1329-1336, 1994

[11] J. E. Sundgren, B. O. Johansson and S. E. Karlsson, *Thin Solid Films*, **105**, 353, 1983

[12] Y. Igasaki and H. Mitsuhashi, *Thin Solid Films,* **70**, 17, 1980

[13] L. Y. Ting, *J. Vac. Sci. Technol.*, **21**, 14, 1982

[14] K. Nakamura, K. Inagawa, K. Tsuruoka and S. Komiya, *Thin Solid Films*, **40**, 155,1977

[15] W. Fleischer, D. Schulze, R. Wilberg, A. Lunk and F. Schiade, *Thin Solid Films,* **63**, 347, 1979

[16] J. Chevallier, J. P. Chabert and J. Spitz, *Thin Solid Films*, **80**, 263, 1981

[17] K. Hieber, *Thin Solid Films*, **24**, 157 1974

[18] S. R. Kurtz and R. G. Gordon, *Ibid*, **140**, 277, 1986

[19] R. I. Hegde, R.W. Fiordalice and P. J. Tobin, *Appl. Phys. Lett*, **62**,19, 1993

[20] C. H. Winter, P. H. Sheridan, T. S. Lewkebandara, M. J. Heeg and J. W. Proscia, *J. Am. Chem. Soc.*, **114**, 1095, 1992

[21] P. Gomez-Sal, A. Martin, M. Mena and C. Yelamos, *J. Chem. Soc., Chem. Commun.*, 2185, 1995

[22] M.Wittmer, *J. Vac. Sci. Technol.*, **A3** 1797 1985

[23] G. Carter and J. Colligon, *'Ion Bombardment of Solids'*, Heinemann, London 1968

[24] J. H. Brannon, *Circuits and Devices*, 18-24, September 1990

[25] R. D. Vispute, J. Narayan and K. Jagannadham, *Journal of Electronic Materials*, **25**, 1 1996

[26] N. Biunno, J. Narayan, S. K. Hofmeister, A. R. Srivaster and R. K. Singh, *Appl. Phys. Lett.* **54**, 16, 1989

[27] O. Auciello, T. Barnes, S. Chevacharoenkul, A. F. Schreiner and G. E. McGuire, *Thin Solid Films*, **181**, 65-73, 1989

[28] N. Biunno, J. Narayan,, A. R. Srivaster and O. W. Holland, *Appl. Phys. Lett.*, **55**, 4, 1989

[29] S. Altshulin, A. Rosen and J. Zahavi, *J. Mat. Sci.*, **28**, 3749-3753, 1993

[30] A. Bittar, D. Cochrane, S. Caughley and I. Vickeridge, *J. Vac. Sci. Technol.*, A **15** (2), 1997

[31] D. Nicholls, *'Inorganic Chemistry in Liquid Ammonia'*, Elsevier Scientific Publishing Company, 1979

[32] G. M. Brown and L. Maya, *J.Am. Ceram. Soc.*, **71** (1) 78-82, 1988

[33] E. G. Gillan and R. B. Kaner, *Inorg. Chem.*, **33**, 5693-5700, 1994

[34] A. Hector and I. P. Parkin, *J. Chem. Soc., Chem. Comm.*, 1095-1096, 1993

[35] T. Goto, M. Tada and Y. Ito, *Electrochimica Acta*, **39**, (8/9), 1107-1113, 1994

[36] J. Schrechenbach, F. Schlottig, D. Dietrich, A. Hofmann and G. Marx, *J. Mater. Sci. Lett.*, **14**, 1344-1345, 1995

[37] J. Schrechenbach, F. Schlottig, D. Dietrich, A. Hofmann and G. Marx, *Appl. Surf. Sci.*, **90**, 2, 129-136, 1995

[38] C. Russel, *C. Chem. Mater.*, **2**, 241, 1990

[39] K. Nakajima and S. Shimada, *J. Mater. Chem.*, **8**, (4), 955-959 1998

[40] J.B. Gill, M. Hall and D. MacIntosh, *Electrochimica Acta*, **32**, (4), 589-595, 1987

[41] C.B. Ross, T. Wade and R.M. Crooks, *Chem. Mater.*, **3**, 5, 1991

[42] T. Wade and R.M. Crooks, *Chem. Mater.*, **8**, 832-835 1996

[43] D. R. Sadoway, *Journal of the Minerals, Metals and Materials Society*, **43**, (7), 15-19, 1991

[44] N. N. Greenwood and A. Earnshaw, '*Chemistry of the Elements*' Pergamon Press 1984

[45] Visual Designer 3.0 Software, Intelligent Instrumentation, Copyright 1993-5, Ron Goodwin

[46] Ed. D. R. Lide, '*CRC Handbook of Chemistry and Physics*', CRC Press, 74th Edition

[47] A. C. Fischer, '*Electrode Dynamics*', Oxford University Press, 33, 1996

[48] C. A. Kraus and W. C. Bray, *J. Am. Chem. Soc.*, **35**, 1315, 1913

[49] R. S. Krishnan, *'Structural Chemistry: Raman Spectra of Alkali Halides'*, Chapter 8, 189-226

[50] I. Duncan and J. H. Stewart, *Light Scattering in Solids*, 308-313

[51] C. C. Chen, N. T. Liang, W. S. Tse, I. Y. Chen and J. G. Duh, *Chinese Journal of Physics*, 32 (**2**), 205-210, 1994

[52] W. Spengler, R. Kaiser and A. N. Christensen, G. Muller-Vogt, *Phys. Rev. B*, 17 (3), 1095-1101, 1978

[53] R. S. Krishnan, '*The Raman Effect Volume 1: Principles*', Chapter 1: '*An Historical Introduction*'

[54] W. Spengler and R. Kaiser, *Solid State Comm.*, 18, 881-884, 1976

[55] Ed. D. Briggs and M. P. Seah, *'Practical Surface Analysis'*, J. Wiley and Sons 1983

[56] C. D. Wagner, W. M. Riggs, L. E. Davis and J. F. Moulder, *'Handbook of X-Ray Photoelectron Spectroscopy'*, Perkin-Elmer Corporation

[57] L. Ramqvist, K. Hamrin, G. Johansson, A. Fahlman and C. Nordling, *J. Phys. Chem. Solids*, **30**, 1835-47, 1969

[58] M. J. Vasile, A. B. Emerson and F. A. Baiocchi, *J. Vac. Sci. Technol. A,* **8,** (1), 99-105, 1990

[59] I. Milosev, H-H. Strehblow, B. Navinsek and P. Panjan, *Surface Science Spectra*, **5**, 145-151, 1998

[60] F. Esaka, K. Furuya, H. Shimada, M. Imamura, N. Matsubayashi, H. Sato, A. Nishijima, A. Kawana, H. Ichimura and T. Kikuchi, *J. Vac. Sci. Technol. A,* **15,** (5), 2521-2528, 1997

[61] C. R. Brundle, *J. Vac. Sci. Technol.* 13, 301, 1976

Chapter 4:

Preparation of Titanium Nitride at Ambient Temperatures

4.1 Strategy

Although the process designed for the synthesis of pure TiN films described in the previous chapter was successful in its goal, the rate of reaction was rather slow. The observed increase in current on raising the temperature of the liquid ammonia solution from -78°C to -33°C allows the calculation of an activation energy for the process in the order of 20 kJ mol^{-1}. Extrapolation to 25°C would predict an approximately 50-fold increase in the current compared with the current passed at -78°C. For this reason, a pressure cell containing a three-electrode assembly was constructed from heavy walled Pyrex glass such that liquid ammonia at 25°C could be safely contained. It was anticipated that this would allow a marked improvement in reaction rate, which would be beneficial if the process were to be scaled up for commercial use. This chapter describes the high pressure development of the system.

4.2 Experimental

4.2.1 Set-up of Electrochemical Cells

The working electrode was a piece of titanium foil, of approximate area of one side $1cm^2$ (Aldrich, 0.025-0.5mm thickness, 99.98% purity), with a titanium wire (Aldrich, 0.81mm diameter, 99.7% purity) connection. The counter electrode was a platinum wire gauze (Johnson Matthey), which was of sufficient area to ensure that the current was never limited by reaction at the counter electrode, and the pseudo-reference electrode was a polished platinum wire (Johnson Matthey). All potentials are quoted with respect to this pseudo-reference electrode. The titanium wire connections were spot welded to the steel electrode supports, which were well clear of the surface of the liquid ammonia, even after the significant expansion in volume of the liquid which occurred on warming from -78°C to 25°C. The electrodes were washed with distilled water and acetone before use.

The potassium amide/liquid ammonia solution was transferred *via* a stainless steel cannula into the nitrogen-flushed Pyrex tube cooled in a dry ice/acetone bath. The electrode assembly was inserted under a flow of nitrogen and the thread-seal was closed. The solutions used for electrolysis (prepared as in *section 3.3.1*), were saturated with KNH_2 during operation as evidenced by the precipitation of the white solid as the pressure cell was warmed from -78°C to 25°C.

4.2.1.1 Single Compartment Pressure Cell

The design of the cell is shown in *Figure 4.1.* It consisted of a 15mm internal diameter thick-walled Pyrex tube closed by a primary Teflon seal system supporting the electrode assembly. The cell could be pressurised when the secondary steel thread seal was in place.

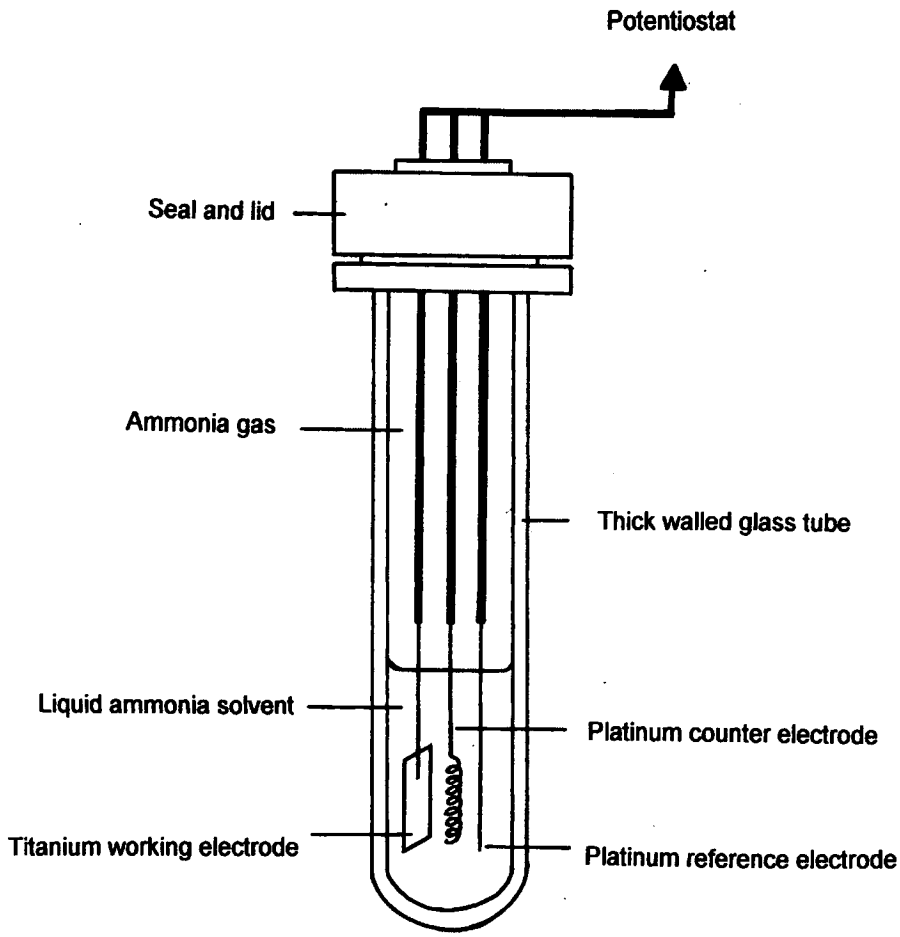

Figure 4.1: Schematic drawing of the single-compartment pressure cell

4.2.1.2 Two-Compartment Pressure Cell

A two-compartment pressure cell was also designed and built. This was to protect the product formed at the working electrode from possible reductive reactions caused by free electrons generated at the counter electrode during nitridation. The cell consisted of two sections of 15mm internal diameter thick-walled pyrex tubing bridged by two narrower sections of tubing, one split by a sintered glass frit and the other present to equalise the pressure between the two compartments. During operation, the liquid level was between the two bridges as shown. Again, the cell was sealed by primary Teflon bungs supporting the electrodes, and secondary steel thread seals, and in addition had a high pressure Teflon tap which aided the flushing of the cell with nitrogen gas. The cell is shown in *Figure 4.2*.

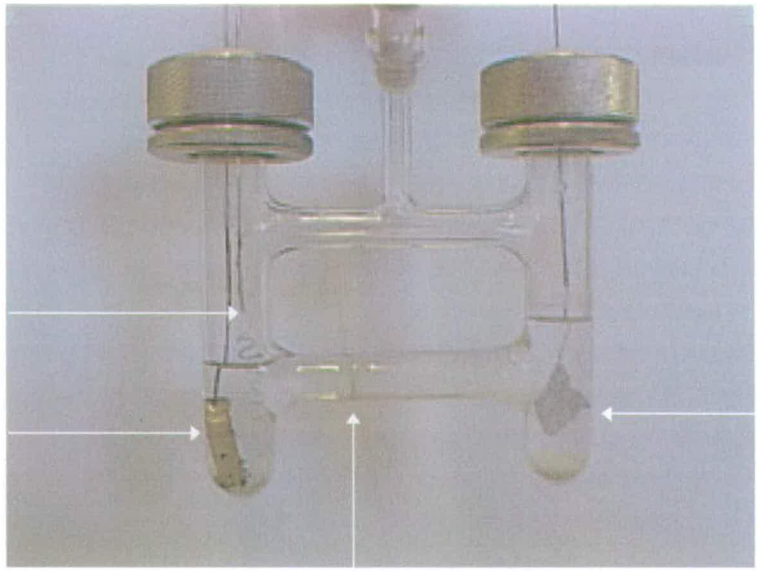

Figure 4.2: Two-compartment pressure cell during operation

4.3 Electrochemistry

4.3.1 Stripping of Oxide Layer

4.3.1.1 Single Compartment Cell

Prior to anodisation of the titanium working electrode, it was cycled for approximately 40 minutes at sweep rates of 50-100 mVs^{-1} between 0.00 V and a negative potential limit, always in excess of -1.50 V, such that a large negative current in the order of several mA was observed.

The cleaning process proceeded in a very similar way as had been observed at ambient pressure at -78°C. The only difference was that the process was faster, with a stripped titanium electrode being produced after less than 30 minutes. This is likely to be a result of the more efficient diffusion of oxide species away from the surface at higher temperature.

4.3.1.2 Two Compartment Cell

In the two-compartment pressure cell, cleaning was attempted both across the cell using all three electrodes, and within the working electrode compartment using a two electrode set up. In the latter case the platinum wire reference electrode became the anode, and was coiled to increase the effective surface area in solution.

Cleaning using all three electrodes and the whole cell produced only very small currents (approximately 0.3mA at -5.00 V), even on application of large negative voltages. A blue

colour was not observed at the working-electrode during this process. It was suspected that either the distance between the working- and counter-electrodes was too great, and/or that the presence of the sintered glass frit introduced a significant resistance which made the cleaning process ineffective. For this reason cleaning was also attempted within one compartment using only two electrodes. This procedure seemed to be successful, as a blue colour was observed at the titanium working-electrode. The CVs obtained were very similar to those obtained at ambient pressure at -78°C.

4.3.2 Nitride Synthesis

4.3.2.1 Single Compartment Cell

Electrochemical modification took place between 0.00 and +5.00 V using a 1 or 100kΩ resistor. The 100kΩ resistor was employed to limit the current at any given potential, according to Ohm's Law. Nitridation was initiated at both -78°C and then the cell allowed to warm up and pressurise after a certain amount of charge had been passed, and directly at 25°C when the cell had previously been pressurised.

4.3.2.1.a Experiment 1

Electrochemical modification began by holding the titanium working electrode at +2.00 V. The current decayed to a steady value of 100μA, and after 10 minutes the dry ice/acetone bath was removed, and the cell was allowed to warm to 21°C. At 21°C and 10 atm, the current had increased to 1.5mA, representing a fifteen-fold increase. White potassium amide crystals precipitated from solution, in line with the negative solubility coefficient of the salt. The

potential was then stepped up in 0.50 V intervals to +5.00 V, and the current reached 4mA. This represents a 40-fold increase in current. This fitted well the predicted increase in current, estimated to be 50-fold at 25°C based on the behaviour observed between -78°C and -33°C. Yellow-gold particles were seen growing on the edges of the titanium working electrode. This is presumably the result of preferential nucleation of the product at positions where the field lines were most intense. As more charge was passed, more particles grew and these were darker brown in colour. The origin of this colour change is unknown, but it is possible that it was caused by the way in which the particles were reflecting light due to a change in size of the particles. 19 Coulombs of charge was passed in total.

4.3.2.1.b Experiment 2

The previous experiment had not led to the formation of a coherent thin film, and it was suspected that this was due to the production of nucleation centres preferentially at the freshly cut edges of the electrode. The stepwise increase in potential had been quite rapid, and so a more gradual approach was taken in the second experiment. Electrochemical modification this time was initiated at +1.00 V and at -78°C. The potential was increased in 0.50 V intervals to +2.50 V, always allowing the current to decay at each potential. After 100mC had been passed, the potential was increased to +3.00 V in 0.10 V intervals. Finally, the potential was increased to +5.00 V in 0.50 V intervals, by which time 1C of charge had been passed. At this stage the dry ice/acetone bath was removed and it was observed that the working electrode was uniformly coated with a bright gold coat, characteristic of titanium nitride and similar to that produced in the low temperature, ambient pressure cell. Again, a very large increase in current was observed as the cell warmed up. At this stage a change in the product morphology was observed. The familiar yellow particles which were initially observed

forming at the edges of the working electrode fell off after reaching a certain size, causing a temporary drop in current. The current then slowly climbed back to close to the original value, presumably as the newly exposed titanium metal reacted. At the end of the experiment, 20C had been passed and the titanium foil was covered in a rough yellow-grey coat (*Figure 4.3*). Even though the titanium electrode had initially been coated evenly, the increase in temperature (and thus current), led to nucleation and growth of particles rather than growth of the existing two-dimensional film on the electrode.

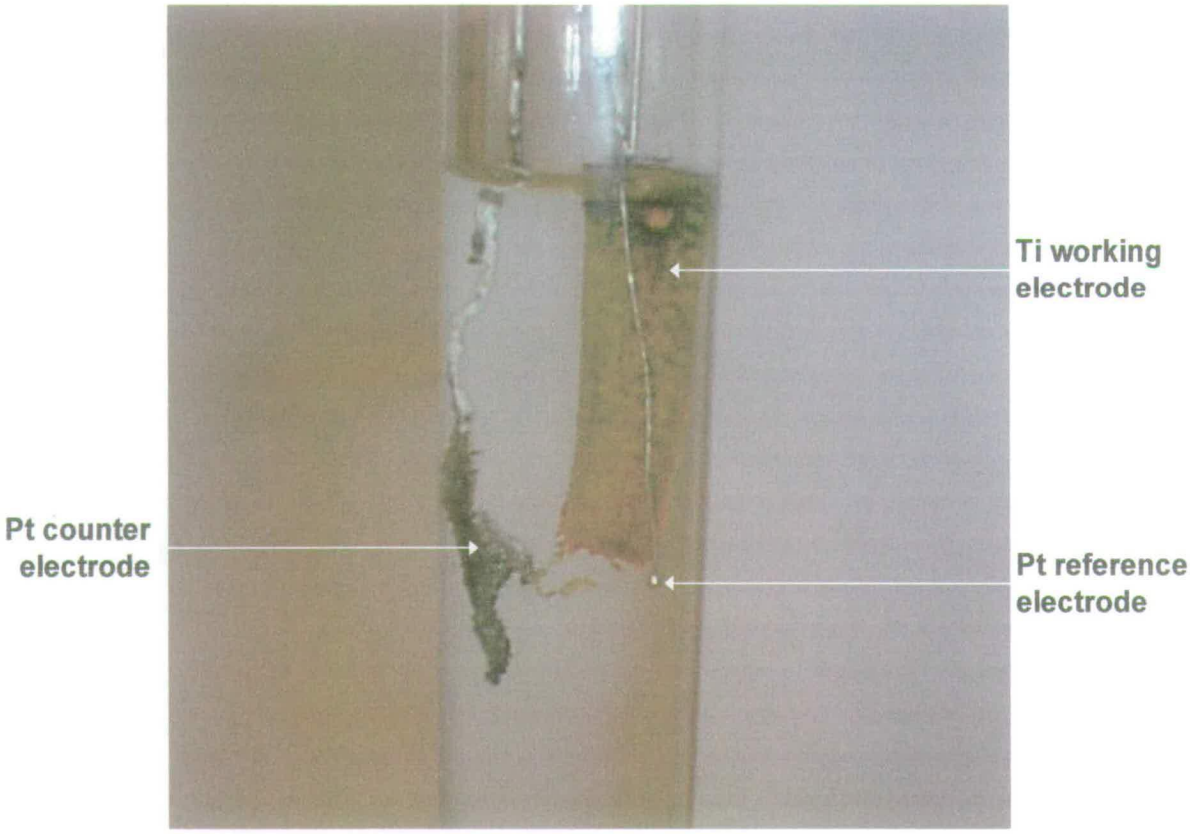

Figure 4.3: The single compartment pressure cell during operation at 10atm and 25°C. A gold-coloured material can be seen on the titanium working electrode

4.3.2.1.c. Experiment 3

The potential was again increased gradually in a stepwise manner to +2.00 V. After 1C of charge had been passed the cell was warmed to 21°C, and the golden-coloured film was again observed on the titanium. A blue coloration was also observed at the platinum counter electrode, confirming that the solution was indeed very dry. The potential was then stepped up to +3.00 V in 0.20 V intervals. Black particles up to several millimetres long were observed to be growing at the edges of the electrode in a dendritic fashion. The pattern of growth was strikingly reminiscent of iron filings aligned around a bar magnet. Such a pattern suggests that field-induced growth was occurring. The particles also looked relatively crystalline.

The black product observed for the first time in this experiment was clearly very different in appearance to stoichiometric titanium nitride, (which can be gold-coloured in thin film form depending on the thickness, and bronze-coloured as a powder). It appeared that gold-coloured titanium nitride was being produced early on in the reactions, but as soon as the temperature, and thus current, was increased the nature of the product changed. It is possible that a non-stoichiometric titanium nitride was produced as a result of these changes, or that the different colour was simply due to a change in particle size.

4.3.2.1.e. Experiment 4

In all previous experiments, electrochemical modification had commenced at -78°C. This time the pressure cell was warmed to room temperature immediately, and the electrochemical modification initiated at 25°C. It was suspected that the possible change in initial nucleation and growth conditions might effect the morphology of the product. More specifically, it was

expected that particles would be produced immediately without the formation of the initial gold-coloured film, which seemed to be associated with conditions of low temperature and low current. This did not appear to be the case. After a stepwise increase in potential to +1.00 V and the passage of 300mC of charge, a gold-coloured film was observed on the titanium working electrode. The potential was then increased slowly to +1.80 V in 0.10 V intervals. The current decayed from its maximum value to a steady value in each step. However, on the step to +1.90 V, the current did not decay, but instead increased rapidly. Small black particles appeared after a period of a few minutes and they continued to grow as this potential was maintained. A value of +1.90 V appeared to be the maximum potential in which a current decay regime would be tolerated.

The gold-coloured film appeared to be the first product of the reaction, regardless of the initial temperature. If the temperature and current had remained low, the film would have continued to grow in the same way. When the temperature and current increased at this stage, particles began to grow on the electrode. It was unclear whether the temperature or current alone was responsible for the change. These variables were inextricably coupled in this cell set up: when the cell was allowed to warm up and pressurise, the currents recorded escalated. Identification of the dominant factor was therefore elusive.

4.3.2.1.e Experiment 5

In Experiment 5 a 100kΩ current-limiting resistor was employed in the circuit in order to consider the two variables of temperature and current separately. It was thought that moderation of the current might avoid particle formation and instead a thick, coherent film might be grown, as in the ambient pressure cell. It was thought at this stage that the dramatic

increase in current was responsible for the change in product morphology, rather than the increase in temperature and pressure. However, the lower current did not affect the course of the experiment as expected. At +5.00 V the current was limited to 0.05mA, approximately half the value recorded in the ambient pressure cell, and 100 times smaller than in the previous experiment. As electrochemical modification began, a gold-coloured film was observed on the titanium working electrode as usual. Gold-coloured particles then began to nucleate and grow, and these became darker in colour as the experiment progressed, eventually becoming black. This behaviour mimicked that observed when the standard 1kΩ resistor was used. Despite the current being comparable to that recorded in the ambient pressure cell, the type of product formed was identical to that seen previously in the pressure cell. This implied that the current was not the governing factor in influencing product morphology, but rather that elevated temperature and pressure was responsible for the formation of particles.

4.3.2.1.f. Experiments 6 onwards

These experiments were performed at a higher voltage in an attempt to collect bulk samples of the product observed in previous experiments. Electrochemical modification was initiated after the cell had been pressurised. It had been noted that the current gradually decreased during the course of these long experiments, so, in order to maintain the current as close to saturation as possible, the potential was increased to a maximum of +8.50 V towards the end of the experiment. After several hundred Coulombs had been passed the working electrodes were covered in a black powder and were severely eroded along the edges, with holes in places. In one experiment there were also some large, black, crystalline-looking particles growing on the titanium wire connection which had been partly immersed in the solution. In

another experiment, the working electrode was observed to be coated with long, spiralling 'wires' of product which extended several millimetres into the solution.

4.3.2.2 Two Compartment Cell

Owing to the relatively high voltages employed in the single-compartment pressure cell, it was possible that the particulate product formed was a titanium compound with titanium in a higher oxidation state which might subsequently be reduced to TiN by free electrons in the vicinity of the counter electrode. This theory would be very difficult to disprove without the use of the two-compartment pressure cell. By ensuring that the counter electrode was separated from the working electrode in another compartment, the possibility of subsequent reduction could be eliminated. If TiN (where titanium is formally in the +3 oxidation state), could be identified as the product of the reaction in the two-compartment cell, it would be reasonable to suppose that the same reaction was occurring in the single-compartment cell. This would show that TiN is resistant to reduction under these conditions, and had not been affected by the free electrons at the counter electrode in the single-compartment cell.

A small amount of potassium metal was added to the working-electrode compartment of the cell. An intense blue colour indicative of ammonia-solvated free electrons was observed. No sign of the blue colour was observed in the other compartment, even after some time. A potential difference was applied in the attempt to drive the electrons through the frit, but this was unsuccessful. This demonstrates that the sintered glass frit was impermeable to ammonia-solvated electrons. A possible reason for this is that the frit presents a very large surface area of glass with surface -OH groups which can react with solvated electrons.

Several electrochemical modification experiments were performed in the two-compartment cell. In all cases the cell was warmed to room temperature and pressurised before electrochemical modification was initiated. At +5.00 V the steady current was found to be approximately 0.3mA. This is comparable to the magnitude of the current passed at +5.00 V in the ambient pressure cell at -78°C, and approximately a factor of ten smaller than the current passed in the single-compartment pressure cell without the frit. It appears that the frit, in effect, was acting as a current limiting resistor in the circuit. The two-compartment cell therefore re-created the current-voltage conditions present in the ambient-pressure cell, whilst raising the temperature and pressure of the process and excluding free electrons. The familiar gold-coloured film was observed in the early stages of the experiment, followed by the growth of small gold then black particles which were observed to be formed preferentially on the side of the working electrode closest to the bridge linked to the counter electrode compartment. This area also become eroded, as shown in *Figure 4.4*. This pattern was observed regardless of the deposition potential. Such experiments confirmed that the increased pressure and temperature were responsible for the growth of particles, and that the absence of free electrons in the vicinity did not appear to markedly alter the nature of the product formed.

Table 4.1 summarises the range of conditions accessible in the two pressure cells, compared with those in the ambient pressure cell (discussed in the previous chapter).

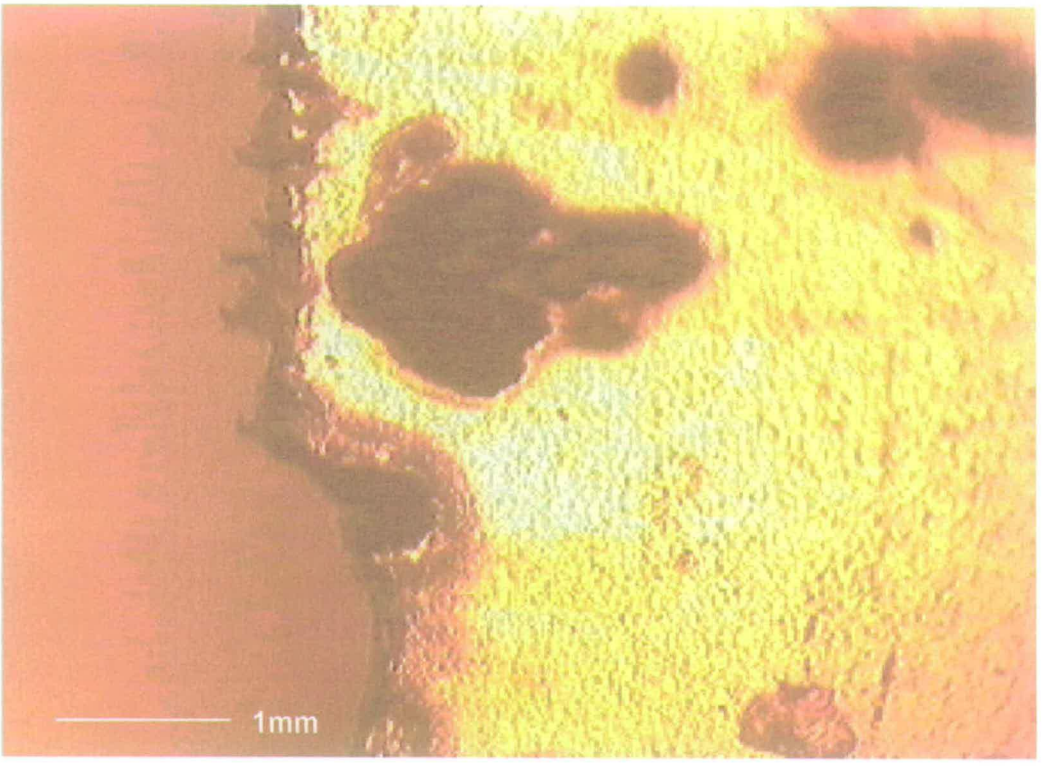

Figure 4.4: Optical microscope image of the eroded titanium electrode after synthesis. The gold-coloured film can be observed, as well as the brown particles.

Variable	Ambient Pressure Cell	Single-Compartment Pressure Cell	Two Compartment Pressure Cell
Pressure / atm	1	10	10
Temperature / °C	-78	25	25
Potential / V (vs. Pt)	1.00-5.00	1.00-8.50	1.00-5.00
Current at +5V / mA	0.1	4.0	0.3

Table 4.1: Summary of the range of conditions accessible in the three different electrochemical cells

4.4 Characterisation of Pressure Cell Products

On evaporation of the ammonia from the cell and quenching of the KNH_2 electrolyte with water, the particles which had fallen from the electrode surface were washed with water, centrifuged, and dried in a stream of nitrogen gas. The Raman spectrum of this powder showed bands characteristic of anatase, TiO_2 [1]. This was very surprising given that the procedures adopted for drying and handling the reagents result in extremely low levels of oxygen-containing species and no sign of TiO_2 was observed for the thin films generated in this way. The obvious source of oxygen in the particles is from their post-treatment with water. Although TiN is normally regarded as being relatively unreactive, it was found that small (<10 μm) TiN particles do indeed react with aqueous base to produce anatase, and a recent electrochemical study of TiN in 6M aqueous KOH solution has shown that even bulk TiN slowly reacts, albeit to form different products [2]. Hence the conditions used for the isolation of these small particles would inevitably result in the production of anatase. Such small particles are more reactive as they have fewer neighbouring atoms in the bulk to stabilise the higher energy surface atoms. This problem was overcome by ensuring that the particles were washed with several portions of dry liquid ammonia after synthesis to remove potassium amide. Only after the last traces of ammonia had been removed *in vacuo*, were the particles exposed to air. The particles were stored under dry nitrogen where possible. Samples used in the following characterisation tests are from the single compartment pressure cell unless otherwise stated.

4.4.1 Raman Spectroscopy

A typical Raman spectrum of one of the particles is shown in *Figure 4.5a*. Comparison with the spectrum of a commercial sample of TiN (*Figure 4.5b*) (composition TiN_x where x = 0.994 by CHN analysis) shows it to be almost identical. As discussed in *section 3.5.4*, this shows the powder produced in the pressure cell to be approximately stoichiometric.

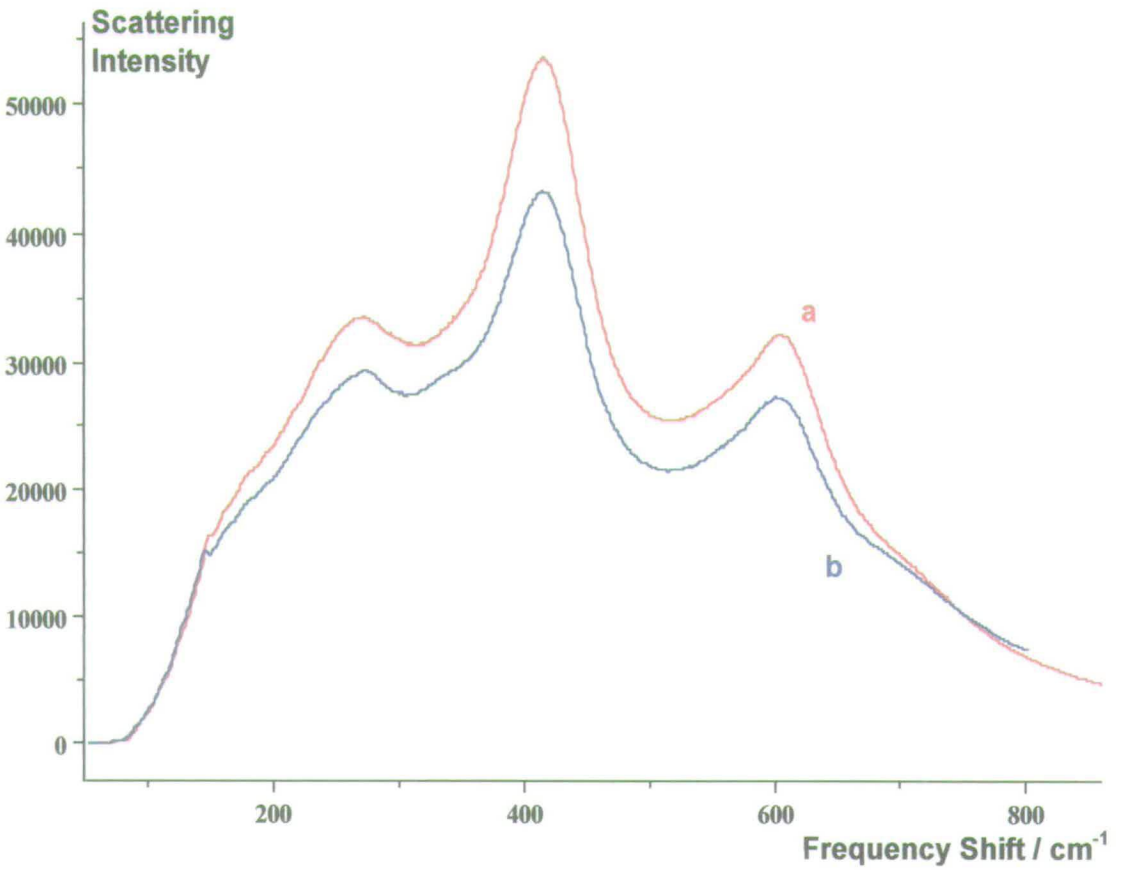

Figure 4.5: Raman spectra of **(a)** the electrochemically produced powder, and **(b)** commercial TiN powder

Figure 4.6 shows the Raman spectrum obtained from the powder synthesised electrochemically in the two compartment pressure cell. This is again compared with the

spectrum for commercial osbornite. It can be seen that the spectrum is broadly similar, but that it has been shifted to higher energy, by 17 cm^{-1}, based on the central, most intense peak. This indicates that the material produced here is slightly nitrogen-deficient compared to the commercial sample.

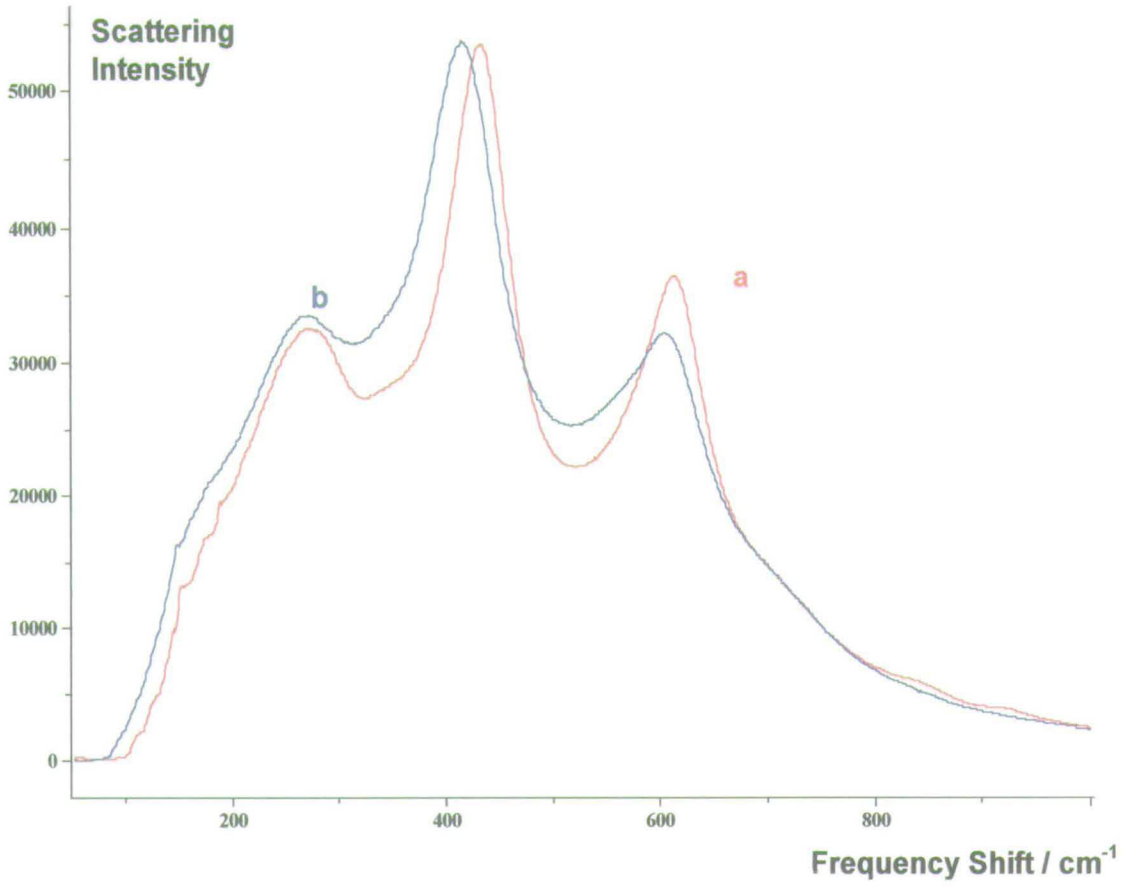

Figure 4.6: Raman spectra of **(a)** the powder produced electrochemically in the two compartment cell, and **(b)** commercial TiN powder

4.4.2 Scanning Electron Microscopy (SEM)

Some SEM images of the particles are shown in *Figure 4.7*. A representative cluster of the particles is shown in *Figure 4.7a*. It can be seen that they consist of straight and spiralling 'wires', and 'tendrils'. *Figure 4.7b* shows an enlargement of the type of particle boxed in

Figure 4.7a. The red arrow shows the direction of growth from the electrode. The material appears to consist of a stack of platelets which lie parallel to the electrode surface. It is possible that these platelets were formed by the successive erosion of the upper surface of the titanium electrode i.e. insertion of 'N' into the metal caused layers to lift off, perhaps due to a lattice mismatch. *Figures 4.7c* and *4.7d* show the tendrils which grew out of the clean electrode edges where the field lines were strongest. The amorphous nature of the material is now very clear. *Figure 4.7e* shows a spiralling wire, and *Figure 4.7f* shows a more brick-like material. Overall it is clear that there is a wide variety of particle morphologies.

4.4.3 Diffraction Methods

4.4.3.1 Single Crystal X-Ray Diffraction

The crystalline-looking 'tendrils' observed growing on the titanium working electrode gave no indication of being either single crystals or even polycrystalline material when mounted on the diffractometer.

4.4.3.2 X-Ray Powder Diffraction (XRD)

Initially the commercial sample of TiN powder showed no diffraction peaks. A sample of the powder prepared in the pressure cell displayed no distinct diffraction peaks either. However, significant background scattering was observed indicative of nano-crystalline or amorphous material. Many nano-crystalline or amorphous materials can be induced to give sharper X-ray diffraction patterns by annealing at high temperatures and so an attempt was made to achieve

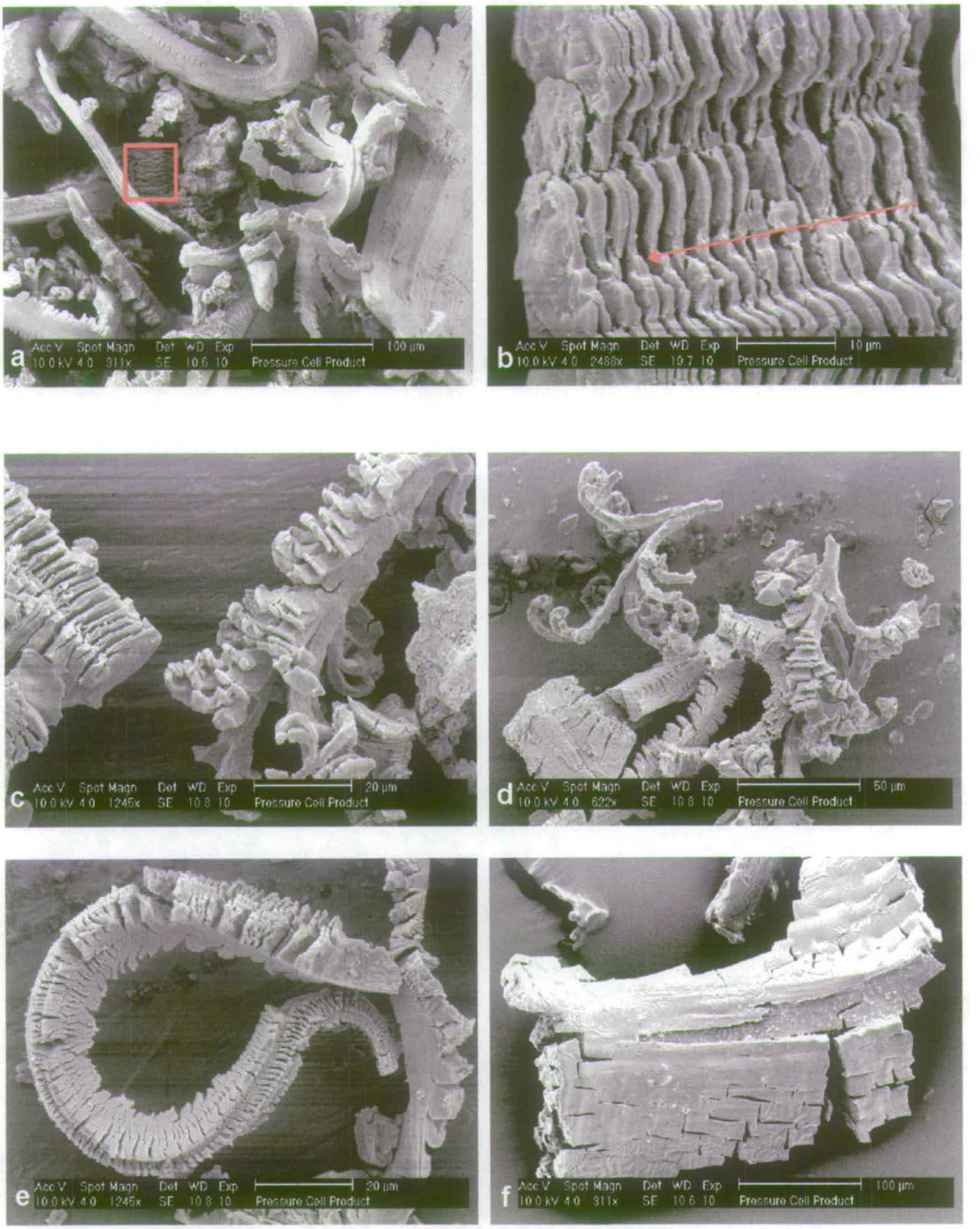

Figure 4.7: SEM images of the particles produced in the pressure cell

this with the powder samples. As a first step in determining a suitable regime for processing the particles, experiments were performed on commercial TiN powder.

An XRD pattern was collected after the commercial TiN powder had been subjected to drying and annealing by stepwise heating under vacuum. This process was performed by transferring a sample of the powder to a Schlenk tube which was equipped with a sintered glass frit below the tap to prevent escape of the fine powder under reduced pressure. This was attached to a mass spectrometer (HAL/3F 301 Residual Gas Analyser) previously evacuated to a pressure of 10^{-6}-10^{-7} Torr. A background spectrum was recorded over a mass/charge range of 1-300 mass units. The tap on the Schlenk tube was then slowly opened. The peak at 18amu was found to increase as water desorbed from the particle surface. A small tube furnace was then placed around the Schlenk tube and the powder was heated at 200°C for 2 hours with continuous pumping. The temperature was then increased to 400°C for 24 hours. Finally the temperature was raised to 600°C for 5 hours. By the end of this heating process, the peak due to water had dropped to background levels, and an XRD pattern characteristic of osbornite was obtained (three intense peaks at *d*-spacings of 2.450Å, 2.117Å and 1.497Å). It appears that this lengthy stepwise heating process both successfully dried and increased the degree of crystallinity of the powder. It was apparent that a considerable amount of water had been adsorbed on the surface of the particles.

The stepwise heating process did lead to the appearance of some broad, low intensity peaks in the XRD pattern of the material prepared in the pressure cell. However, conclusive identification of the material was not possible. It is conceivable that these very small particles had reacted with adsorbed water to form surface oxide, making identification difficult. Attempts at annealing the powders under argon or in a tube under vacuum led to the formation of titanium(IV) oxide (anatase). It was decided that characterisation methods which relied on minimal post-processing of the product were desirable, and therefore this work was not pursued.

4.4.3.3 Transmission Electron Microscopy (TEM) - Electron Diffraction

TEM was employed in order to elucidate the size of the particles produced, and to attempt to record an electron diffraction pattern of the material for structural determination. Finding an area of the sample which was thinned to the optimum thickness so as to be transparent to electrons was not trivial. TiN is a difficult material to thin by ion bombardment as it is very resistant to erosion. The epoxy thinned at a much greater rate, sometimes leading to some of the powder becoming loose and falling out of the resin. However, *Figure 4.8* shows the TEM image of a suitable area of the thin section of the powder produced in the pressure cell mounted in epoxy resin. The dark area (*bottom left*), indicates bulk powder, and the light area (*top right*), indicates resin. The morphology of the central section consists of very small (5-10nm), spherical particles. These basic building blocks of the material go on to produce the larger structures seen with the SEM. This explains why the particles showed no X-ray powder diffraction.

Electron diffraction of the particles produced a simple pattern of distinct rings with the occasional appearance of spots, indicating the presence of nano-crystallites (*Figure 4.9*). The separation of the rings corresponds to d-spacings as shown in *Table 4.2.* Simulated powder patterns for the osbornite and Ti_2N phases of titanium nitride, and four oxide phases anatase, rutile, brookite (TiO_2) and hongquiite (cubic TiO) were generated by the DRAGON program [3] between 0 and 80° 2θ by entering the appropriate unit cell parameters (*Table 4.3*) [4-9]. The program lists all the reflections that would be observed by X-ray powder diffraction, removing those which are extinct due to general space group symmetry (see *section 2.6*).

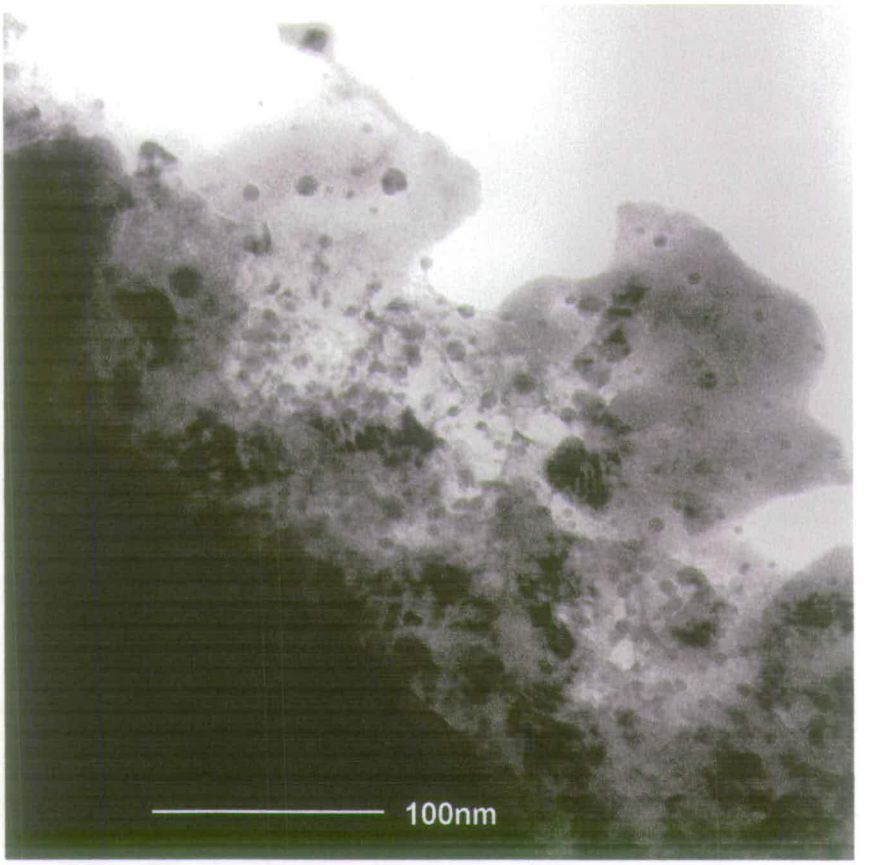

Figure 4.8: TEM image of a thin section of the pressure cell product mounted in epoxy resin

The data obtained from experimental electron diffraction closely match the generated d-spacings of both osbornite and hongquiite (cubic TiO). It is not possible to distinguish between these two materials using this method, although the results from Raman spectroscopy (see *section 4.4.1*) would support the osbornite phase and rule out hongquiite. If the material is osbornite, the reflections observed take values of h, k and l that are all odd or even. This reveals that the material forms a face-centred cubic cell in the solid state. The d-spacings are clearly different to those of the oxides anatase, rutile and brookite (these materials also show many more reflections) confirming that careful post-synthesis handling had prevented aerial oxidation of the material.

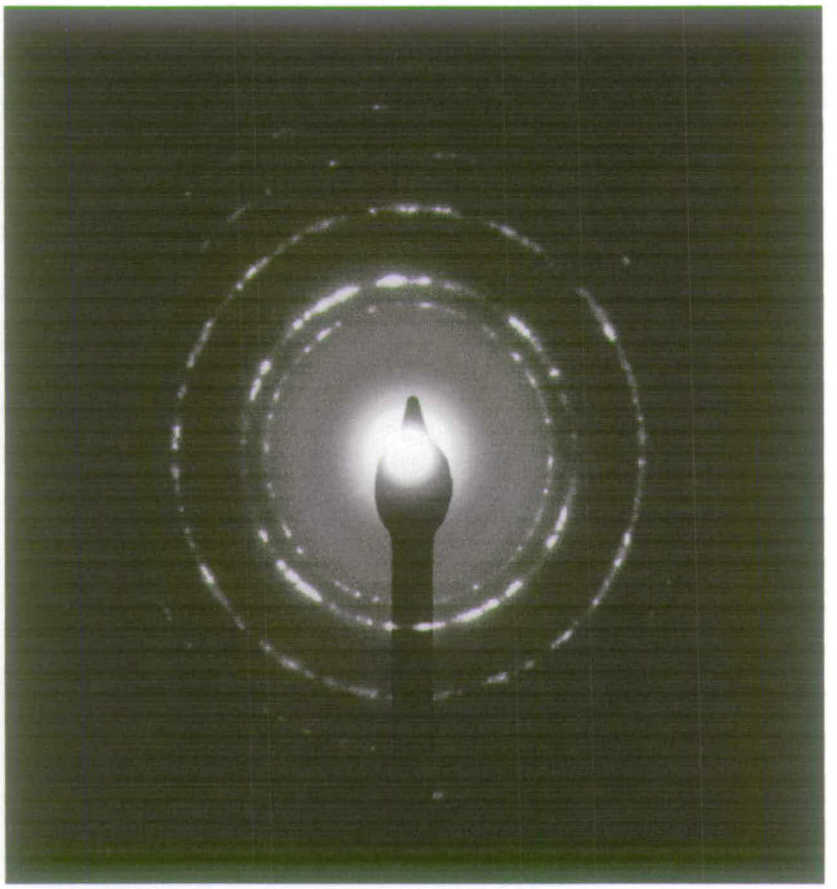

Figure 4.9: Electron diffraction pattern of a sample of the powder produced in the pressure cell

ED	Osbornite		Tetragonal Ti_2N		Anatase		Rutile		Brookite		Cubic TiO	
2.47	2.46	111	2.44	112	2.43	103	2.49	101	2.47	102	2.48	111
2.12	2.12	200	-	-	-	-	2.19	111	2.09	401	2.15	200
1.52	1.50	220	1.51	204	1.49	213	1.53	300	1.52	520	1.52	220
1.29	1.28	311	1.28	215	1.29	222	1.30	311	-	-	1.29	311
1.23	1.22	222	1.22	224	1.23	223	1.24	202	-	-	1.24	222
1.06	1.06	400	-	-	1.06		1.08		1.04		1.07	400
0.95	0.95	420	-	-	0.95		0.94		0.98		0.96	420
0.85	0.87	422	-	-	0.85		0.84		-	-	-	-

Table 4.2: Experimental d-spacings (± 0.02 Å) from electron diffraction compared with the closest d-spacings (in Å) and hkl values from some known titanium nitrides and oxides. The figures in red have a good match with the experimental result.

Material	a	b	c	Reference
Osbornite	4.235	= a	= a	[4]
Tetragonal Ti_2N	4.1493	= a	8.7858	[5]
Anatase	3.78216	= a	9.50226	[6]
Rutile	4.5940	= a	2.9589	[7]
Brookite	9.166	5.436	5.135	[8]
Cubic TiO (hongquiite)	4.293	= a	= a	[9]

Table 4.3: Lattice parameters (in Å) of some known titanium nitrides and oxides

4.4.4 Carbon, Hydrogen, Nitrogen (CHN) Analysis

CHN analysis of the commercial TiN powder gave 0 (0)% C, 0 (0) % H and 22.77 (22.63)% N (expected values are shown in parentheses). CHN analysis of the pressure cell powder gave 4-10 (0)% C, 1-2 (0)% H, and 1-11(22.63)% N. The data for the commercial TiN are in good agreement with the expected values, suggesting that the drying/annealing process successfully removed adsorbed water. However, good data for the pressure cell products could not be obtained. The percentage of nitrogen detected was always very low, and there was a significant amount of carbon present. Given that there are no carbon-containing materials involved in the electrochemical preparation of the titanium nitride, carbon can only have been incorporated during the post-processing. This may be a result of the reaction of trace amounts of potassium amide with atmospheric carbon dioxide to form potassium carbonate or potassium hydrogen carbonate. If the powders were non-stoichiometric, as previously suggested, then very little of the mass might be due to nitrogen and results would be low, although this is not in line with other results. Given the very small size of these particles as seen by TEM, they are likely to be very reactive towards water leading to the formation of titanium(IV) oxide. This is the most likely explanation for the low CHN results.

4.5 Summary and Conclusions

This chapter describes the high pressure scale-up of the electrochemical method designed for the synthesis of titanium nitride introduced in the previous chapter. The construction of a pressure cell which would safely contain the liquid ammonia solvent at ambient temperatures (and 10 atms pressure) was successful. The predicted 40-fold increase in current (at +5V vs. Pt) was observed, presumably due to the surpassing of an activation barrier for the diffusion of 'N' atoms into the titanium.

The procedure developed for the reduction of the native oxide layer on the metal prior to nitridation was also implemented in the pressure cell, and in fact gave a more efficient cleaning of the electrode under these conditions.

In the experiments described in the previous chapter the morphology of the product did not change as a result of the applied potential (0.00-5.00 V) or the amount of charge passed, and under these conditions there was only a low current density at the electrode surface (approximately 0.1mA at +5.00 V). The low rate of reaction allowed slow diffusion of 'N' atoms into the titanium, which was able to accommodate changes in its lattice parameters without loss of its structural integrity.

The nature of the product formed at ambient temperature was very different from that produced at -78°C. The rate of product growth was significantly faster under these conditions and was not compliant with the continued formation of a coherent film. Instead erosion of the electrode eventually resulted in the formation of discrete particles. It is thought that the exact particle nucleation regime was dependent on the initial quality of the surface. It was observed

that the particles formed preferentially at the edges of the electrode which were freshly cut surfaces with the highest current density. The success of the oxide-stripping step undoubtedly had an influence on the site of particle formation too.

After initial formation of a characteristic golden-coloured film (always the first reaction product) yellow, bronze then black particles were observed as the reaction proceeded, independent of the applied potential (in the range 1.00-5.00 V). At +5.00 V the typical current was approximately 4mA. The variable colour was thought to be a result of the changing particle size, which varied greatly as shown by both SEM and TEM. Evidence that these particles were electrically conducting was provided by the observations that (a) the particles grew as 'tendrils' towards the counter electrode, and (b) when dislodged from the electrode surface by gentle tapping the current decreased, indicating a reduction of electrically conducting surface area. Use of a current limiting resistor in the circuit had no effect on the product morphology. It was concluded that the increase in temperature and pressure was responsible for the production of particles not thin films, rather than the current or potential.

The material produced by this method was found to be air- and/or moisture-sensitive owing to its extremely small particle size (5-10nm by TEM). This made reliable characterisation of the material very challenging. Larger assemblies were constructed from these basic building blocks in the shape of straight or spiralling 'wires' (up to several mm in length), 'tendrils' or stacked layers. Raman spectroscopy and electron diffraction together gave good evidence for the production of stoichiometric TiN in the cell, and demonstrated that the products were free from significant amounts of TiO_2.

Finally a two compartment pressure cell was constructed in order to exclude the possibility of reaction of the product with nearby free electrons generated at the counter electrode during nitridation. It was possible that a higher oxidation state titanium nitride was initially produced at the electrode (feasible at the chosen applied potential) and subsequently reduced by the neighbouring free electrons. The working electrode and the counter electrode were therefore housed in two compartments separated by a sintered glass frit. In practice the frit acted as a current limiting resistor; currents comparable to those observed in the low temperature cell were observed. Raman spectroscopy showed that the particulate product formed in the two compartment pressure cell was a slightly nitrogen-deficient titanium nitride, demonstrating that higher oxidation state nitride has not formed. Further investigations are required to quantify the degree of nitrogen-deficiency, and to ascertain its significance.

4.6 Bibliography

[1] M. Franck, J-P. Celis, and J.R. Roos, *J. Mater. Res.*, **10**, 119, 1995

[2] C.F. Windisch, Jr., J.W. Virden, S.H. Elder, J. Liu, and M.H. Engelhard, *J. Electrochem. Soc.*, **145**, 1211, 1998

[3] J. K. Cockcroft, DRAGON Program, © 1998 Birkbeck College, available at: http://gordon.cryst.bbk.ac.uk/htbin/dragon.exe

[4] N. Schoenberg, *Acta Chem. Scand.*, **8** 213-220, 1954

[5] A. N. Christensen, A. Alamo and J. P. Landesman, *Acta Crystallogr.*, Sect. C (Cr. Str. Comm.), **41**, 1009-1011, 1985

[6] J. K. Burdett, T. Hughbanks, G. J. Miller, J. W. Richardson and J. V. Smith, *J. Am. Chem. Soc.*, **109**, 3639-3646, 1987

[7] I. E. Grey, C. Li, C. M. MacRae and L. A. Bursill, *J. Solid State Chem.*, **127**, 240-247, 1996

[8] R. W. G. Wyckoff, '*Crystal Structures*', **1**, InterScience 1948

[9] T-H. Yu, S-J. Lin, P. Chao, C-S. Fang and C-S. Huang, *Acta Geologica Sinica*, **2**, 202-218, 1974

Chapter 5:

Electrochemical Synthesis of Group 6 Nitrides

5.1 Introduction

5.1.1 Properties and Applications

The Group 6 nitrides are potentially useful materials for diffusion barriers and gate electrodes in many modern electronic devices [1]. They also form hard, wear-resistant coatings suitable for application on machine tools [2]. In addition they are used as optical and decorative layers [3].

The insertion of nitrogen atoms into a transition metal lattice brings about an increase in the distance between metal atoms. This modifies many of the properties of the material, in particular, the ability to favour adsorption on the surface which is interesting in the field of catalysis. The γ-Mo_2N cubic variety of molybdenum nitride has recently been found to show catalytic activity for CO hydrogenation, C_2H_6 hydrogenation, CO_2 methanation, hydrodesulfurisation and NH_3 synthesis [4]. Molybdenum nitride, both supported and unsupported, has been found to be more active than a commercial sulfided Ni-Mo/Al_2O_3 catalyst in quinoline hydrodenitrogenation (HDN) and favoured formation of the desired propylbenzene product rather than propylcyclohexane. Not only was the nitride catalyst highly active and selective for HDN, but it was also sulfur-resistant even under severe conditions [5]. In the last few years molybdenum nitride has attracted attention in other hydroprocessing studies. In the heteroatom removal from indole, benzothiophene and benzofuran, Mo_2N was found to be an effective catalyst for X-C (X= N, O, S) bond scissions and selective for the formation of aromatic products [5]. In another study, supported molybdenum nitride catalysts were found to be 1.3-3.1 times more active than a sulfided

catalyst in the HDN of carbazole. The catalyst was also found to be extremely active for the selective C-S bond cleavage of dibenzothiophene to produce biphenyl [5].

5.1.2 The Mo-N System

Three compounds were predicted by Hagg for the Mo-N system [6]. Firstly, β-Mo_2N which has a tetragonal structure (a = 4.210Å, c = 8.060Å), and is stable above 600°C. Secondly, γ-Mo_2N which is stable at elevated temperature and which has a face-centred cubic structure (a = 4.163Å), with nitrogen atoms randomly occupying half of the octahedral voids. The melting point has not been determined because of the very high equilibrium pressure of nitrogen, but it has been estimated to be about 2000°C at a nitrogen pressure of 100MPa [7]. Thirdly there is δ-MoN with a hexagonal superlattice structure which has a double-cell dimension (a = 5.725Å, c = 5.608Å) [8]. In general, these materials are rather unstable and decompose at moderate temperatures [4].

Recently, cubic mononitride MoN with a B1-type NaCl structure has been reported and anticipated to have a moderate superconducting transition temperature of 29K. This nitride, not predicted in the phase diagram was found to have a lattice parameter a = 4.212Å. It was prepared as a thin film by PVD processes, with an experimental T_c value between 3 and 14K. The composition was apparently stoichiometric, but the crystal structure was not perfect. In particular, some of the nitrogen atoms were located in interstitial sites, inducing vacancies in the N-sublattice. The quantity of the vacancies could be as high as 10-15%, leading to a decrease in the T_c value. Direct synthesis of B1-MoN and annealing of B1-MoN or hexagonal δ-MoN using high temperatures and high pressures were used in order to stabilise the B1-

MoN phase and consequently to reduce the number of N vacancies which are filled by interstitial N atoms under high pressure. Even at temperatures and pressures as high as 2300K and 7GPa, the final products were always hexagonal δ-MoN, with a relatively high critical temperature, T_c=14.9-15.9K [4].

5.1.3 The W-N System

Both the molybdenum and tungsten nitride systems can exhibit tremendous polymorphism, although most are contaminated with oxygen. The tungsten system is quite similar to molybdenum, although an even larger number of hexagonal supercells have been observed. Many of these can only be prepared as thin films and observed by electron microscopy. The expected composition WN_2 has been observed as a brown coating on W filaments. A composition near WN_2 (trigonal unit cell) has been observed by electron microscopy in the thinnest regions of nitrided films, but the derived structure contained three notably short N-N distances of 1.71Å with eight corresponding W-N ones of 2.91-3.03Å. The suggested structure is reminiscent of that of fluorite, but it is not firmly established [9].

5.1.4 Synthesis

Traditionally, Group 6 nitrides are prepared using techniques that employ energised particles i.e. ion implantation, sputtering, ion-beam-assisted deposition, plasma jet spray and plasma enhanced chemical vapour deposition. Alternatively, chemical nitridation of the metal or reduction of molybdenum(V)/tungsten(VI) chloride or fluoride or MoO_3 / WO_3 by ammonia (and sometimes hydrogen), at high temperature are employed [1]. The reduction of the metal

fluorides has thermodynamic and kinetic advantages as compared with chemical vapour deposition using the corresponding chlorides. The reduction temperatures are much lower that those of the chlorides, and the common reduction product is HF which has lower acidity than HCl [10].

5.1.3.1 Molybdenum Nitrides

Maoujoud *et al* [3] have prepared molybdenum nitride thin films on magnesium oxide and silica substrates by d.c. reactive sputtering of a molybdenum target in a nitrogen atmosphere. By controlling the substrate temperature and the deposition rate it was possible to produce three different phases: cubic $Mo_2N_{1\pm x}$, tetragonal β-Mo_2N and hexagonal δ-MoN .

The reaction between MoF_6 and ammonia as studied by Nakajima *et al* [10] yielded only powdery MoF_3 at 450°C and powdery cubic molybdenum nitride with MoF_3 (coated in a molybdenum nitride layer) at 500 and 600°C. Metallic molybdenum was deposited at the higher temperature of 700°C and became dominant in the samples prepared at 800 and 900°C. Hydrogen gas was introduced to the reaction mixture to promote the reduction of MoF_6; this was successful, but the product was still deposited as a powder not a coherent film. Argon gas was then added and this led to the production of smooth MoN films on graphite in the temperature range 500-700°C. Above this temperature a mixture of phases was produced.

A preparation of hexagonal MoN has also been reported based on MoS and BN as starting materials. The two solids were pressed in a pellet in a 1:1 ratio and heated at 950°C for 20 hours. The reaction mixture was then held overnight at 40kbar in a boron nitride crucible at a

temperature of 1000°C. The resulting MoN (15% yield) showed a superconducting transition temperature in the range 14.8-13.0K. The structure deviates very slightly from the hexagonal WC structure, resulting in a superlattice stabilised by the clustering of molybdenum atoms [11].

Fix *et al* [2] have reported the chemical vapour deposition at atmospheric pressure of amorphous molybdenum nitride thin films from the volatile precursor tetrakis(dimethlyamido) molybdenum(IV), $Mo[N(CH_3)_2]_4$ and ammonia (10% ammonia in Helium carrier), at low substrate temperatures (200-400°C). The N:Mo ratios were 1.4-1.5, and these did not vary with deposition temperature. The gold-coloured coatings showed good adhesion to silicon and glass substrates. When the ammonia was omitted from the experiment, no deposition was observed in the above temperature range, demonstrating that the source of nitrogen was not from the precursor, but ammonia. XPS studies revealed that the films contained approximately 1 atomic % carbon and oxygen.

Wang *et al* [4] have prepared Mo_2N and MoN *via* a solvothermal technique using the supercritical nitriding solvents liquid ammonia and hydrazine. This was with the aim of producing high surface area powders resistant to aerial oxidation suitable for catalysis. The appropriate solvent was introduced into the reaction vessel (made from a nickel-based alloy able to withstand 500MPa), containing the $MoCl_5$ precursor and heated to 600-800°C. At low temperatures δ-MoN was formed (up to 600°C in liquid ammonia and up to 700°C in hydrazine). At constant temperature, increasing the pressure favoured the formation of γ-Mo_2N.

5.1.3.2 Tungsten Nitrides

The preparation of tungsten nitride films from WF_6 (b.pt. 17.5°C), has been attempted by Nakajima *et al* [10] (unsuccessfully by reaction with $(CH_3)_3N$ and hydrogen; the reaction products were tungsten carbides), Kim *et al* [12] and Marcus and Foster [13] (by reaction with ammonia). Marcus and Foster prepared films of W_2N on silicon by low pressure chemical vapour deposition using a single-wafer semiconductor processing machine at temperatures between 450-700°C. The fluorine levels in the film varied from a maximum of 0.9 atomic % at the lower temperature to an acceptable 0.1 atomic % at the higher temperature.

Tungsten nitride thin films were grown by Chiu and Chuang [1] from an organoimido complex of tungsten as a single source precursor using the metallo-organic chemical vapour deposition (MOCVD) technique. The $(^tBuN)_2W(NH^tBu)_2$ precursor was vaporised into the reactor at 60-90°C assisted by a flow of argon or hydrogen gas. Deposition on silicon and glass was performed at temperatures between 450-650°C for 3 hours at a pressure of 30Pa. The deposited films were polycrystalline with a cubic structure (a = 4.137-4.175Å, greater than that of β-W_2N), and composition WN_x (x = 0.7-1.8). Trace carbon impurities were detected. Similar experiments with this system were performed by Currie *et al* [14], although a mixture of metallic tungsten and β-W_2N was formed. Interestingly, the $(^tBuN)_2W(NH^tBu)_2$ precursor is soluble in hexane and toluene, so solution-phase routes (such as dip-coating, spot-spraying and aerosol pyrolysis) may also be possible.

The thermal reaction between WS_2 and flowing ammonia (a method originally developed for the production of molybdenum nitrides), has been studied by Tessier *et al* [15, 16].

Ammonolysis of a commercial sample of WS_2 under low flow rates of ammonia produced β-W_2N at approximately 850°C; this was accompanied by increasing amounts of tungsten metal at higher temperature. Sulfur was lost as gaseous hydrogen sulfide. At higher flow rates of ammonia a new nitride phase was produced. This was synthesised in high purity when using a high surface area WS_2 starting material (prepared by reacting WO_3 with molten NaSCN at 550°C). The new phase was found to be of the formula W_5N_6, and decomposed at approximately 900°C to produce $W_{4.6}N_4$ (synthesised previously in thin film form by Khitrova *et al* [17]) and tungsten metal.

5.2 Strategy

The Group 6 nitrides have similar potential applications to titanium nitride, and there is certainly scope for improving the routes used for their synthesis. Current methodologies operate at relatively high temperatures (lowest reported temperature 400°C [2]), close to the point at which silicon and aluminium begin to alloy. Expensive equipment and/or precursors are also required. It would be desirable to access a synthetic method which allowed formation of Group 6 nitrides under moderate conditions.

Preparation of titanium nitride thin films and particles *via* a novel electrochemical route employing liquid ammonia solutions of potassium amide was successful (see *chapters 3* and *4*). It was decided to apply that same method in the attempt to prepare the nitrides of the group 6 metals. Experiments with molybdenum and tungsten are described in this chapter.

5.3 Experimental

Liquid ammonia solutions of potassium amide were prepared as in *section 3.3.1*. The single compartment pressure cell (described in *section 4.2.1.1*) with a three electrode set-up (described in *section 4.2.1*), was used for all experiments, except early experiments on molybdenum when the ambient pressure cell was used (as in *section 3.3.2*). The working electrode was either a molybdenum foil (0.025mm thickness, 99.9+% purity, Aldrich), or a tungsten foil (0.05mm thickness, 99.9+% purity, Aldrich).

5.4 Electrochemistry

5.4.1 Stripping of Oxide Layer

Prior to anodisation of the working electrode, it was cycled for approximately 30 minutes at a sweep rate of 50 mVs^{-1} between 0.00 V and a negative potential limit, always in excess of -1.50 V, such that a large negative current in the order of several mA was observed. The results shown here were obtained in the pressure cell at 25°C.

5.4.1.1 Molybdenum

A typical cyclic voltammogram obtained when using molybdenum foil as the working electrode is shown in *Figure 5.1*. The initial scan (*Figure 5.1a*) shows a large negative current (A) on the reductive sweep. This is most likely to be caused by reduction of the oxide layer and the production of free electrons, which gave rise to a blue colour near the working electrode. During the reverse sweep to 0.00 V, an associated oxidation peak was observed at *ca.* -750 mV (B). On continued cycling, this oxidation peak was observed to diminish as the reduction wave shifted to more negative potentials. The cyclic voltammogram recorded after 20 minutes showed little decrease in the negative sweep and no oxidation peak in the positive sweep at these potentials (*Figure 5.1b*). It seems likely that this reaction is associated with the initial reduction of the thin layer of molybdenum(VI) oxide at negative potentials, followed by re-oxidation on the reverse sweep. On repeated cycling, a fraction of the reduced oxide would be lost to the bulk by diffusion. Thus the cycling eventually results in the production of an oxide-free molybdenum surface.

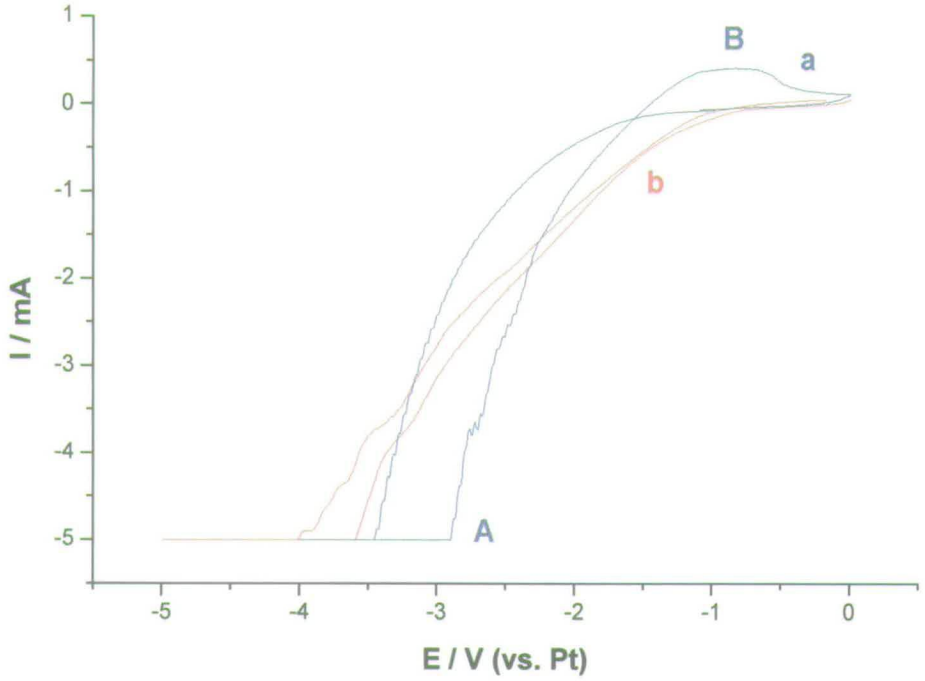

Figure 5 1: Cyclic voltammogram of molybdenum working electrode in liquid ammonia solution of potassium amide (**a**) initial scan, and (**b**) after 20 minutes

5.4.1.2 Tungsten

A typical cyclic voltammogram obtained when using tungsten foil as the working electrode is shown in *Figure 5.2*. Blue ammonia-solvated electrons were observed at the working electrode on the sweep to negative potentials. There is a marked difference between the two CVs recorded indicating a change in the nature of the electrode surface. Unlike with the stripping of oxide from molybdenum and titanium, the gradient of the final CV on tungsten is of a significantly shallower gradient than the initial CV. This indicates that the electrode has become more resistive over the course of the experiment, an unexpected consequence of oxide removal. The potential window accessible by the working electrode is relatively unaltered by

the cycling. It is unclear exactly what is happening during this electrochemical treatment of tungsten, and whether the oxide layer has successfully been removed.

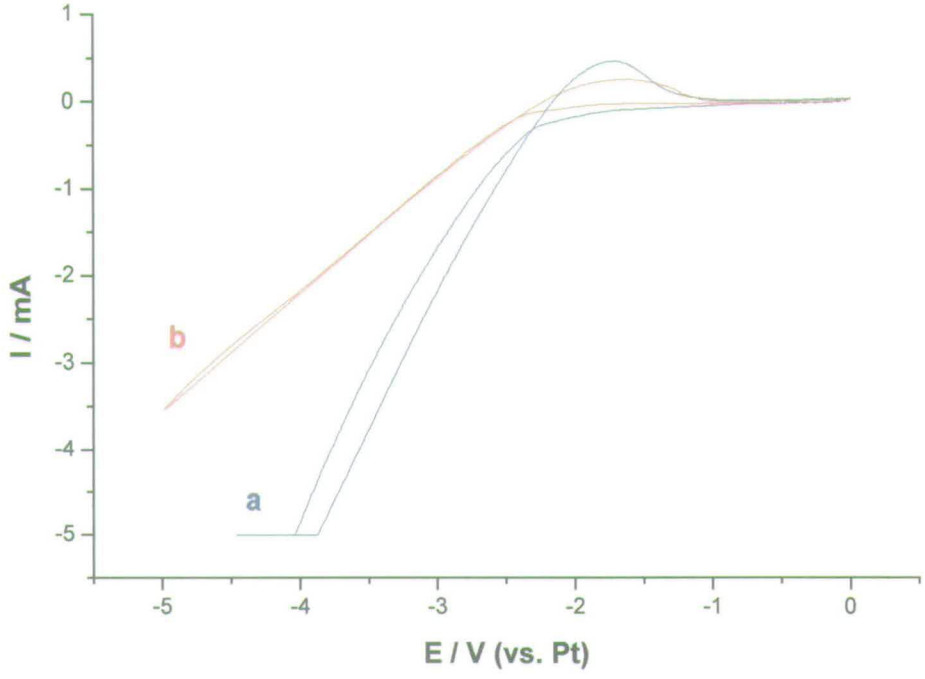

Figure 5 2: Cyclic voltammogram of tungsten working electrode in liquid ammonia solution of potassium amide (**a**) initial scan, and (**b**) after 20 minutes

5.4.2 Nitride Synthesis

Electrochemical modification took place between 0.00 and +5.00 V using a 1kΩ measuring resistor. The first experiment was performed at -78°C in order to study the mechanism of film formation. In the remaining experiments, the cell was allowed to warm up to 25°C and pressurised to 10 atms before nitridation was initiated.

5.4.2.1 Molybdenum

5.4.2.1.a Experiment 1

This experiment was performed at -78°C in the ambient pressure cell. The molybdenum working electrode was first stripped of its native oxide layer and then the potential was increased to +5.00 V. The steady current was approximately 20μA after the initial maximum had decayed, although this did continue to drop slowly over the course of the experiment. After 100mC of charge had been passed, a gold-coloured coating was observed on the working electrode. A total of 1C of charge was passed, by which time a red colour was observed on the molybdenum. This disappeared on contact with air when the electrode was removed from the cell.

Figure 5.3 shows the Cottrell plot of charge against the square root of time for data recorded during the initial stages of the experiment. These data follow a linear trend. As explained in *section 3.4.3* the gradient of this plot can be used to calculate a diffusion coefficient for the process occurring [18]. A linear fit of the data plotted in *Figure 5.3* gave a value for the gradient of $1.16(4)\times10^{-3}$ $Cs^{-1/2}$. This allows the calculation of a diffusion coefficient of 1.14×10^{-12} cm^2s^{-1} for the process assuming that the overall reaction occurring is as given in *Equation 5.1*.

$$2\,Mo + 3\,NH_2^- \rightarrow Mo_2N + 3\,e^- + 2\,NH_3 \qquad \textbf{(5.1)}$$

This value is seven orders of magnitude smaller than the value of the diffusion constant calculated for the amide ion in liquid ammonia solution, and approximately 20 times smaller than the diffusion coefficient calculated by the same method in the titanium experiment.

Again, interpretation is complicated by the fact that the values of the concentration and conductivity of amide were taken at different temperatures. Even so, the diffusion coefficient calculated above is probably too small to be attributed to the diffusion of amide in liquid ammonia, and is more likely to be a measure of the slow diffusion of 'N' atoms in molybdenum metal. It is interesting to note that this is significantly slower in molybdenum than in titanium.

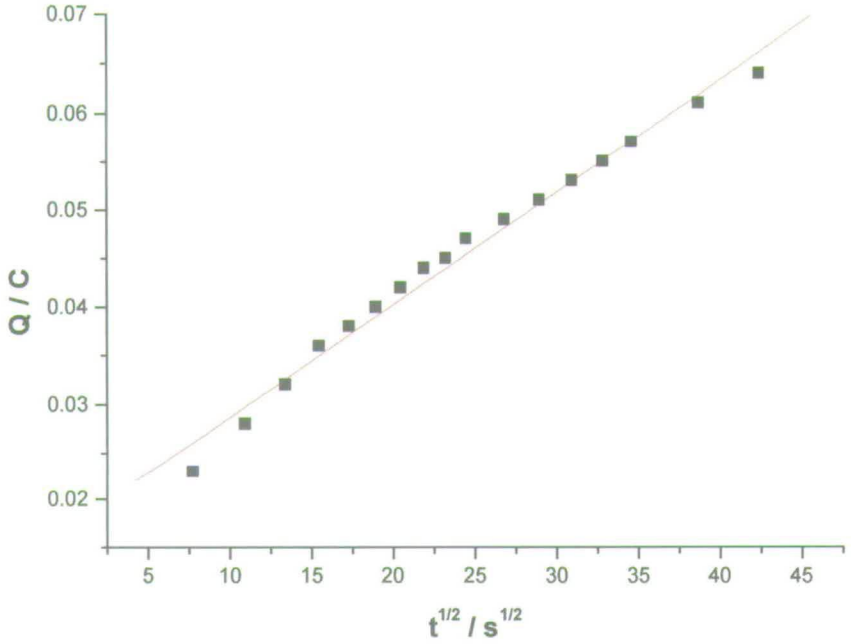

Figure 5.3: Cottrell plot of Q against $t^{1/2}$ for the electrochemical modification of molybdenum in experiment 1 at -78°C

5.4.2.1.b Experiment 2

Electrochemical modification was performed by increasing the potential from 0.00 V in 0.50 or 1.00 V intervals to +5.00 V. *Figure 5.4* shows the current-time transient from +2.00 V during these potential increases. A golden colour was observed on the molybdenum electrode after 500mC of charge had been passed. A total of 171C of charge was passed, by which

time a red-brown gelatinous solid had formed on the working electrode. This was washed thoroughly with dry liquid ammonia and dried under vacuum to form a brown powder.

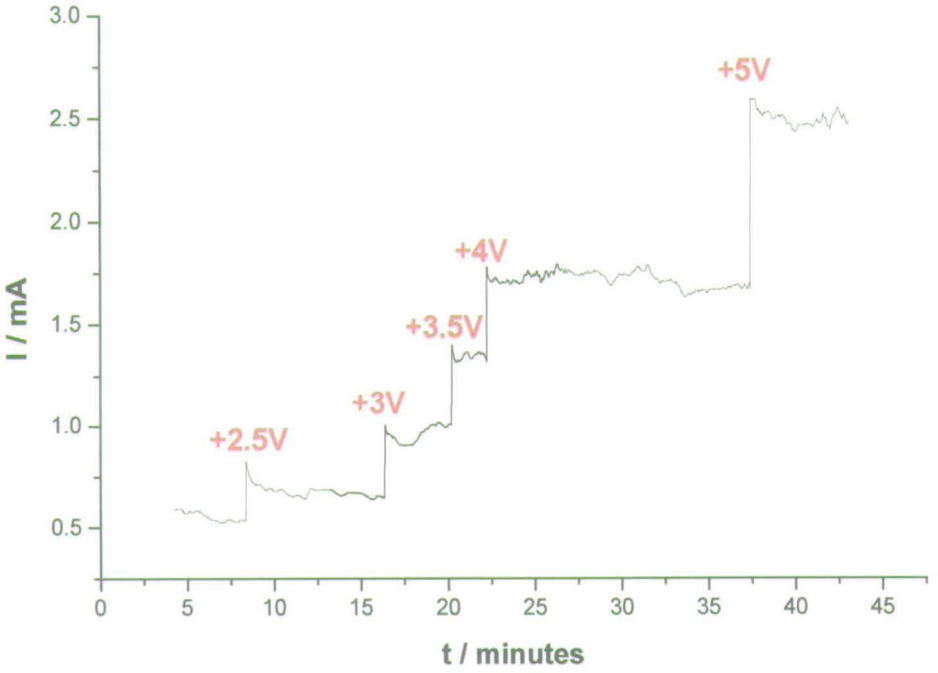

Figure 5.4: Current-time transient for the electrochemical modification of molybdenum carried out in experiment 2

5.4.2.1.c Experiment 3

The potential of the working electrode was increased to +2.00 V in 0.50 or 1.00 V intervals, always allowing the current to decay at each potential. *Figure 5.5* shows the current-time transient during this process. The steady current at +2.00 V was 1.3mA. A total of 6C of charge was passed, and a gold-coloured film was observed on the molybdenum electrode. This was washed with distilled water and acetone after removal from the cell.

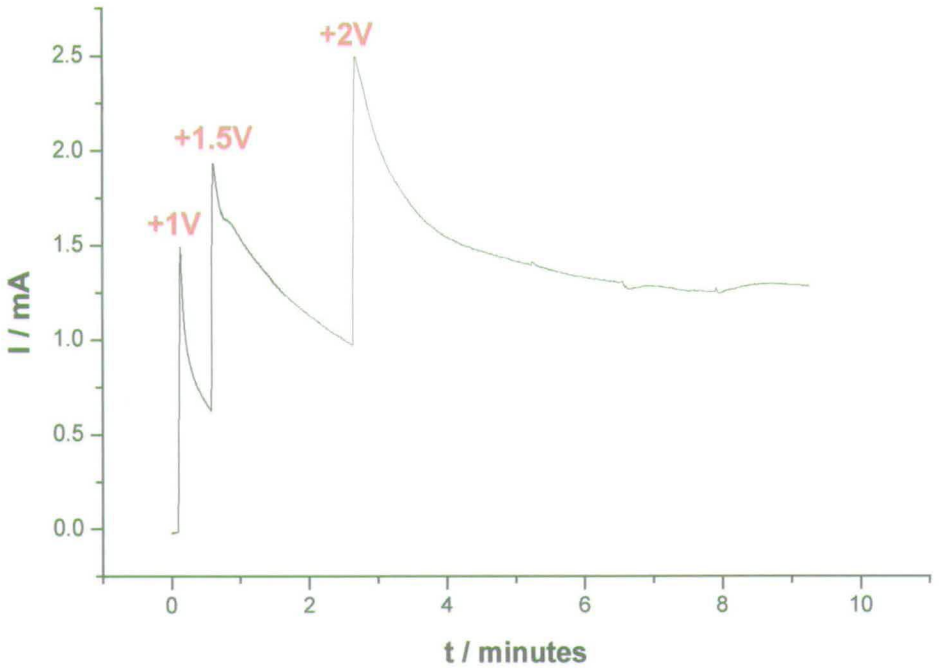

Figure 5.5: Current-time transient for the electrochemical modification of molybdenum carried out in experiment 3

5.4.2.2 Tungsten

5.4.2.2.a Experiment 1

In this experiment the potential of the tungsten working electrode was increased in 1.00 V intervals to +5.00 V. *Figure 5.6* shows the effect of this potential step-up on the current over time. A total of 100C of charge was passed, and this produced a golden and 'rainbow'-like film on the tungsten metal. The electrode was washed with dry liquid ammonia (to remove any precipitated electrolyte), and dried in a stream of dry nitrogen after removal from the cell.

5.4.2.2.b Experiment 2

Experiment 2 followed the same regime of potential increase as experiment 1. The current decayed after the increase to +1.00 V and +2.00 V, but remained steady at approximately 2mA on the increase to +3.00 V. When the potential was increased to +4.00 V the current began to climb, with no further increase after +5.00 V. The current was to be 7.8mA at this time. After 1C of charge had been passed, a gold-coloured film was observed on the tungsten working electrode. Shortly after this, a red-brown solid began to form. A total of 343C was passed, by which time a large amount of the red-brown solid had collected in the bottom of the cell. This was washed with dry liquid ammonia and dried *in vacuo* to leave a brown powder; the electrode was washed with dry liquid ammonia and dried in a stream of dry nitrogen.

5.4.2.2.c Experiment 3

The potential of the electrode in this experiment was also increased in 1.00 V intervals to +5.00 V. *Figure 5.7* shows the current-time transient for this process. A total of 214C of charge was passed. Initially a white-grey solid was produced on the tungsten electrode, and during the later stages of the experiment a brown solid was formed. The electrode was washed with dry liquid ammonia and dried in a stream of dry nitrogen after modification.

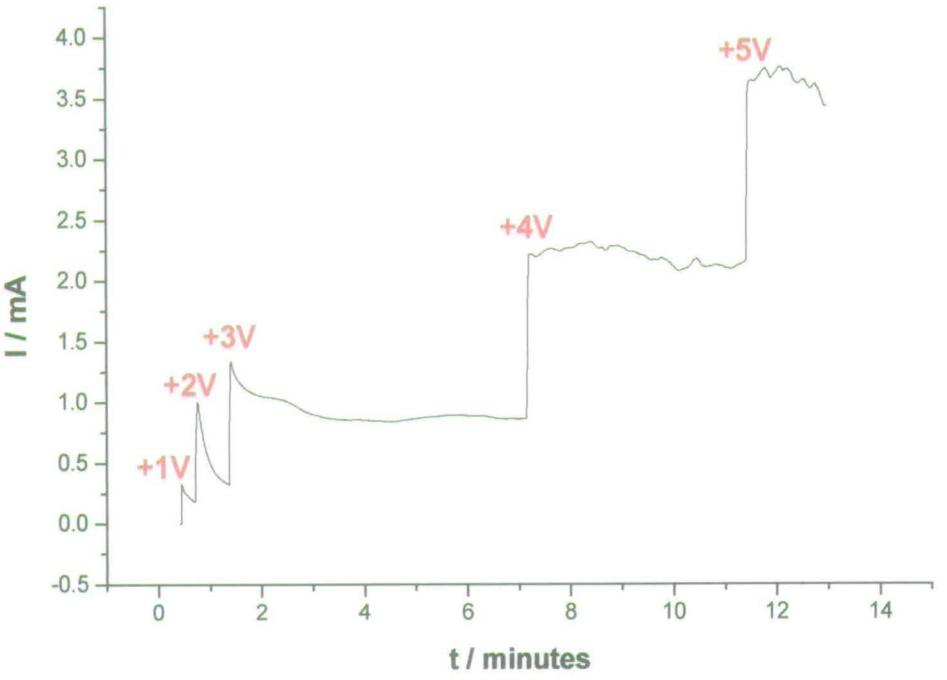

Figure 5.6: Current-time transient for the electrochemical modification of tungsten carried out in experiment 1

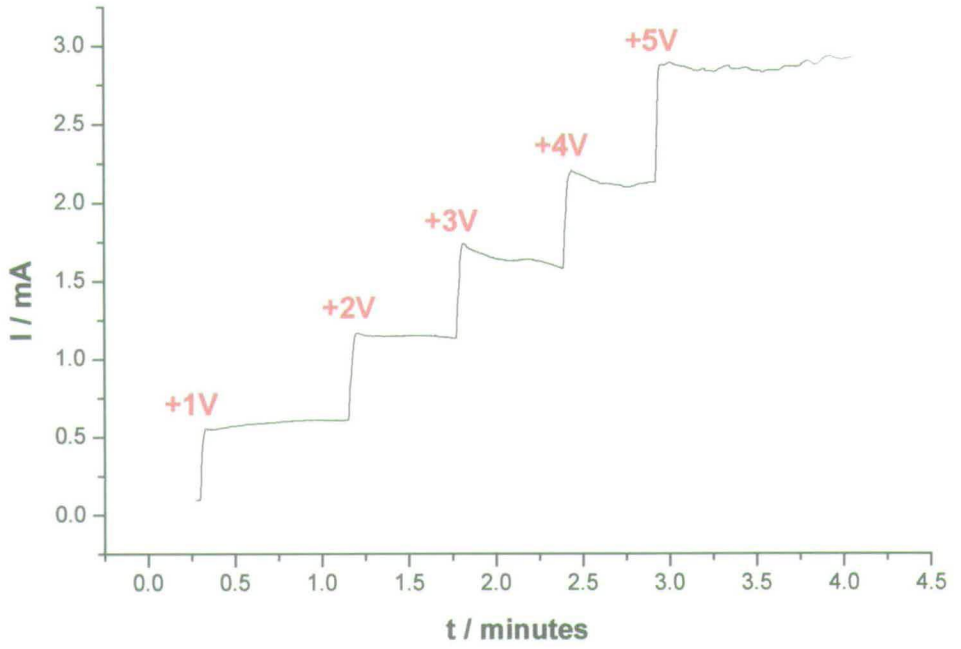

Figure 5.7: Current-time transient for the electrochemical modification of tungsten carried out in experiment 3

5.4.2.2.d Experiment 4

This experiment was performed at the lower potential of +2.00 V in an attempt to avoid the production of the gelatinous solids observed previously, with the expectation of producing an even film. A very uniform, orange-coloured film was observed on the tungsten electrode. After 3C of charge had been passed, the electrode was removed from the cell and washed with distilled water. Unfortunately the orange-coloured film completely disappeared on contact with water. This experiment demonstrated the necessity of treating the products of these electrochemical modifications as air- and moisture-sensitive, and the need for careful washing with dry liquid ammonia and storage under dry nitrogen.

5.4.2.2.e Experiment 5

The electrode was not stripped of its oxide layer prior to modification with the hope of increasing the binding of any film produced with the substrate. The potential was immediately increased to +3.00 V, and a total of 6C of charge was passed. The electrode was washed with distilled water and acetone and a faint gold-coloured film was visible.

Experiment	E / V	Charge Passed / C	Appearance of Product	Characterisation
1 (-78°C)	5.00	1	Gold-coloured film red product	Cottrell analysis
2 (25°C)	5.00	171	Gold-coloured film red-brown powder	Raman TEM-ED
3 (25°C)	2.00	6	Gold-coloured film	XPS

Table 5.1: Summary of the electrochemical modification experiments performed with a molybdenum working electrode, and the methods used to characterise the resulting films

Experiment	E / V	Charge Passed / C	Appearance of Product	Characterisation
1	5.00	100	Gold- and 'rainbow'-coloured film	Raman
2	5.00	343	Gold-coloured film Red-brown powder	Raman
3	5.00	214	White-grey then brown solid	TEM-ED
4	2.00	3	Orange film, moisture-sensitive	-
5	3.00	6	Gold-coloured film	XPS

Table 5.2: Summary of the electrochemical modification experiments performed with a tungsten working electrode, and the methods used to characterise the resulting films

5.5 Characterisation of Molybdenum Nitride

5.5.1 X-Ray Photoelectron Spectroscopy (XPS)

5.5.1.1 Surface Measurements

Figures 5.8 and *5.9* show the wide scan spectra for the electrochemically produced film and molybdenum metal, respectively. The first feature to note is that the background generally increases to the high photon (or binding) energy end of the spectrum, with step-like increases on the right hand side of each peak. This effect is due to secondary electrons created by inelastic photo-emission (energy loss within the solid). There is also a broad background due to photoemission by Bremsstrahlung, or background, radiation which is caused by the non-monochromatic x-ray source. This effect dominates in the low binding energy region of the spectrum [19].

The sharp peaks superimposed on the background are due to photoemission from core levels. In both spectra, singlets due to oxygen and carbon 1s peaks are visible at 531eV and 285eV respectively. The carbon is a consequence of hydrocarbon vapour deposited on the sample from the high vacuum pump equipment, and the oxygen peak arises because of adsorbed moisture or oxygen or aerial oxidation of the surface after preparation. In both spectra, the Mo 3d doublet is visible at 227 and 238eV, and the 3p doublet at 396 and 410eV. The Mo $3p_{3/2}$ line at 393eV is very close to expected N 1s line position at 396eV. However it is difficult to discern nitrogen on this scale. In addition the Mo LMM Auger line is clearly observed at 740eV.

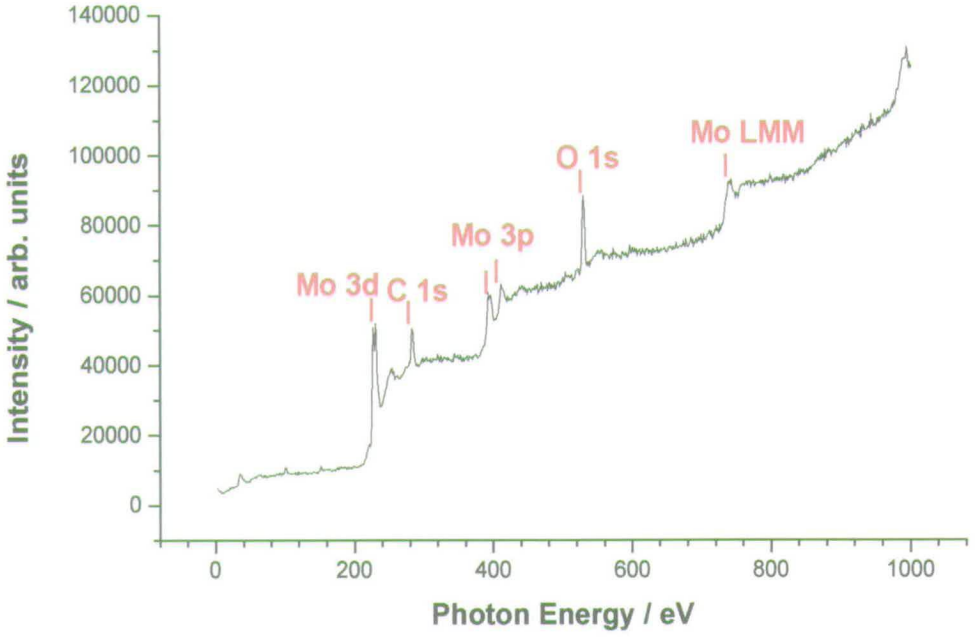

Figure 5.8: Wide scan XPS spectrum of the electrochemically produced film

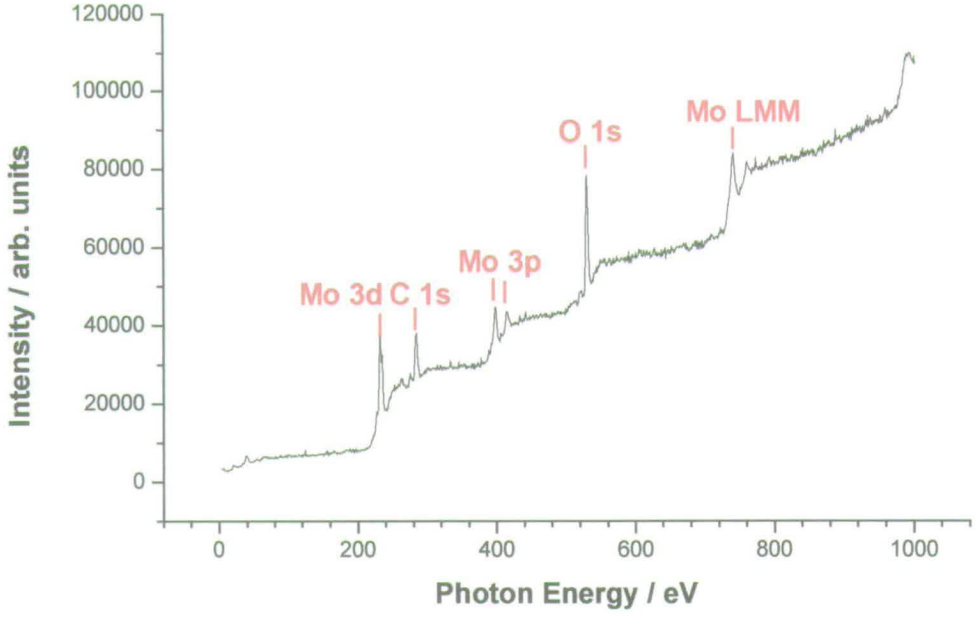

Figure 5.9: Wide scan XPS spectrum of molybdenum metal

Figures 5.10-5.12 show the molybdenum, oxygen and nitrogen narrow scan spectra respectively for the electrochemically produced film and molybdenum metal.

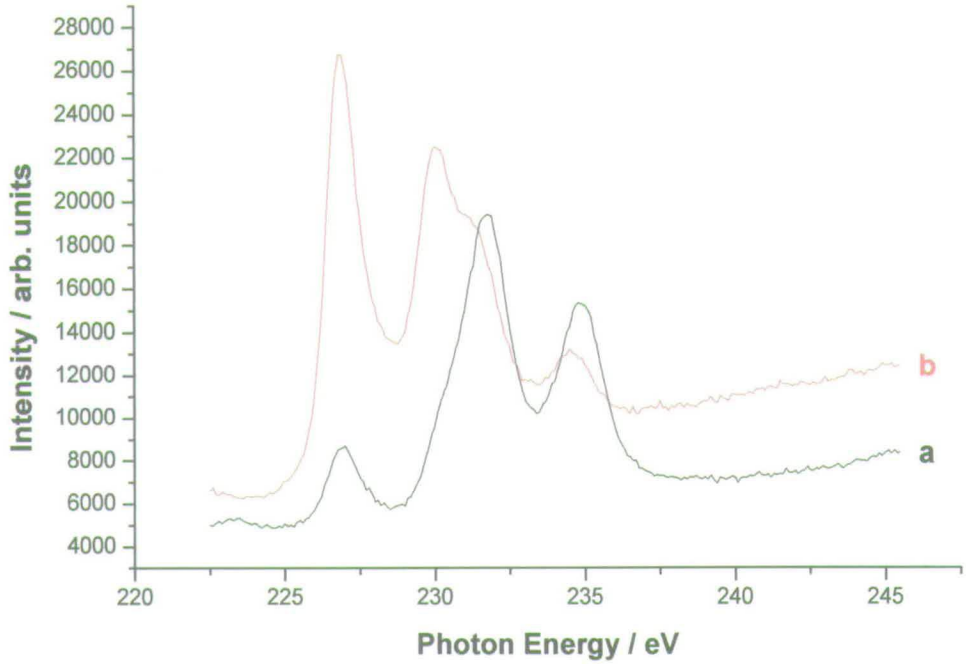

Figure 5.10: Molybdenum 3d XPS spectra for (**a**) molybdenum metal, and (**b**) the electrochemically produced film

The molybdenum 3d spectra are split into two overlapping doublets for both the electrochemically produced film and the molybdenum metal. This indicates that the molybdenum is present in two different chemical oxidation states. The two most intense peaks in the spectrum of the molybdenum metal ($3d_{5/2}$ at 231.8eV and $3d_{3/2}$ at 234.8eV in the expected area ratio of 3:2) are due to Mo in the +6 oxidation state present as MoO_3. The two weaker peaks ($3d_{5/2}$ at 227.0eV and $3d_{3/2}$ present as a shoulder at 230.5eV) are due to underlying metallic molybdenum. The $3d_{5/2}$ peak shift of +4.8eV from metal to metal oxide is in agreement with reported data [19]. The same pattern is observed for the electrochemically produced film, except that the metallic peaks are of stronger intensity than the oxidised peaks.

This indicates that the surface oxide layer is thinner on this sample, probably as a result of the electrochemical modification.

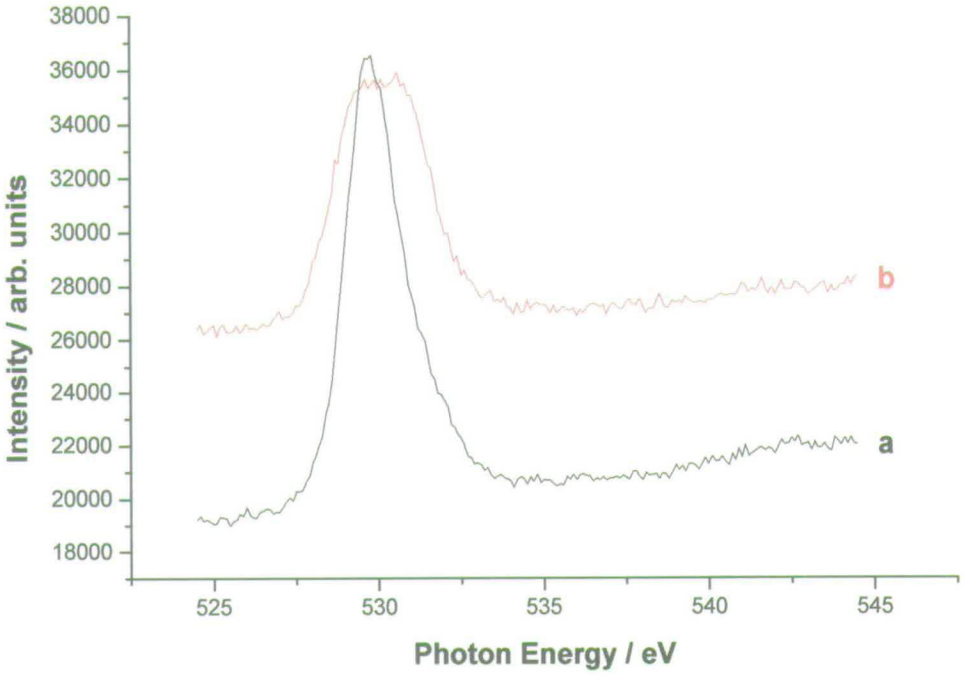

Figure 5.11: Oxygen 1s XPS spectra for (**a**) molybdenum metal, and (**b**) the electrochemically produced film

The oxygen 1s spectrum obtained from the molybdenum metal is a singlet (at 529.8eV) attributable to oxygen present as oxide. The peak in the spectrum of the electrochemically produced film (at approximately 530eV) is broader and less intense than that of the metal. This suggests that as well as the existence of oxide at the surface, there may also be hydroxide present, perhaps due to reaction with atmospheric moisture. Differences between hydroxide (OH^-) and oxide (O^{2-}) are usually recognised by an O 1s shift of 1 to 1.5eV [19].

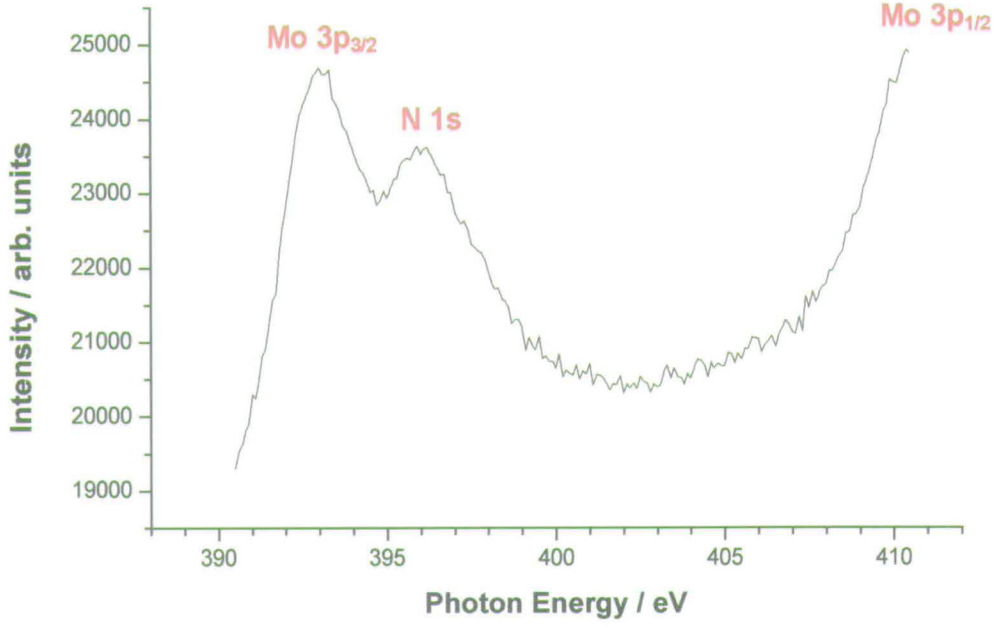

Figure 5.12: Nitrogen 1s XPS spectrum for the electrochemically produced film

The N 1s peak can be observed at 395.9eV, confirming the presence of nitrogen in the film and the successful production of a nitride layer. This is in agreement with data previously reported by Fix *et al* [2] (397.3eV) and Fujimoto *et al* [20] (398eV for a film with N:Mo ratio of 1.3). The spectrum is complicated by the overlap of the molybdenum 3p doublet; the Mo $3p_{3/2}$ peak is observed at 393.0eV. Unfortunately, quantification of nitrogen is not possible for this sample due to such peak overlap.

5.5.1.2 Sputtering Experiments

As both the electrochemically produced film and the molybdenum metal were found to be coated in a surface oxide layer, sputtering experiments were performed in order to investigate the composition of the samples with depth. An accelerating voltage of 500V was used for the

argon ion beam. *Figures 5.13-5.15* show the narrow scan stack plots in the molybdenum, oxygen and nitrogen regions respectively obtained for the electrochemically synthesised film through sputtering.

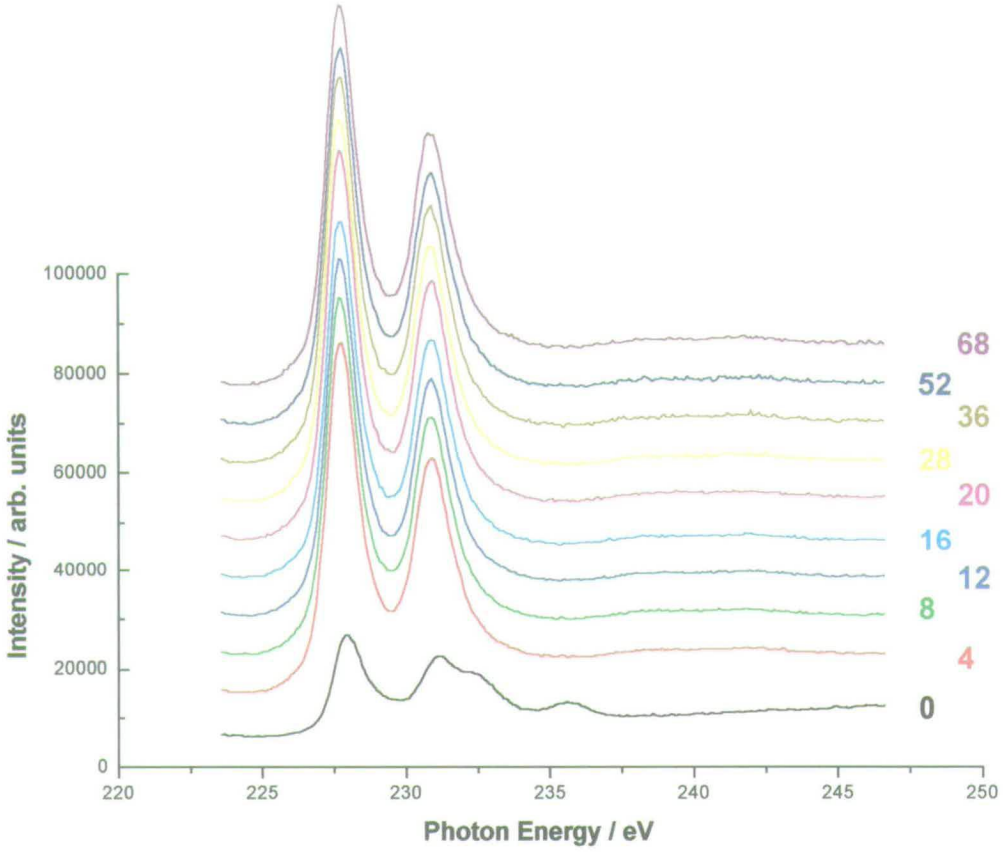

Figure 5.13: Molybdenum 3d XPS spectra obtained through sputtering. Sputtering time (in minutes), is given at the right hand side of each trace

After just four minutes sputtering the lower intensity 3d doublet observed in the surface scan spectrum disappeared leaving only the stronger 3d doublet at 227.7 and 230.8eV. This indicates a removal of molybdenum in the +6 oxidation state, i.e. exfoliation of the oxide layer to reveal metallic molybdenum. If nitride was present the position of the Mo 3d doublet would

be expected to be intermediate between that of the oxide and the metal. Unfortunately there is no intermediate Mo 3d peak observed, so it is likely that the nitride had been sputtered away in the first 4 minutes. This is perhaps not surprising as such a high accelerating voltage (500V) would rapidly exfoliate the surface. It would have been desirable to have collected a spectrum after, say, 2 minutes sputtering as this could be the depth where most of the surface oxide has been removed revealing the nitride layer. As sputtering continues, the intensity of the metallic molybdenum doublet further increases, as bulk metal is analysed.

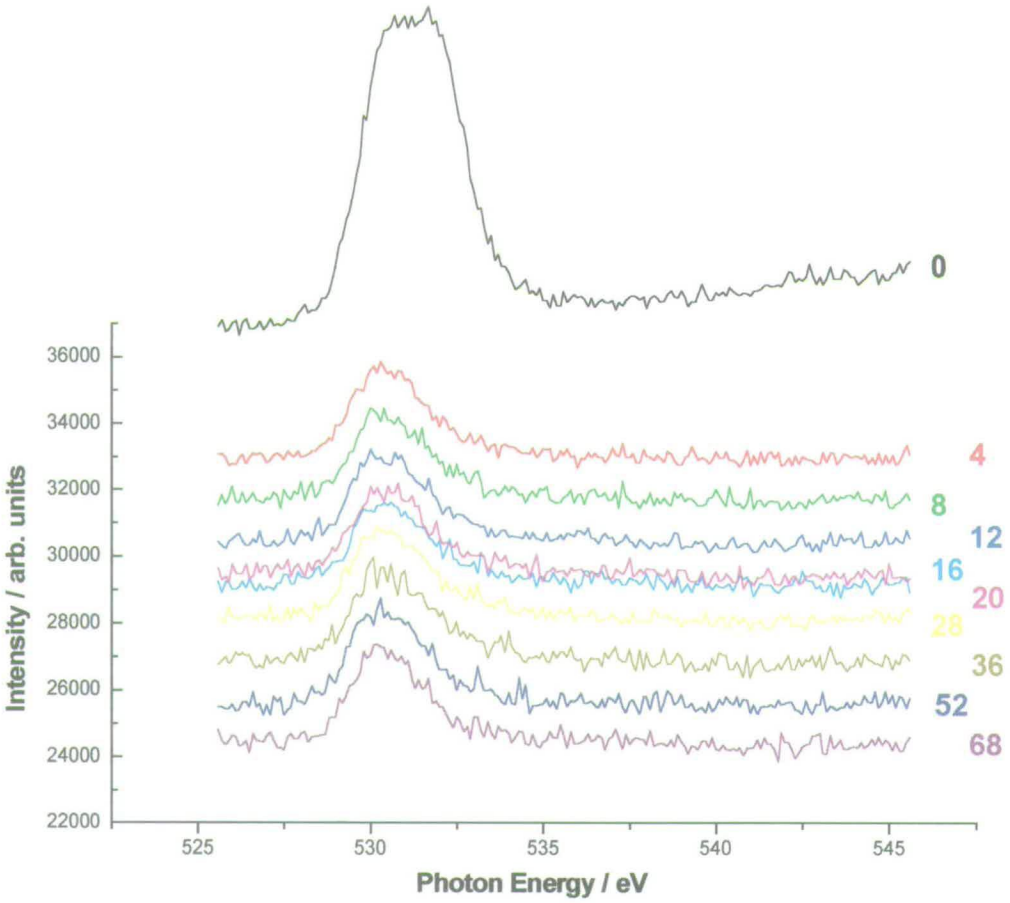

Figure 5.14: Oxygen XPS spectra obtained through sputtering. Sputtering time (in minutes), is given at the right hand side of each trace

The effect of sputtering on the O 1s peak is to reduce its intensity dramatically. This decrease is especially marked after 4 minutes of sputtering, when the peak shape also becomes sharper. The immediate sharpening of the O 1s peak indicates removal of surface hydroxide, and the decrease in intensity indicates that oxide is also progressively eroded by the sputtering process.

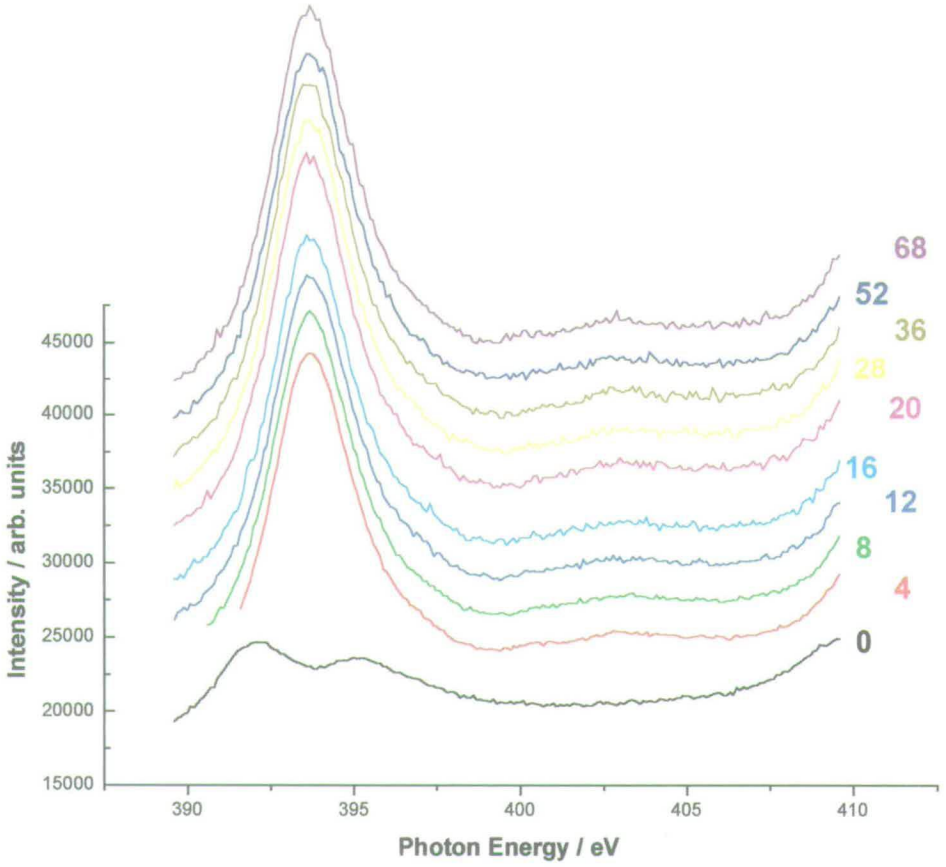

Figure 5.15: Nitrogen XPS spectra obtained through sputtering. Sputtering time (in minutes), is given at the right hand side of each trace

The N 1s spectrum shows a dramatic change after only four minutes sputtering. The two low intensity peaks observed in the surface scan (due to Mo $3p_{3/2}$ and N 1s) are replaced by one

intense peak at 393.7eV in the ensuing spectra, although a shoulder on its right hand side is certainly still present as sputtering progresses. This result demonstrates the effect of removing surface oxide, and possibly also most of the nitride layer. Again, a spectrum should have been collected after 2 minutes sputtering to reveal the peak positions in the region of greatest change i.e. between 0 and 4 minutes. The peak at 393.7eV can be attributed to Mo $3p_{3/2}$ in metallic molybdenum, and dominates the spectrum, making it very difficult to gauge the depth to which nitrogen persists. This is an unfortunate coincidence for the analysis of the film.

Figures 5.16-5.18 show the 'depth profile' plots for the molybdenum, oxygen and nitrogen spectral regions respectively in the electrochemically produced film. These plots were obtained by integrating peaks (between 226.5 and 229.5eV for molybdenum, 528.6 and 535.6eV for oxygen, and 391 and 397eV for nitrogen), in the spectra obtained through sputtering and plotting the values obtained against a depth based on sputtering times for silicon at 500V as no nitride standards were available (see *section 2.9.3*). The error in the peak area (plotted as error bars on the graphs) was approximately 5%.

The integration range of 226.5-229.5eV was chosen to capture the most intense Mo $3d_{5/2}$ peak (in the surface scan) i.e molybdenum present as the metal or as a nitride, but not as oxide. *Figure 5.16* indicates the prevalence of this peak with depth. The plot shows that the proportion of molybdenum increases dramatically in the first 100nm of the film, and then remains steady as bulk metal is reached. This suggests that the oxide layer is relatively thin and well defined.

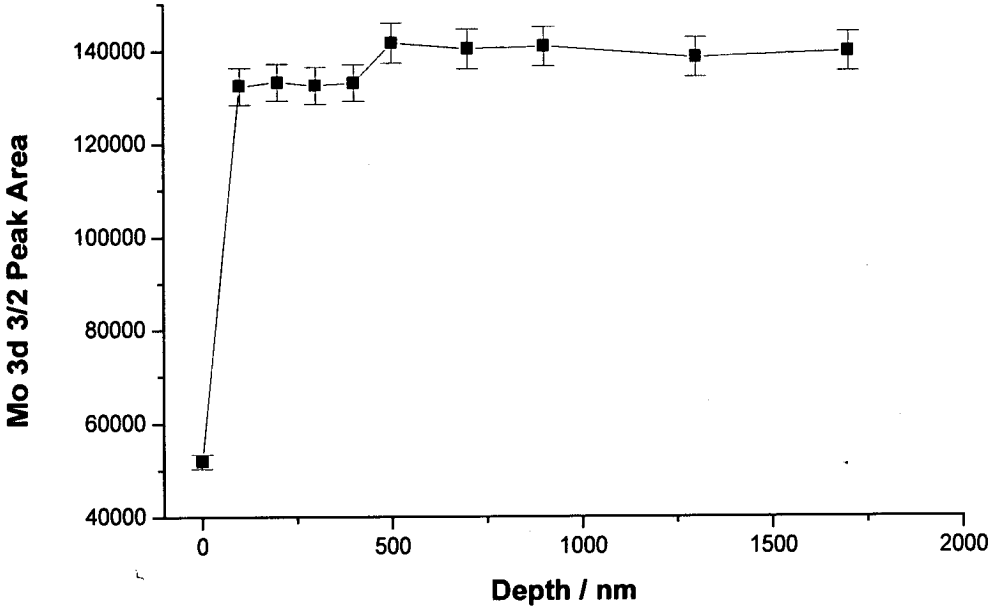

Figure 5.16: Depth profile plot of non-oxidised molybdenum in the electrochemically produced film

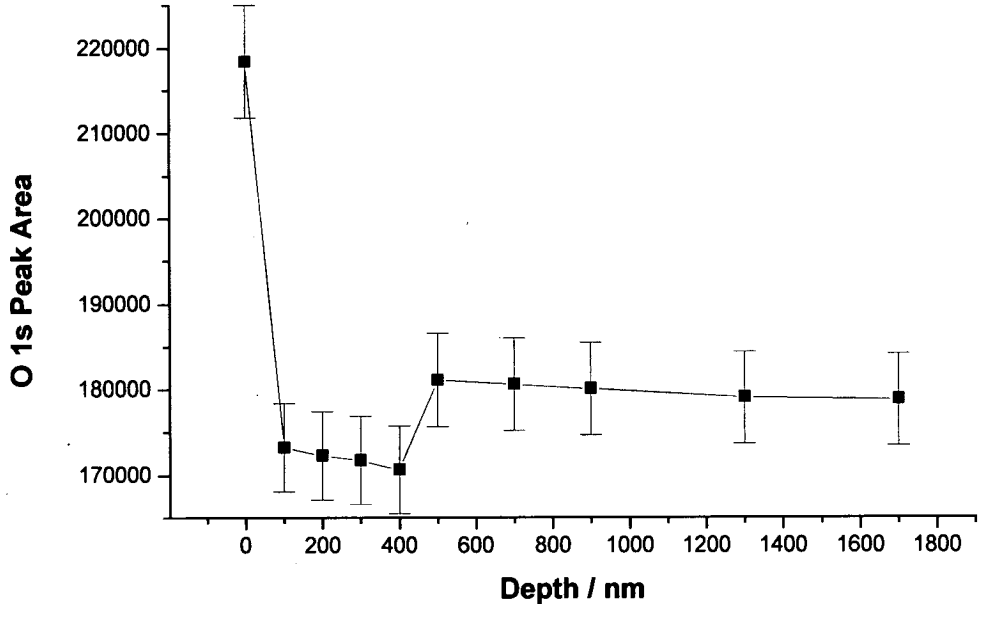

Figure 5.17: Depth profile plot of oxygen in the electrochemically produced film

The observations made from the molybdenum depth profile are reinforced by the oxygen gradient, shown in *Figure 5.17*. The chosen integration range (529-533eV), encompasses the O 1s peak. There is a dramatic decrease in the amount of oxygen present in the first 100nm of sputtering. After a further decrease and a small rise the oxygen levels remain steady. This residual amount of oxygen is likely to be due to re-oxidation of the cleanly sputtered metal surface by adventitious oxygen in the vacuum chamber, and is not necessarily an inherent part of the sample.

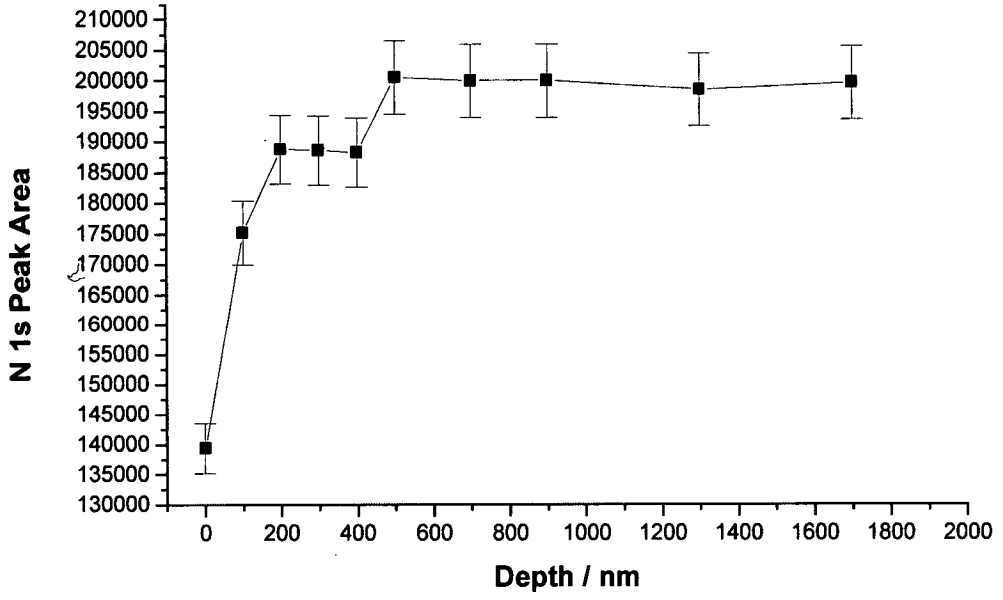

Figure 5.18: Depth profile plot obtained from the nitrogen region in the electrochemically produced film

Due to the overlap of the N 1s line with the Mo $3p_{3/2}$ line, *Figure 5.18* cannot be used to gauge simply the concentration of nitrogen with depth. The chosen integration range (391-397eV), includes both the N 1s and Mo $3p_{3/2}$ lines. The plot therefore shows the variation of molybdenum and nitrogen with depth, although the plot is likely to be dominated by the behaviour of the molybdenum line. The general trend is that of an initial increase followed by

a levelling off. The initial increase is due to the removal of surface oxide; the step in this increase could be due to the conflicting factors of a decrease in the amount of nitrogen and oxygen and an increase in the amount of molybdenum. The steady end value is likely to indicate that bulk metal has been reached.

5.5.2 Transmission Electron Microscopy (TEM) - Electron Diffraction

As with the titanium nitride, location of an area of the sample which was thinned to the optimum thickness so as to be transparent to electrons was not trivial. Molybdenum nitride is a difficult material to thin by ion bombardment as it is very resistant to erosion. The epoxy thinned at a much greater rate, sometimes leading to some of the powder becoming loose and falling out of the resin. However, *Figure 5.19* shows the TEM images obtained from a suitable area of the thin section sample of the brown powder produced in experiment 1 mounted in epoxy resin. The light areas indicate epoxy, and the dark areas indicate bulk powder. The powder can be seen, especially well in *Figure 5.19b*, to be composed of very small (5-10nm) spherical particles. The observed morphology is similar to that of the titanium nitride powder (see *section 4.4.3.3*).

Figure 5.20 shows the electron diffraction pattern obtained from the a thin section of the brown powder mounted in epoxy resin. Electron diffraction of the particles produced distinct rings with the occasional appearance of spots, indicating the presence of nano-crystallites. The separation of the rings corresponds to d-spacings as shown in *Table 5.3*. The three rings at d-spacings of 2.97 Å , 2.47 Å and 1.50 Å are more diffuse and may correspond to a different phase. The d-spacings are compared with the nearest d-spacings from some known molybdenum nitrides and oxides. These values were generated by the DRAGON program

[21] between 0 and 80° 2θ by entering the appropriate unit cell parameters (*Table 5.4*) [4, 8, 22-29]. The program lists all the reflections that would be observed by X-ray powder diffraction, removing those which are extinct due to general space group symmetry (see *section 2.6*).

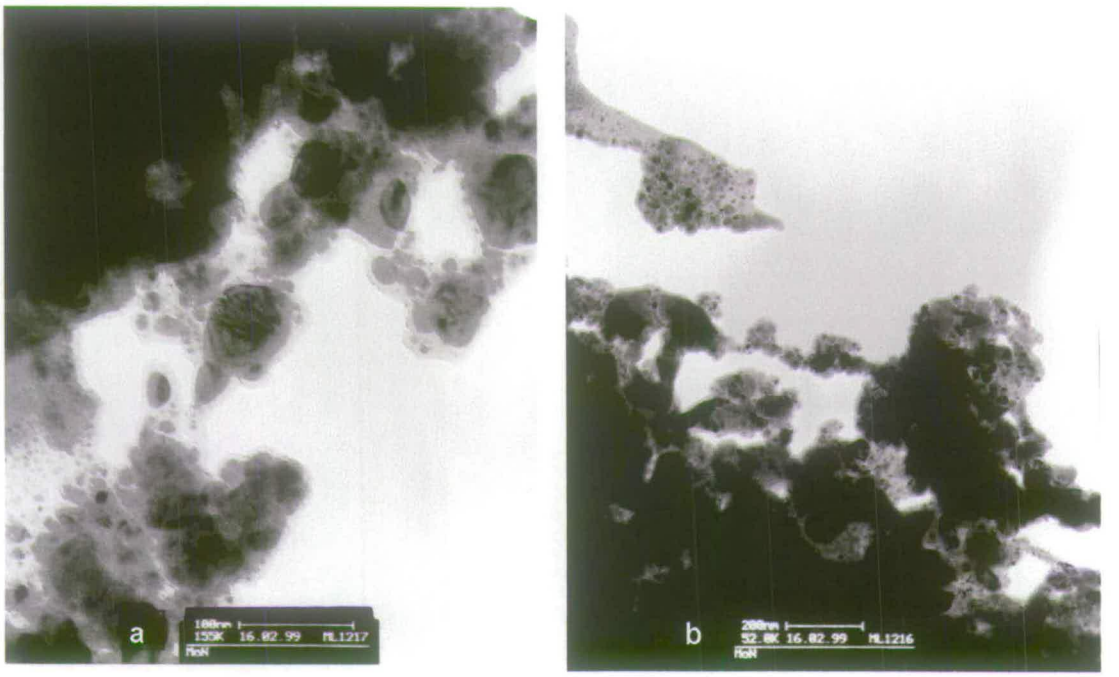

Figure 5.19: TEM images of a thin section of the material produced at a molybdenum electrode mounted in epoxy resin

It can be seen that the various nitride and oxide phases share many similar d-spacings, and are not clearly distinguishable. There are several close matches between the electron diffraction data and the known phase results. However, hexagonal Mo_2N appears to be the most likely candidate, although the material could also be hexagonal MoO_3 indicating a degree of aerial oxidation. The identity of the material cannot be confidently ascertained with this method.

Figure 5.20: Electron diffraction pattern of a sample of the material produced at a molybdenum electrode

5.5.3 Raman Spectroscopy

The molybdenum electrode modified in experiment 1, and the resulting brown powder were both analysed by Raman spectroscopy. *Figure 5.21* shows the Raman spectrum of the gold-coloured film on the electrode. This is a poorly resolved spectrum as the film was highly reflective. However, a pattern of broad peaks in the low energy region of the spectrum due to lattice phonons can be observed, and this is similar in character to the spectrum obtained from the thin film of titanium nitride (see *section 3.5.4*). The brown powder showed no Raman scattering. Only one published Raman spectrum of molybdenum nitride was found [30]. This was for the fcc γ- Mo_2N phase and displayed two broad peaks at approximately 600 and

ED	Tetragonal β- Mo_2N		fcc γ- Mo_2N		Hexagonal δ- Mo_2N		Cubic MoN		Tetragonal MoO_2		MoO_2 tugarinovite		Hexagonal MoO_3		Orthorhom. MoO_3		β'- MoO_3	
2.97	2.98	110	2.94	110	2.86	110	2.98	110	2.79	001	-	-	2.88	204	3.01	130	3.05	211
2.47	2.39	112	2.40	111	2.48	200	2.43	111	2.43	200	2.44	-202	2.53	310	2.53	041	2.47	300
1.92	1.88	210	1.86	210	1.87	210	1.88	210	-	-	-	-	1.95	404	1.96	061	1.92	004
1.81	1.82	104	-	-	1.78	211	-	-	1.83	201	1.81	201	1.82	500	1.82	230	1.81	140
1.50	1.51	105	1.47	220	1.49	203	1.49	220	1.54	310	1.52	310	1.50	430	1.50	260	-	-
1.29	-	-	1.26	311	1.27	222	1.27	311	1.29	112	1.29	-411	1.30	700	-	-	1.29 1.29 1.29 1.29 1.29	053 343 135 433 315
1.09	-	-	-	-	1.09	105	-	-	-	-	-	-	1.12	720	-	-	-	-
1.05	-	-	-	-	1.06	411	-	-	-	-	-	-	1.05	2213	-	-	-	-
0.83	-	-	-	-	-	-	-	-	-	-	-	-	0.84	6114	-	-	-	-
0.81	-	-	-	-	-	-	-	-	-	-	-	-	0.81	9011	-	-	-	-

Table 5.3: Experimental d-spacings (± 0.02 Å) from electron diffraction compared with the closest d-spacings (in Å) and hkl values from some known molybdenum nitrides and oxides. The figures in red have a good match with the experimental result.

Material	a	b	c	Reference
Tetragonal β- Mo_2N	4.210	= a	8.060	[4], [22]
fcc γ- Mo_2N	4.163	= a	= a	[4]
Hexagonal δ- Mo_2N	5.725	= a	5.608	[8]
Cubic MoN	4.212	= a	= a	[23], [24]
Tetragonal MoO_2	4.86	= a	2.79	[25]
MoO_2 (tugarinovite)	5.6096	4.8570	5.6259	[26]
Hexagonal MoO_3	10.531	= a	14.876	[27]
Orthorhombic MoO_3 (molybdite)	3.962	13.858	3.697	[28]
β'- MoO_3	7.4245	7.4780	7.6898	[29]

Table 5.4: Lattice parameters (in Å) of some known molybdenum nitrides and oxides

1100cm^{-1}. This is not similar to the spectrum of the sample produced here, although electron diffraction suggested production of the hexagonal δ- Mo_2N phase which might be expected to show a different Raman spectrum.

Figure 5.22 show the Raman spectrum obtained from a commercial sample of molybdenum oxide (MoO_3) powder. This compares well with a spectrum obtained by Gardiner *et al* [31] and is quite different from the spectrum of the electrochemically produced film indicating that careful post-synthesis handling had prevented aerial oxidation of the sample. Commercial MoO_2 powder produced no Raman scattering; difficulties were also experienced by Gardiner *et al*, although a spectrum was obtained by a spinning pressed disc method. The resulting spectrum showed strong bands at 502, 595 and 750cm^{-1} [31]

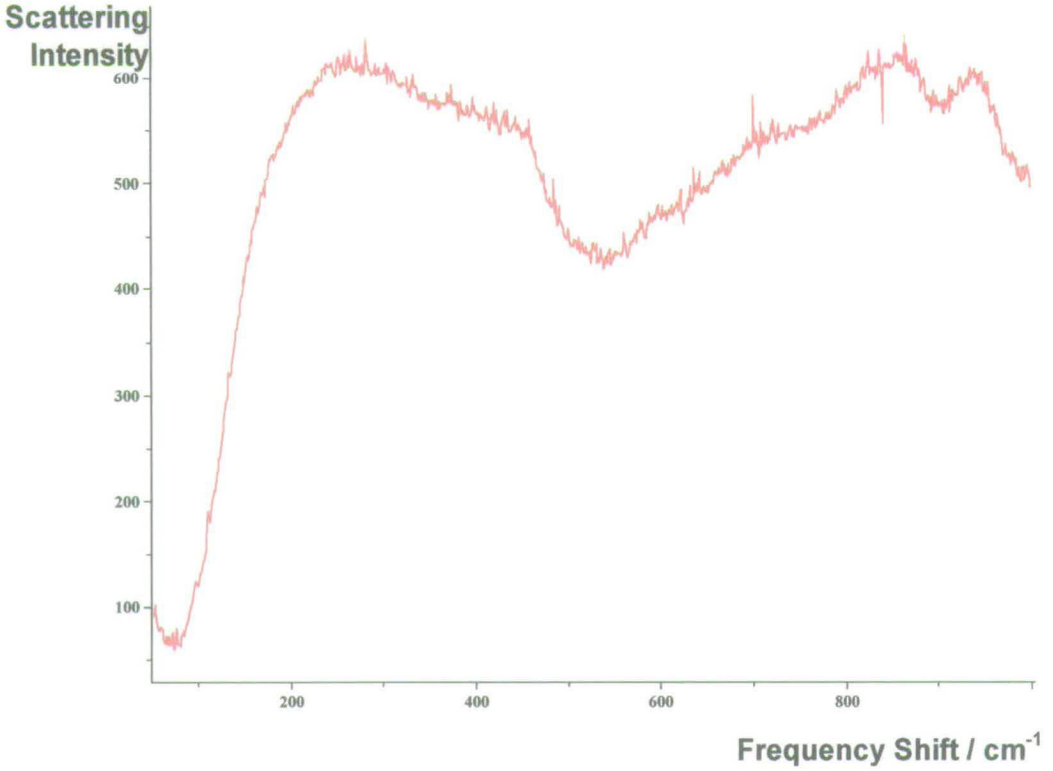

Figure 5.21: Raman spectrum of the electrochemically produced film

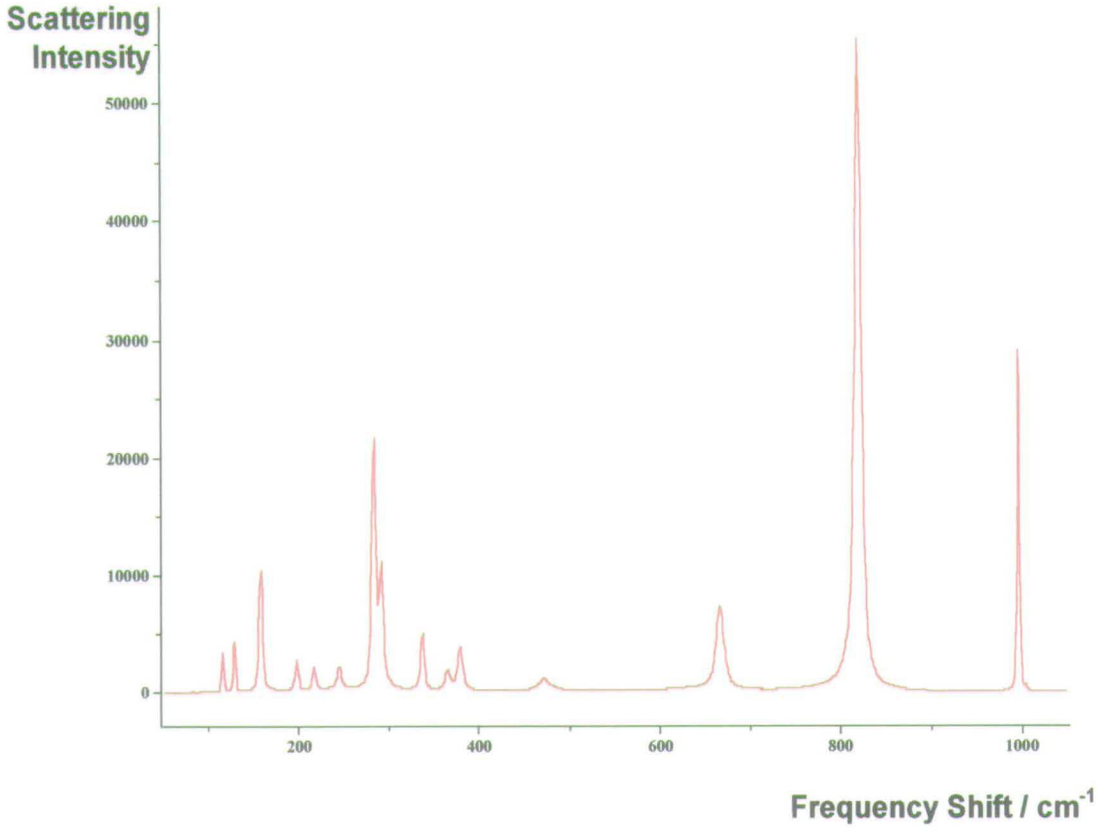

Figure 5.22: Raman spectrum of the commercial MoO_3 powder

5.6 Characterisation of Tungsten Nitride

5.6.1 X-Ray Photoelectron Spectroscopy (XPS)

5.6.1.1 Surface Measurements

Figures 5.23 and *5.24* show the wide scan spectra obtained for the electrochemically synthesised film and tungsten metal respectively. In both spectra, singlets due to oxygen and carbon 1s peaks are visible at 531eV and 285eV respectively. The tungsten 4f doublet is also visible at 34 and 37eV, and the tungsten 4d doublet at 246 and 259eV. Peaks due to nitrogen are not visible on the scale of *Figure 5.23*.

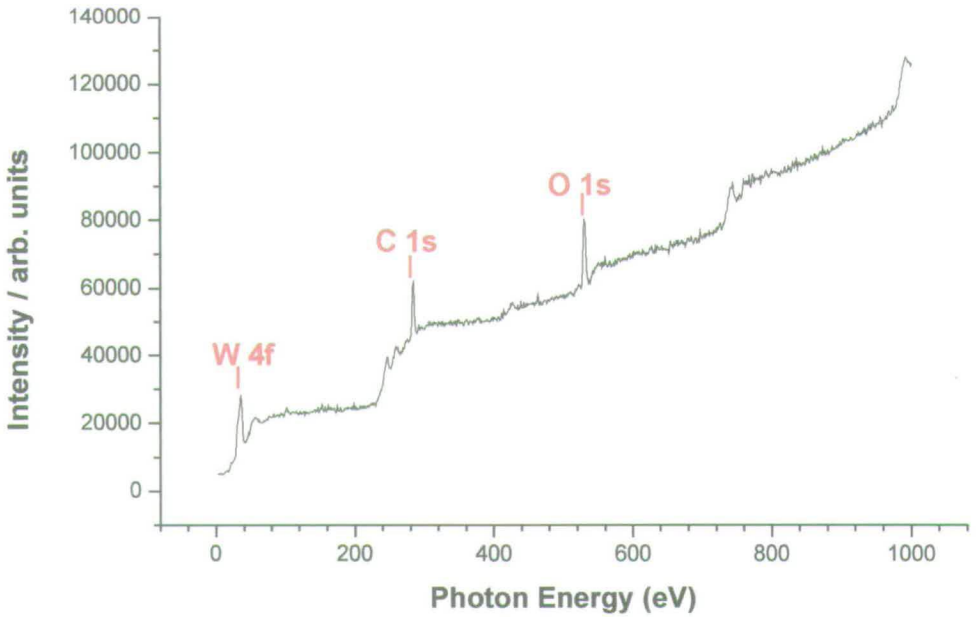

Figure 5.23: Wide scan XPS spectrum of the electrochemically produced film

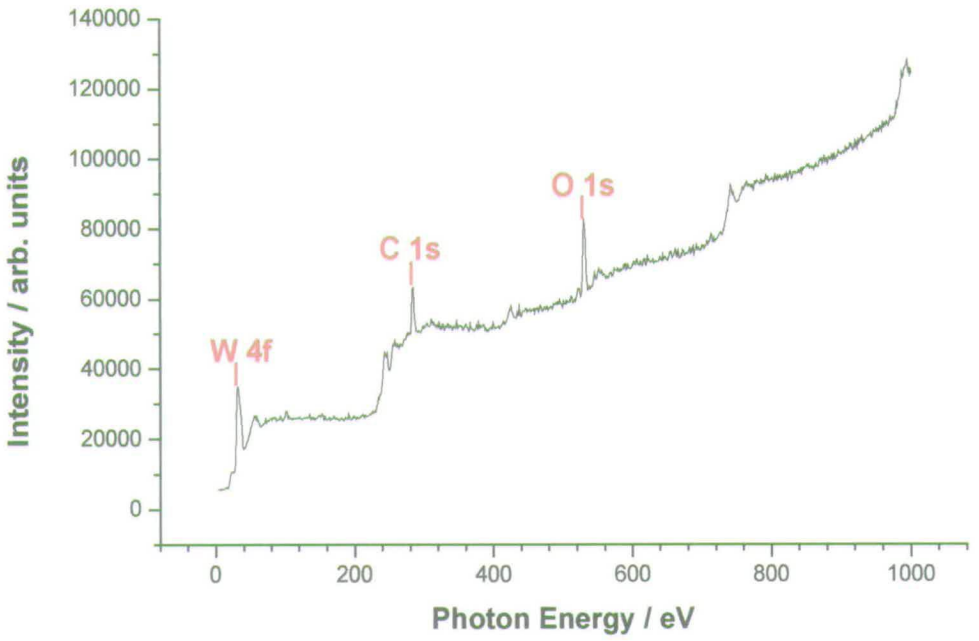

Figure 5.24: Wide scan XPS spectrum of tungsten metal

Figures 5.25-5.27 show the tungsten, oxygen and nitrogen narrow scan spectra respectively for the electrochemically produced film and tungsten metal.

The tungsten 4f spectra are split into two overlapping doublets for both the electrochemically produced film and the tungsten metal (*Figure 5.25*). This indicates that the tungsten is present in two different chemical oxidation states. The two most intense peaks in the spectrum of the tungsten metal ($4f_{7/2}$ at 30.2eV and $4f_{5/2}$ at 32.4eV in the expected area ratio of 4:3) are due to metallic tungsten. The two weaker peaks ($4f_{7/2}$ at 34.7eV and $4f_{5/2}$ at 36.5eV) are due to tungsten in the +6 oxidation state present as WO_3. The $4f_{7/2}$ peak shift of +4.5eV from metal to metal oxide is in line with reported data [19]. Peaks due to β-W_2N would be expected at 33.0 ($4f_{7/2}$) and 35.0 ($4f_{5/2}$) eV [32]. The same pattern is observed for the electrochemically produced film, except that the oxidised peaks are of stronger intensity than the metallic peaks. This indicates that the surface oxide layer is thicker on this sample.

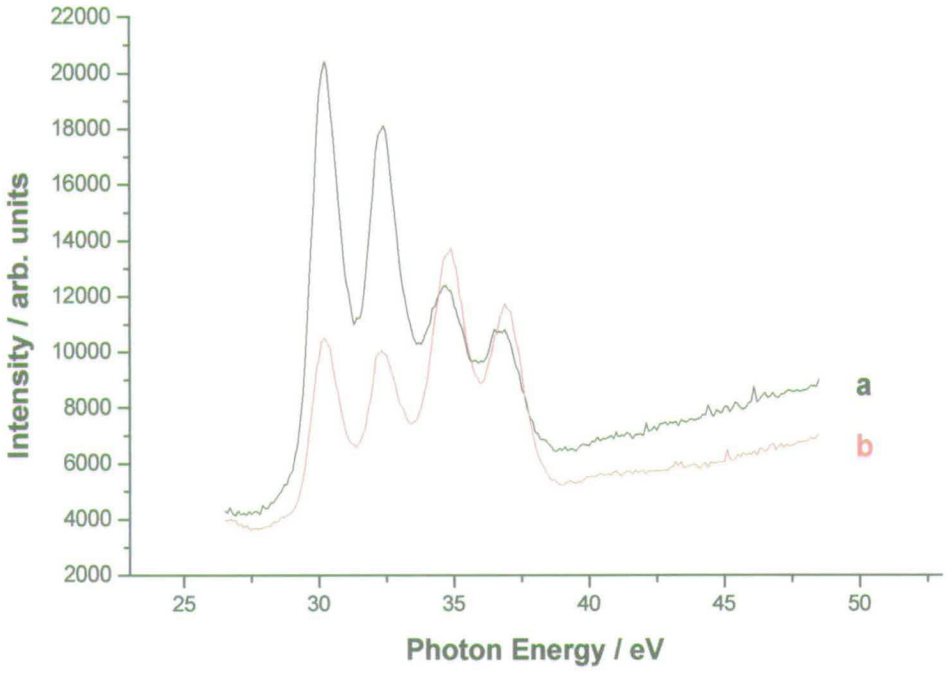

Figure 5.25: Tungsten 4f XPS spectra for (**a**) tungsten metal, and (**b**) the electrochemically produced film

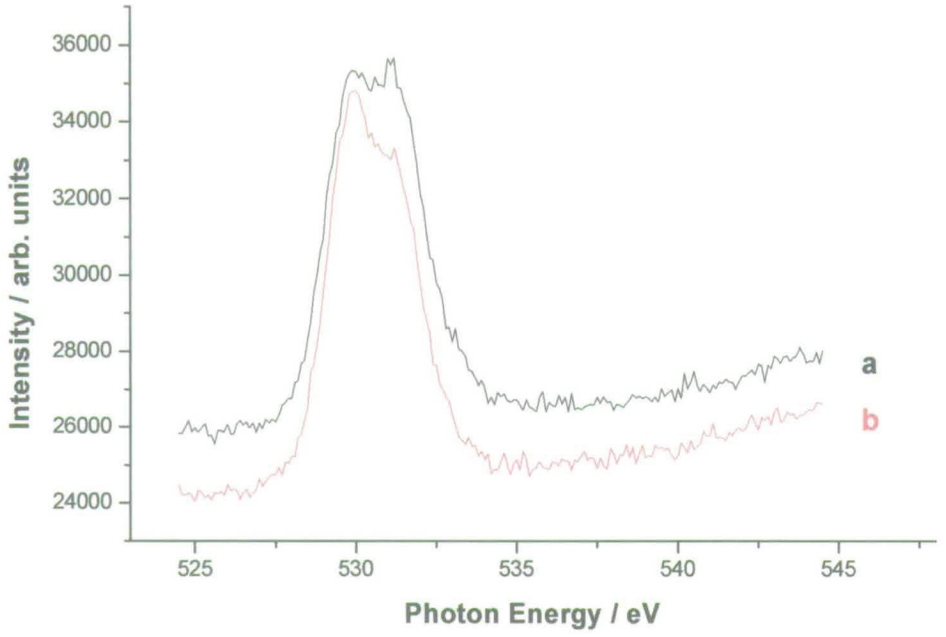

Figure 5.26: Oxygen 1s XPS spectra for (**a**) tungsten metal, and (**b**) the electrochemically produced film

Both oxygen 1s spectra are slightly uneven singlets of roughly similar intensity. The peak in the tungsten metal spectrum is centred on 529.9eV, and the peak in the spectrum of the electrochemically produced film is centred on 527.5eV. The binding energy of O 1s electrons in WO_3 has been reported as 530.3eV [33]. This confirms that the surface of both samples is contaminated with tungsten oxide.

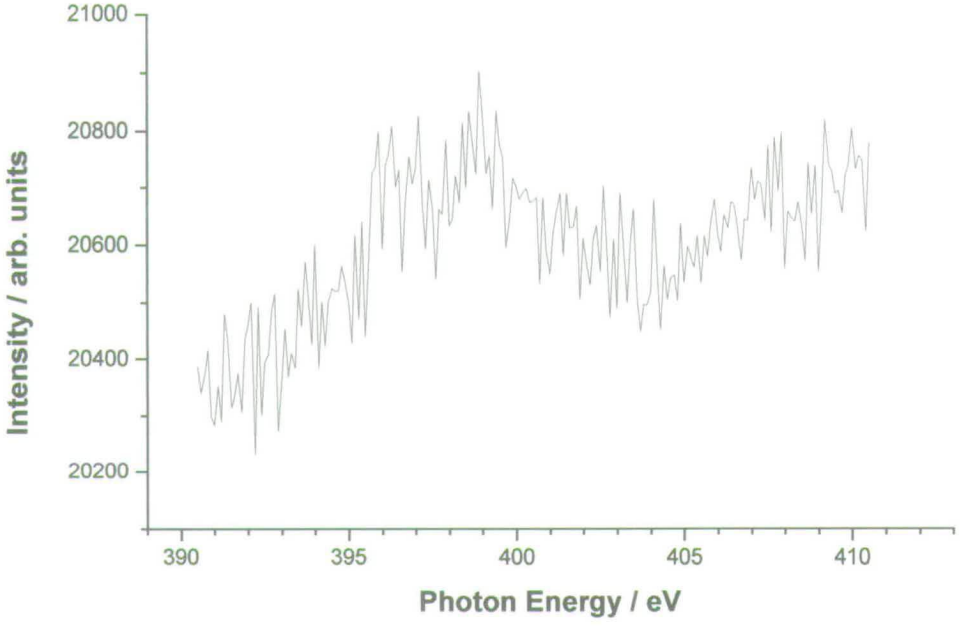

Figure 5.27: Nitrogen 1s XPS spectrum for the electrochemically produced film

The data collected in the N 1s spectral region for the electrochemically produced film are very noisy. There is a suggestion that some nitrogen might be present (peak at 396-399eV), and that this was difficult to detect due to the presence of surface oxide. The binding energy of N 1s electrons in β-W_2N has been reported as 397.0eV [32]. A sputtering experiment might elucidate the situation, although unfortunately time did not allow this to be carried out.

5.6.2 Transmission Electron Microscopy (TEM) - Electron Diffraction

Figure 5.28a shows the TEM images obtained from a thin section sample of the grey-brown powder produced in experiment 3 mounted in epoxy resin. The sample appears to be rather granular, but with none of the small spherical particles observed for titanium and molybdenum.

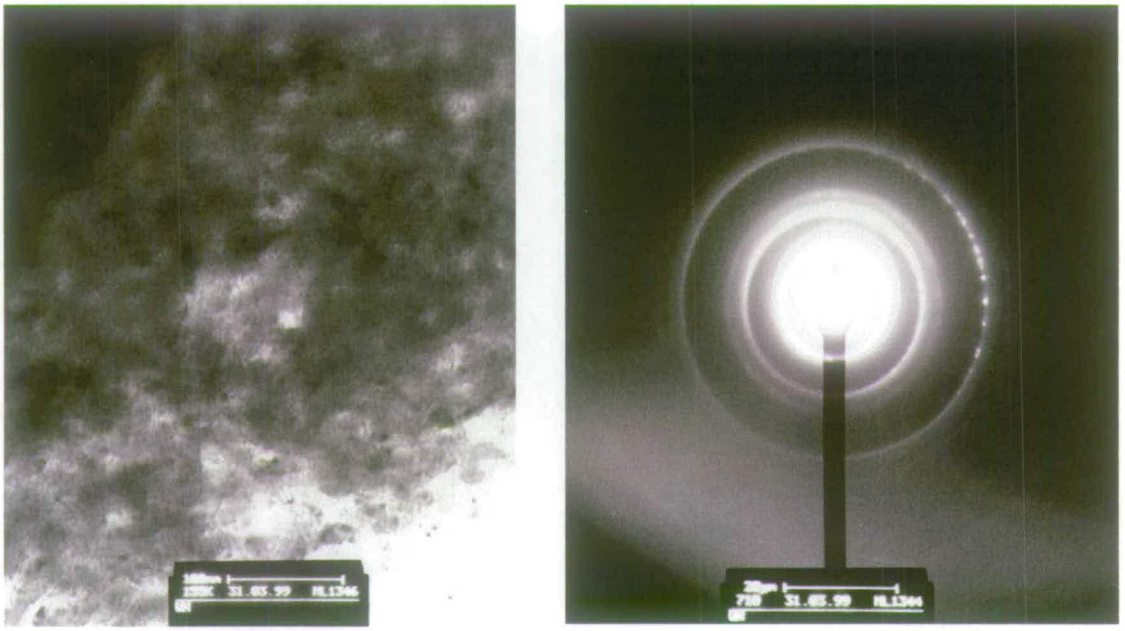

Figure 5.28: (**a**) TEM image and (**b**) electron diffraction pattern of a thin section of the material produced at a tungsten electrode

Figure 5.28b shows the electron diffraction pattern obtained from the a thin section of brown powder mounted in epoxy resin. The rings are rather diffuse and this made the pattern difficult to index. The approximate d-spacings are shown as compared with the closest d-spacings of some known tungsten nitrides (*Table 5.5)* and oxides (*Table 5.6)* as generated by the DRAGON program [21] between 0 and 80° 2θ. The lattice parameters of some of the known phases are given in *Table 5.7* [15, 25, 34-44]. As with the molybdenum nitrides and

oxides it can be seen that the various nitride and oxide phases share many similar d-spacings, and are not clearly distinguishable. The pattern does not seem to match exactly that of any of the known materials, and it is likely that the powder is a mixture of oxide (closest matches WO_2 1, ε-WO_3, and WO_3 1) and nitride (closest match hexagonal W_5N_6). The material cannot be confidently identified with this method. The XPS results suggested that the material was prone to aerial oxidation. WO_3 is known to exist in at least seven different polymorphs, and is unique in that it is the only oxide of any element that can undergo numerous facile crystallographic transitions near room temperature [45]. This is bound to complicate the identification if oxidation has commenced.

ED	Hexagonal WN_2		Cubic W_2N		Hexagonal WN		Hexagonal W_5N_6		Cubic W_3N_4		Hexagonal W_2N	
3.60	-	-	-	-	-	-	-	-	-	-	-	-
2.12	2.14	104	2.06	200	2.51	100	2.10	114	-	-	2.09	106
1.76	-	-	1.84	210	1.88	101	1.77 1.75	205 108	-	-	1.76	0013
1.23	1.23	117	1.24	311	1.23	102	1.24 1.22	222 1012	1.24	311	1.23	203

Table 5.5: Experimental d-spacings (± 0.05 Å) from electron diffraction compared with the closest d-spacings (in Å) and hkl values from known tungsten nitrides. The figures in red have a good match with the experimental result.

ED	WO_2 1		WO_2 2		Tetragonal WO_2		ε-WO_3		WO_3 1		WO_3 2		Orthorhombic WO_3	
3.60	-	-	-	-	3.44	110	3.67	110	3.65	200	3.71	110	3.69	200
2.12	2.12	330	2.15	210	2.16	111	2.12	-113	2.12	023	2.18	201	2.10	031
1.76	1.76	511	1.73 1.73	-213 -113	1.72	220	1.76	300	1.77 1.77	401 410	1.75	300	1.81 1.71	112 022
1.23	1.23 1.23 1.23 1.23	551 503 243 542	1.23 1.23	-224 -233	1.22	400	1.23 1.23	106 330	1.23 1.23	235 -253	1.23	113	-	-

Table 5.6: Experimental d-spacings (± 0.05 Å) from electron diffraction compared with the closest d-spacings (in Å) and hkl values from known tungsten oxides. The figures in red have a good match with the experimental result.

Material	a	b	c	Reference
Hexagonal WN_2	2.89	= a	16.40	[34]
Cubic W_2N	4.126	= a	= a	[35]
Hexagonal WN	2.893	= a	2.826	[36]
Hexagonal W_5N_6	5.014	= a	15.260	[15]
Cubic W_3N_4	4.122	= a	= a	[37]
Hexagonal W_2N	2.89	= a	22.85	[38]
WO_2 1	9.7164	8.4380	4.7564	[39]
WO_2 2	5.57690	4.8986	5.6644	[40]
Tetragonal WO_2	4.86	=a	2.77	[25]
ε-WO_3	5.27754	5.16257	7.67684	[41]
WO_3 1	7.30131	7.53895	7.68932	[42]
WO_3 2	5.250	= a	3.915	[43]
Orthorhombic WO_3	7.384	7.512	3.846	[44]

Table 5.7: Lattice parameters (in Å) of some known tungsten nitrides and oxides

5.6.3 Raman Spectroscopy

Figure 5.30 shows the Raman spectra obtained from the electrochemically produced film and powder, and a commercial tungsten oxide (WO_3) powder reference sample. Although the spectra of the pressure cell products are very poorly resolved, some broad peaks are observed, and these correspond with the most intense peaks in the WO_3 spectrum. It seems that both the electrochemically produced film and the powder had oxidised by the time analysis was performed. Great care had been taken to wash the samples with dry liquid ammonia and then store them under nitrogen, although the analysis itself was performed in air. It is possible that oxidation occurred in the laser beam during the Raman experiment. The pressure cell products were clearly very air- and/or moisture-sensitive, making characterisation difficult.

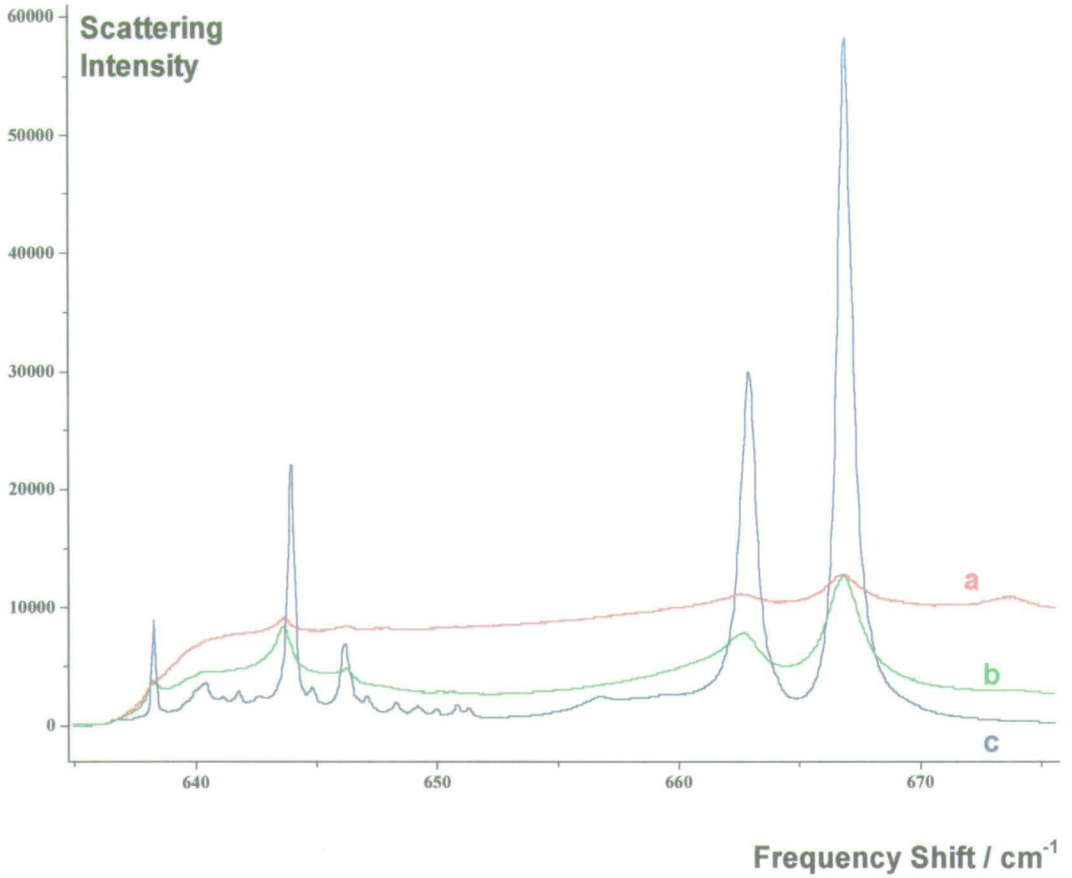

Figure 5.30: Raman spectra of (**a**) the electrochemically produced film, (**b**) the electrochemically produced powder, and (**c**) commercial WO_3 powder

5.7 Summary, Conclusions and Further Work

This chapter described the attempts to synthesise molybdenum and tungsten nitrides *via* the novel electrochemical method introduced in *chapters 3* and *4*.

The protocol developed for the reduction of the native oxide layer on titanium prior to nitridation was also applied to the two group 6 metals. This appeared to proceed in a similar fashion for molybdenum as it had for titanium with the generation of blue ammonia-solvated electrons at the metal surface and an eventual expansion of the accessible potential window of the electrode. It was unclear whether the cleaning process had been effective for tungsten.

Nitridation of molybdenum was performed first at -78°C when initially a gold-coloured film was observed on the electrode followed by the appearance of a red-coloured material. The steady current at +5.00 V (vs. Pt) was 20μA. Cottrell analysis allowed the calculation of a diffusion coefficient for the process of 1.14×10^{-12} cm^2s^{-1}. This is too low to be attributed to the diffusion of amide through liquid ammonia, and was instead accounted to the slow diffusion of 'N' atoms (formally nitride) through the molybdenum lattice. This process is likely to be the rate determining step of the reaction.

Electrochemical modification in the pressure cell at ambient temperature and 10 atms pressure also produced a gold-coloured film as the initial reaction product. As the experiment proceeded the red-brown gelatinous solid was generated again. This is analogous to the titanium system whereby bulk samples of the reaction product could be isolated at elevated

temperature and pressure. However, in the molybdenum case this powder product was also observed at -78°C, unlike with titanium.

XPS of the gold-coloured film revealed the presence of molybdenum oxide and hydroxide and this was attributed to the post-processing aerial oxidation of the surface, as the synthetic method itself excluded all sources of oxygen/moisture. Nitrogen was also detected at the surface, confirming the production of a nitride phase. Sputtering experiments revealed that the nitride layer was less than 500nm in thickness. The overlap of the N 1s line with the Mo $3p_{3/2}$ line meant that it was difficult to ascertain the exact depth to which nitrogen persisted in the metal. A total of 6C was passed during the synthesis of the film. Assuming 100% current efficiency, a layer of approximately 200nm would be expected to form (assuming reaction product is cubic MoN, a = 4.212nm, giving a density of $4.89gcm^{-3}$. Other molybdenum nitrides have a similar density.).

TEM showed that the material was composed of spherical particles of approximately 5-10nm diameter. They had morphology very similar to the TiN particles generated previously. Interpretation of electron diffraction results was complex as there are many known phases of molybdenum nitrides and oxides, all with rather similar d-spacings. However, it was concluded that the reaction product was most likely to be hexagonal Mo_2N, although the data were also in agreement with hexagonal MoO_3. It was known that the particles were prone to aerial oxidation owing to their very small size. Raman spectroscopy of the film produced only a poorly resolved spectrum probably owing to the very thin layer and possibly the presence of several phases of variable stoichiometry. The pattern of lattice phonons was reminiscent of that observed for TiN, and indicated that the sample was free from significant amounts of MoO_3 in this instance.

Nitridation of tungsten was performed at ambient temperature and 10atms pressure. At +5.00 V (vs. Pt) the steady current was approximately 3mA. The experiments followed a similar pattern to those on molybdenum in that initially a gold- or rainbow-coloured film was produced and as the experiment continued a highly air-/moisture-sensitive coloured solid was formed. In the tungsten case the solid was red-brown, white-grey or orange, and this was probably governed by the particle size of the product, which was in turn determined by the initial nature of the electrode surface.

XPS of the film revealed a heavily oxidised surface, with extremely low nitrogen levels. Time did not permit a sputtering study to be performed. The bulk solid produced in the later stages of the experiments was shown to be of granular morphology by TEM. Again the interpretation of the electron diffraction results was hampered by the multitude of known nitride and oxide phases with close d-spacings. The electron diffraction did not match that of any one known phase and it was concluded that a mixture of a nitride and an oxide was present.

Owing to the extreme air-/moisture-sensitivity of these materials, coupled with their very small particle size, complete characterisation has been difficult to obtain. The thin films appear to be more stable and probably represent the greater likelihood of obtaining further analysis. It would be interesting to measure the superconducting behaviour of these films in future.

5.8 Bibliography

[1] H. Chiu and S. Chuang, *J. Mater. Res.*, **8**, (6), 1353-1360, 1993

[2] R. Fix, R. G. Gordon and D. M. Hoffmann, *Thin Solid Films*, **288**, 116-119, 1996

[3] M. Maoujoud, L. Binst, P. Delcambe, M. Offergeld-Jardinier and F. Bouillon, *Surface and Coatings Technology*, **52**, 179-185, 1992

[4] A. Wang, F. Capitain, V. Monnier, S. Matar and G. Demazeau, *Journal of Materials Synthesis and Processing*, **5**,(3), 235-248, 1997

[5] S. Ramanathan and S.T. Oyama, *J. Phys. Chem.*, **99**, 16365-16372, 1995

[6] G. Hagg, *Z. Phys. Chem. Abt. B*, **7**, 339, 1930

[7] H. Jehn and P. Ettmayer, *J. Less-Common Metals*, **58**, 85, 1978

[8] N. Schonberg, *Acta. Chem. Scand.* **8**, 204, 1954

[9] N. E. Brese and M. O'Keeffe, '*Crystal Structure of Inorganic Nitrides*' in '*Structure and Bonding*', **79**, 309-378, 1992

[10] T. Nakajima and T. Shirasaki, *J. Electrochem. Soc.*, **144**, (6), 2096-2100,1997

[11] J. M. Vandenberg and B. T. Matthias, *Mat. Res. Bull.*, **9**, 1085-1090, 1974

[12] Y. T. Kim, C. W. Lee and S. Min, *Appl. Phys. Lett.*, **61**, (5), 537, 1992

[13] S. D. Marcus and R. F. Foster, *Thin Solid Films*, **236**, 330-333, 1993

[14] A. L. Currie and K. E. Howard, *J. Mat. Sci.*, **27**, (10), 2739-2742, 1992

[15] F. Tessier and R. Marchand, *J. Alloys and Compounds*, **262-263**, 410-415, 1997

[16] F. Tessier, R. Marchand and Y. Laurent, *J. European Ceram. Soc.*, **17**, 1825-1829, 1997

[17] V. I. Khitrova and Z. G. Pinsker, *Sov. Phys. Crystallogr.*, **6**, 712, 1962

[18] A. C. Fischer, '*Electrode Dynamics*', Oxford University Press, 33, 1996

[19] Ed. D. Briggs and M. P. Seah, *'Practical Surface Analysis'*, J. Wiley and Sons 1983

[20] F. Fujimoto, Y. Nakane, M. Satou, F. Komori, K. Ogata and Y. Andoh, *Nucl. Instrum. Meth. Phys. Res. Sect. B*, **B19/20**, 791, 1981

[21] J. K. Cockcroft, DRAGON Program, © 1998 Birkbeck College, available at: http://gordon.cryst.bbk.ac.uk/htbin/dragon.exe

[22] P. Ettmayer, *Monatsh. Chem.*, **101**, 127-140, 1970

[23] G. Linker, R. Smithey and O. Meyer, *J. Phys. F Met. Phys.*, **14**, L115, 1984

[24] N. V. Troitskaya and Z. G. Pinsker, *Kristallografiya*, **6**, 43-48, 1961

[25] R. W. G. Wyckoff, '*Crystal Structures*', **1**, InterScience 1948

[26] A. A. Bolzan, B. J. Kennedy and C. J. Howard, *Aust. J. Chem.*, **48**, 1473-1477, 1995

[27] Joint Committee on Powder Diffraction Standards 1971, card 21-569 (Spangenberg, Westinghouse Electric Corp., Horseheads, N. Y.)

[28] Joint Committee on Powder Diffraction Standards 1971, card 5-0508 (Swanson and Fuyat, NBS Circular, **539**, 3, 1953)

[29] J. B. Parise, E. M. McCarron and A. W. Sleight, *Mater. Res. Bull.*, **22**, 803-811, 1987

[30] E. J. Markel and J. W. Van Zee, *J. Catal.* 126, 643-657, 1990

[31] D. J. Gardiner, C. J. Littleton and K Strafford, *Comm. Eur. Communities, High Temp. Alloys*, (Rep) Eur. **11365**, 155-164, 1987

[32] T. Nakajima, K. Watanabe and N. Watanabe, *J. Electrochem. Soc.*, **134**, 3175, 1987

[33] R. J. Colton and J. W. Rabalais, *Inorg. Chem.*, **15**, 236, 1976

[34] V. I. Khitrova, *Kristallografiya*, **6**, 549-552, 1961

[35] C. J. Smithells, '*Crystal Structure*' in Metals Reference Book 1, Plenum Press, 4th Ed., 1967

[36] Joint Committee on Powder Diffraction Standards 1975, card 25-1256, (Fiala, Central Research Institute, Skoda, Czechoslovakia, 1973)

[37] F. Guenther and H. G. Schneider, *Kristallografiya*, **11**, 683-686, 1966

[38] V. I. Khitrova and Z. G. Pinsker, *Kristallografiya*, **5**, 711-717, 1960

[39] M. Sundberg, P-E. Werner and I. P. Zibrov, *Z. Kristallogr.*, **209**, 662-666, 1994

[40] A. A. Bolzan and B. J. Kennedy, *Aust. J. Chem.*, **48**, 1473-1477, 1995

[41] E. K. H. Salje, S. Rehmann, F. Pobell, D. Morris, K. S. Knight, T. Herrmannsdoerfer and M. T. Dove, *J. Less-Common Met.*, **9**, 6563-6577, 1997

[42] P. M. Woodward and A. W. Sleight, T. Vogt, *J. Phys. Chem. Solids*, **56**, 1305-1315, 1995

[43] W. L. Kehl, R. G. Hay and D. Wahl, *J. Appl. Phys.*, **23**, 212-215, 1952

[44] Joint Committee on Powder Diffraction Standards 1975, (Roth and Waring, *J. Res. National Bureau of Standards*, **70A**, (4), 281-303, 1966)

[45] N. N. Greenwood and A. Earnshaw, '*Chemistry of the Elements*' Pergamon Press, 1990

Chapter 6:

Electrochemical Synthesis of Tantalum, Aluminium & Iron Nitrides

6.1 Introduction

6.1.1 Tantalum Nitride

6.1.1.1 Properties and Applications

Tantalum nitrides (TaN_x, $0<x<2$) are refractory materials with extremely high thermal stability, excellent mechanical robustness, enhanced chemical inertness, and good resistance to corrosion. This combination of properties leads to a wide range of technological applications, ranging from commonly used Ta_2N and TaN thin film resistors to the proposed use of Ta-based diffusion barriers and adhesion promoters in integrated circuitry metallisation [1]. Although at present aluminium alloys are conventionally used as interconnect materials, it is predicted that as interconnects become smaller, copper will eventually take over from aluminium owing to its lower resistivity and enhanced resistance to electromigration. However, copper diffuses more rapidly in silicon than aluminium, potentially severely degrading device performance. The implementation of copper-based metallisation architectures will depend on the production of a suitable diffusion barrier to prevent this. Tantalum nitride is believed to be just such a material. For example, sputtered TaN barriers of 50nm thickness have demonstrated their resistance to copper diffusion for up to 1 hour at 550°C (100°C above the failure point of metallic tantalum) [2]. TaN melts at 3090°C [3].

Similarly, a suitable diffusion barrier material is also required for use between platinum and ferroelectric materials (such as barium strontium titanate, strontium titanate and lead zirconium titanate), and platinum and silicon in stacked-capacitor memory cells. Production of silicon oxides and platinum silicides otherwise results [4].

6.1.1.2 Methods of Synthesis

Tantalum nitride thin films have been conventionally deposited *via* reactive sputtering of pure metal targets in an argon and nitrogen atmosphere, or by chemical vapour deposition from tantalum(V) chloride and ammonia [5]. However, the former route suffers from poor step coverage of substrates caused by the shadowing effect in small features and the potential mechanical damage that these high energy techniques may cause to structurally and chemically fragile substrates. The latter method requires a high deposition temperature (>600°C) to minimise chlorine impurities and substantial incorporation of hydrogen (up to 40 atomic %), carbon and oxygen are difficult to avoid [2].

6.1.1.2.a Chemical Vapour Deposition

Several studies concerning the metal organic chemical vapour deposition (MOCVD) of TaN have been reported. Sugiyama *et al* have reported that TaN thin films can be obtained from pyrolysis of *pentakis*-(diethylamino)-tantalum, $Ta(NEt_2)_5$ [6]. Chiu *et al* attempted to produce TaN from $(NEt_2)_3Ta{=}NEt$ [7], and Tsai *et al* reported that films with low oxygen and carbon contents could be produced by pyrolysis of $(NEt_2)_3Ta{=}N^tBu$ [8, 9]. There has been speculation that the metal-nitrogen double bond in these molecules plays an important role in the mechanism of incorporating nitrogen in the films [10]. The attempt to deposit TaN from the simple precursor $Ta(NMe_2)_5$ in ammonia resulted in the production of tetragonal Ta_3N_5 with a high resistivity [11]. However Cho *et al* have deposited thin films of tantalum nitride by remote plasma-assisted MOCVD of *pentakis*-(dimethylamino)-tantalum, $Ta(NMe_2)_5$ with different activating radicals. At temperatures below 300°C, amorphous films were obtained independent of the reacting species. At higher temperatures, (111)-oriented cubic TaN films

were obtained from an ammonia plasma, whilst reaction in a hydrogen plasma produced amorphous films. The materials produced were judged to be successful barrier layers between platinum and silicon [3, 5]. Chen *et al* have produced low resistivity, cubic TaN films *via* a plasma assisted CVD technique. Tantalum(V) bromide, hydrogen and nitrogen were reacted at substrate temperatures of 350-450°C, to produce oxygen and carbon free films with a 3 atomic % bromine content. The films were found to be a suitable barrier layer between copper and silicon up to 550°C [1, 2].

6.1.1.2.b Physical Methods

Min *et al* [12] (and Sun *et al* [13]) have synthesised tantalum nitride (Ta_2N and TaN) films on (100) silicon substrates by using d.c magneton sputtering at various nitrogen/argon ratios. The properties of the films as diffusion barriers were enhanced as the nitrogen concentration increased. Radhakrishnan *et al* have performed a similar deposition onto gallium arsenide substrates [14].

Single phase stoichiometric B1-type tantalum nitride (TaN) was produced by shock compression. This was found to be a high temperature, high pressure phase, with a relatively high superconducting critical temperature. WC-type tantalum nitride was also synthesised by static compression, and was found to be a low temperature, high pressure phase [15, 16].

6.1.1.2.c Solid State Methods

Tantalum nitride was formed by the solid-gas reaction of tantalum with molecular nitrogen driven by mechanical alloying. Nanoparticulate Ta_2N and trace amounts of Ta_3N_5 were

produced, believed to be by the chemisorption of nitrogen on clean metal surfaces created by milling [17].

Parkin and Rowley have reported a solid-state route which is a hybrid of a molecular precursor approach and a metathesis reaction. The reaction of $TaCl_5$ with $LiNH_2$ at 300°C under nitrogen induced a spontaneous (1-2s) exothermic reaction and the production of a black solid. This could be washed free from LiCl with thf, and annealing at 700°C in vacuo or under ammonia for 1 hour produced cubic TaN. The intermediate contained amide groups and chlorine. Similarly, reaction of an equimolar mix of $LiNH_2$ and $LiNMe_2$, or just $LiNMe_2$ with $TaCl_5$ followed by thermolysis produced red Ta_3N_5 [18].

6.1.2 Aluminium Nitride

6.1.2.1 Properties and Applications

The nitrides of group 13 are primarily of interest because of their semiconducting properties. The physical properties of these materials suggests a shift from covalent to partially ionic to metallic-type bonding as the group is descended. Aluminium nitride, AlN, is isoelectronic with silicon carbide and in the solid state adopts the wurtzite, hexagonal ZnS structure (a = 3.10, c = 4.97 Å). It is a pale yellow or brown ceramic solid with a melting point in excess of 2200°C, after which it decomposes. AlN has a band gap of 411kJmol^{-1}. It is chemically resistant to both acids and alkalis, although it does react slowly with water to produce hydrated Al_2O_3 and ammonia gas [3].

AlN features high thermal conductivity, low thermal expansion, high electrical resistivity and greater mechanical strength than Al_2O_3. In the field of microelectronics AlN has been used as a heat radiating substrate material suitable for mounting high power, high speed semiconductors and large silicon chips [19]. Niobium/corundum laminates are currently used as ceramic-metal units in electrical and vacuum devices. AlN/Mo multilayer composites with high electrical and corrosion resistance are promising replacements for such conventional materials, and can be synthesised conveniently by chemical vapour deposition [20].

6.1.2.2 Methods of Synthesis

6.1.2.2.a Calcination of Aluminium-Containing Precursors

The complex $AlCl_3.6NH_3$ was produced by reaction of $AlCl_3$ and NH_3 at room temperature by Pouget *et al* [21]. On heating to 900°C in an ammonia stream, the intermediate decomposed to produce AlN in low yield with NH_4Cl as a by-product. Pyrolyses were also performed under nitrogen and at reduced pressure. Crystalline AlN powders have been produced by the gas-phase reaction of $AlCl_3$, ammonia and nitrogen. The yield was as high as 80% when the reactor temperature was 1000°C and the mole ratio of NH_3:$AlCl_3$ was 8:1. Most of the HCl by-product was recovered as NH_4Cl outside the reactor [22].

A novel low temperature chemical approach has been developed for synthesising aluminium nitride powders by Kim and Kumta [23]. The process involved the reaction of aluminium(III) chloride with anhydrous hydrazine in acetonitrile solution in the presence of metallic lithium to induce a reductive precipitation reaction. The precipitate was pyrolysed at 800°C under either argon or ammonia to produce hexagonal AlN and lithium chloride. The latter could be

washed out with acetone, or excluded by performing the pyrolysis reaction at 1000°C, when only AlN was produced.

Uheda *et al* [19] have synthesised crystalline AlN powder from an aluminium-urea precursor. Aluminium chloride was dissolved in molten urea at 135°C to form the precursor (identity not described) which was then calcined at 900°C under nitrogen for 1 hour. The AlN powder was obtained in 80% yield; a volatile $Al(NH_3)_6AlH_4Cl_2$ by-product was also produced, as identified by powder XRD.

Dialkylaluminium μ-dialkylamido compounds of formula $[(R_2AlNR'_2)Al]_2$ (R = Me, Et, ^{i}Pr, ^{i}Bu, ^{t}Bu, R' = Me, Et, ^{i}Pr, ^{i}Bu, Ph) were synthesised by alkane or arene elimination from the corresponding adduct of the formula $(R_3Al)Al.NHR'_2$. These precursors were used to produce films of aluminium nitride by low pressure (10^{-2} Torr) thermal decomposition at 500-600°C [24].

Aluminium nitride powder has also been prepared by pyrolysing poly(ethyliminoalane) under argon (at 1600°C for 2 hours), ammonia (at 600°C for 2 hours), and nitrogen (1350°C for 8 hours). Pyrolysis under ammonia or nitrogen produced fine particles in 57% yield with little oxygen or carbon contamination. The product formed under argon, however, contained 17% carbon [25].

AlN films have been deposited by electron cyclotron resonance plasma-enhanced chemical vapour deposition using trimethylaluminium as a precursor at temperatures between 25-600°C. The layers contained a high concentration of oxygen [26].

6.1.2.2.b Auto-Ignition of Powders

Reaction between $Al(OH)_3$ and carbon powder under flowing nitrogen in the temperature range 1300-1700°C was found to produce AlN. Alumina was produced first, and was subsequently reduced and nitrided to produce AlN via the intermediate spinel-type aluminium oxynitride [27, 28]. The carbothermal synthesis has also been performed directly from alumina [29].

AlN was also produced in air by grinding powder mixtures of aluminium metal and graphite (in a molar ratio 3:1) in a planetary ball mill through self-ignition and subsequent propagation reactions. The product was also found to contain aluminium carbide, aluminium oxynitride, aluminium oxycarbide and α-alumina by X-ray diffraction. By varying the depth of the graphite crucible, AlN could be obtained in 97% purity at the bottom of the vessel [30]. Self-propagating high-temperature (combustion) synthesis of oxygen-free, high density aluminium nitride from aluminium powder in a pressurised nitrogen atmosphere has also been successfully performed [31, 32, 33]. Haussonne *et al* have also successfully synthesised aluminium nitride ceramics by heating mixtures of aluminium powder and lithium salts in nitrogen at 800-1200°C [34].

Aluminium nitride powders were synthesised by a spark discharge method in liquid ammonia between 0 and 130°C using a 2.5-11kV spark discharge voltage. An aluminium pellet was used as the starting material. Significant amounts of Al coexisted with the product, but this could be converted to AlN by calcining the powder in a nitrogen atmosphere at 900-1200°C [35].

6.1.2.2.c Physical Methods

Watanabe *et al* have synthesised aluminium nitride films by ion beam assisted deposition by evaporation of aluminium and simultaneous irradiation with nitrogen ions at a substrate temperature of room temperature or 175°C. The substrate was single crystal Si (100). The morphology of the films could be controlled by means of the substrate temperature and deposition rate [36, 37, 38]. CalvoBarrio *et al* have carried out similar work [39].

AlN films can also be deposited by reactive r.f. magnetron sputtering in a mixed atmosphere of Argon, nitrogen and hydrogen. An r.f. power of 200W, a sputtering pressure of 5 mTorr and a nitrogen concentration of 25% were employed. As the concentration of hydrogen increased, the deposition rate decreased rapidly and the grains on the film surface changed from conical to needle-shaped [40].

A hollow-cathode discharge-type ion plating method using r.f. bias potential has been used to deposit AlN films on glass substrates from aluminium and nitrogen [41].

6.1.3 Iron Nitride

6.1.3.1 Properties and Applications

Iron nitrides are regarded as promising materials from the viewpoint of magnetic applications, in particular recording media. Several magnetic phases are known, including α''-$Fe_{16}N_2$, γ'-Fe_4N, ε-Fe_3N and ξ-Fe_2N [42]. They display various types of magnetism with large magnetic moments comparable to that of metallic iron, and chemical stabilities superior to the metallic

phase [43]. Introduction of nitrogen atoms into the iron lattice also substantially increases mechanical durability and corrosion resistance. Fe_4N exhibits an electrical resistivity more than an order of magnitude higher than that of iron [44]. Iron nitrides have also seen use as heterogeneous catalysts, specifically in the Fischer-Tropsch hydriding of carbonyls [3].

6.1.3.2 Methods of Synthesis

6.1.3.2.a Precursor Routes

Nanoparticles of iron nitride have been produced by Koltypin *et al via* two methods [45]. In the first, $Fe(CO)_5$ was sonicated in a decane solution under a gaseous mixture of ammonia and hydrogen (7:2 molar ratio) at 0°C. This method produced amorphous $Fe_{2-3}N$ and a small quantity of iron oxide. The second method involved the nitridation of sonochemically prepared amorphous iron at 400°C for 4 hours under a mixed stream of ammonia and hydrogen (7:2 molar ratio). This method produced Fe_4N as the main product.

6.1.3.2.b Milling of Powders

Fe_3N, γ-Fe_4N and a supersaturated solid solution of N in Fe were formed by the ball milling of pure iron powder in a nitriding atmosphere of nitrogen or ammonia. This was performed at -197, 20 and 200°C. Ammonia was found to be the more effective nitriding gas, and at high nitrogen concentrations and low milling temperatures, Fe_3N was the dominant product [46].

Novel mechanically activated solid state synthesis reactions between elemental α-Fe powder and the amine compounds piperazine and pyrazine have been studied by Kaczmarek *et al* [47].

Powder samples prepared after 144 and 228 hours of milling time were found to contain predominantly fine Fe_3N submicrometer particles, with up to 2.5% carbon content.

Lee *et al* have investigated the synthesis of iron nitride powders using a combined mechanical alloying and vacuum annealing technique [48]. Nitrogen-supersaturated iron and amorphous phases with the composition $Fe_{100-x}N_x$ (x=11,14,20) were formed from mechanically alloyed powder mixtures of $Fe_{2.33}N$ and iron. The saturation magnetisation of the amorphous phase could be improved by vacuum annealing.

6.1.3.2.c Physical Methods

Fe_2N particles were prepared by nitriding acicular γ-Fe_2O_3 particles (precoated with sodium silicate to prevent the particles from sintering) at 450°C for 3-6 hours under a mixed stream of hydrogen and ammonia (1:4 molar ratio). X-ray diffraction showed mostly Fe_4N and small amount of α-Fe and Fe_2O_3 [49].

The possibility of synthesising ultra-fine particles of iron nitride was investigated by arc melting, vaporisation and condensation of iron in nitrogen/hydrogen/argon and ammonia/argon mixed atmospheres at 0.1MPa pressure. Only single phase α-Fe was found after reaction with nitrogen/hydrogen/argon. Besides the α-Fe phase, γ-Fe_4N, Fe_3N and γ-Fe was found in the powder product synthesised in the ammonia/argon atmosphere [50].

Iron nitride films have been deposited on germanium (100) wafers by a reactive ion beam sputter deposition of iron in an ammonia atmosphere. A mixture of α'-martensite and α''-$Fe_{16}N_2$ phases was obtained [51]. Similar experiments were performed by Rauschenbach; at

100°C implantation produced α'-martensite, at 175°C α''-$Fe_{16}N_2$ precipitated, and at 250°C ε-Fe_3N was the favoured phase. On continued annealing at these temperatures the microstructure was evolved to form α''-$Fe_{16}N_2$, γ'-Fe_4N and ξ-Fe_2N precipitates respectively [52]. Single phase Fe_4N has been produced by heat treating iron sheets in an ammonia-hydrogen atmosphere [44].

Shinno *et al* [53, 54] have prepared iron nitride thin films by the implantation of nitrogen ions into [100] oriented α-iron thin films (of 250nm thickness) on (100) magnesium oxide substrates at room temperature. The films were annealed at a low temperature of 175°C to form α'-$Fe_{16}N_2$ and α'-martensite phases (up to 60% volume fraction) with a higher saturated magnetisation than the unimplanted iron films. When the iron film of 500nm thickness was used as the starting material, only the α'-martensite phase was produced.

Stoichiometric iron nitride layers have been synthesised by high dose, high energy nitrogen implantation into iron using a two-step implantation process. First, a nitrogen preimplantation at -100°C was used to form nitride precipitates. Secondly, 1MeV implantation at 300°C led to the formation of a stoichiometric γ-Fe_4N layer at the position of the pre-implanted N atoms. Growth of this layer proceeded by diffusion of nitrogen [55, 56]. $Fe_{16}N_2$ was produced in high density in an iron sheet in a similar multi-implantation method by Tsubakino *et al* [57]

6.2 Strategy

Having had success in producing titanium, molybdenum and tungsten nitrides by the electrochemical anodisation of the appropriate metal in a solution of potassium amide in liquid ammonia, it was decided to attempt to apply the method to a selection of other metals. Tantalum, aluminium and iron were chosen because of their interesting industrial applications. The initial experiments reported in this chapter represent the first steps in this area of work, but time constraints have prevented a thorough investigation.

6.3 Experimental

Liquid ammonia solutions of potassium amide were prepared as in *section 3.3.1*. The single compartment pressure cell (described in *section 4.2.1.1*) with a three electrode set-up (described in *section 4.2.1*), was used for all experiments. The working electrode was either a tantalum foil (~0.5mm thickness, Vickers), an aluminium foil (0.13mm thickness, 99.99+% purity, Aldrich), or an iron foil (0.05mm thickness, 99.5% purity, Goodfellow).

6.4 Electrochemistry

Prior to anodisation of the working electrode, it was cycled for approximately 40 minutes at sweep rates of 50-100 mVs^{-1} between 0.00 V and a negative potential limit, always in excess of -1.50 V, such that a large negative current in the order of several mA was observed. Electrochemical modification took place between 0.00 and +5.00 V using a 1kΩ measuring resistor. The results shown here were obtained in the pressure cell at 25°C.

6.4.1 Tantalum

6.4.1.1 Stripping of Oxide Layer

Figure 6.1 shows the cyclic voltammograms recorded whilst attempting to clean the tantalum electrode. The initial scan (*Figure 6.1a*) shows a large negative current (A) on the reductive sweep to -3.00 V. This is most likely to be caused by reduction of the oxide layer and the production of free electrons, which gave rise to a blue colour near the working electrode. Unlike with the other metals (Ti, Mo, W) an associated oxidation peak was not observed on the positive sweep. The final CV recorded after 35 minutes cycling down to -5.00 V (*Figure 6.1b*) is shifted slightly to more negative potential compared with the initial scan. There was no further change on continued cycling. This demonstrates an increase in the effective potential window of the electrode, and is most likely due to the removal of a thin resistive oxide layer.

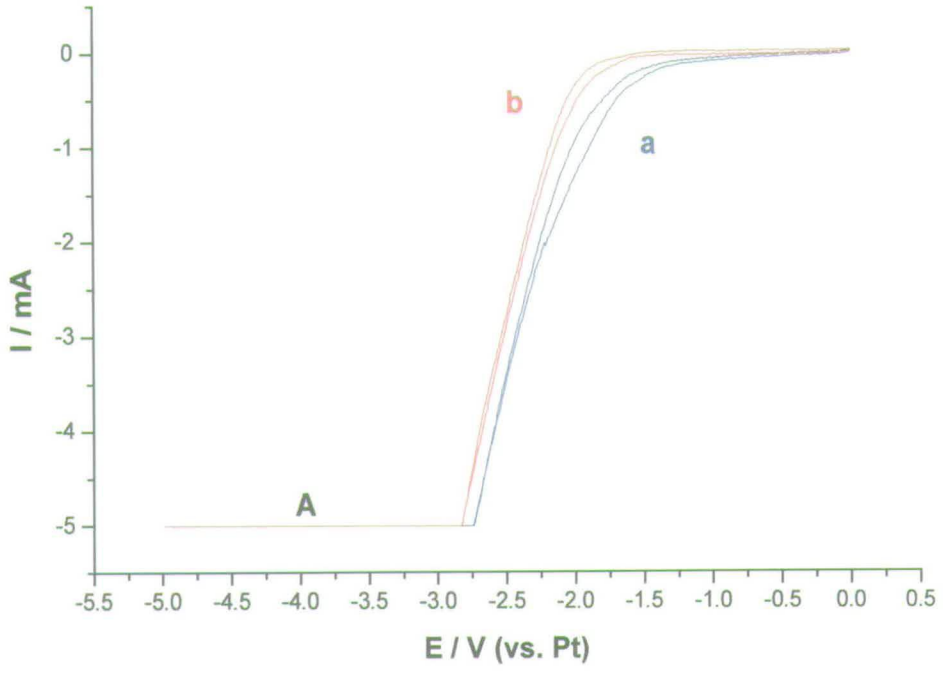

Figure 6 1: Cyclic voltammogram of tantalum working electrode in liquid ammonia solution of potassium amide (**a**) initial scan, and (**b**) after 35 minutes

6.4.1.2 Nitride Synthesis

Electrochemical modification was performed by increasing the potential of the working electrode to +1.00 V; the steady current after initial decay was approximately 0.1mA. The potential was then increased to +3.00 V in 0.50 or 1.00 V intervals and the current reached saturation (5mA) and gas was seen to evolve from the working electrode. The potential was reduced to +2.00 V to avoid this. *Figure 6.2* shows the current-time transient during these changes. After a short time (10 minutes) a yellow solid was seen growing on the tantalum, and this eventually became more orange in colour and formed 'tendrils' as the experiment progressed. A total of 900C of charge was passed. The resulting yellow-orange solid was washed thoroughly with dry liquid ammonia and dried under flowing nitrogen.

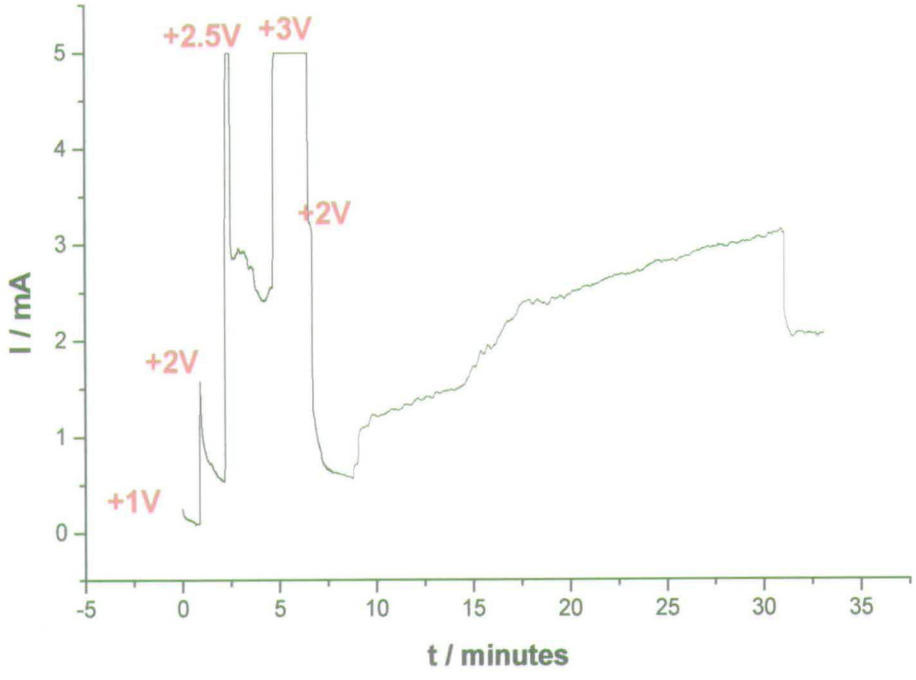

Figure 6.2: Current-time transient for the electrochemical modification of tantalum

6.4.2 Aluminium

6.4.2.1 Stripping of Oxide Layer

The cleaning of the aluminium electrode did not progress in the same manner as for the other metals. A blue coloration (indicative of ammonia-solvated electrons) was not observed at the working electrode on the sweep to negative potential. Similarly, a positive current was not observed on the positive sweep. There was no change in the cyclic voltammogram after 40 minutes of cycling.

6.4.2.2 Nitride Synthesis

It was decided to persevere with an attempt to produce aluminium nitride, even though the electrode had retained its native oxide layer. Electrochemical modification was initiated at +1.00 V, and the potential increased in 1.00 V intervals to +5.00 V. *Figure 6.3* shows the current-time transient during this process. On the increase to +5.00 V the current increased at first, and then decayed. After 3C of charge had been passed, a white-grey solid was observed on the aluminium working electrode. The sudden increase in current after approximately 22 minutes (*Figure 6.3)* is due to the cell being tapped and product falling from the electrode to expose fresh metal surface. A total of 50C of charge was passed, and the resulting white-grey solid was washed thoroughly in dry liquid ammonia and dried under a flow of nitrogen.

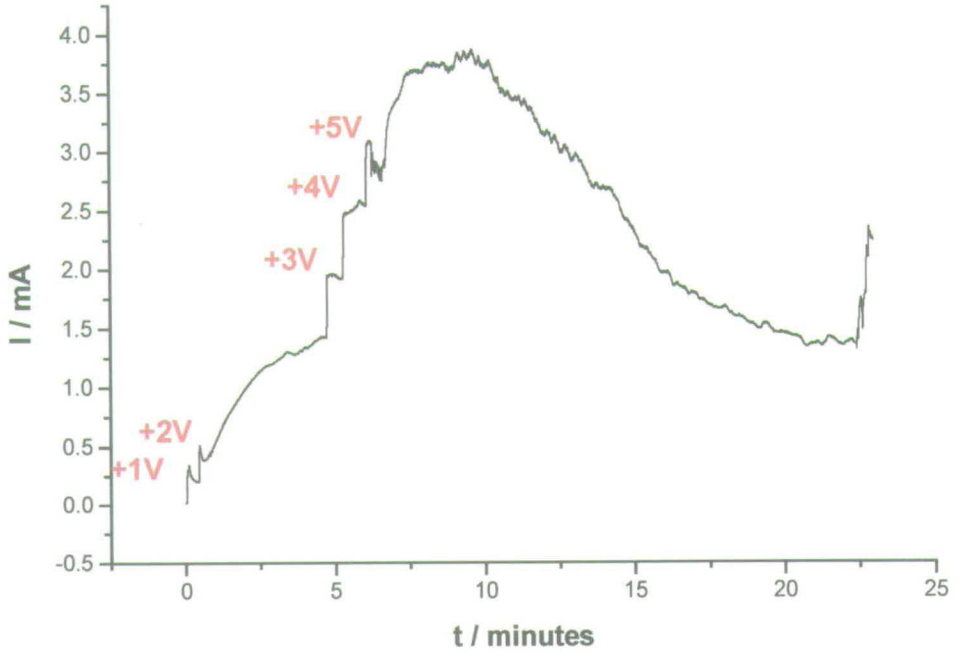

Figure 6.3: Current-time transient for the electrochemical modification of aluminium

6.4.3 Iron

6.4.3.1 Stripping of Oxide Layer

Like aluminium, the cleaning of the iron electrode did not progress in the same manner as for the other metals. A blue coloration (indicative of ammonia-solvated electrons) was not observed at the working electrode on the sweep to negative potential. Similarly, a positive current was not observed on the positive sweep. There was no change in the cyclic voltammogram after 45 minutes of cycling.

6.4.3.2 Nitride Synthesis

6.4.3.2.a Experiment 1

In the first experiment electrochemical modification was initiated at +1.00 V, and the potential stepped in 0.50 or 1.00 V intervals to +5.00 V. The current-time transient during these changes is shown in *Figure 6.4*. The steady current at +5.00 V was approximately 3mA. A bronze-coloured solid was observed on the iron working electrode, and as the experiment progressed this became darker in colour, and eventually black. A total of 94C was passed and the resulting black solid was washed thoroughly with dry liquid ammonia and dried under a flow of nitrogen.

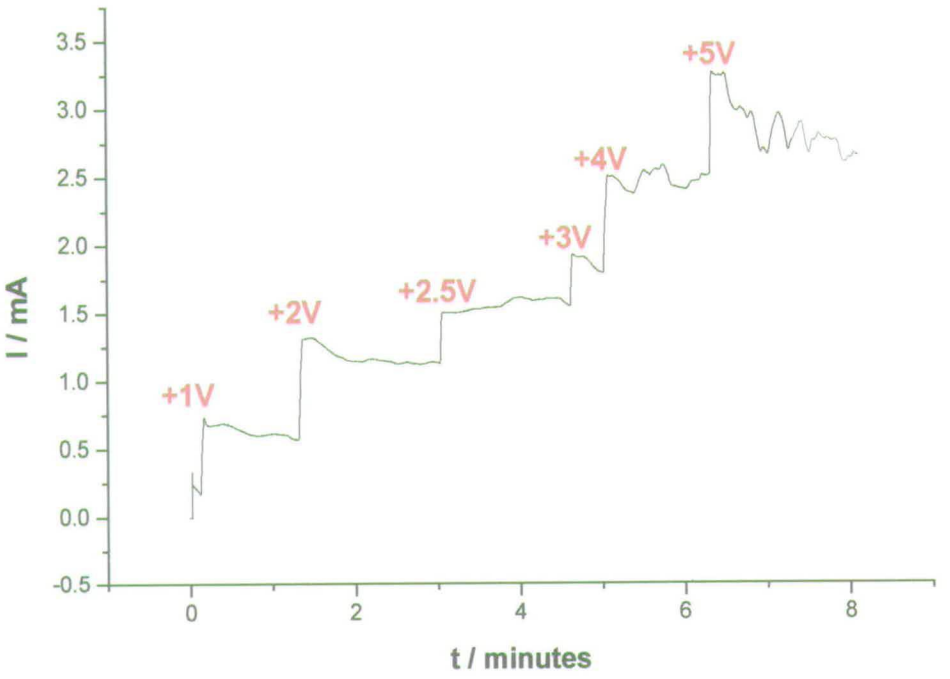

Figure 6.4: Current-time transient for the electrochemical modification of iron in experiment 1

6.4.3.2.b Experiment 2

This second experiment was performed at a lower potential with the aim of producing a thin film sample suitable for XPS analysis. Electrochemical modification was initiated at +1.00 V. The steady current at this potential was 0.4mA after initial decay. The potential was then increased to +2.00 V and then decreased to +1.50 V to keep the current steady. The steady current at +1.50 V was 0.4mA. *Figure 6.5* shows the current-time transient during the first part of the experiment. A total of 3C of charge was passed and an even, gold-coloured film was observed on the iron working electrode. On removal from the electrochemical cell, the electrode was washed with distilled water, acetone and dried in a flow of nitrogen.

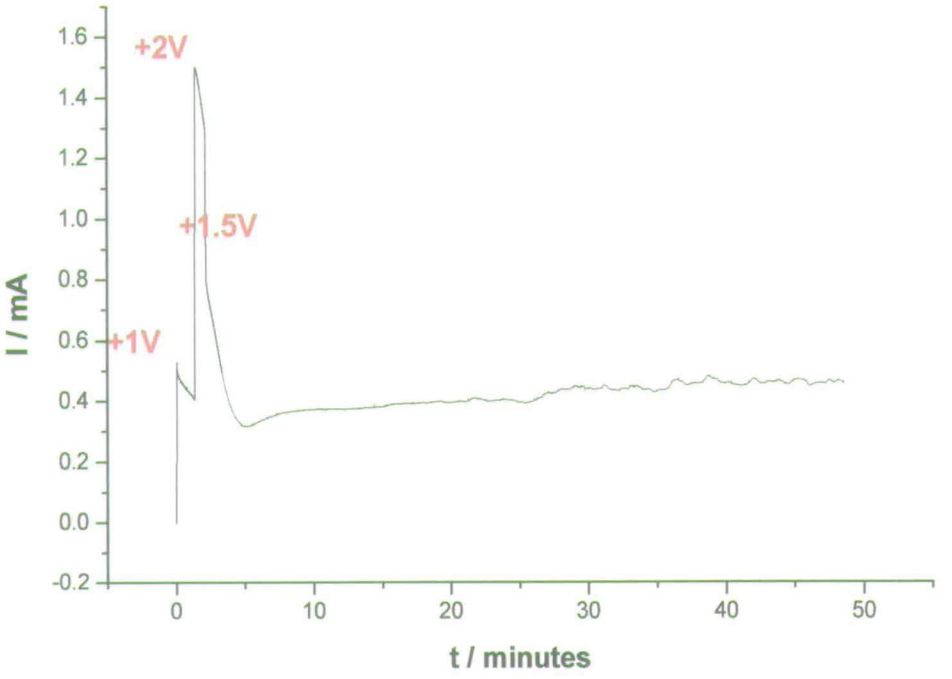

Figure 6.5: Current-time transient for the electrochemical modification of iron in experiment 2

6.5 Characterisation of Tantalum, Aluminium and Iron Nitrides

6.5.1 Tantalum

6.5.1.1 Transmission Electron Microscopy (TEM) - Electron Diffraction

The yellow-orange solid produced at the tantalum electrode was mounted in epoxy resin and ion-thinned so as to be suitable for viewing in the TEM. *Figure 6.6* shows two such images of the solid. *Figure 6.6a* shows the edge of one of the 'tendrils' observed to be growing from the edge of the electrode. These are similar to the titanium nitride particles observed by SEM (see *section 4.4.2*). It is possible that such a product has grown perpendicular to the electrode by the successive nitriding of the surface followed by exfoliation of layers of product, to reveal further, reactive metallic surfaces. This might explain the fringing observed on the edges of the tendril. *Figure 6.6b* shows some very small (approximately 10-50nm) spherical and tubular particles suspended in the epoxy resin close to regions of bulk powder.

Figure 6.7 shows the electron diffraction pattern obtained from one of the small particles as seen in *Figure 6.6b*. This consists of a pattern of rings containing bright spots, indicating the presence of some nanocrystalline material. The separation of the rings corresponds to d-spacings as listed in *Table 6.1*. These are compared with the nearest d-spacings of several known phases of tantalum nitrides and oxides [58-64] generated using the program DRAGON between 0 and 80° 2θ which calculates diffraction patterns based on unit cell parameters [65]. The lattice parameters of these known phases are shown in *Table 6.2*. This program lists all the reflections that would be observed by X-ray powder diffraction, removing those which are extinct due to general space group symmetry (see *section 2.6*).

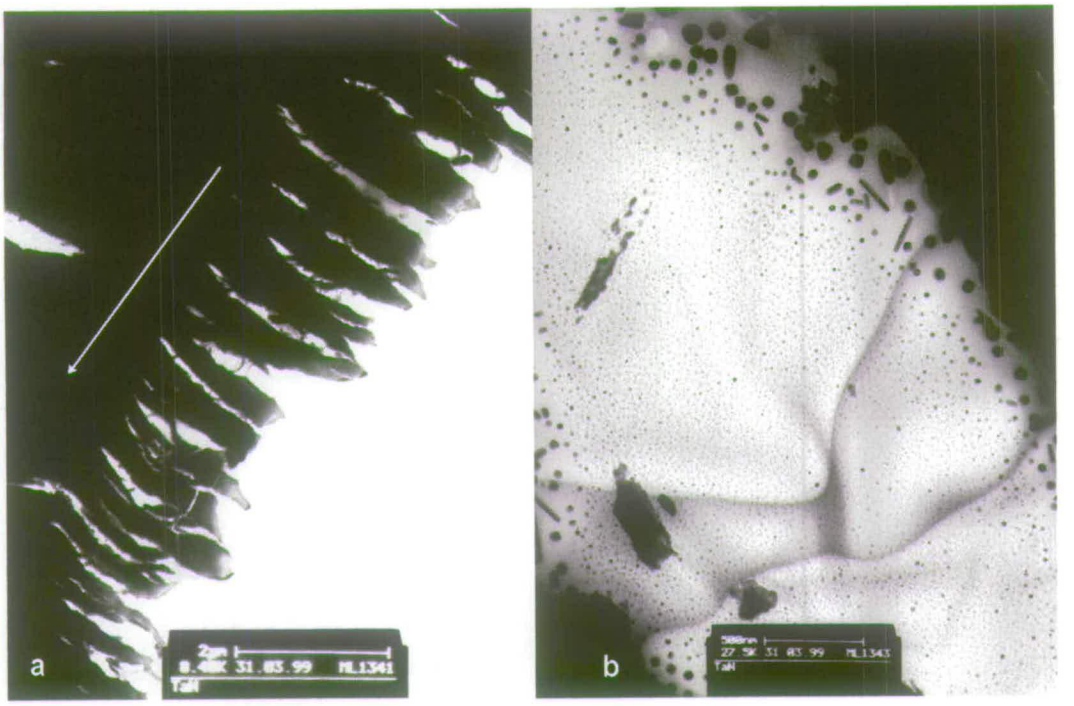

Figure 6.6: TEM images of material produced at tantalum electrode (**a**) edge of 'tendril' (the white arrow indicates the direction of growth), (**b**) smaller particles

The d-spacings obtained from electron diffraction of the sample match well with those of tetragonal Ta_3N_5 and TaO_2. These two materials cannot be differentiated by electron diffraction on the limited number of reflections observed in this experiment. Thus it is possible that the pattern represents diffraction from either (a) Ta_3N_5, (b) TaO_2 or Ta_2O_5, or (c) a mixture of Ta_3N_5 and TaO_2 or Ta_2O_5, with any formation of the oxide occurring during the post-processing of the very small particles. It seems unlikely that TaO_2 would be formed from Ta_3N_5 as this would involve reduction of tantalum. The formation of Ta_2O_5 from Ta_3N_5 is more likely.

Figure 6.7: Electron diffraction pattern of material produced at tantalum electrode

6.5.1.2 Raman Spectroscopy

Figure 6.8 shows the Raman spectra obtained from the gold-coloured tantalum electrode after electrochemical modification, and the bulk yellow-orange powder collected. The two spectra are largely similar, although the scattering intensity of the spectrum obtained from the powder is greater. The spectra are dominated by an intense peak at 530cm^{-1} with weaker peaks visible at 241, 456, 532, 573 and 775cm^{-1}. A search of the literature found no published Raman spectra of tantalum nitride. The Raman spectrum of Ta_2O_5 powder has been recorded by Yeung *et al* [66] and by Gardiner *et al* [67] and shows a sharp peak at 250cm^{-1} and broad peaks at 475, 620, 710 and 840cm^{-1}. This is clearly very different from the one obtained from the electrochemical nitridation and rules out formation of Ta_2O_5 during post-processing. Since

Ta_2O_5 would be expected to be the ultimate product of reaction between Ta_3N_5 and oxygen, the Raman spectra suggest that reaction of Ta_3N_5 to form oxides is not occuring. Hence this lends support to the electron diffraction study suggesting that the reaction product isTa_3N_5.

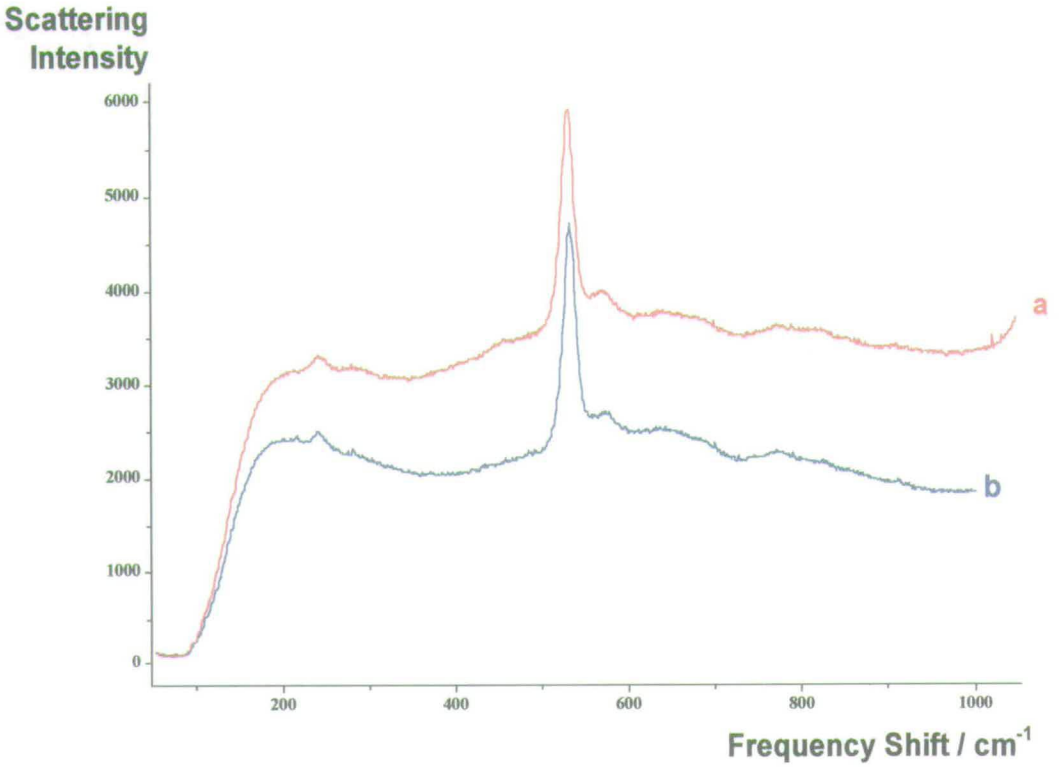

Figure 6.8: Raman spectra of (**a**) the electrochemically produced powder and (**b**) the electrochemically produced film

ED	Hexagonal ε-TaN		Cubic TaN		Cubic δ-TaN		Hexagonal Ta_2N		Tetragonal Ta_3N_5		Ta_4N_5		Hexagonal Ta_5N_6		Ta_2O		TaO_2		Ta_2O_5 (tantite)	
2.05	1.94	111	2.16	200	2.05	101	-	-	2.05 2.05 2.05	331 500 430	2.04	102	2.06	202	2.01	311	2.04	003	2.05	303
1.79	1.78	201	1.77	211	1.68	111	1.80	102	1.79 1.79	212 511	1.81	202	1.83	114	1.79	321	1.79	323	1.79	513
1.27	-		-	-	1.29	102	1.27	201	1.27 1.27 1.27	731 810 740	1.27	520	1.28 1.28 1.26	117 221 222	1.29	511 333	1.27 1.27 1.27	534 823 951	-	-
1.06	-		-	-	-	-	-	-	-	-	-	-	-	-	-	-	-	-	-	-

Table 6.1: Experimental d-spacings (± 0.02 Å) from electron diffraction compared with the closest d-spacings (in Å) and hkl values from known tantalum nitrides and oxides. The figures in red have a good match with the experimental result.

Material	a	b	c	Reference
Hexagonal ε-TaN	5.196	= a	2.911	[58]
Cubic TaN	4.329	= a	= a	[59]
Cubic δ-TaN	2.925	= a	2.876	[59]
Hexagonal Ta_2N	3.0420	= a	4.9230	[59]
Tetragonal Ta_3N_5	3.893	= a	10.264	[60]
Ta_4N_5	6.831	= a	4.269	[61]
Hexagonal Ta_5N_6	5.176	= a	10.353	[61]
Ta_2O	6.68	= a	= a	[62]
TaO_2	13.32	= a	6.12	[63]
Ta_2O_5 (tantite)	43.997	3.894	6.209	[64]

Table 6.2: Lattice parameters (in Å) of some known tantalum nitrides and oxides

6.5.1.3 Scanning Electron Microscopy (SEM)

Figure 6.9 Shows an SEM image of the tantalum electrode after electrochemical modification. The circular growths are the remains of the yellow-orange 'tendrils' observed forming on the electrode. Many of these have fallen off to form the bulk sample of powder. The tendrils are of variable size, ranging between 100-300μm diameter. This growth pattern suggests that a finite number of nucleation sites are generated on the electrode surface during nitridation, and the growth of these to form tendrils as the experiment progresses. This is in contrast to the formation of many nucleation sites eventually leading to the formation of a coherent film.

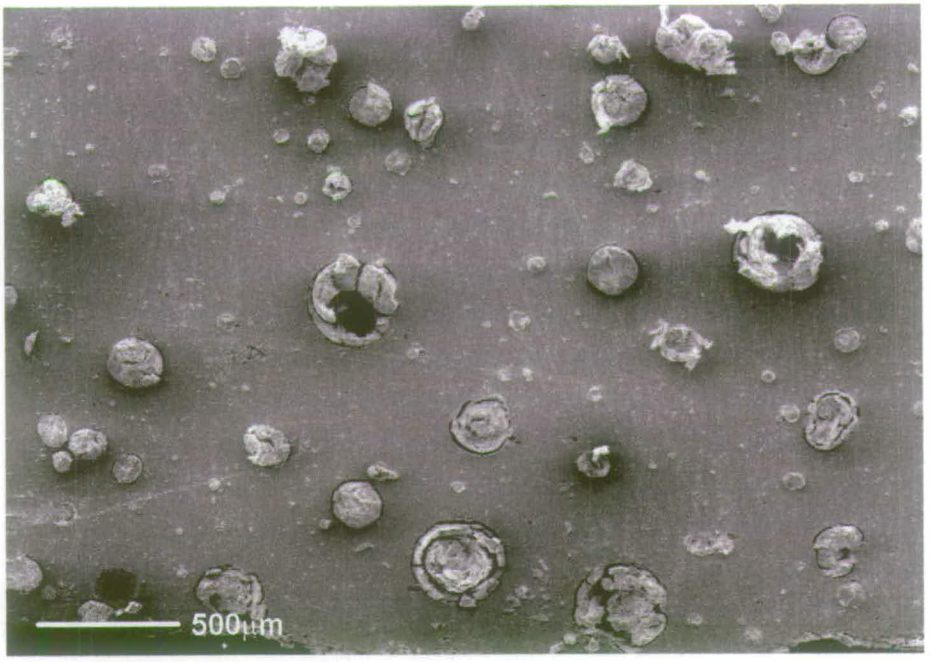

Figure 6.9: SEM image of the electrochemically modified tantalum electrode

6.5.2 Aluminium

6.5.2.1 Transmission Electron Microscopy (TEM) - Electron Diffraction

Figure 6.10a shows a TEM image of the powder formed at the aluminium electrode mounted in epoxy resin. The material does not appear to have any regular particle morphology. The electron diffraction pattern shows that the material is amorphous (*Figure 6.10b*). There are no rings or dots present in the pattern, indicating that the material is non-crystalline.

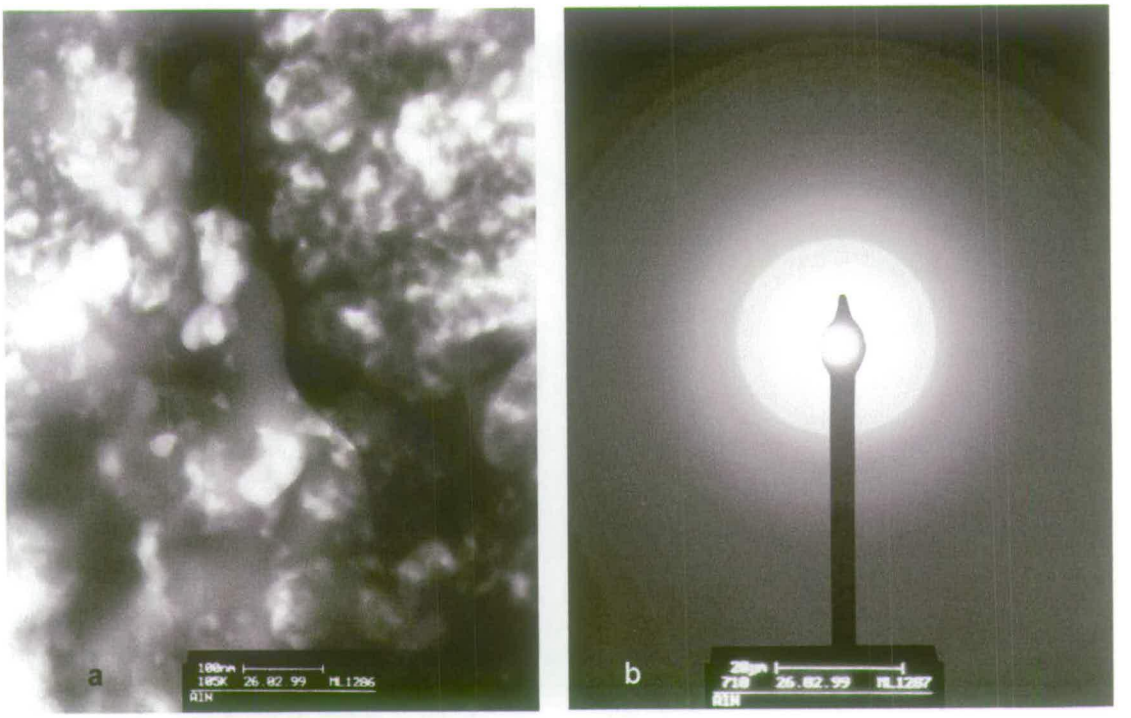

Figure 6.10: (a) TEM image and (b) electron diffraction pattern of material produced at aluminium electrode

6.5.3 Iron

6.5.3.1 X-Ray Photoelectron Spectroscopy (XPS)

Figures 6.11 and *6.12* show the wide scan spectra for the electrochemically produced film and iron metal, respectively. The sharp peaks superimposed on the background are due to photoemission from core levels. In both spectra, singlets due to oxygen and carbon 1s peaks are visible at 531eV and 285eV respectively. The carbon is a consequence of hydrocarbon vapour deposited on the sample from the high vacuum pump equipment, and the oxygen peak arises because of aerial oxidation of the surface after preparation. In both spectra, the Fe 2p doublet is visible at 725 and 711eV. The oxygen Auger lines are visible at 743eV ($KL_{23}L_{23}$) and 764eV (KL_1L_{23}) and the iron Auger lines at 553eV ($L_3M_{45}M_{45}$) and 608eV ($L_3M_{23}M_{45}$). It is difficult to discern peaks from nitrogen on this scale.

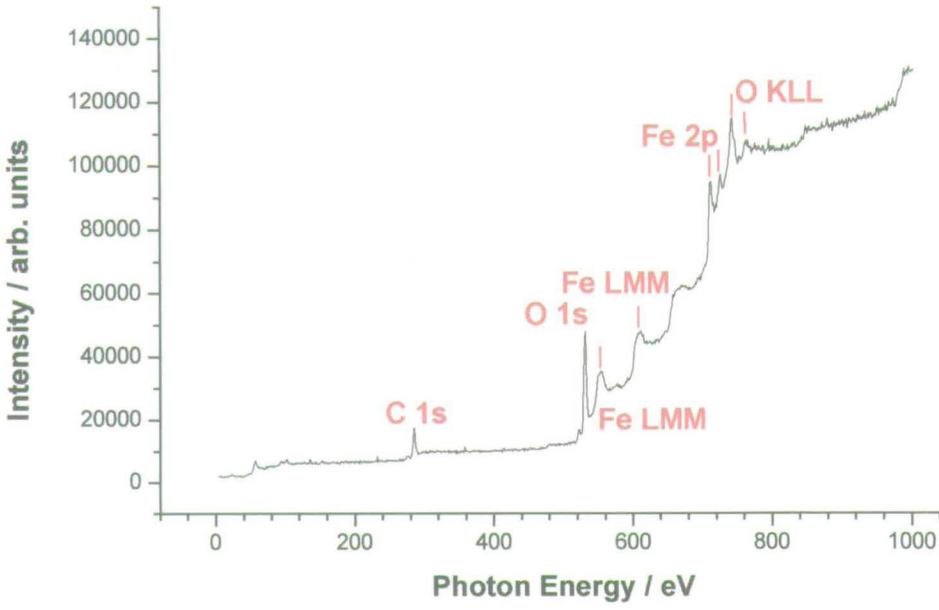

Figure 6.11: Wide scan XPS spectrum of the electrochemically produced film

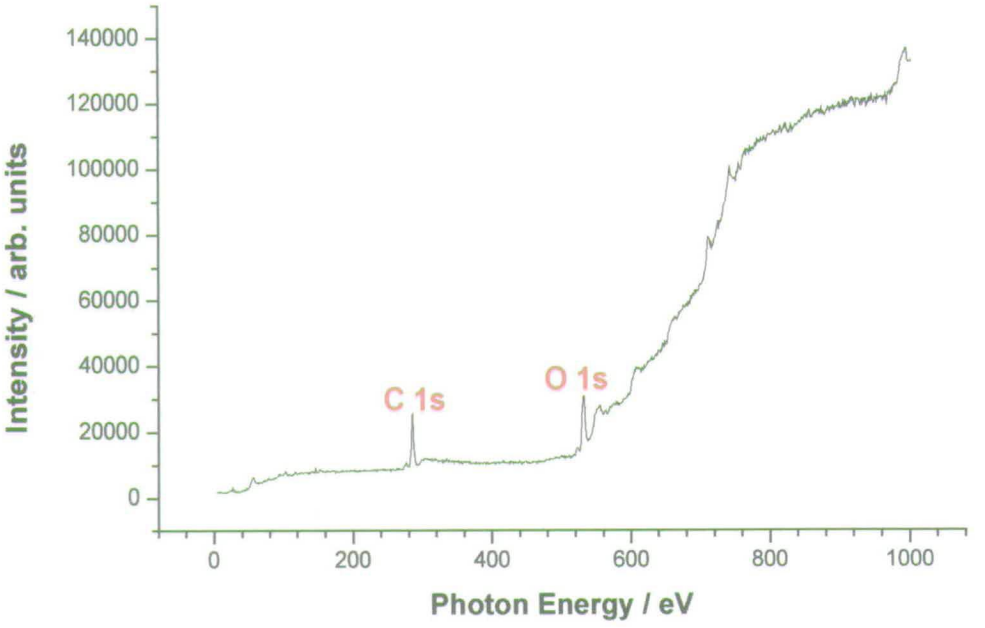

Figure 6.12: Wide scan XPS spectrum of iron metal

Figures 6.13-6.15 show the iron, oxygen and nitrogen narrow scan spectra respectively for the electrochemically produced film and iron metal.

The iron 2p spectrum obtained from the electrochemically produced film is split into a doublet with peaks at 711.0 ($2p_{3/2}$) and 724.7eV ($2p_{1/2}$) (*Figure 6.13*). The peak separation is 13.7eV. This is in concordance with the iron being present as Fe_2O_3 [68], and indicates that the surface of the film is oxidised. There is also an indication of a weak peak at approximately 720eV; this is likely to be the Fe $2p_{1/2}$ peak due to iron metal itself. The partner $2p_{3/2}$ peak would be observed at 706.75eV for metallic iron [68]. The peak at 743eV is due to the oxygen $KL_{23}L_{23}$ Auger transition. The spectrum obtained from iron metal is similar to that of the electrochemically produced film, although of lower intensity, indicating that the surface of the sample was also oxidised, but perhaps to a lesser extent.

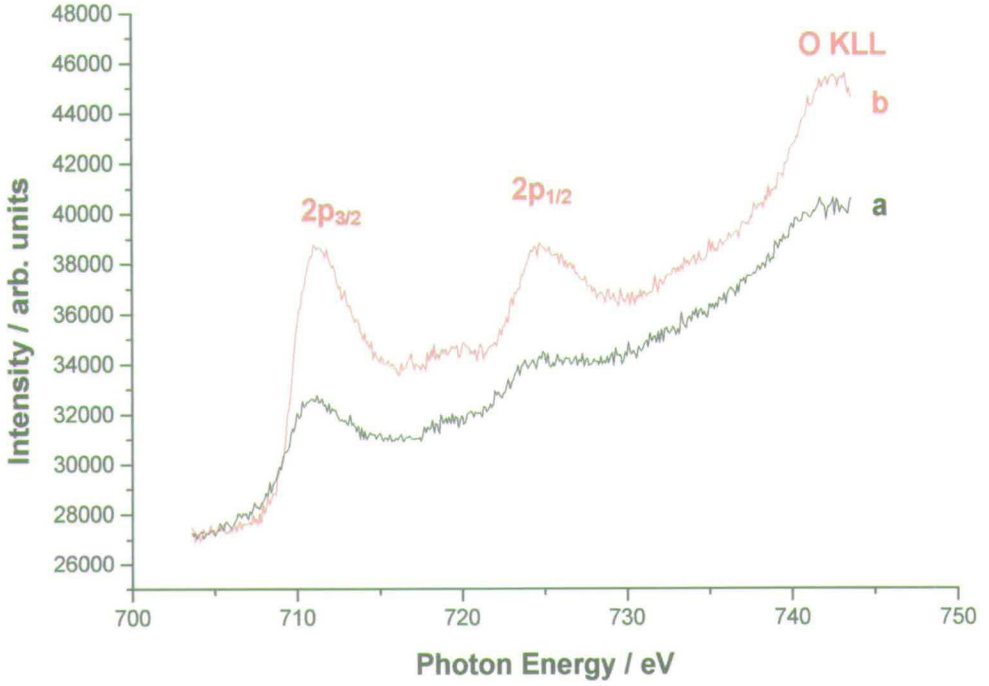

Figure 6.13: Iron 2p XPS spectra for (**a**) iron metal, and (**b**) the electrochemically produced film

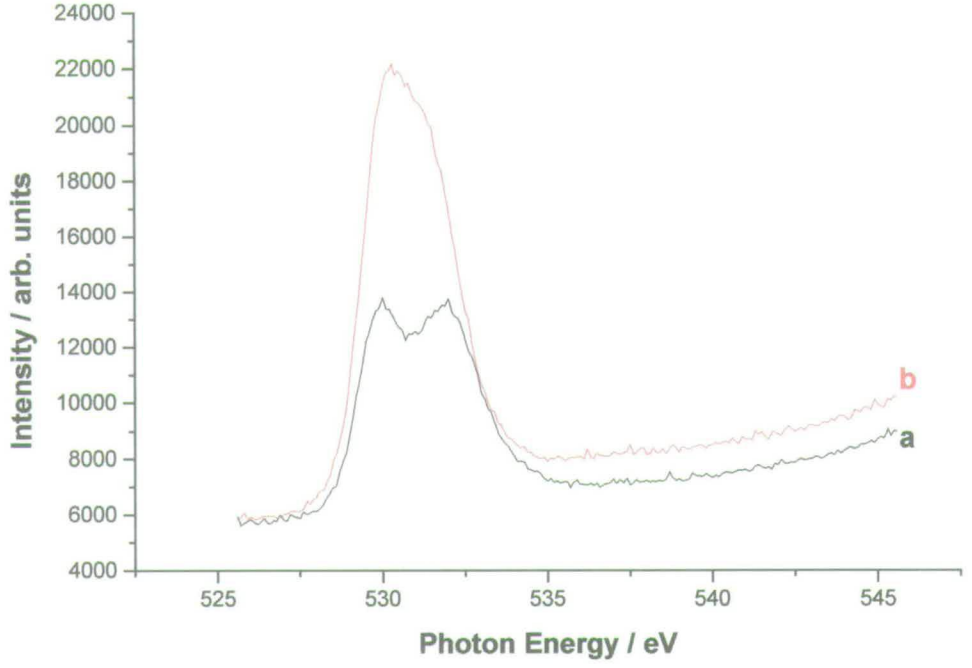

Figure 6.14: Oxygen 1s XPS spectra for (**a**) iron metal, and (**b**) the electrochemically produced film

The O 1s spectrum obtained from the electrochemically produced film contains an intense, broad singlet at 530.3eV (*Figure 6.14*). This confirms that the surface is heavily oxidised. Two peaks (at 530 and 532eV) can be observed in the spectrum obtained from the iron metal. This suggests that there are two types of oxygen present. Differences between hydroxide (OH^-) and oxide (O^{2-}) are usually recognised by an O 1s shift of 1 to 1.5eV [68]. This is line with the experimental observations; the peak at 530eV is likely to be due to oxide, and that at 532eV can be attributed to hydroxide (from atmospheric moisture). This has been observed before for the mixed hydroxide compound FeO(OH) by McIntyre *et al* and demonstrates the complex nature of the surface [69].

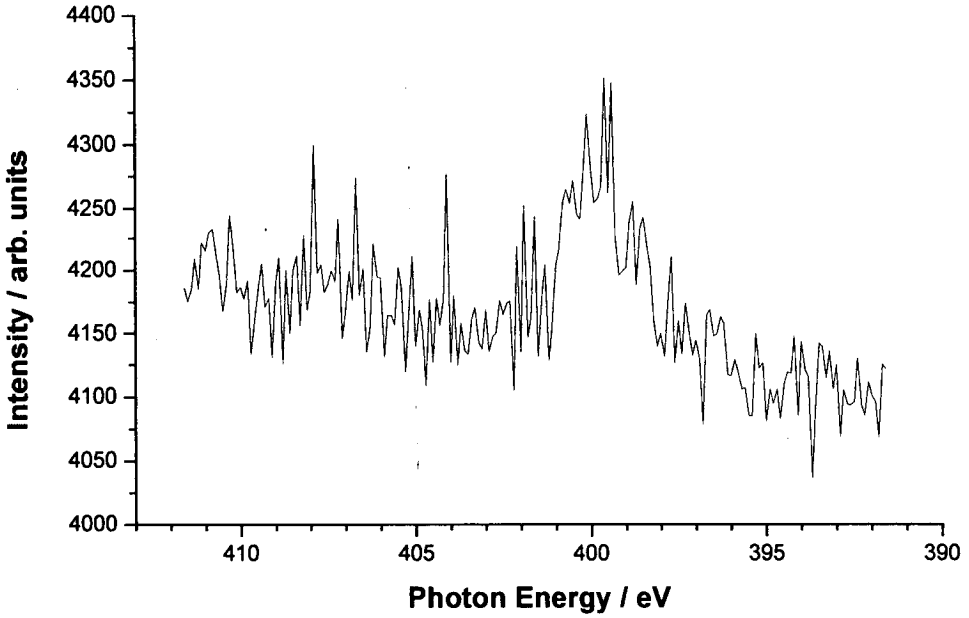

Figure 6.15: Nitrogen 1s XPS spectrum for the electrochemically produced film

The data collected in the N 1s spectral region for the electrochemically produced film have only a low signal-to-noise ratio. There is a suggestion that some nitrogen might be present (peak at approximately 400eV), and that this was difficult to detect due to the presence of

surface oxide. A sputtering experiment might elucidate the situation, although unfortunately time did not allow this to be carried out.

6.5.3.2 Transmission Electron Microscopy (TEM) - Electron Diffraction

Figure 6.16a shows a TEM image of the iron nitride powder mounted in epoxy resin. Particles and crystallites of 10-50nm dimensions can be observed. *Figure 6.16b* shows the electron diffraction pattern obtained from one of these particles. It consists of a pattern of rings and bright spots, indicative of a nanocrystalline material. These are compared with the nearest d-spacings of several known phases of iron nitrides and oxides (*Table 6.3*) [70-76] generated by the DRAGON program [65] between 0 and 80° 2θ. The lattice parameters of these known phases are shown in *Table 6.4*. None of the known materials can account for all of the rings observed in the electron diffraction pattern (many of which occur at low values of d). However, the three most intense rings correlate well with those of tetragonal Fe_8N, an iron-rich nitride phase. There is also a good match of these rings with those of Fe_2O_3 or Fe_3O_4, which would suggest a degree of post-processing aerial oxidation of the sample. The material may be a mixture of Fe_8N and Fe_2O_3 or Fe_3O_4. In addition the formation of an iron oxynitride species might account for the unassigned rings at low d-spacing.

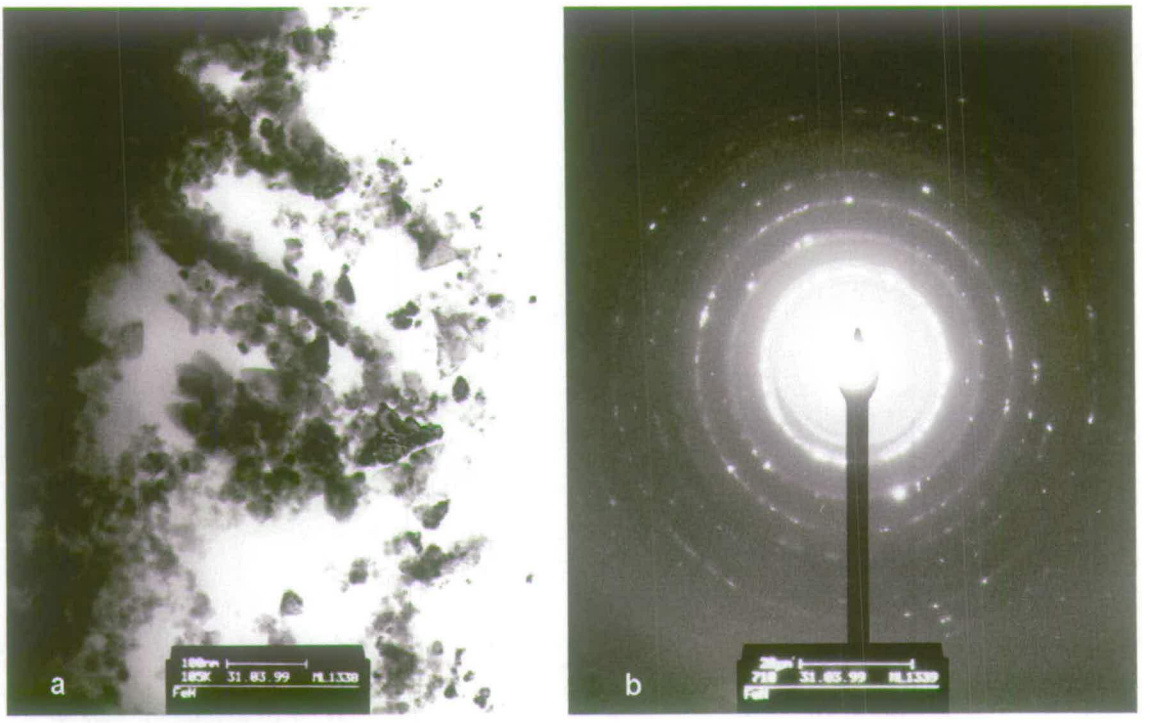

Figure 6.16: (**a**) TEM image and (**b**) electron diffraction pattern of the material produced at an iron electrode

6.5.3.3 Raman Spectroscopy

The powder produced by electrochemical nitridation and the thin film sample produced no Raman scattering.

ED	Hexagonal Fe_2N		Hexagonal ε-Fe_3N		γ-Fe_4N		Tetragonal Fe_8N		$Fe_2N_{0.94}$		FeO		Fe_2O_3		Fe_3O_4	
2.56	2.39	100	2.36	110	2.68	110	2.56	210	2.76	200	2.49	111	2.52	110	2.53	311
2.03	2.10	101	2.04	200	1.90	200	2.02	220	2.01	012	1.93	210	2.03	114	2.04 2.04	410 322
1.49	1.48	003	1.50	202	1.55	211	1.47	114	1.48	003	1.52	220	1.49	214	1.48	440
1.17	-	-	-	-	-	-	-	-	-	-	-	-	-	-	-	-
1.01	-	-	-	-	-	-	-	-	-	-	-	-	-	-	-	-
0.90	-	-	-	-	-	-	-	-	-	-	-	-	-	-	-	-
0.82	-	-	-	-	-	-	-	-	-	-	-	-	-	-	-	-
0.76	-	-	-	-	-	-	-	-	-	-	-	-	-	-	-	-

Table 6.3: Experimental d-spacings (± 0.02 Å) from electron diffraction compared with the closest d-spacings (in Å) and hkl values from known iron nitrides and oxides. The figures in red have a good match with the experimental result.

Material	a	b	c	Reference
Hexagonal Fe_2N	2.765	= a	4.41	[70]
Hexagonal ε-Fe_3N (siderazot)	4.7209	= a	4.4188	[71]
γ-Fe_4N (roaldite)	3.7900	= a	= a	[71]
Tetragonal Fe_8N	5.72	= a	6.29	[72]
$Fe_2N_{0.94}$	4.4373	5.5413	4.8429	[73]
FeO (wuestite)	4.3090	= a	= a	[74]
Fe_2O_3 (hematite)	5.0353	= a	13.7495	[75]
Fe_3O_4 (magnetite)	8.3941	= a	= a	[76]

Table 6.4: Lattice parameters (in Å) of some known iron nitrides and oxides

6.7 Summary, Conclusions and Further Work

This chapter described the initial attempts to synthesise tantalum, aluminium and iron nitrides *via* the electrochemical route previously applied to titanium, molybdenum and tungsten nitrides (*chapters 3-5*). Electrochemical modifications were performed at ambient temperature and 10 atms pressure.

The method devised for the reduction of the native oxide layer on the metal foils prior to nitridation was also implemented here. Cycling of the tantalum electrode between 0.00 V and a negative potential limit, always in excess of -1.50 V, resulted in a large negative current of the order of several mA. On the positive sweep, there was no associated oxidation peak, in contrast to the behaviour observed for titanium, molybdenum and tungsten. On continued cycling there was a slight increase in the effective potential window of the electrode. These final two observations suggest that the oxide layer on the tantalum electrode was in fact very thin. Attempts to strip the aluminium and iron electrodes of their native oxide layers did not appear to be successful; no blue ammonia-solvated electrons were observed, and there was no change in the CVs recorded. This demonstrates that for these metals the oxide layers are very strongly bound and resistant to reduction under the conditions of the experiment.

Nitridation of tantalum at +5.00 V (vs. Pt) led to the growth of yellow-orange 'tendrils' of up to several mm in length. On closer inspection by TEM, the tendril structures were composed of stacked sheets, suggesting that the product was formed by the successive erosion of layers from the electrode. TEM also showed the presence of tubular and spherical particles of 10-50nm dimensions. SEM of the electrode showed a pattern of a finite number of preferred

nucleation sites followed by growth into tendrils. Electron diffraction suggested that the identity of the particles was either Ta_3N_5 and/or TaO_2/Ta_2O_5. The oxides would have to be formed by the post-processing aerial oxidation of Ta_3N_5 as the synthetic method itself excluded all sources of oxygen and/or moisture. It was concluded that TaO_2 would be an unlikely reaction product as it would require reduction of tantalum in Ta_3N_5. Raman spectroscopy demonstrated that Ta_2O_5 had not been formed. The spectra from the electrode and powder were dominated by an intense peak at $530cm^{-1}$. No published Raman spectra of tantalum nitrides could be found. Through the use of electron diffraction and Raman results together, it was concluded that the nitridation product was Ta_3N_5. Unfortunately time did not allow an XPS study of the electrochemically modified tantalum electrodes to be performed. This experiment is required to confirm the presence of nitrogen in the product.

Nitridation of aluminium at +5.00 V (vs. Pt) led to the production of a white-grey solid which was found to be amorphous by electron diffraction. No other characterisation has yet been performed. Raman spectroscopy, energy dispersive X-ray spectroscopy (for positive nitrogen identification) and possibly conductivity tests could be employed to differentiate the material from the oxide. XPS studies would also be useful if a thin film of the material could be grown.

Nitridation of iron at +1.50 V (steady current 0.4mA) produced a gold-coloured film. XPS showed the surface to be contaminated by Fe_2O_3 which could be from the native oxide layer on the metal, or from post-processing oxidation. Nitrogen was also weakly detected at the surface suggesting a nitride phase, although measurements were hampered by a poor signal-to-noise ratio. Unfortunately time constraints did not allow a sputtering study to be performed. Nitridation was also performed at a higher potential of +5.00 V (vs. Pt) when the

steady current was 3mA. In this experiment a bronze then black powder was produced which was observed by TEM to be composed of particles and crystallites of 10-50nm dimensions. Electron diffraction could not differentiate between Fe_8N, Fe_2O_3 and Fe_3O_4, the latter two materials suggesting the onset of post-processing oxidation. However not all the rings in the diffraction pattern could be accounted for by these three materials. It is possible that an oxynitride phase was also produced through incomplete aerial oxidation. Previous experience showed that Raman spectroscopy was useful in the elucidation of the identity of nitridation products, but unfortunately the iron-containing materials did not scatter in this case. Perseverance might lead to the eventual collection of a spectrum. Other workers have employed Mossbauer spectroscopy to distinguish between various iron oxide and nitride phases [45], and this might also be an area to pursue. Magnetic measurements would also be interesting in order to see whether materials produced by this route could have applications in recording devices. The method could also be extended to steel to increase hardness, although electrochemical modification might lead to preferential nitridation of certain components of the alloy (Mo, Cr).

In order to produce thin films of all three materials it would be desirable to attempt synthesis in the original ambient pressure cell at -78°C. As it has been seen for titanium and molybdenum, these conditions tend to favour the formation of coherent films which are more stable towards aerial oxidation than the particles generated at ambient temperature. Such structures would provide a better chance of obtaining reliable characterisation for these materials.

6.8 Bibliography

[1] X. Chen, H. L. Frisch, A. E. Kaloyeros, B. Arkles and J. Sullivan, *J. Vac. Sci. Technol.* **B 17** (1), 182-185, 1999

[2] A. E. Kaloyeros, X. Chen, T. Stark. K. Kumar, S-C. Seo, G. G. Peterson, H. L. Frisch, B. Arkles and J. Sullivan, *J. Electrochem. Soc.*, **146** (1), 170-176, 1999

[3] N. N. Greenwood and A. Earnshaw, *'Chemistry of the Elements'* Pergamon Press, 1990

[4] C-H. Han, K-N. Cho, J-E. Oh, S-H. Paek, C-S. Park, S-I. Lee, M. Y. Lee and J. G. Lee, *Jpn. J. Appl. Phys.* **37** 2646-2651, 1998

[5] K-N. Cho, C-H. Han, K-B. Noh, J-E. Oh, , S-H. Paek, C-S. Park, S-I. Lee, M. Y. Lee and J. G. Lee, *Jpn. J. Appl. Phys.* **37**, 6502-6505, 1998

[6] Y. Sugiyama, S. Pac, Y. Takahashi and S. Motojima, *J. Electrochem. Soc.*, **122**, 1545, 1975

[7] H-T. Chiu and W. P. Chang, *J. Mater. Sci. Lett.*, **11**, 570, 1992

[8] M. H. Tsai, S. C. Sun, H-T. Chiu, C-E. Tsai and S-H. Chuang, *Appl. Phys. Lett.*, **67**, 1128, 1995

[9] M. H. Tsai, S. C. Sun, C-E. Tsai, S-H. Chuang and H-T. Chiu, *J. Appl. Phys.*, **79** (9), 6932-6938, 1996

[10] H-T. Chiu, S-H. Chuang, C-E. Tsai, G-H. Lee and S-M. Peng, *Polyhedron*, **17**, (13-14), 2187-2190, 1998

[11] R. M. Fix, R. G. Gordon and D. M. Hoffman, *Chem. Mater.*, **5**, 614, 1993

[12] K-H. Min, K-C. Chun and K-B. Kim, *J. Vac. Sci. Technol.*, **B 14** (5), 3263-3269, 1996

[13] X. Sun, E. Kolawa, J. S. Chen, J. S. Reid and M. A. Nicolet, *Thin Solid Films*, **236**, (1-2), 347-351, 1993

[14] K. Radhakrishnan, N. G. Ing and R. Gopalakrishnan, *Mat. Sci. Eng. B Solid State Materials for Advanced Technology*, **57**, (3), 224-227, 1999

[15] T. Mashimo, S. Tashiro, M. Nishida, K. Miyahara and E. Eto, *Physica B*, **239**, (1-2), 13-15, 1997

[16] T. Mashimo, S. Tashiro. T. Toya, M. Nishida, H. Yamazaki, S. Yamaya, K. Ohishi and Y. Syono, *J. Mat. Sci.*, **28**, (13), 3439-3443, 1993

[17] Y. Qin, L. Liu and L. Chen, *J. Alloys & Compounds*, **269**, (1-2), 238-240, 1998

[18] I. P. Parkin and A. T. Rowley, *Adv. Mater.*, **6**, (10), 780-782, 1994

[19] K. Uheda, M. Takahashi, H. Takizawa, T. Endo and M. Shimada, *Key Engineering Materials*, **159**, 53-58, 1999

[20] V. P. Kobyakov, *J. Mat. Sci.*,**32**, (16), 4347-4353, 1997

[21] M. Pouget and J. P. Lecompte, *J. European Ceramic Soc.*, **16**, (5), 521-527, 1996

[22] J. R. Park, S. W. Rhee and K. H. Lee, *J. Mat. Sci.*, **28**, (1), 57-64, 1993

[23] J. Y. Kim and P. N. Kumta, *Mat. Lett.* **34**, (3-6), 188-195, 1998

[24] D. C. Bradley, I. S. Harding, I. A. Maia and M. Motevalli, *J. Chem. Soc. Dalton Trans.* **17**, 2969-2979, 1997

[25] S. Koyama, H. Takeda, Y. Saito, Y. Sugahara and K. Kuroda, *J. Mat. Chem.*, **6**, (6), 1055-1058, 1996

[26] T. Stauden, G. Eichhorn, V. Cimalla, J. Pezoldt and G. Ecke, *Diamond & Related Materials*, **5**, (10), 1210-1213, 1996

[27] P. Wei, Y. Qing and C. Juan, *Thermochemica Acta*, **325**, (1), 89-93, 1999

[28] Y. W. Cho and J. A. Charles, *Mat. Sci. Tech.*, 7, (6), 495-504, 1991

[29] R. G. O'Donnell and M. B. Trigg, *Micron,* **25**, (6), 575-579, 1994

[30] T. Tsuchida, T. Hasegawa, T. Kitagawa and M. Inagaki, *J. Eur. Ceram. Soc.*, **17**, (15-16), 1793-1795, 1997

[31] A. Witek, M. Bockowski, A. Presz, M. Wroblewski, S. Krukowski, W. Wlosinski and K. Jablonski, *J. Mat. Sci.*, **33**, (13), 3321-3324, 1998

[32] G. J. Jiang, H. R. Zhuang, W. L. Li, F. Y. Wu and B. L. Zhang, *J. Inorg, Mat.* **13**, (1), 105-108, 1998

[33] T. Tsuchida, T. Kitagawa and M. Inagaki, *J. Mat. Sci.*, **32**, (19), 5123-5126, 1997

[34] J. M. Haussonne, J. Lostec, J. P. Bertot, L. Lostec and S. Sadou, *J. Physique III*, **3**, (4), 689-701, 1993

[35] T. Sato, K. Usuki, Y. Goto and A. Okuwaki, *Nippon Kagaku Kaishi*, **10**, 1432-1437, 1991

[36] Y. Watanabe and Y. Nakamura, *Ceramics International*, **24**, (6), 427-432, 1998

[37] Y. Watanabe, Y. Nakamura, S. Hirayama and Y. Naota, *Ceramics International*, **22**, (6), 509-513, 1996

[38] Y. Watanabe, Y. Nakamura, S. Hirayama and Y. Naota, *Surface & Coatings Technology*, **76**, (1-3), 337-340, 1995

[39] L. CalvoBarrio, A. PerezRodriguez, A. RomanoRodriguez, J. R. Morante and J. Montserrat, *Materials Science & Technology*, **11**, (11), 1187-1190, 1995

[40] H. C. Lee, K. Y. Lee, Y. J. Yong, J. Y. Lee and G. H. Kim, *Thin Solid Films*, **271**, (1-2), 50-55, 1995

[41] M. Kishi, M. Suzuki and K. Ogawa, *Jap. J. Appl. Phys.* **1**, (31), 12A, 3963-3968, 1992

[42] O. Yoshida, J. Ishikawa, K. Endo and N. Kitaori, *Jap. J. Appl. Phys.*, **36**, 777-780, 1987

[43] T. A. Yamamoto, K. Nishimaki, T. Harabe, K. Shiomi, T. Nakagawa and M. Katsura, *Nanostructured Materials*, **12**, (1-4), A SISI, 523-526, 1999

[44] S. K. Chen, S. Jin, G. W. Kammlott, T. H. Tiefel, D. W. Johnson, E. M. Gyorgy and J. *Magnetism & Magnetic Materials*, **110**, (1-2), 65-72, 1992

[45] Y. Koltypin, X. Cao, R. Prozorov, J. Balogh, D. Kaptas and A. Gedanken, *J. Mat. Chem.*, 7, (12), 2453-2456, 1997

[46] Y. Chen, T. Halstead and J. S. Williams, *Mat. Sci & Eng.* A, **206**, (1), 24-29, 1996

[47] W. A. Kaczmarek, B. W. Ninham and I. Onyszkiewicz, *J. Mat. Sci.*, **30**, (21), 5514-5521, 1995

[48] P. Y. Lee, T. R. Chen and T. S. Chin, *J. Alloys & Compounds*, **222**, 179-183, 1995

[49] X. H. Bao, R. M. Metzger and W. D. Doyle, *J. Appl. Phys.*, **73**, (10) 2B, 6734-6736, 1993

[50] S. Ohno, H. Okuyama, K. Honma, K. Takagi, T. Honjo and M. Ozawa, *J. Jap. Inst. Metals*, **59**, (4), 408-414, 1995

[51] X. Z. Ding, F. M. Zhang, J. S. Yan, H. L. Shen, X. Wang, X. H. Liu and D. F. Shen, *J. Appl. Phys.*, **82**, (10), 5154-5158, 1997

[52] B. Rauschenbach, *Nuclear Instruments & Methods in Physics Research* **B53**, 35-45, 1991

[53] H. Shinno, M. Uehara and K. Saito, *J. Mat. Sci.*, **32**, (9), 2255-2261, 1997

[54] H. Shinno and K. Saito, *J. Jap. Inst. Metals*, **60**, (8), 757-764, 1996

[55] A. M. Vredenberg, C. M. Perezmartin, J. S. Custer, D. O. Boerma, L. Dewit, F. W. Saris, N. M. Vanderpers, T. H. Dekeijser and E. J. Mittemeijer, *J. Mat. Res.*, 7, (10), 2689-2712, 1992

[56] A. M. Vredenberg, C. M. Perezmartin, J. S. Custer, D. O. Boerma, L. Dewit, F. W. Saris, N. M. Vanderpers, T. H. Dekeijser and E. J. Mittemeijer, *Surface & Coatings Technology*, **51**, (1-3), 79-86, 1992

[57] H. Tsubakino, M. Ando, A. Yamamoto, S. Fukumoto, N. Terasawa and T. Mitamura, *Mat. Chem & Phys.* **54**, (1-3), 301-304, 1998

[58] A. N. Christensen and B. Lebech, *Acta Crystallogr.*, B, **34**, 261-263, 1978

[59] D. Brown in '*Comprehensive Inorganic Chemistry*', Volume 3, Chapter 35, 553-622, Pergamon Press 1973

[60] J. Straehle, *Z. Anorg. Allg. Chem.*, **402**, 47-57, 1973

[61] A. Fontbonne and J. C. Gilles, *Revue Internationale des Hautes Temperatures et des* **6** 181-191, 1969

[62] S. Steeb and J. Renner, *J. Less-Common Met.*, **9**, 181-189, 1965

[63] V. I. Khitrova, V. V. Klechkovskaya and Z. G. Pinsker, *Kristallografiya*, **12**, 1044-1050, 1967

[64] H. U. Hummel, R. Fackler and P. Remmert, *Chem. Ber.*, **125**, 551-556, 1992

[65] K. Cockcroft, DRAGON Program, © 1998 Birkbeck College, available at: http://gordon.cryst.bbk.ac.uk/htbin/dragon.exe

[66] H. Y. H. Chan, C. G. Takoudis and M. J. Weaver, *J. Am. Chem. Soc.*, **121**, 9219-9220, 1999

[67] D. J. Gardiner, C. J. Littleton and K Strafford, *Comm. Eur. Communities, High Temp. Alloys*, (Rep) Eur. **11365**, 155-164, 1987

[68] Ed. D. Briggs and M. P. Seah, '*Practical Surface Analysis*', J. Wiley and Sons 1983

[69] N. S. McIntyre and D. G. Zetaruk, *Anal. Chem.* **49**, 1521, 1977

[70] Z. G. Pinsker and S. V. Kaverin, *Dokl. Akad. Nauk. SSSR*, **96**, 519-522, 1954

[71] H. Jacobs, D. Rechenbach and U. Zachwieja, *J. Alloys & Compounds*, **227**, (10-17), 1995

[72] C. J. Smithells, '*Crystal Structure*' in Metals Reference Book 1, Plenum Press, 4th Ed., 1967

[73] D. Rechenbach and H. Jacobs, *J. Alloys & Compounds*, **235**, 15-22, 1996

[74] A. H. Jay and K. W. Andrews, *J. Iron & Steel Inst.* **152**, 15-18, 1946

[75] H. Sawada, *Mater. Res. Bull.* **31**, (2), 141-146, 1996

[76] M. E. Fleet, *Acta Crystallogr.*, 917-920, 1981

Chapter 7:

Electrodeposition of Titanium Metal

7.1 Introduction [1]

Titanium is a silver-white ductile metal which has wide spread technological uses, often as a thin film coated onto a less expensive substrate. It has two phases; hexagonal α-Ti converts to the body-centred cubic form (β-Ti) at 885°C, which melts at 1730°C. Titanium has a high tensile strength, is lightweight and shows excellent cold working properties. It has seen use in aircraft construction, in the cladding of steel reactors, in pressure vessels, in load bearing and corrosion-resistant components and in electrical components.

The preparation of pure titanium metal is difficult owing to its high affinity for many other elements. Nitrogen, carbon and oxygen are particularly difficult to exclude in this respect, and make the metal brittle if present even in small quantities. Extraction of the metal from its compounds therefore requires high temperature and energy conditions. Conventional extraction techniques involve the reduction of titanium dioxide, but extraction with halides as starting materials give a higher purity product. More recently titanium has been obtained through the electrolysis of melts.

High operating temperatures preclude the deposition of titanium on thermally fragile substrates. Furthermore, pure titanium films cannot be formed on substrates which readily alloy with the metal at elevated temperatures. Titanium films also show poor adherence with substrates which have significantly different coefficients of thermal expansion. Even physical deposition methods, e.g. sputtering, which avoid these very high temperatures, suffer from these effects to some extent and have other disadvantages, namely, high capital costs for deposition equipment and difficulty in coating irregularly shaped objects.

7.1.1 Existing Methods for the Isolation of Pure Titanium

7.1.1.1 From Ore to Metal: Reduction of Titanium Dioxide

Crude titanium can be produced on heating titanium dioxide to 1000°C in a bomb with calcium metal (*equation 7.1*).

$$TiO_2 + 2\,Ca \rightarrow Ti + 2\,CaO \qquad (7.1)$$

The oxide must be free from silicon and water to prevent the production of silicides, and addition of some sodium to the calcium improves the process. Further heating with calcium chloride, barium chloride, calcium and calcium hydride then leads to the formation of malleable titanium.

The reaction between titanium dioxide and excess calcium hydride and hydrogen at 950-1075°C also yields titanium metal. After washing with dilute hydrochloric acid the resulting powder is 96% pure.

The reaction between titanium dioxide and warm 20-40% hydrofluoric acid followed by sodium or potassium hydroxide leads to the formation of the alkali metal fluorotitanates, M_2TiF_6. These react with sodium at 1000°C to form titanium and the alkali metal fluorides (e.g. *equation 7.2*)

$$K_2TiF_6 + 4\,Na \rightarrow Ti + 2\,KF + 4\,NaF \qquad (7.2)$$

The fluorides are removed from the reaction mixture by boiling in water. Unfortunately this also results in considerable oxidation of the titanium as well (up to 20%). The metal is then boiled with aqueous sodium hydroxide, and finally treated with cold, dilute hydrochloric acid.

7.1.1.2 Reduction of Titanium Tetrachloride

The reduction of titanium tetrachloride with sodium metal in a red hot steel bomb at 700-800°C produces titanium metal and sodium chloride (*equation 7.3*). Industrially this is known as the Degussa Process, and produces an alloy which is 98% Ti and 2% Fe.

$$TiCl_4 + 4\,Na \rightarrow Ti + 4\,NaCl \qquad \textbf{(7.3)}$$

The titanium is washed free from unreacted sodium and sodium chloride with alcohol, water and then dilute hydrochloric acid.

In the Kroll Process, magnesium replaces sodium as the reductant in the above reaction. The reaction vessel must be lined with molybdenum as titanium attacks iron at high temperatures. Titanium tetrachloride is slowly added to magnesium in the preheated reaction chamber, and the temperature is raised to 1050°C. At the end of the reaction, the vessel is cooled in an atmosphere of argon. Embedded magnesium chloride crystals are dissolved in water and dilute hydrochloric acid. The yield of the resulting porous titanium 'sponge' is 95.9%.

7.1.1.3 The Van Arkel and De Boer Process

This process can be used to prepare small quantities of pure titanium powder from more crude samples. Initially the crude titanium metal is degassed under vacuum by heating to 500°C. Iodine is then introduced at 200°C, and titanium tetraiodide is formed (*equation 7.4*).

$$Ti + 2\,I_2 \rightarrow TiI_4 \qquad \textbf{(7.4)}$$

The temperature is then raised to 550°C in a furnace, and the titanium tetraiodide reacts with more crude titanium to form titanium diiodide (*equation 7.5*).

$$TiI_4 + Ti \rightarrow 2\,TiI_2 \qquad \textbf{(7.5)}$$

As the vapour pressure of the volatile titanium diiodide builds up, deposition of titanium single crystals occurs on tungsten filaments which are heated to 1400°C and mounted within the reaction vessel.

7.1.1.4 Electrochemical Methods

Electrochemical methods provide attractive means for depositing titanium films owing to the high degree of control of reactivity that can be attained through relatively small changes in electrode potential. This avoids, in principle, the need for high temperatures. Furthermore, control of the current allows control of the rate of deposition and hence the morphology of the resulting film. Aqueous solutions are unsuitable media for electrodeposition because at potentials negative enough for titanium to be deposited hydrogen evolution occurs [2].

7.1.1.4.a Electrolysis of Molten Salts

Titanium may be obtained electrochemically in a number of different ways, but moisture must always be excluded from the melts employed. Titanium oxide or titanium oxide/carbide mixtures can be introduced into a calcium chloride melt at 700-850°C. Electrolysis results in deposition of crude titanium at the cathode.

Potassium fluorotitanate, K_2TiF_6 (discussed in *section 7.1.1.1*), can be dissolved in molten sodium chloride at above 800°C and electrolysed to produce very pure, coarsely crystalline titanium at the cathode and chlorine at the anode (*equation 7.6*). The melt becomes progressively richer in NaF and KF.

$$K_2TiF_6 + 4\,NaCl \rightarrow 2\,KF + 4\,NaF + Ti + 2\,Cl_2 \qquad \textbf{(7.6)}$$

By the use of an electrolysis cell divided by a sintered alumina diaphragm, titanium tetrachloride vapour can be dissolved into a melt of alkali/alkali-earth metal chloride in the cathode chamber. Lower chlorotitanates are formed electrochemically which later decompose to give titanium.

Anodic dissolution of titanium, obtained from crude starting material or titanium waste, in an alkali metal chloride melt can also be achieved. If a small amount of a low oxidation state titanium chloride is added to the melt, titanium can be recovered at the cathode.

Alkali halide melts are good solvent systems for titanium deposition as (a) they are able to dissolve appreciable amounts of titanium complexes, (b) have a wide electrochemical window

before solvent breakdown occurs, and (c) have high conductivity. The drawbacks with such systems are low cathode current efficiency, the product morphology (often dendritic or powdery), high viscosity, the corrosion of cell components and the heat balance of the cell. Titanium can exhibit multiple valency in these melts and this can lead to loss of power efficiency through side reactions. This can be overcome by introducing a diaphragm into the cell to separate certain ions from each other, while allowing selected mass transfer between regions [2].

7.1.1.4.b Lower Temperature Molten Salt Systems

The molten alkali-metal chlorides used as media for titanium metal electrodeposition have extremely high melting points (e.g. NaCl m.pt. = 803°C, KCl m.pt. = 772°C). The use of eutectic melts does lower this temperature significantly (NaCl-KCl eutectic m.pt. = 658°C). The melting point can be further lowered by increasing the size of the anion in the melt. The introduction of an equal amount of aluminium trichloride (m.pt. = 192°C) to sodium chloride forms a liquid which melts at 151°C. The electrochemistry of Ti(II) in acidic mixtures of NaCl-$AlCl_3$ in the temperature range 150-300°C has been investigated by Fung and Mamantov [3]. Ti(II) can be oxidised to Ti(IV) in two one-electron steps. In addition Stafford and Moffat have reported the electrodeposition of aluminium-titanium alloys containing up to 28 atom percent titanium from the $2AlCl_3$-NaCl melt [4]. At these high Ti(II) concentrations, electrodeposits with titanium stoichiometry up to Al_3Ti were accessible. Recently Seddon has described the use of some ionic solvents which are liquid at room temperature, for example 1-butylpyridinium chloride - aluminium(III) chloride (BupyCl-$AlCl_3$), and 1-ethyl-3-methylimidazolium chloride - aluminium(III) chloride (EmimCl-$AlCl_3$) [5]. Electrochemistry of Ti(IV) has been performed in basic BupyCl-$AlCl_3$ melts [6] and

more recently in the acidic EmimCl-$AlCl_3$ system [7]. No reduction to titanium metal was found, although this is unlikely in melts containing an appreciable activity of $AlCl_3$ as the standard electrode potential of titanium is close to that of aluminium. Ni(II), Co(II), Fe(II), Ag(I), Cu(I) and Sb(III) cations can all be reduced to the metal in the zero oxidation state from the BupyCl- $AlCl_3$ acidic melt [8-13]. It is possible that adaptation of these 'ionic liquids' may eventually make titanium deposition viable.

7.1.1.4.c Electrodeposition from Organic Solvent Systems

Most of the existing electrochemical methods described above operate under severe, high temperature conditions. The development of a solvent system which shared the advantages of molten salts and which operated at, or close to, room temperature would constitute a significant technological advance in this area. Polar organic solvents are in principle good media for the process, but the common ones tend to have poor electrochemical stability and high vapour pressure. Oxygen-donor solvents (for example tetrahydrofuran), also introduce the risk of the production of oxo-titanium compounds.

Abbott *et al* therefore turned their attention towards the use of non-polar, aromatic solvents [14]. These solvents have only a low relative permittivity/dielectric constant (ε_r = 2-4). This means that solubilities and conductivities are low and these effects must be compensated for by the use of elevated temperatures and addition of an inert electrolyte. However, they do have an electrochemical window of about 4V and sustain a large liquid range. The solvents of choice in their experiments were 15 mole % phenanthrene in anisole (at 120°C), 15 mole % phenanthrene in benzene (at 45°C) and molten naphthalene (at 120°C). The electrolyte was tetrabutyl ammonium fluoroborate, $TBABF_4$. The titanium precursors were formed *in situ* by

reaction of titanium(III or IV) chloride with primary and secondary amines or nitriles. Cyclic voltammetry of one of the titanium(III) species showed a one electron oxidation peak (at +0.5V vs. $Ag/AgBF_4$) on the positive sweep, and a reduction peak (at -1V vs. $Ag/AgBF_4$) of three times the current on the negative sweep. This is likely to be due to the three electron reduction of Ti(III) to Ti(0). Constant electrolysis at this potential did not however lead to the formation of a titanium metal deposit on the platinum working electrode. The authors propose that this was because it had been deposited in a finely divided form, causing rapid reaction on exposure to air. Titanium metal was obtained at this potential if a foreign metal was added. Both silver and copper salts were introduced to the solution, with the aim of modifying the kinetics of titanium nucleation. It was suggested that the co-deposited metal reduced the air sensitivity of small particles of titanium, although the exact mechanism was unclear.

Electrochemical deposition of titanium has been reported from a solution of $TiCl_4$ in DMSO/LiCl [15]. This resulted in the deposition of very thin Ti-containing films which oxidised to TiO_2 on exposure to air. Thicker films could be formed at very negative potentials (more negative than -2.8 V with respect to the saturated calomel electrode) which is close to the solvent limit and is likely to lead to significant contamination of the film. No assessment of the extent of film contamination was made.

This use of organic solvents represents a significant lowering of operating temperatures compared with the use of molten salts. However, the chemistry of these reported systems is quite complex, and the purity of the product is low.

7.1.1.4.d Electrodeposition from Liquid Ammonia

Taft and Barham have studied the electrodeposition of a series of metals (Pb, Ni, Cd, Cu, Ag, Zn, Cr, and Al), from their liquid ammonia solutions [16]. This work was undertaken in the attempt to improve the quality of the metallic deposits obtained from conventional aqueous systems. In most cases both anode and cathode were made of the metal under study, and the electrolyte was a salt of the metal which was soluble in liquid ammonia (usually chloride, nitrate or acetate). The morphology of the product was considered in terms of the current density, temperature, electrolyte concentration, and acidity. As yet, the electrodeposition of titanium from liquid ammonia solutions has not been successful.

7.2 Strategy

Having successfully designed a protocol for the synthesis of titanium nitride thin films on bulk titanium (*chapter 3*), the obvious challenge was to investigate ways of laying down thin films of titanium metal itself. It was envisaged that these films could be deposited on industrially relevant substrates (e.g. steel) and then electrochemically nitrided. The aim of this project therefore was to devise a method for the electrodeposition of high purity titanium on various metals at ambient temperatures. This required the design of a titanium-containing precursor which should be soluble in a non-aqueous solvent suitable for electrochemistry.

Thiocyanato complexes of Ti(III) and Ti(IV) have been previously reported and these have substantial solubilities in liquid ammonia and acetonitrile. Acetonitrile is a good electrochemical solvent with a wide window available for redox reactions. Schmitz-DuMont *et al* have prepared the potassium salt of *hexakis*(thiocyanato)titanate(III) in liquid ammonia from titanium(III) sulfate and potassium thiocyanate (*equation 7.7*) [17].

$$Ti_2(SO_4)_3 + 12\ KSCN \rightarrow 2\ K_3[Ti(SCN)_6].6\ NH_3 + 3\ K_2SO_4 \qquad (7.7)$$

As the reaction proceeded, the solution turned violet in colour and potassium sulfate precipitated. The product was isolated as green crystals, but was not extensively characterised.

Schmitz-DuMont and Ross have also prepared red potassium *hexakis*(thiocyanato)titanate(IV) in acetonitrile from titanium tetrachloride and an excess of potassium thiocyanate (*equation 7.8*) [18].

$$TiCl_4 + 6\,KSCN \rightarrow K_2[Ti(SCN)_6] + 4\,KCl \qquad (7.8)$$

During the reaction, the solution turned orange-yellow then dark red with the concurrent separation of potassium chloride. Red crystals of the complex were obtained which are soluble in ether, water and liquid ammonia, but again have not been extensively characterised.

It was thought that such complexes might be suitable as precursors for the electrodeposition of titanium metal from various solvents.

7.3 Synthesis and Characterisation of Titanium-Containing Precursors

7.3.1 Preparation and Purification

All manipulations were performed under dry nitrogen using Schlenk techniques, unless otherwise stated.

7.3.1.1 Synthesis of $M_3[Ti(SCN)_6]$, (M = K, NH_4)

In this work, the preparative route reported by Schmitz-DuMont *et al* (see *section 7.2*), has been simplified by the use of titanium(III) chloride and potassium thiocyanate as starting materials as in *equation 7.9*. This was because titanium(III) sulfate is difficult to synthesise in high purity.

$$TiCl_3 + 6\,KSCN \rightarrow K_3[Ti(SCN)_6] + 3\,KCl \qquad (7.9)$$

Potassium thiocyanate (Aldrich) was dried until free from water of crystallisation (dry weight 3.76g, 38.7 mmol) on a high vacuum line by heating to approximately 150°C. Liquid ammonia (BOC, *ca.* 20 cm^3), which had been previously dried over potassium and distilled under vacuum, was added *via* a cannula to the KSCN, and the solution stirred to aid dissolution. Titanium(III) chloride (Aldrich, 0.5g, 3.24 mmol), was loaded into a Schlenk tube in a nitrogen-filled dry box. Dry liquid ammonia (*ca.* 20 cm^3) was added *via* a cannula to the titanium(III) chloride and stirred to form a green-grey suspension. The KSCN solution was then transferred *via* a cannula to the $TiCl_3$ suspension with stirring at -78°C. After 4 hours

the deep violet solution was warmed to room temperature and the ammonia was allowed to evaporate to produce a dark green solid. This green solid was insoluble in water but soluble in dry acetonitrile, dry tetrahydrofuran (Prolabo, dried by distillation from CaH_2) and the ionic liquid BmimSCN (see section *7.3.3*). Dry tetrahydrofuran was added, and the dark purple solution was filtered to remove KCl and excess KSCN solids. On removing the tetrahydrofuran by evaporation under reduced pressure, a dark purple solid was produced.

The product was also prepared directly from the reagents in dry acetonitrile. In this preparation the potassium thiocyanate was dissolved in hot (70°C) acetonitrile and the solution was transferred to the $TiCl_3$-acetonitrile suspension at room temperature. The reaction mixture was stirred until it had cooled to room temperature when the precipitated KCl was filtered off leaving a bright violet solution. Note that any excess potassium thiocyanate is not removed using this method.

The ammonium salt $(NH_4)_3[Ti(SCN)_6]$ was also produced in a similar manner, by using dry NH_4SCN (Fisons) as a starting material. This complex was synthesised because NH_4SCN sublimes under reduced pressure, and this was considered to be one potential method for removing trace amounts of the excess precipitated salt from any deposited titanium film.

7.3.1.2 Synthesis of $K_2[Ti(SCN)_6]$

As the *hexakis*(thiocyanato)titanate(III) complex was found to be rather air sensitive (showing facile oxidation to the titanium(IV) analogue), it was thought that the thiocyanato complex of Ti(IV) itself might be a more convenient precursor for titanium electrodeposition in terms of ease of handling. The complex should show less tendency to react with moisture or oxygen.

The complex was prepared in acetonitrile according to *equation 7.8*. KSCN (dry weight 5.79g, 59.6 mmol) was dissolved in hot (70°C) acetonitrile. Titanium(IV) chloride (Aldrich, 1cm^3, 1.726g, 9.09 mmol) was added to the KSCN solution *via* syringe. The solution turned from yellow through orange to deep red, and was stirred until it reached room temperature. Removal of precipitated KCl by filtration yielded a deep red solution which on evaporation of acetonitrile gave red micro-crystals of the complex.

7.3.2 Analysis and Spectroscopy

7.3.2.1 Carbon, Hydrogen, Nitrogen (CHN) Analysis

Dry powder samples of $K_3[Ti(SCN)_6]$ prepared as in *section 7.3.1.1* from liquid ammonia and THF, then pumped dry under reduced pressure, were analysed for C, H and N content. Three milligram-scale samples were loaded and sealed in pre-weighed aluminium capsules in a nitrogen-filled dry box. CHN analysis of the $K_3[Ti(SCN)_6]$ solid gave 17.88 (14.03) % C, 2.20 (0) % H, and 19.92 (16.36) % N (expected values are shown in parentheses). The deviation of experimental analysis from the expected values suggests that the solid was not completely free from ammonia and perhaps tetrahydrofuran. The high nitrogen content could be accounted for as the capsules were packed in a nitrogen atmosphere.[1]

7.3.2.2 UV-Visible Spectroscopy

UV-visible spectra of the violet $K_3[Ti(SCN)_6]$ complex in both acetonitrile and THF were recorded. Owing to the air-sensitive nature of these solutions, samples were transferred under

[1] If the volume of the aluminium capsule is approximately 0.3cm^3, up to 0.4mg of nitrogen gas could be included from the dry box atmosphere.

dry nitrogen into sealed cuvettes *via* cannula. Blank spectra of the dry solvents were also recorded. The spectrum of the complex in both acetonitrile and THF (shown in *Figure 7.1*) showed a very wide absorption centred at *ca.* 530nm. This is most obvious in the acetonitrile case.

The Ti^{3+} cation has the d^1 electronic configuration, and in this complex has an octahedral crystal field splitting. Absorption of light causes the promotion of the single *d* electron from a lower T_{2g} orbital to a higher E_g orbital. The broad band in the UV-visible spectrum can be attributed to this metal-based transition. This absorption of light is in the yellow-green region of the visible spectrum, explaining the resulting violet colour of the solution. The transition appears rather asymmetric, perhaps with a shoulder visible on the low energy side [19]. The presence of two superimposed peaks in the spectrum of Ti^{3+} is usually explained in terms of the Jahn-Teller effect acting on the excited ^2E_g state. This effect acts to remove orbital degeneracy and is a result of the elongation along the z-axis of the complex to give a tetragonal ligand arrangement [20]. This term splits into two components corresponding to the $(d_{z2})^1$ and $(d_{x2-y2})^1$ configurations and causes two distinct excitations [19].

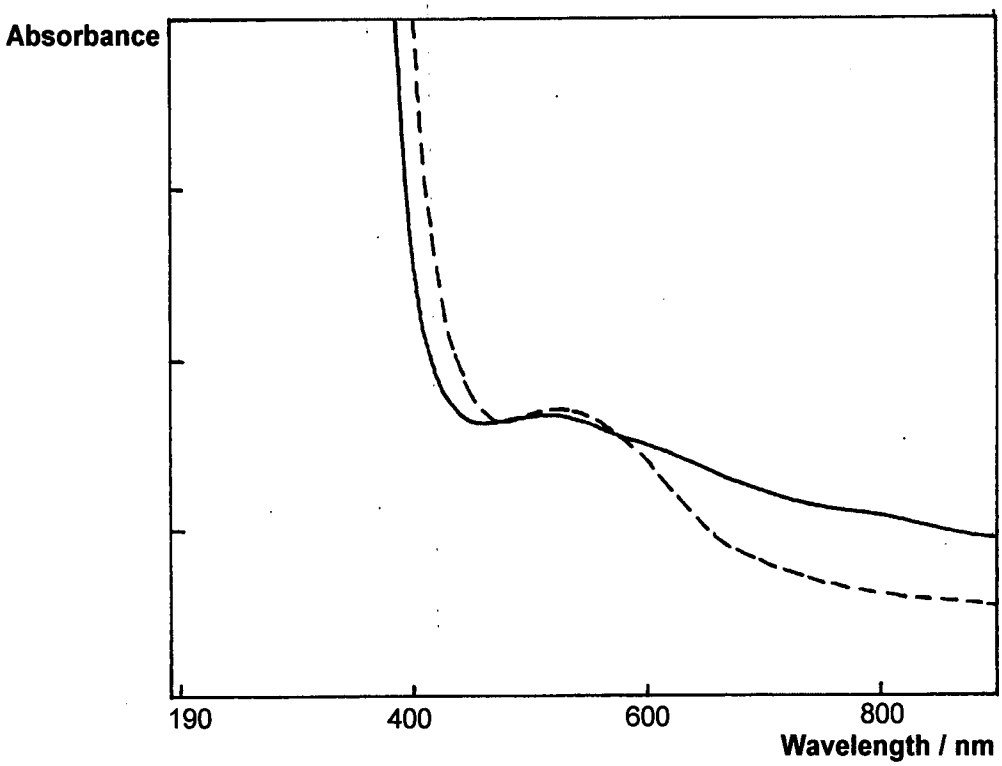

Figure 7.1: UV-visible spectra of $K_3[Ti(SCN)_6]$ complex in (**a**) acetonitrile (dashed line), and (**b**) THF (solid line)

A portion of the red-orange solution obtained after extensive electrolysis in experiment 1 (see *section 7.4.3.2.a*), was diluted with acetonitrile and transferred to a glass cuvette for UV-visible spectroscopy. The solution was yellow at lower concentration. The spectrum showed two intense absorptions at 292 and 414nm (*Figure 7.2a*). This species is likely to be the potassium hexathiocyanatotitanate(IV) complex described by Schmitz-DuMont and Ross [18], produced during electrolysis at the counter electrode by oxidation of the violet hexathiocyanatotitanate(III).

A portion of the original violet Ti(III) solution was then oxidised by bubbling oxygen gas through it. The solution turned red-orange, similar to the electrochemically produced solution. This was also diluted to give a yellow solution, and the UV-visible spectrum showed the same two absorptions as the electrochemically oxidised solution (*Figure 7.2b*).

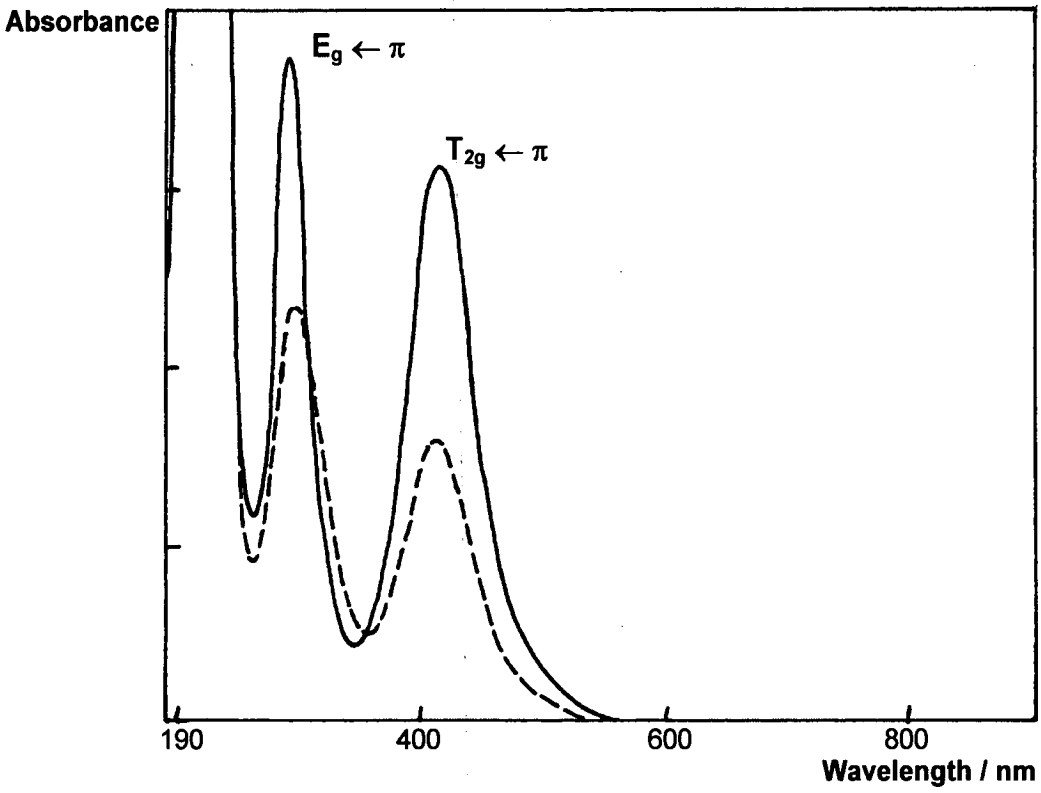

Figure 7.2: UV-visible spectra of red-orange solution in acetonitrile (**a**) produced after extensive electrolysis (dashed line), and (**b**) $K_3[Ti(SCN)_6]$ oxidised by O_2 (solid line)

The Ti^{4+} cation has a d^0 electronic configuration, and again in this complex has an octahedral crystal field splitting. The two peaks observed in the UV-visible spectrum of this complex are not due to metal-based transitions, but rather ligand-to-metal charge-transfer transitions. In this case these involve transfer of electrons from lower lying ligand-based π-orbitals to the higher energy empty titanium d-orbitals (T_{2g} and E_g levels). As there are two levels (owing to the octahedral field splitting) two transitions are possible, resulting in two spectral peaks.

The thiocyanate ion is known to co-ordinate to metals as an ambidentate ligand (in which either S or N is the donor atom). It is also less commonly found to act as a bidentate bridging ligand -SCN-, and even as a tridentate ligand >SCN-. The mode of monodentate bonding of

the SCN group is largely determined by the nature of the acceptor metal atom, i.e. 'hard' metals tend to be N-bonded whereas 'soft' metals tend to be S-bonded. Titanium is a typical 'hard' metal in that it forms its most stable complexes with ligands containing N, O, or F donor atoms which favour electrostatic bonding, and is itself electropositive. The thiocyanate group would certainly be expected to be N-bonded to titanium in the complex $K_x[Ti(SCN)_6]$, especially in a high relative permattivity solvent such as acetonitrile. Kinetic and solubility factors as well as relative thermodynamic stability are also sometimes an influence [21].

7.3.2.3 Crystal Growth

Attempts to obtain single crystals of the Ti(III) precursor from THF at a variety of temperatures were unsuccessful, as the solutions oxidised slowly, even when stored under nitrogen. Acetonitrile solutions of the Ti (III) and Ti(IV) precursors also failed to crystallise, since when small amounts of solvent were removed under reduced pressure, excess potassium thiocyanate began to precipitate. However in the synthesis of the Ti(IV) complex by Schmitz-DuMont and Ross [17] an equivalent amount of silver nitrate was added to the acetonitrile solution to remove this excess potassium thiocyanate as silver thiocyanate and potassium nitrate (both insoluble in acetonitrile). Crystals of the pure compound were then obtained after filtration. This approach was attempted, but without success.

7.4 Electrochemical Studies of the Thiocyanato Complexes and Characterisation of Electrodeposited Films

7.4.1 Set-up of Electrochemical Cell

Electrochemical experiments were performed at room temperature on approximately 15 millimolar solutions of the potassium or ammonium salts of the Ti(III) or Ti(IV) complexes in 200 cm^3 dry acetonitrile as required. The working electrode was copper wire or foil (Aldrich 0.1mm, 99.98%) or iron foil (Goodfellow 0.025mm, 99.5%). Copper was chosen as it was thought that it might promote adhesion of any atomic titanium formed at the surface, perhaps with the formation of an alloy. Copper-titanium binary alloys (up to 5 weight % Ti) are known to attain high strength through precipitation hardening. They have been considered as replacements for the highly toxic and expensive Cu-Be-Co alloys [22,23]. Iron was chosen as an industrially applicable substrate, drawing analogies with steel. The counter electrode was a platinum gauze wire (Johnson Matthey), of approximate area 2 cm^3, which was of sufficient area to ensure that the current was never limited by reaction at the counter electrode, and the pseudo-reference electrode was a polished platinum wire (Johnson Matthey). All potentials are quoted with respect to this pseudo-reference electrode. Ideally a well defined reference electrode should be used e.g. the standard hydrogen electrode, or a calomel electrode. Unfortunately these electrodes, whilst being very stable, may introduce small amounts of contaminant into the solution, which may in turn be incorporated into the deposited film. It was found that the platinum wire pseudo-reference electrode was stable for any given system, although clearly caution must be exercised when comparing with potentials measured in different systems.

7.4.2 Electrochemical Protocol

Electrochemical control was by means of a PP2 3-electrode potentiostat (Oxford Electrodes), and data were recorded using a Bryans 60000 x-y-t chart recorder (Advance Bryans), and later on a PC using in-house software written using the Visual Designer 3.0 package [24].

7.4.2.1 Cyclic Voltammetry

The electrochemistry of the solutions was explored by repeatedly sweeping the potential of the working electrode at a rate of $50mVs^{-1}$ between +1.00 V and -3.00 V. A variable sweep rate study (with rates 10, 20, 50 and $100mVs^{-1}$), was also performed in experiment 1. *Table 7.1* summarises the CV studies accomplished.

Experiment	Working Electrode	Cation in $M_y[Ti(SCN)_6]$	Oxidation State of Ti	Solvent
1	Cu	K	III	Acetonitrile
2	Cu	K	IV	Acetonitrile
3	Fe	K	III	Acetonitrile
4	Fe	NH_4	III	Acetonitrile

Table 7.1: Summary of the four CV studies performed

7.4.2.2 Electrodeposition

Electrodeposition took place between -1.00 V and -2.00 V, in the attempt to isolate bulk samples of titanium metal. 1kΩ (maximum current ~ 13mA) or 100kΩ (maximum current ~

130μA) current limiting resistors were used in the circuit in the attempt to limit the deposition current and modify film morphology. Care was taken to ensure that the solutions did not oxidise during electroplating by avoiding the production of the red Ti(IV) species capable of dissolving the copper electrode. *Table 7.2* summarises the details of the seven experiments performed.

7.4.3 $K_3[Ti(SCN)_6]$ solution with a copper working-electrode

7.4.3.1 Cyclic Voltammetry

A typical cyclic voltammogram of the Ti(III) complex is shown in *Figure 7.1*. The pair of redox peaks centred around -0.20 V can be attributed to the stripping (A, oxidation) and re-plating (B, reduction) of copper from the working-electrode. At approximately -1.00 V there is a small reduction peak (C), and at -1.60 V there is a larger reduction peak (D). There is also the beginning of a further reduction wave at -2.20 V (E). There are no significant re-oxidation peaks observed. The first of these reduction peaks at -1.00 V is attributed to the three-electron reduction of Ti(III) to Ti(0) and the production of titanium metal species on reactive sites of the copper surface. The peak at -1.60 V is attributed to the reduction of Ti(III) to Ti(0) at less reactive but more numerous sites on the copper surface. In support of this, it was found that continued cycling of the potential around -0.20 V to induce copper stripping and re-plating resulted in an increase in the size of the reduction peak at -1.00 V compared to the peak at -1.60 V. This stripping and re-plating results in the atomic reconstruction of the copper surface producing more active sites, potentially beneficial for titanium deposition. The wave at -2.20 V could also be due to a titanium reduction reaction,

but may also correspond to solvent breakdown. Electrodeposition performed at such a negative potential may lead to the incorporation of contaminants from the solvent into any film obtained.

The absence of any reoxidation peaks indicates that reduction is chemically irreversible and has resulted in the irreversible loss of the Ti(III) electroplating species. This is entirely consistent with the formation of a Ti(0) metal film.

The peak current of the reduction waves were found to be proportional to the square root of the voltage scan rate confirming that the reduction reaction involves diffusion and reaction of the Ti(III) solution species. This is because depletion of the reactant at the working-electrode is less marked during fast sweeps since there is a shorter reaction time. There is less time for the reactant to diffuse away from the electrode surface. This results in a thinner diffusion layer and therefore a steeper concentration gradient. Fick's first law states that the current reflects this concentration gradient of the reactant near the electrode [25].

7.4.3.2 Electrodeposition and Characterisation of Films

7.4.3.2.a Experiment 1

In experiment 1, constant potential electrodeposition was performed at -1V with a copper wire working electrode. After initial decay, the steady current passing with a 1kΩ resistor was approximately 0.3mA. After 20C of charge had been passed the electrode was removed from the cell and washed with water and acetone. A black coating could be seen on the wire. A new copper working electrode was connected and the solution electrolysed overnight at

Experiment	Working Electrode	Deposition Potential / V	Resistor used / kΩ	Charge passed / C	Appearance of Deposit	Characterisation
1	Cu wire	-1.00	1	20.0	Black coating	Chemical test, SEM-EDXS
2	Cu foil	-1.00	1	31.0	Silver-grey metallic film	SEM-EDXS
3	Cu foil	-2.00	1	11.4	black, powdery deposit	SEM-EDXS
4	Cu foil	-2.00	100	11.4	Black at edge, silver-coloured on face	SEM-EDXS, Powder XRD
5	Fe foil	-1.50	1	11.0	Loose grey film	SEM-EDXS
6	Fe foil / NH_4 salt	-1.00	1	25.0	Gold-coloured film	SEM-EDXS
7	Cu foil / bmimSCN solvent	-2.00	1	9.1	Very even, metallic film	SEM-EDXS

Table 7.2: Summary of the seven electrodeposition experiments performed on acetonitrile solutions of $K_3[Ti(SCN)_6]$, unless otherwise stated.

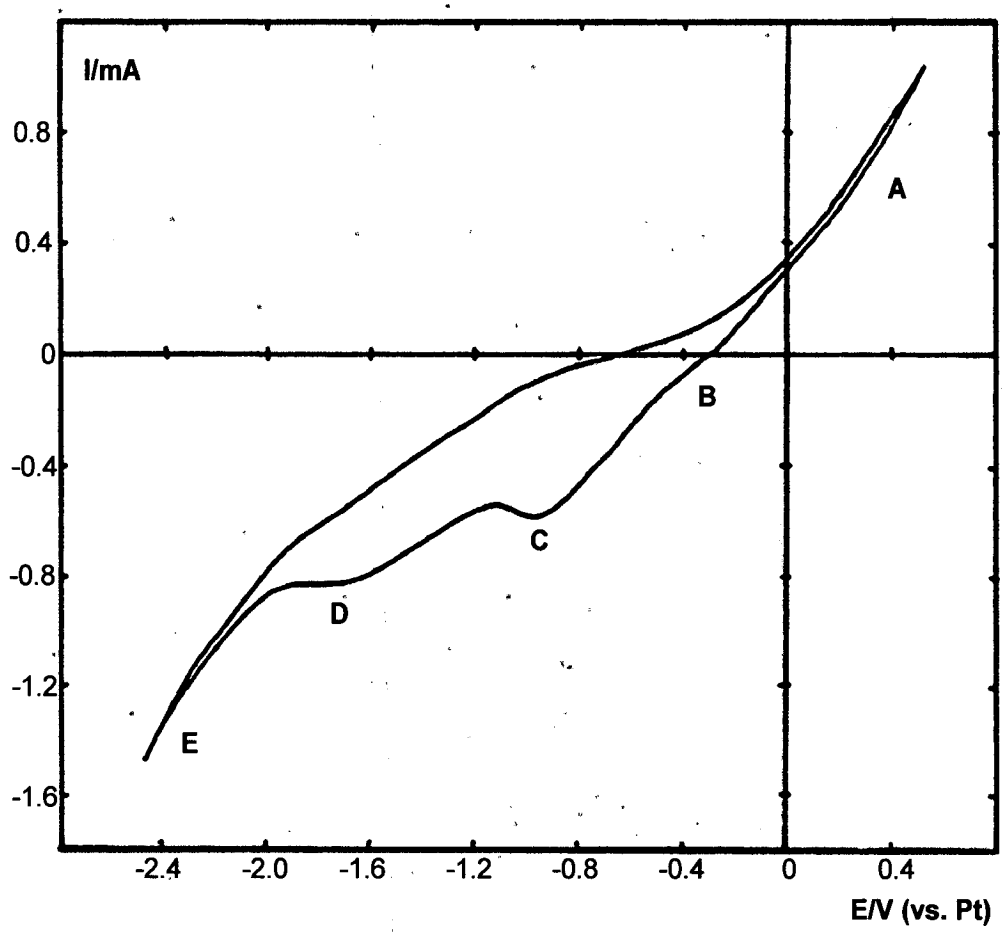

Figure 7.1: Cyclic Voltammogram of $K_3[Ti(SCN)_6]$ in acetonitrile using a Cu working-electrode

-1.00 V. By the morning, the violet solution had turned orange-red (this solution was analysed as in *section 7.3.2.2*).

After deposition, the copper wire was washed thoroughly with acetonitrile, water and then acetone to remove any precipitated electrolyte. A portion of the black deposit was scraped from the electrode and dissolved in boiling concentrated sulfuric acid. A yellow-orange solution formed, which was diluted with water. Addition of hydrogen peroxide caused the yellow colour to intensify, indicating a positive test for titanium [26]. Whilst this does not provide unequivocal evidence for the production of titanium metal, it does show that an insoluble titanium-containing solid has been deposited which might be titanium metal.

The deposit obtained was analysed by SEM-EDXS. *Figure 7.2* shows the EDX spectrum of a sample of copper foil. The two K lines of copper are clearly visible, and there are no other features in the spectrum which indicates that the starting material was pure.

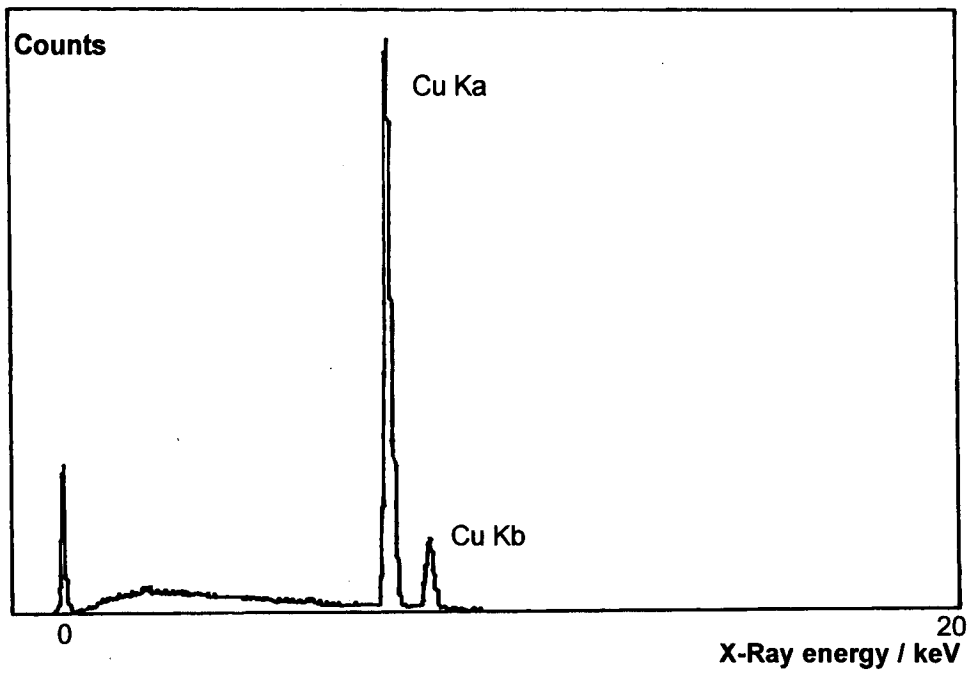

Figure 7.2: EDX spectrum of the copper foil starting material

Under the electron microscope, the black coating on the copper wire was clearly visible. A patchy film had been formed where the wire had been in solution (*Figure 7.3*). It is possible that this coating had been deposited uniformly, but when the electrode was removed from solution evaporation of solvent had induced cracking. The flakes are of approximately 50μm dimensions.

The energy dispersion spectrum of an area of one of these flakes showed only the two K lines due to titanium. Washing in water and acetone had removed any trace electrolyte residue, as peaks due to potassium, sulfur and chlorine were absent. Peaks due to copper were not observed, demonstrating that the film must be of the order of 3μm thick or greater, as the

analysing electron beam penetrates to approximately this depth. The deposit appears to be composed of titanium metal, although the possibility that oxygen, nitrogen or carbon are present cannot be dismissed.

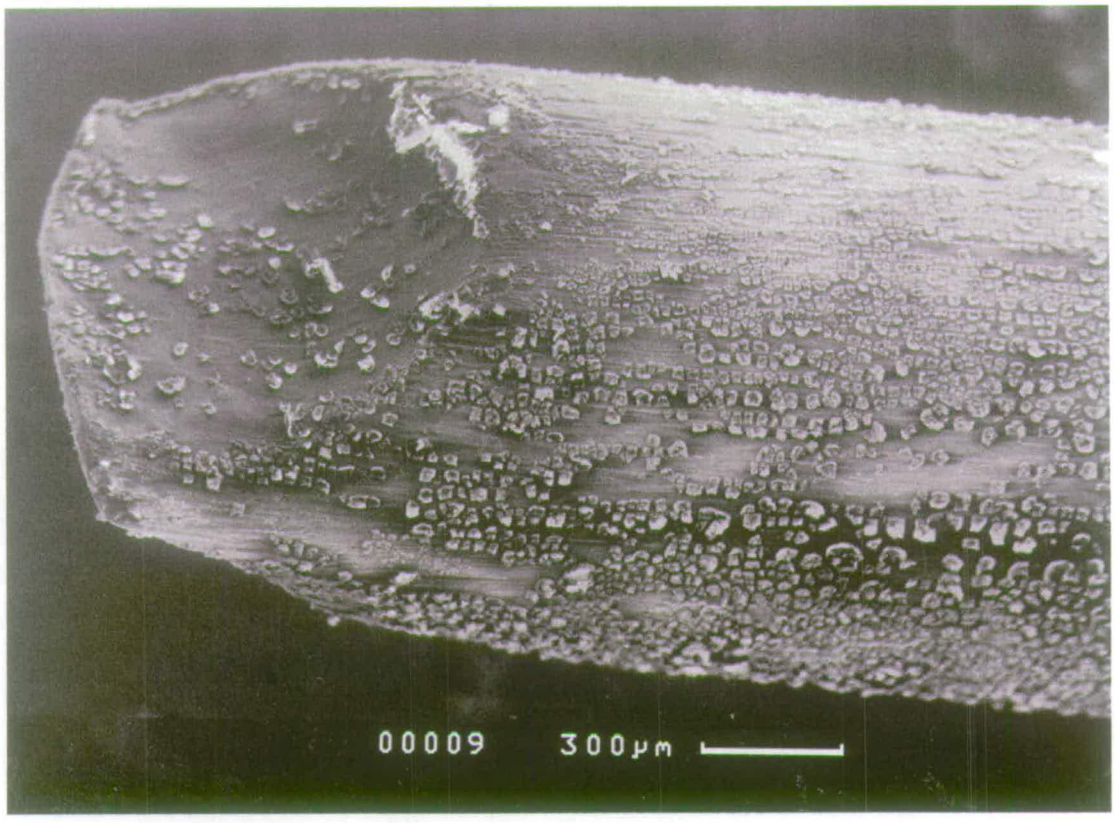

Figure 7.3: SEM image of titanium deposited at -1.00 V (vs. Pt) on a copper wire

7.4.3.2.b Experiment 2

Experiment 2 was performed at -1.00 V with a copper foil working electrode in the attempt to avoid the cracking of the film seen in the previous experiment. It was thought that a flat rather than a curved surface might be more conducive to this. After 31C of charge had been passed, a silver-grey metallic-looking film was obtained which was washed with acetonitrile, water and acetone. The SEM secondary electron image (shown in *Figure 7.4*) shows lines of

even, spherical particles which have nucleated in scratches on the copper foil. The particle size distribution is reasonably small with the average diameter at approximately 2μm.

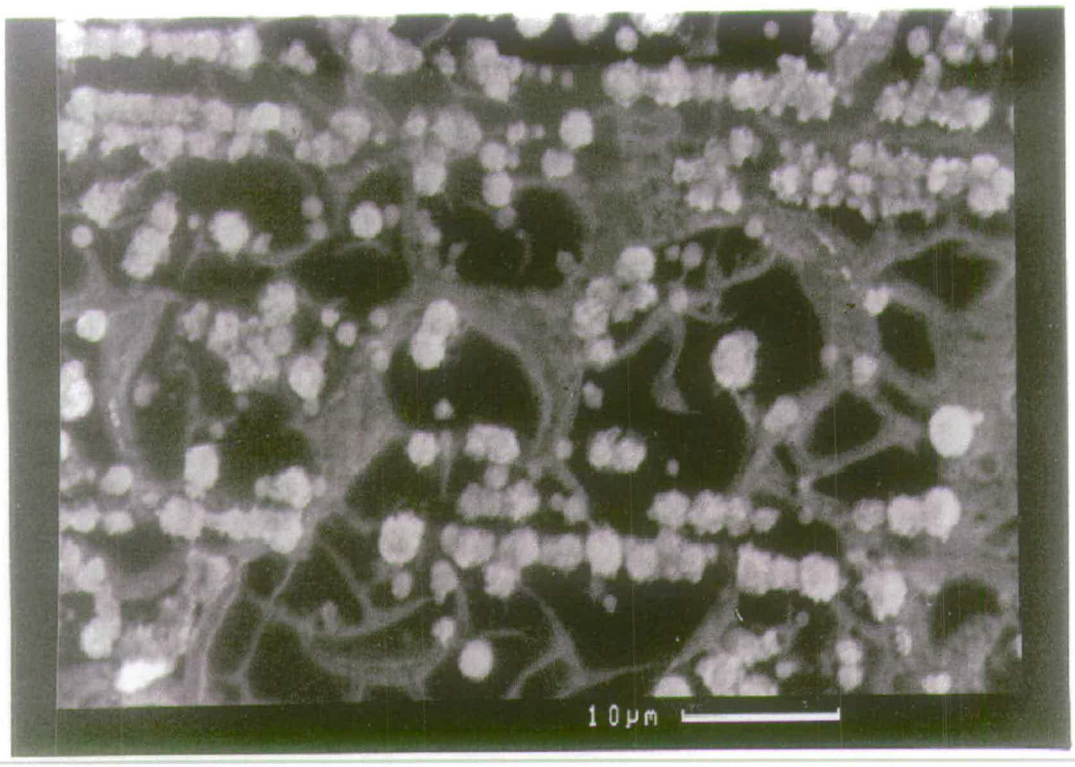

Figure 7.4: SEM image of clean titanium particles deposited on copper foil at -1.00 V (vs. Pt)

The EDX spectrum of one of the spherical particles on the surface is shown in *Figure 7.5.* The two K lines due to titanium are very prominent. This time the two K lines due to copper are also observed, demonstrating that the electron beam has penetrated through to the underlying substrate, thereby showing that the particle under analysis was smaller than 3μm in diameter. No other elemental peaks are present. It is interesting to note that the morphology of samples 1 and 2 are very different, even though they were deposited at the same potential. The wire electrode led to the formation of a reasonably coherent film which looked black, whereas the flat foil promoted nucleation and growth of much smaller spherical particles, giving a more metallic appearance. It is likely that the foil was a much cleaner surface.

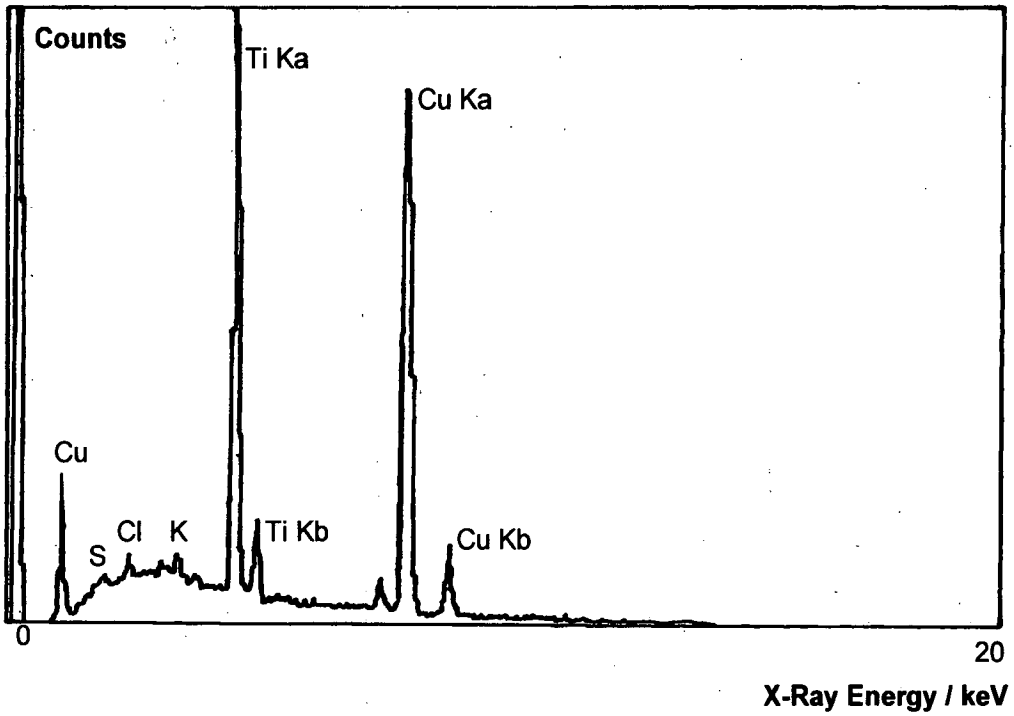

Figure 7.5: EDX spectrum of a spherical particle, as pictured in *Figure 7.4*

7.4.3.2.c Experiment 3

Experiment 3 was performed at -2.00 V to discover whether the same type of deposit would be produced at this more reducing potential. After initial decay, the steady current passing with a 1kΩ resistor was approximately 1.5mA. After 11.4C of charge had been passed, a black, powdery deposit had been produced on the electrode. The electrode was washed with acetonitrile, water and acetone . SEM showed the deposit to be made up of spherical particles similar to those observed previously in experiment 2. The EDX spectrum confirmed that they were composed of pure titanium. The average particle size was approximately 2μm, but there was also a considerable degree of aggregation to form larger clusters. It is possible that the greater current density at the more negative operating potential of this experiment led to the

production of a greater number of nucleation sites or a more random distribution of particle size. This agglomeration could explain why the sample appeared less reflective when viewed by eye.

X-ray powder patterns were recorded of the copper foil starting material, and from the electrode plated in experiment 3. Due to the broad scattering at high *d*-spacing in the latter pattern, the electrode was sealed in a quartz tube under high vacuum and annealed at 500°C for 70 hours in a tube furnace. Further patterns were then recorded. The pattern of the electrodeposited sample is displayed in *Figure 7.6*. The two peaks due to copper are clearly visible at d-spacings of 2.085Å (111 plane) and 1.805Å (200 plane). In addition, there is an intense peak at a *d*-spacing of approximately 7.847Å and some lower intensity peaks which appear at approximately 2.75Å and 3.15Å. The intensity of these may increase on further annealing. The peaks are likely to be due to the alloying of titanium with copper.

Table 7.3 lists the closest match d-spacings of some known copper-titanium alloys with those recorded for the annealed film. The β′-Cu_4Ti and β-Cu_3Ti phases have been implicated in the precipitation hardening of copper-titanium binary alloys [22, 23]. It can be seen that all but two of the known alloys show a peak in the powder XRD pattern at a large d-spacing, although none exactly coincides with the observed d-spacing of 7.847 Å. The phase produced cannot be positively identified, but is likely to be a mixed copper-titanium alloy of unresolved composition.

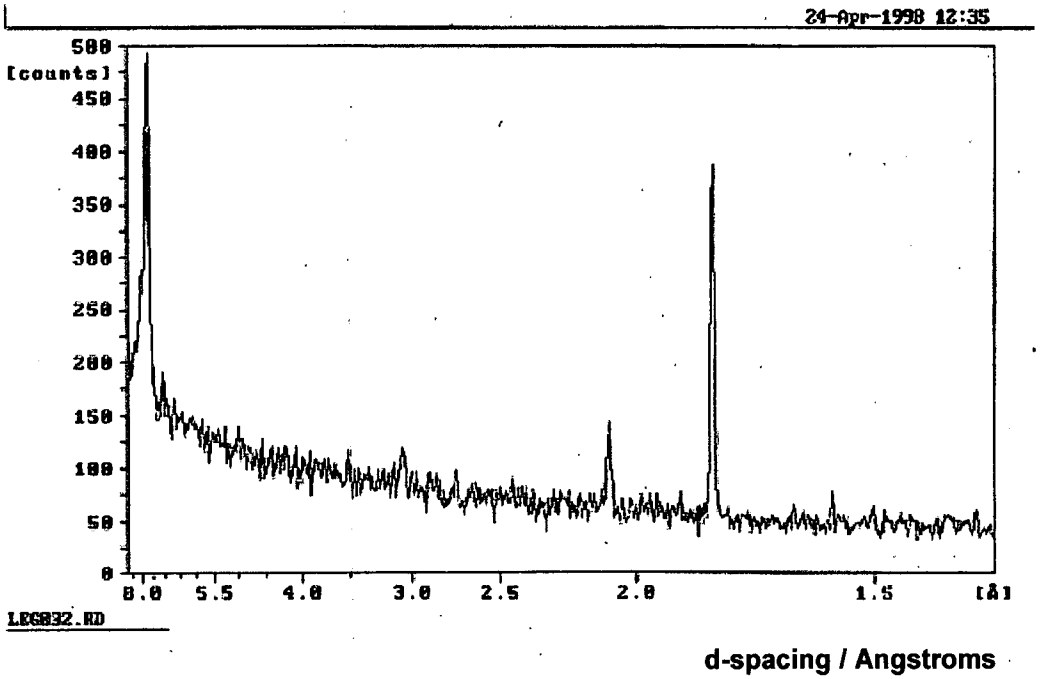

Figure 7.6: Glancing angle XRD pattern of the electrodeposited and annealed film on copper foil

Alloy	d-spacing / Å			File Index No.
Unknown	7.847	~3.15	~2.75	-
Cu_4Ti	6.490	3.230	2.819	20-370
Cu_3Ti	4.540	3.130	2.687	7-108
Cu_2Ti	-	-	2.227	20-371
CuTi	5.910	-	2.194	7-114
Cu_4Ti_3	9.970	4.960	2.456	18-460
$CuTi_2$	5.390	2.840	2.690	15-717
$CuTi_3$	-	4.158	2.719	25-1144

Table 7.3: D-spacings from powder XRD of some known copper-titanium alloys, as compared with the result from the annealed film

7.4.3.2.d Experiment 4

Experiment 4 was also performed at -2.00 V but a 100kΩ resistor was also used to limit the rate of charge passing to approximately 130μA so as to investigate whether a reduction in the current would promote an increase in the importance of nucleation over growth leading to greater coverage of the surface. Having established complete two dimensional coverage at an early stage it was speculated that growth in the third dimension away from the electrode could occur in a concerted manner to produce a coherent film.

Electrodeposition performed in this way did superficially affect the appearance of the film. The deposit looked more silver-coloured and metallic on the face of the electrode compared to sample 3 plated at -2V with the 1 kΩ resistor, although the edges were black, presumably because the field lines are strongest at the edge of the electrode. An additional factor is that these edges were freshly cut before the experiment and so are likely to have a minimal oxide layer thereby making them more favourable sites for reduction of the titanium complex. The electrode was washed with acetonitrile, water and acetone prior to analysis. The SEM secondary electron image obtained from the face of sample 4 is shown in *Figure 7.7*. The type of particles seen here are very similar to those produced in experiment 2 using the 1 kΩ resistor, with an average size of approximately 2μm. The particles were more uniformly distributed over the surface, rather than being clustered along scratches, or aggregated as in experiment 3. It is likely that an even coverage of discrete particles would make the film appear more reflective. However, caution must be exercised when comparing the relative particle distributions as the original morphologies may have been altered somewhat during the washing process.

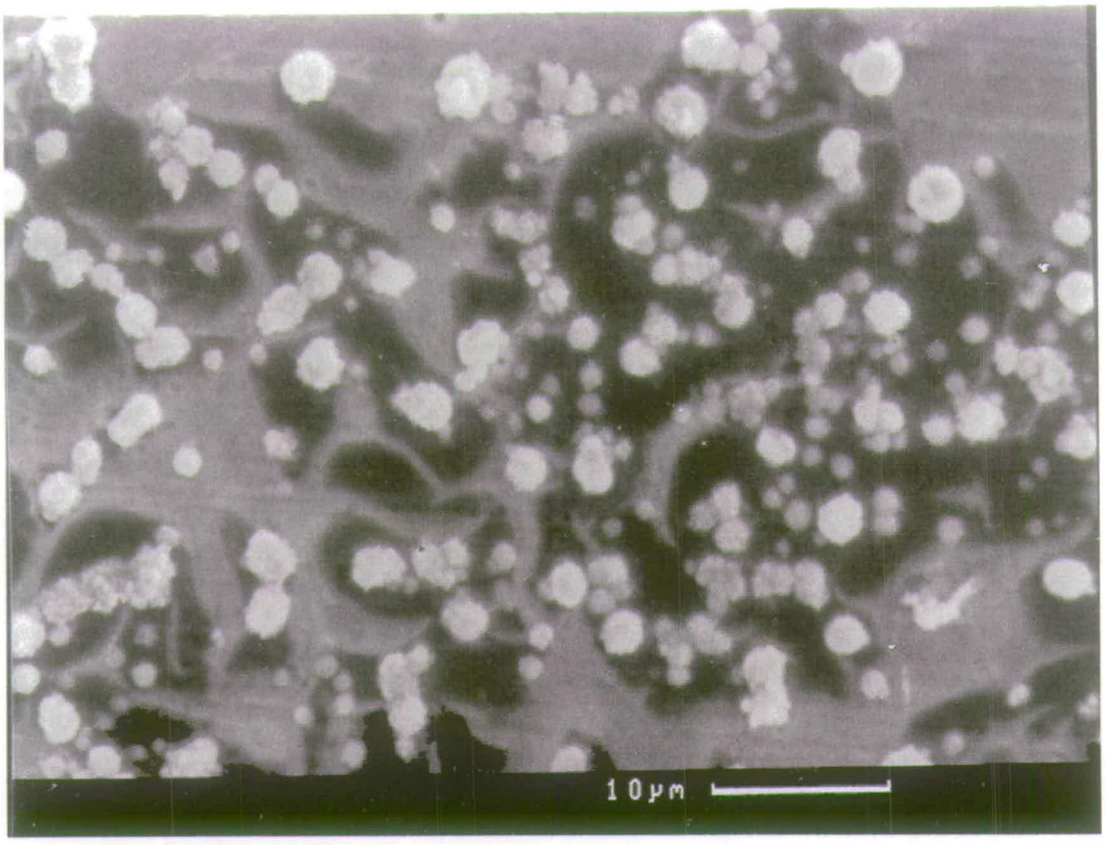

Figure 7.7: SEM image of particles deposited on copper foil at -2V (vs. Pt) with a 100 kΩ resistor

The nature of the electrode surface seems to be the governing factor in determining the morphology of the product film, rather than the reaction potential or the rate of deposition. The surface scratches or newly cut edges on the copper are likely to be very clean areas on the electrode with minimal oxide layer contamination. A freshly exposed metal surface will undoubtedly provide a site of higher reactivity for reduction of the complex and hence a preferred location for titanium particle formation.

7.4.4 $K_2[Ti(SCN)_6]$ with copper working-electrode

It was hoped that the Ti(IV) complex would be more resistant to aerial oxidation than the Ti(III) analogue and might therefore be a more stable precursor for the deposition of titanium metal.

7.4.4.1 Cyclic Voltammetry

A typical cyclic voltammogram of the Ti(IV) complex is shown in *Figure 7.8*. Note that the platinum pseudo reference electrode would be expected to have a reference potential slightly more positive than that in the Ti(III) experiment, owing to the greater oxidising power of the Ti(IV) complex, and that peaks in this voltammogram should therefore occur at slightly more negative potentials (perhaps shifted by a few tens of mV), than in the Ti(III) experiment (assuming the couple $Ti^{4+} + e^- \leftrightarrow Ti^{3+}$ sets the reference potential).

The voltammogram is a similar shape to that recorded in the Ti(III) experiment except that it is shifted to more negative current (by approximately -6mA), and potential (by approximately +0.50 V) overall. The main feature is the presence of a reduction current at approximately -0.50 V (A). This is due to the two electron reduction (re-plating) of Cu(II) to Cu(0). This indicates that the Ti(IV) complex is sufficiently oxidising to oxidise chemically the copper working-electrode (*equation 7.10*); in other words the copper electrode was dissolved by the solution at 0.00 V. After the CV study the electrode was visibly etched and had become very thin due to the dissolution of copper by Ti(IV). Application of a reductive current of approximately -6mA would be required to avoid such copper stripping. As the CV is shifted

to more negative current and potential, a peak due to the reduction of Ti(IV) or Ti(III) to Ti(0) is not seen before current saturation is reached.

$$Cu + 2Ti^{4+} \rightarrow Cu^{2+} + 2Ti^{3+} \qquad (7.10)$$

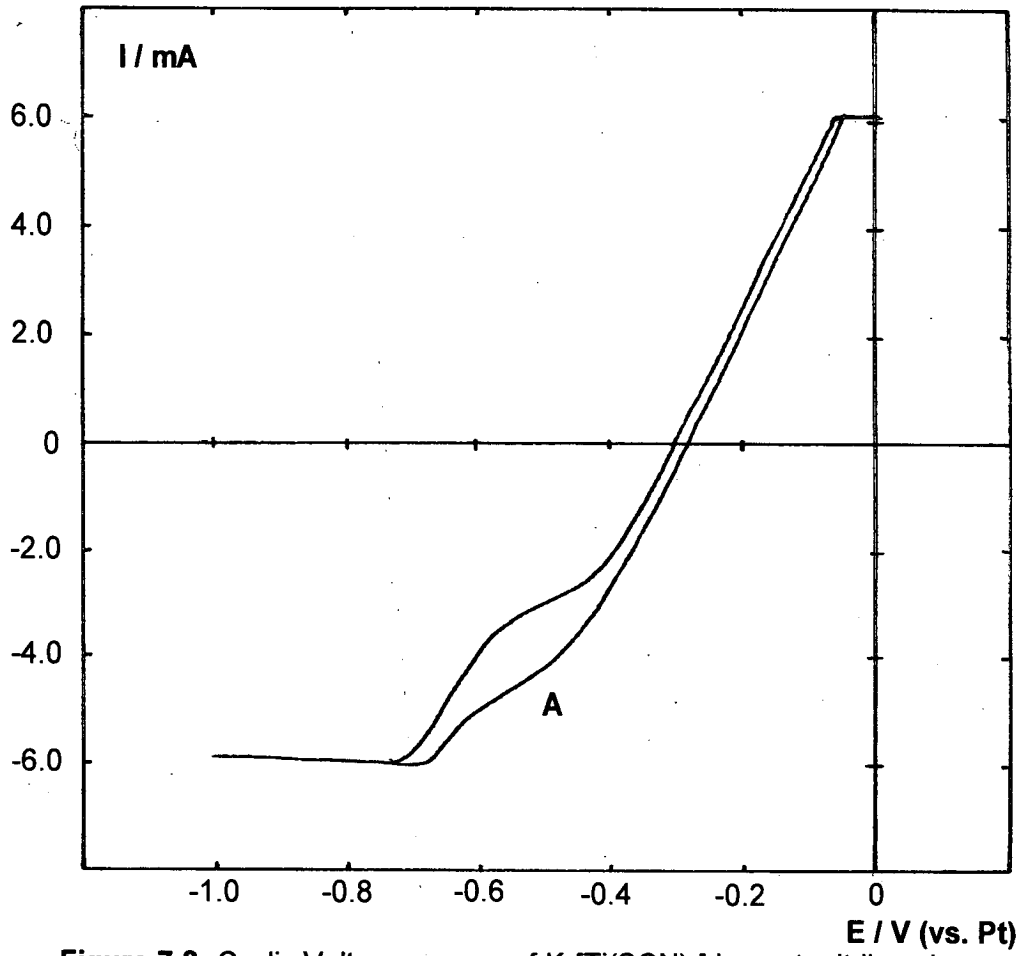

Figure 7.8: Cyclic Voltammogram of $K_2[Ti(SCN)_6]$ in acetonitrile using a Cu working-electrode

7.4.4.2 Electrodeposition

Constant potential electroplating at -2.00 V and -5.00 V did not lead to the isolation of titanium deposits. The copper electrode became rather etched through oxidation as in

equation 7.10. Even though the Ti(IV) solution was easier to handle in terms of the scrupulous exclusion of air, it was simply too oxidising for use with copper. Further experiments on this system were not pursued.

7.4.5 $(NH_4)_3[Ti(SCN)_6]$ with a copper working-electrode

7.4.5.1 Cyclic Voltammetry

As expected, the CV of the above complex was similar to that recorded for $K_3[Ti(SCN)_6]$ on copper. The change in counter ion from potassium to ammonium had no effect on the potential at which oxidation and reduction reactions were taking place.

7.4.6 $K_3[Ti(SCN)_6]$ with an iron working-electrode

7.4.6.1 Cyclic Voltammetry

The cyclic voltammogram of the above complex on an iron working-electrode is shown in *Figure 7.9.* The first two scans are shown. On the negative sweep the initial CV *(Figure 7.9a)* shows a reduction wave at approximately -0.90 V (A). In the second CV *(Figure 7.9b)*this wave has shifted to a more positive potential at approximately -0.50 V (B) indicating that the reaction is now more facile. These waves may be due to the reduction of the oxide layer on the iron electrode; an oxidation current is observed in both CVs on the positive sweep (C) and this may be attributable to re-oxidation of the iron surface by solution oxide species. In both scans a large reductive current is observed on the negative sweep at approximately -

1.30 V (D). Based on knowledge gained in the previous experiments, this is probably attributable to the three electron reduction of Ti(III) to Ti(0).

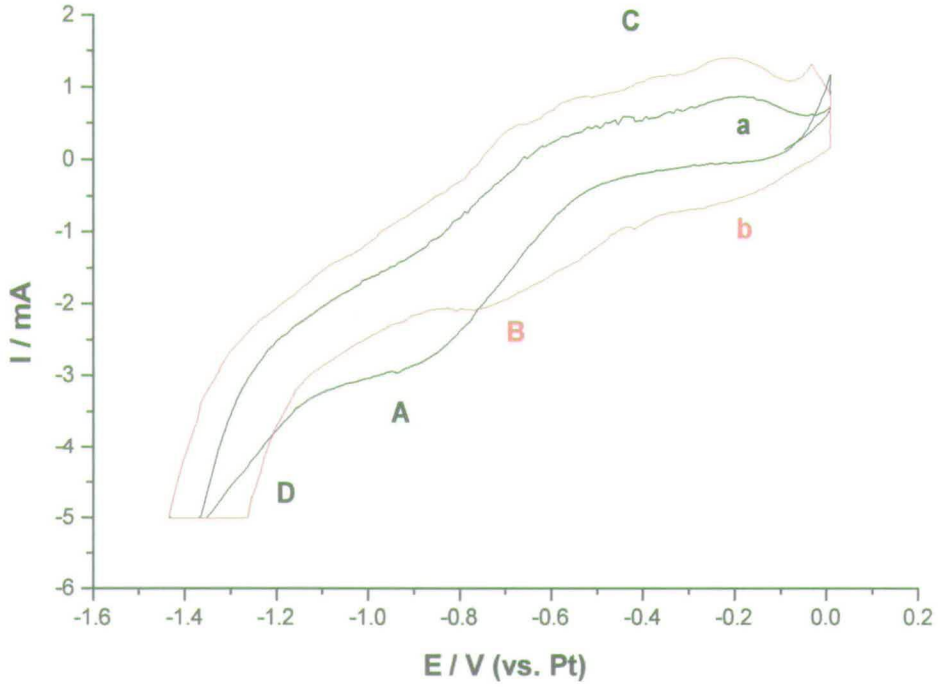

Figure 7.9: Cyclic Voltammogram of $K_3[Ti(SCN)_6]$ in acetonitrile using an Fe working-electrode (**a**) initial scan, (**b**) second scan

7.4.6.2 Electrodeposition and Characterisation of Films

Experiment 5 was performed using an iron foil working-electrode in order to discover whether the choice of metal substrate influenced the titanium particle nucleation mode. The current-time transient was very uneven, but the average current at -1.50 V was approximately 4.5mA. After 11C of charge had been passed, a loose grey film was produced which after washing with acetonitrile, water and acetone and drying turned white. *Figure 7.10* shows the secondary electron SEM image of the film obtained in experiment 5. This shows a cracked film which EDXS shows to be rich in titanium and potassium, the latter probably present

because of insufficient washing. The film is approximately 10μm thick. The product morphology is quite different to that produced on copper foil. The spherical particles as produced on copper were not observed on iron.

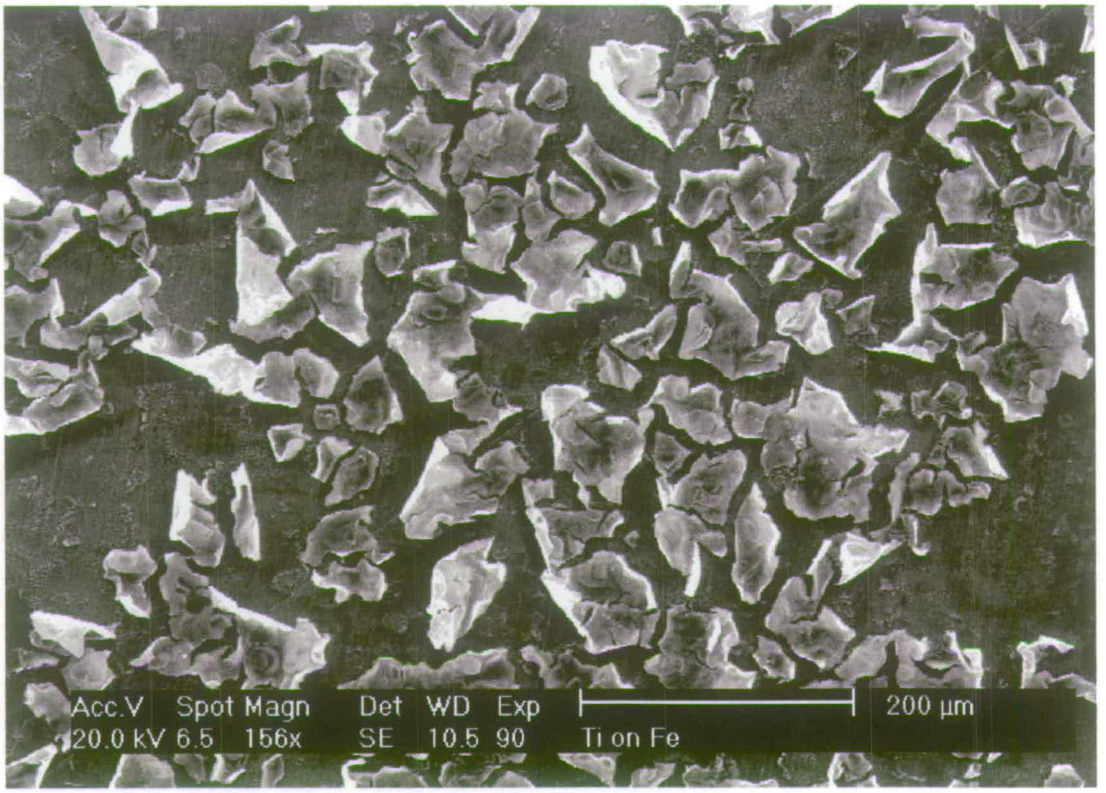

Figure 7.10: SEM image of cracked titanium-containing film on iron

7.4.7 $(NH_4)_3[Ti(SCN)_6]$ with an iron working electrode

7.4.7.1 Cyclic Voltammetry

The cyclic voltammogram of the above complex on an iron working-electrode is shown in *Figure 7.11*. Within the observable window a reduction current can again be observed (A) and an oxidation peak on the positive sweep (B). The reduction current may represent the

stripping of the native oxide layer on the iron foil; the associated oxidation peak would then be attributable to re-oxidation of the surface by solution oxide species. A peak attributable to the reduction of Ti(III) to Ti(0) would be expected to appear at a potential more negative than that encompassed within this CV.

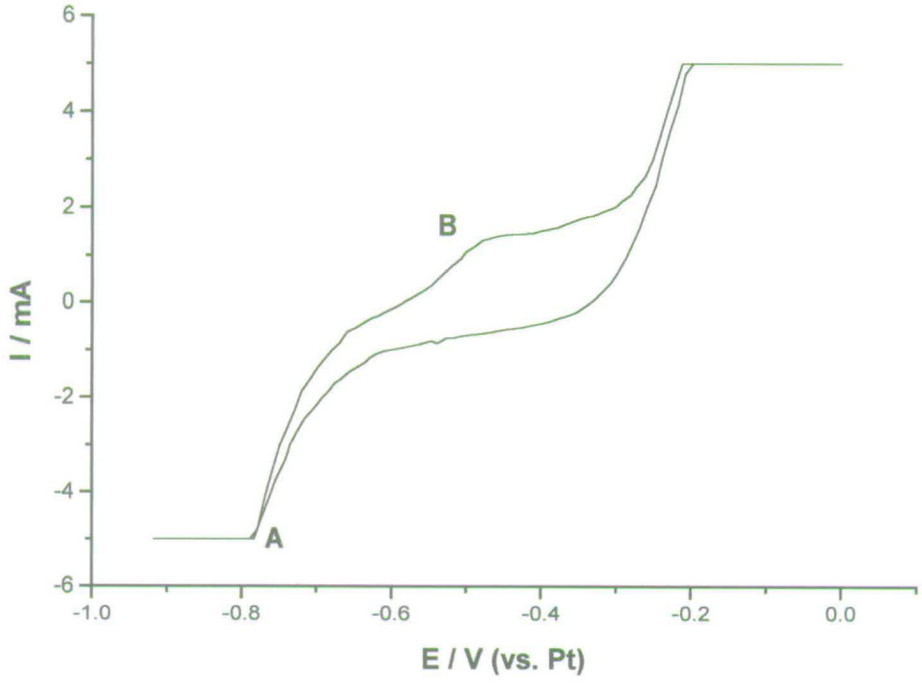

Figure 7.11: Cyclic Voltammogram of $(NH_4)_3[Ti(SCN)_6]$ in acetonitrile using an Fe working-electrode

7.4.7.2 Electrodeposition and Characterisation of Films

With the potential at -1.00 V, the current saturated at 5mA. After 1 hour, 25C of charge had been passed, and a gold-coloured film was produced. This was in contrast to previous observations when either a silver-coloured film or black powdery deposit had been produced. The deposit was washed with acetonitrile, water and acetone prior to analysis. *Figure 7.12* shows the secondary electron SEM image of the film obtained, which can be seen to be made

up of clusters of spherical particles which are approximately 3μm in diameter on average. These clusters are similar to those observed previously on copper in experiment 3. These two experiments had in common the fact that the current density at the electrode during plating was fairly high.

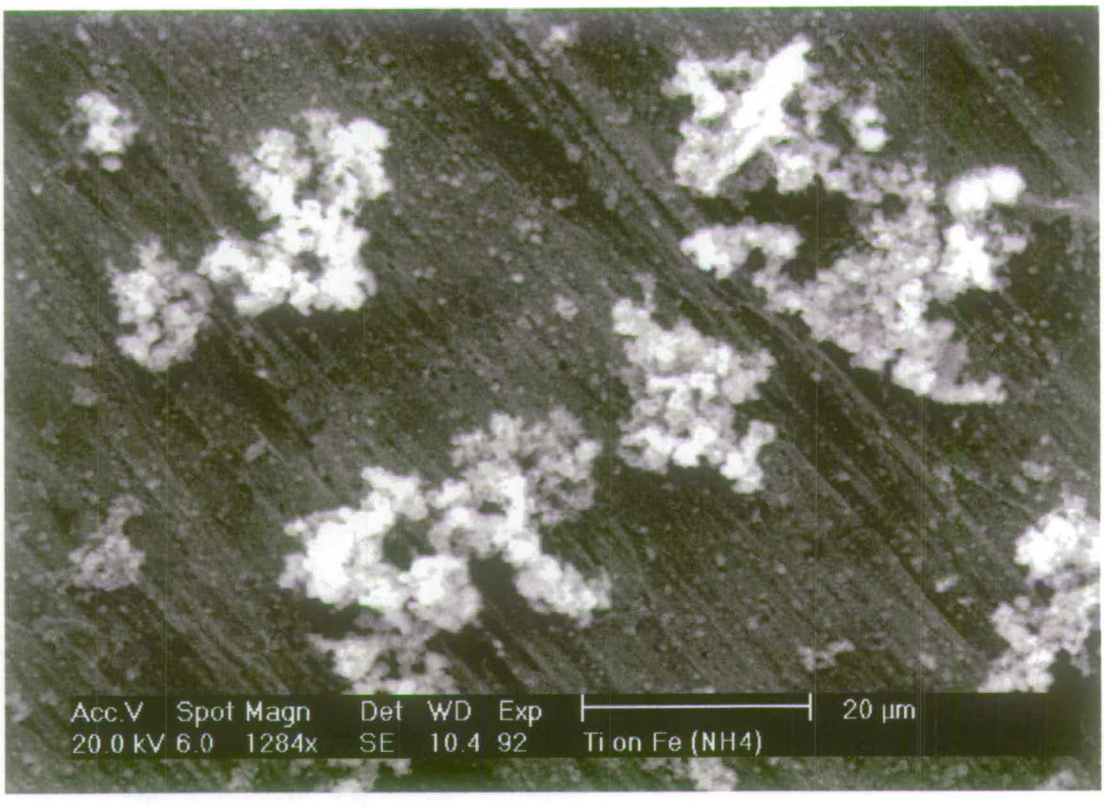

Figure 7.12: SEM image of titanium-containing particles on iron

Figure 7.13 shows the EDX spectrum of one of these particles. Peaks due to the iron substrate are observed as well as intense lines due to titanium. There is a small amount of chlorine and sulfur present, and a significant amount of oxygen. This could be from the native oxide layer on the iron electrode, or from the surface of the small, potentially reactive titanium particles which may be prone to aerial oxidation.

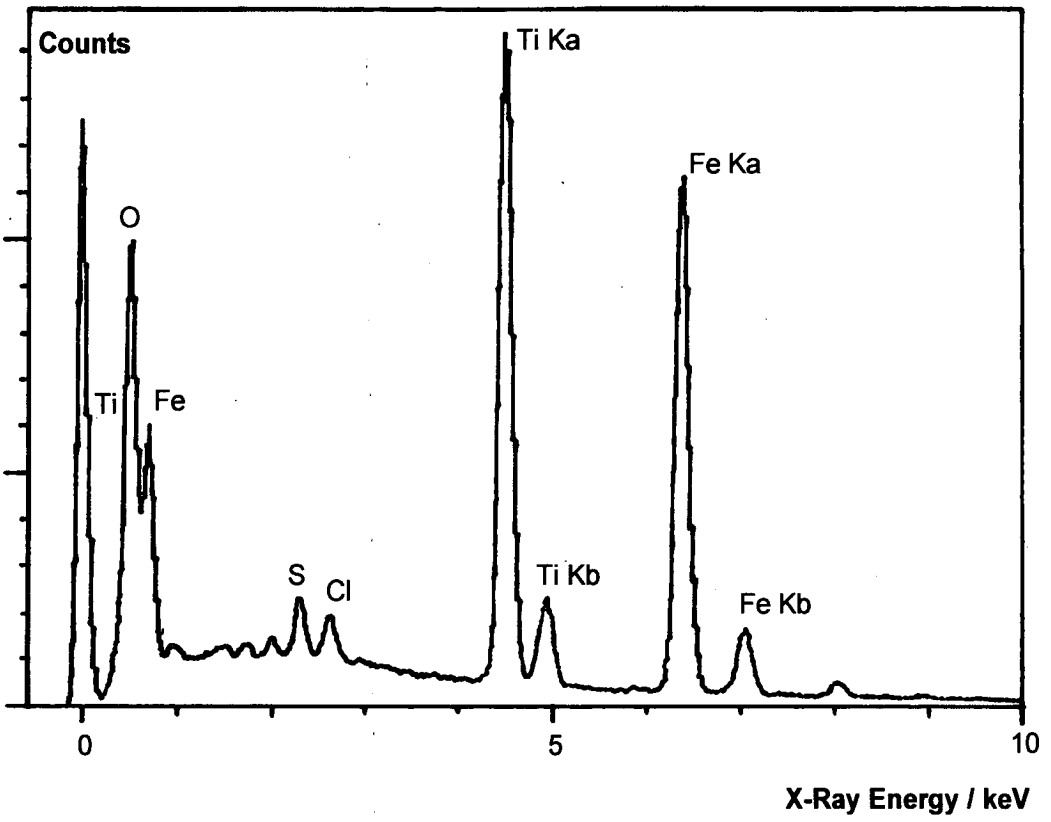

Figure 7.13: EDX spectrum of titanium-containing deposit on iron

7.5 Electrochemistry of Thiocyanato Derivatives in and Electrodeposition from an 'Ionic Liquid'

7.5.1 Strategy

The so called 'ionic liquids' (as introduced in *section 7.1.1.4.b*) have several desirable physical properties which make them good alternatives to conventional solvents. They have negligible vapour pressure due to the purely electrostatic interactions between ions. This is a benefit in environmental terms and in some circumstances may also allow facile separation of volatile by-products from the reaction medium. They also have a wide liquid temperature range, for example approximately 300°C for 1-ethyl-3-methylimidazolium chloride, EmimCl. Such ionic liquids also show a wide electrochemical window (approximately 3V for EmimCl/$AlCl_3$) with stability towards reductants and oxidants and with a potential stabilising effects on high oxidation state species. The imidazole-based ionic liquids are miscible in significant proportions with a wide range of solvents e.g. acetonitrile, benzene, toluene and methylene chloride. They can also solvate various organic, organometallic and inorganic compounds e.g. aromatics, ferrocene, $CuCl_2$ and $TiCl_4$. A disadvantage of these systems is their photosensitivity; they show discoloration after several days. They are also expensive to produce.

It was decided to attempt to prepare the novel ionic liquid 1-butyl-3-methylimidazolium thiocyanate, BmimSCN, for use as a solvent medium for titanium electrodeposition. This work was inspired by the recent attempts of Seddon *et al* to deposit titanium from EmimCl-$AlCl_3$ or Bupy-$AlCl_3$ melts without success [6, 7]. The $K_3[Ti(SCN)_6]$ complex was used as a

titanium-containing precursor following previous successes. It was hoped that this salt would have appreciable solubility in the BmimSCN owing to the common presence of -SCN groups. The BmimCl ionic liquid was not used itself as it was felt the presence of potentially corrosive chloride might eventually lead to film deterioration. The $K_3[Ti(SCN)_6]$ precursor was not synthesised directly in BmimSCN as it was considered essential to remove excess KCl and KSCN solids prior to electrodeposition.

7.5.2 Synthesis and Characterisation of 1-Butyl-3-Methylimidazolium Thiocyanate

BmimSCN was prepared by fusing BmimCl (10g, 57.2 mmol) with excess KSCN (Aldrich, as received), at approximately 200°C and stirring for 20 minutes (*equation 7.11*). On cooling, the product was extracted into dichloromethane (Prolabo) leaving behind the KCl residue, and the solution was dried over 4Å molecular sieve (BDH), which had been baked out under vacuum. The dichloromethane was then removed under reduced pressure and the liquid BmimSCN was warmed on a high vacuum line until it was free from solvent, leaving a yellow-pink viscous liquid.

$$\text{BmimCl (s)} + \text{KSCN (s)} \rightarrow \text{BmimSCN (l)} + \text{KCl (s)} \qquad \textbf{(7.11)}$$

BmimCl was prepared by the reaction between 1-chlorobutane (Acros) and 2-methylimidazole (Acros) (*equation 7.12*). The two reagents were refluxed under nitrogen for 24 hours, then any unreacted chlorobutane was removed under reduced pressure, which yielded a pale yellow glassy solid.

$$BuCl\ (l) + MeIm\ (s) \rightarrow BmimCl\ (s) \qquad (7.12)$$

CHN analysis of the BmimCl liquid gave 54.25 (55.01) % C, 9.20 (8.67) % H, and 16.91 (16.04) % N. CHN analysis of the BmimSCN liquid gave 52.56 (54.79) % C, 5.51 (7.66) % H, and 21.44 (21.30) % N. A trace of dichloromethane may still have been left. It is notoriously difficult to obtain good analyses of such ionic liquids.

7.5.3 Set-up of the Electrochemical Cell

Approximately 15 millimolar solutions of the Ti(III) complex in 50 cm^3 dry BmimSCN were prepared by adding the solvent *via* cannula to the dry $K_3[Ti(SCN)_6]$ salt (prepared as in *section 7.3.1.1*), which had been weighed into the cell in a nitrogen-filled dry box. The suspension was then stirred for 15 minutes with warming to aid dissolution. The experiment was initiated at room temperature and then the cell was warmed with an oil bath to 85°C to prevent the $K_3[Ti(SCN)_6]$ / BmimSCN solution from solidifying.

Copper foil was used as the working electrode, following the previous success with this substrate. The other electrodes were as those described in *section 7.4.1* and the electrochemistry was controlled as in *section 7.4.2*.

7.5.4 Electrochemistry of $K_3[Ti(SCN)_6]$ in BmimSCN with a copper working-electrode

7.5.4.1 Cyclic Voltammetry

The cyclic voltammogram of the above complex on copper working-electrode is shown in *Figure 7.14*. This is very similar to the CV observed for the complex in acetonitrile. This confirms that the electroactive species $K_3[Ti(SCN)_6]$ was soluble in BmimSCN. Again the pair of redox peaks centred around approximately 0.20 V can be attributed to the stripping (oxidation, A) and re-plating (reduction, B) of copper from the working electrode. At -1.00 V there is a small reduction peak (C), probably due to the deposition of titanium metal on certain energetically favoured sites on the copper, and at approximately -1.50 V there is a larger reduction peak (D) which is also attributed to this reaction, but on a larger number of less reactive sites. The beginning of the wave at approximately -2.50 V (E) may also involve reduction of Ti(III), but is probably also attributable in part to solvent breakdown.

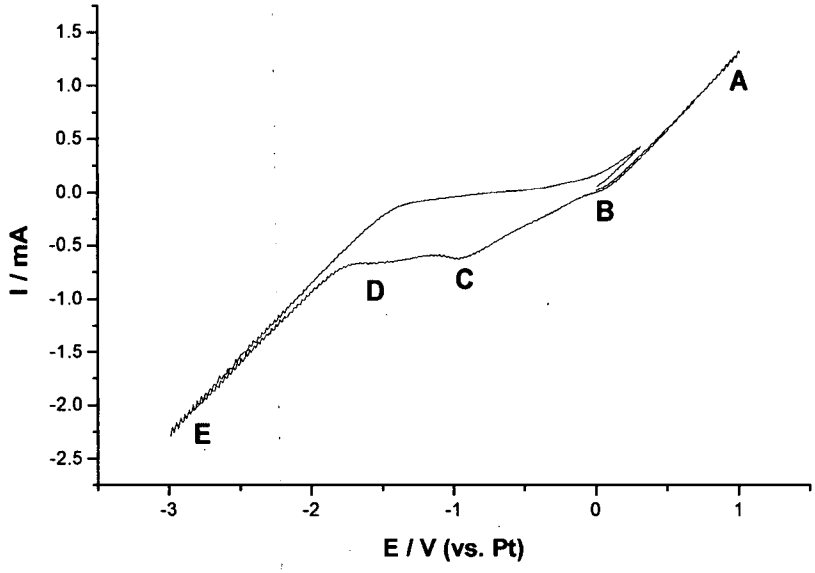

Figure 7.14: Cyclic Voltammogram of $K_3[Ti(SCN)_6]$ in BmimSCN using a Cu working-electrode

7.5.4.2 Electrodeposition and Characterisation of Films

Experiment 8 was executed at -2.00 V. The steady state current at room temperature was 1.3mA, and this increased to saturation (5mA) as the solution was heated to 85°C. After the passage of 9.1C, the electrode was removed from the cell and immediately washed with dichloromethane to remove the viscous BmimSCN solution, then washed with water and acetone. After electrolysis the electrode was coated with a light silver-coloured metallic-looking film where it had dipped into solution. Under the optical microscope, black particles could be seen which appeared to closely follow vertical grooves in the copper foil. Under the SEM, it was clear that the film was composed of the familiar clusters of spherical particles of approximately 0.5μm in diameter (arrow, *Figure 7.15*). Above these clusters was a considerable amount of a more floccular material which is likely to be precipitated electrolyte, present due to insufficient washing of the electrode.

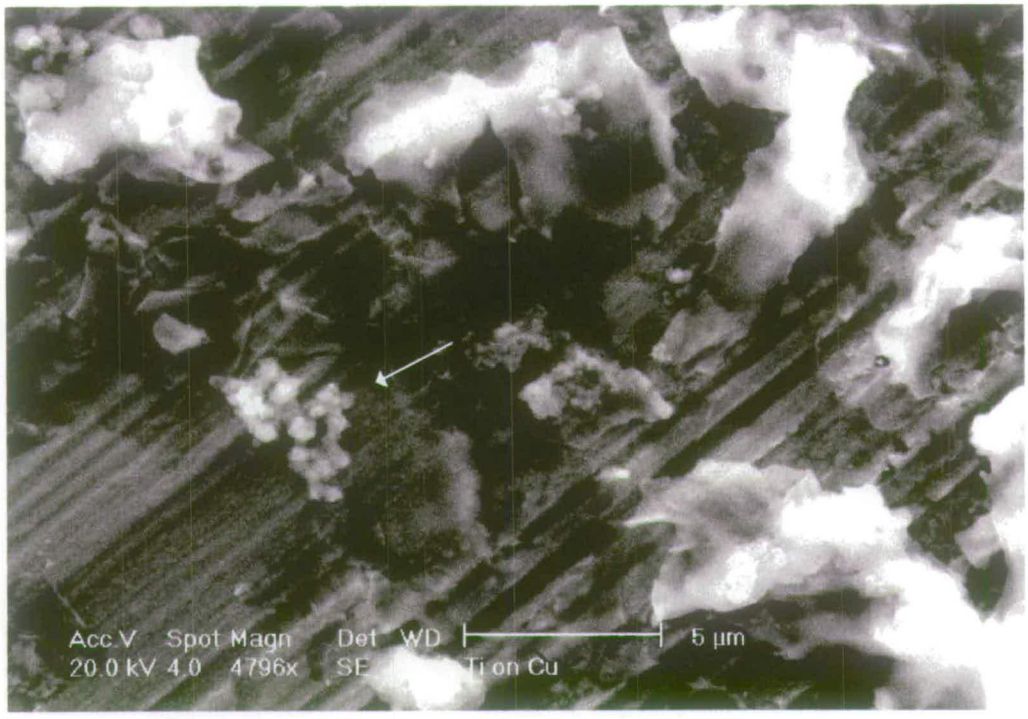

Figure 7.15: SEM image of titanium-containing particles on copper, and more floccular material (precipitated electrolyte)

The EDX spectrum of a cluster of particles in shown in *Figure 7.16.* Peaks due to the copper substrate can be observed, as well as intense peaks due to titanium. There are trace amounts of sulfur and chlorine, and a significant amount of potassium. These elements are likely to be present in the form of precipitated electrolyte, so the sample was washed more thoroughly in warm water and briefly in an ultrasound bath, before rinsing in acetone and viewing again. Unfortunately the use of the ultrasound bath had dislodged a high proportion of the particles. However, the EDX spectrum of those still remaining showed them to be composed of pure titanium.

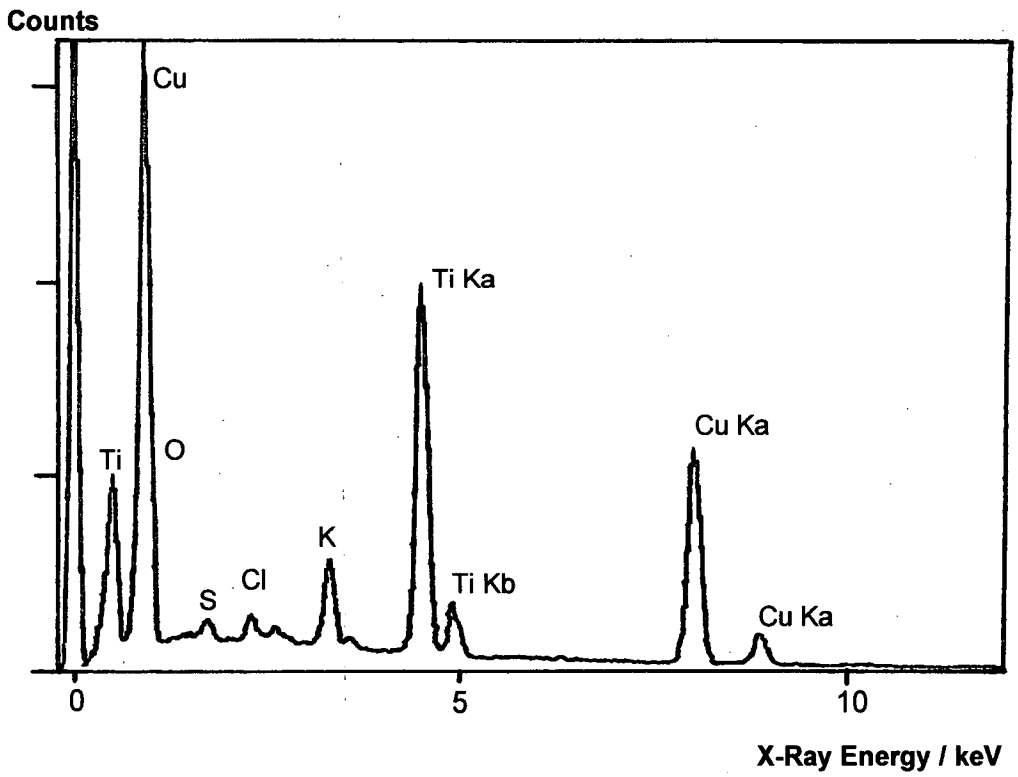

Figure 7.16: EDX spectrum of titanium-containing deposit on copper

7.6 Summary, Conclusions and Further Work

This chapter demonstrated a new method for the production of clean, titanium-containing microparticles from $M_3[Ti(SCN)_6]$ (M = K, NH_4) solutions at room temperature and at moderate negative potential (-1.00 or -2.00 V vs. Pt). Electrodeposition was performed on copper and iron substrates in both acetonitrile solution and the novel solvent 1-butyl-3-methylimidazolium thiocyanate (BmimSCN); it may be possible to use other solvents too. As the deposits were conducting and shown to be free from other elements by EDXS it is reasonable to suppose that they were composed of metallic titanium. If time had permitted it would have been desirable to confirm the oxidation state of the titanium by XPS.

The complex $M_3[Ti(SCN)_6]$ (M = K, NH_4) was synthesised in liquid ammonia or acetonitrile from titanium(III) chloride and the appropriate thiocyanate salt. The air-sensitive potassium salt was characterised by CHN analysis, and its acetonitrile and THF solutions studied by UV-visible spectroscopy. Unfortunately single crystals could not be obtained. However it was concluded that the complex was of octahedral symmetry at titanium, with the six thiocyanate ligands bound through nitrogen. The analogous titanium(IV) complex, $K_2[Ti(SCN)_6]$, was also synthesised in acetonitrile and a UV-visible spectroscopic study was performed. The complex was found to be too oxidising towards copper to be of use as a electrodeposition precursor.

Cyclic voltammetry of the $M_3[Ti(SCN)_6]$ complex in acetonitrile using a copper foil working electrode revealed two reduction waves at -1.00 V and -1.60 V (vs. Pt). These were both attributed to the three electron reduction of Ti^{3+} to produce Ti^0, but on two energetically

distinct types of surface site. The wave at -1.00 V was assigned to reduction at reactive sites on the copper, whilst that at -1.60 V was assigned to reduction at less reactive but more numerous sites.

Electrodeposition from acetonitrile solutions of $K_3[Ti(SCN)_6]$ was performed at -1.00 V on copper wire and copper foil electrodes. The steady current was approximately 0.3mA demonstrating that the deposit was conducting. A patchy black coating was produced on the copper wire which was observed by SEM to be cracked, possibly by the evaporation of solvent after electrodeposition. The coating gave a positive chemical test for titanium, and was found to be composed of titanium only by EDXS. A silver-grey metallic-looking film was produced on the copper foil which was observed by SEM to be composed of approximately 2μm diameter spherical particles which had nucleated in scratches in the substrate surface. These were also found to be composed of clean titanium by EDXS.

Electrodeposition was also performed at -2.00 V on a copper foil working electrode, when the steady current was 1.5mA. The same 2μm diameter spherical titanium particles were obtained, but this time distributed more randomly as clusters on the surface giving the film a black, powdery appearance when viewed by eye. The sample was annealed under vacuum at 500°C for 70 hours. The powder XRD pattern of the resulting film showed an intense peak at 7.847Å and weaker peaks at 2.75 and 3.15Å, in addition to the peaks due to copper itself. The appearance of these peaks was attributed to the formation of an unknown Cu-Ti alloy. Electrodeposition on copper foil at -2.00 V using a 100kΩ current-limiting resistor also generated 2μm diameter spherical titanium particles, although these were distributed very evenly on the substrate surface

Iron foil was also used as a substrate for titanium deposition from acetonitrile solutions of $K_3[Ti(SCN)_6]$. Electrodeposition performed at -1.50 V (vs. Pt) with a steady current of 4.5mA produced an even conducting film of 10μm thickness which appeared cracked when viewed by SEM, again probably owing to post-deposition solvent evaporation. EDXS revealed that the film was composed of titanium, with significant amounts of potassium present because of insufficient washing. An acetonitrile solution of $(NH_4)_3[Ti(SCN)_6]$ was also used to deposit titanium on iron. At -1V and a steady current of 5mA a gold-coloured film was produced. SEM showed that the film was composed of clusters of spherical particles of approximately 3μm diameter. The EDX spectrum displayed peaks due to iron, titanium, trace amounts of chlorine and sulfur, and a significant amount of oxygen. The latter could be from the native oxide layer on the iron, or due to the post-processing aerial oxidation of the titanium particles.

A novel ionic liquid 1-butyl-3-methylimidazolium thiocyanate, BmimSCN, was synthesised by fusing BmimCl with KSCN at 200°C and extracting the product into dichloromethane. The precursor $K_3[Ti(SCN)_6]$ was found to be soluble in BmimSCN, as confirmed by cyclic voltammetry. Electrodeposition was initiated at room temperature at -2.00 V when the steady current was 1.3mA. The current increased to 5mA as the temperature of the ionic liquid was raised to 85°C. A silver-coloured metallic-looking film was produced on copper. SEM showed the film to be composed of clusters of spherical particles of 0.5μm diameter, much smaller than those obtained from acetonitrile solution. This may be an advantage for certain industrial applications. EDXS showed the particles to be composed of titanium, although again trace sulfur and chloride and significant potassium was present owing to the presence of precipitated electrolyte.

It was concluded that the morphology of the product was determined by the nature of the substrate surface and the deposition current density at the electrode. On copper and iron, spherical microparticles (2-3μm diameter) were usually produced. These were found to preferentially nucleate at surface irregularities or areas with minimal oxide layer (e.g. scratches, freshly cut edges), and at high current densities tended to aggregate to form clusters. When the current was limited by the use of a resistor in the circuit the particles could be made to nucleate evenly on the substrate. In a couple of experiments, coherent films were produced which cracked after deposition probably owing to solvent evaporation and drying. It is likely that films were produced in these cases because the initial surfaces were very smooth and extensive nucleation resulted. Further studies could attempt pre-treatment of the substrate by chemical or mechanical means. Repeated electrochemical stripping and re-plating of copper prior to deposition might also promote the formation of an even surface conducive to film rather than particle formation. Alternatively a single crystalline copper substrate (cleaved along one lattice plane) could be employed.

In future it would be interesting to extend this method to the deposition of other electropositive metals such as zirconium, hafnium, the lanthanides and aluminium.

7.7 Bibliography

[1] P. Ehrlich, '*Preparative Inorganic Chemistry*', Section 22, 1161-1172

[2] D. R. Sadoway, *Journal of the Minerals, Metals and Materials Society*, **43**, (7), 15-19, 1991

[3] K.W. Fung and G. Mamantov, *J. Electroanal. Chem.*, **35**, 27, 1972

[4] G.R. Stafford and T.P. Moffat, *J. Electrochem. Soc.*, **142**, 10, 1995

[5] K.R. Seddon, http://www.ch.qub.ac.uk/resources/ionic/review/review.html

[6] H. Linge, Z. Stojek and R.A. Osteryoung, *J. Am. Chem. Soc.*, **103**, 3754-3760, 1981

[7] R.T. Carlin, R.A. Osteryoung, J.S. Wilkes and J. Rovang, *Inorg. Chem.*, **29**, 3003-3009, 1990

[8] R.J. Gale, B. Gilbert and R.A. Osteryoung, *Inorg. Chem.*, **18**, 2723, 1979

[9] T.M. Laher and C.L. Hussey, *Inorg. Chem.*, **20**, 4201, 1981

[10] T.M. Laher and C.L. Hussey, *Inorg. Chem.*, **21**, 4079, 1982

[11] T.M. Laher and C.L. Hussey, *Inorg. Chem.*, **22**, 1279, 1983

[12] C. Nanjundiah and R.A. Osteryoung, *J. Electrochem. Soc.*, **130**, 1312, 1983

[13] D.A. Habboush and R.A. Osteryoung, *Inorg. Chem.*, **23**, 1726, 1984

[14] A.P. Abbott, A. Bettley and D.J. Schiffrin, *J. Electroanal. Chem.*, **347**, 153-164, 1993

[15] N.V. Petrova, V.N. Titova and V.A Kazakov, *Soviet Electrochemistry*, **21**, (6), 758-761 1985

[16] R. Taft and H. Barham, book? 929-953

[17] O. Schmitz-DuMont, P. Simons and G. Broja, *Z. Anorg. Allgem. Chem.*, **258**, 307, 1949

[18] O. Schmitz-DuMont and B. Ross, *Z. Anorg. Allgem. Chem. Internat. Edit.*, **3**, (4), 315, 1964

[19] N. N. Greenwood and A. Earnshaw, '*Chemistry of the Elements*', Pergamon Press 1984, pages 1089 & 1132

[20] E. A. V. Ebsworth, D. W. H. Rankin and S. Cradock, '*Structural Methods in Inorganic Chemistry*', Blackwell Scientific Publications (2nd Edition) 1987, page 292

[21] N. N. Greenwood and A. Earnshaw, '*Chemistry of the Elements*', Pergamon Press 1984, pages 343 & 1065

[22] A. A. Hameda and L. Blaz, *Mat. Sci. & Eng.* **A254**, 83-89, 1998

[23] S. Nagarjuna, K. Balasubramanian and D. S. Sarma, *Mater. Trans. JIM*, **36**, (8), 1058-1066, 1995

[24] Visual Designer 3.0 Software, Intelligent Instrumentation, Copyright 1993-5, Ron Goodwin

[25] A.C. Fisher, '*Electrode Dynamics*', Oxford Science Publications 1996

[26] G. Svehla, '*Vogel's Textbook of Macro and Semimicro Qualitative Inorganic Analysis*', 5th Edition, Longman 1979

Appendix 1:

Conferences & Courses

A.1 Conferences & Courses

A.1.1 Conferences Attended

Date	Meeting
12-13th September 1996	*'Universities of Scotland Inorganic Club'*, The University of St. Andrews
11th December 1996	*Dalton Structural Symposium*, The University of Edinburgh
5th February 1997	*RSC Scottish Dalton Meeting*, The University of Edinburgh
23-25th April 1997	*The University of Edinburgh Inorganic Chemistry Section Meeting*, Firbush Field Centre, (oral presentation)
27th May 1997	*Science & Engineering Faculty Materials Science Forum*, The University of Edinburgh
4th June 1997	*Butler Electrochemistry Meeting XI*, Glasgow Caledonian University
2-5th September 1997	*RSC Predoctoral Symposium and Autumn Meeting*, The University of Aberdeen
18-19th September 1997	*'Universities of Scotland Inorganic Club'*, The University of Edinburgh (organiser)
12th March 1998	*'Molecules to Materials'* RSC Symposium, Royal Society of Chemistry, London

Date	Meeting
29th April-1st May 1998	*The University of Edinburgh Inorganic Chemistry Section Meeting*, Firbush Field Centre, (poster presentation)
11th May 1998	*Science & Engineering Faculty Materials Science Forum*, The University of Edinburgh (poster presentation)
18th-23rd June 1998	EPSRC-funded CRAC '*Insight into Management*' Course, The University of Stirling
24th-26th September 1998	*MD1: 'Solid State Chemistry: Novel Syntheses & New Materials'*, ICMCB, The University of Bordeaux, France (poster presentation)
7th December 1998	'*New People, New Chemistry*' RSC Meeting, Royal Society of Chemistry, London (oral and poster presentations)
19th April 1999	'*Students in Materials*' EPSRC (Materials Section) Meeting, Motorcycle Museum, Birmingham
28th-30th April 1999	*The University of Edinburgh Inorganic Chemistry Section Meeting*, Firbush Field Centre, (final year seminar)

A.1.2 Lecture Course Attendance

I have attended most Inorganic Chemistry section meetings (where I have given four oral presentations), several Inorganic and Physical Chemistry Colloquia, local RSC lectures and many meetings of the Department of Chemistry Materials Group (where I have given two oral presentations).

Date	Course
31st October 1996	Radiation Protection (X-Rays)
10th April 1997	'Surface Techniques'
11th April 1997	'Protecting and Commercialising Inventions'
6th January 1998	Merck safety lectures
22nd April 1998	'Ligand Design'
6th May 1998	'Computers in Chemistry'
12th November 1998	Radiation Protection (Lasers)
16th February 1999	'Inorganic Synthesis'

A.1.3 Fellowships

28th June-28th August 1999	Monbusho Research Fellowship funded by The British Council, undertaken in the research group of Prof. T. Ohta, Department of Chemistry, The University of Tokyo, Japan.